

The Development of Infrared Scanning Near-Field Optical Microscopy for the Study of Cancer and Other Biological Problems

Timothy Craig

A thesis submitted in accordance with the requirements of the
University of Liverpool for the degree of Doctor in Philosophy



UNIVERSITY OF
LIVERPOOL

Department of Physics
University of Liverpool
UK
October 29, 2016

One of the greatest challenges faced by modern medicine is the increasing prevalence of cancers. Oesophageal cancer has one of the fastest rising incidences in the western world and is often undiagnosed before it has reached an advanced and inoperable state. Early, accurate diagnosis and detailed understanding are crucial in the war on cancer, requiring the development of novel investigative and analytical techniques. The application of infrared (IR) microscopy and spectroscopy to the study of the development, diagnosis, and understanding of cancer has become well established in recent decades, and techniques such as Fourier transform infrared (FTIR) spectroscopy have great potential to further this field. The spatial resolution obtainable by IR techniques, however, is limited by the fundamental diffraction limit of optics to length-scales comparable to typical cellular sizes, limiting the information that can be accessed. There is, therefore, a great need for the development of complimentary techniques that are able to circumvent the diffraction limit and probe the behaviour and progression of cancer on a sub-cellular level.

This thesis describes the development of a fibre-based IR scanning near-field optical microscope (SNOM) with an IR free electron laser (FEL) source, applied to the study of oesophageal cancer tissue samples and cell cultures, with the potential to be applied to many different biological problems. As with the development of any new instrument and technique there were many unforeseen technical difficulties encountered during this work, related to the fibres used, the adaptation of the source and the data acquired during imaging. These were overcome in a coherent and logical process presented in this thesis. This development is reinforced by investigations into different possible analysis techniques using FTIR hyperspectral imaging results obtained on the same tissue samples. The imaging results obtained by the combination of an IR-FEL and fibre-based SNOM demonstrate the potential of this

technique to acquire high spatial and spectral resolution images on cancerous tissues and cells and progress our understanding of cancer. A further study involving many more high spatial resolution images acquired on five different cell lines taken with the IR-SNOM developed in this work is now in progress and the SNOM instrument developed has the capability to be applied to a wide range of biological problems.

Abstract	i
Acknowledgements	v
List of Abbreviations	vi
1 Introduction	1
2 Infrared Microscopy and Spectroscopy	4
2.1 Microscopy	4
2.2 Interaction of Light with an Object	5
2.3 Spectroscopy	7
2.4 The Diffraction Limit	10
2.5 Breaking the Diffraction Limit	13
2.6 Oesophageal Cancer	17
3 Numerical Methods	23
3.1 Software	23
3.2 FTIR Preprocessing	24
3.3 Cluster Analyses	27
3.4 SNOM Preprocessing	29
4 FTIR Hyperspectral Imaging of Oesophageal Tissue	39
4.1 Introduction	40
4.2 FTIR-HSI Experimental Details	40
4.3 Image Data	41
4.4 Hierarchical Cluster Analysis	43
4.5 k-Means Cluster Analysis	49
4.6 Metric Analysis	59
4.7 Conclusions	78
5 ALICE-SNOM Instrument Development	80
5.1 Instrumentation	81
5.2 Characterisation and Principal Developmental Hurdles	90
5.3 Phase I SNOM: Preliminary Investigation	121
5.4 Phase II SNOM: FEL Reference	124
5.5 Phase III SNOM: Inverted Microscope	130

5.6	Phase IV SNOM: Accelerator Development and Transmission Path	138
6	IR-SNOM Imaging of Oesophageal Tissue	142
6.1	Phases II and III: Sets A and B	143
6.2	Phase IV: Sets C and D	151
6.3	Conclusions to Phases I-IV	165
6.4	Phase V: Further SNOM Development	166
6.5	Future Work	171
7	Conclusion	173
A	Sample Information	174
A.1	Tissue Samples	174
A.2	Cell Cultures	174
A.3	Cell Culture Growth Procedure	175
B	Procedures	176
B.1	Sample Dewaxing Procedure	176
B.2	Fibre Etching and Gold Coating Procedure	176
B.3	Cell Slide Preparation for Imaging	177
C	MATLAB Code	178
C.1	RMie-EMSC	178
C.2	Principle Component Analysis	178
C.3	Hierarchical Cluster Analysis	179
C.4	k-Means Cluster Analysis	179
C.5	Fourier Transform Filtering	179
C.6	Other Functions	180
	References	181

ACKNOWLEDGEMENTS

I would like to thank Professor Peter Weightman for the opportunity given to me to work in his group, and for his endless optimism and energy that is a constant inspiration to all of us. I also want to thank the members of the Liverpool SCAnCan group, including Michele Siggel-King, James Ingham, Caroline Smith and Paul Harrison, who have been incredibly supportive and have been a joy to work with over the last four years. Thanks must also go to the Engineering and Physical Sciences Research Council (EPSRC) for the funding necessary for this PhD as well as funding the SCAnCan project.

There were many collaborators involved with the SCAnCan project, all of whom were necessary for it to succeed. Many thanks must go to the team based at Daresbury, especially to Mark Surman along with the team of key commissioners, including Neil Thompson, Yuri Savaliev, David Dunning, Ben Shepherd and many others. I would also like to thank Professor Peter Gardner, Mike Pilling and Paul Bassan for the time on their FTIR equipment in Manchester and their help with both the FTIR-HSI data and with the running of ALICE. I am grateful to all of the second commissioners who have up their time to support the SNOMers and keep everything moving forward. It has never been truer to say that this project would not have been possible without their help.

All this work has, for me, been made possible by the care and support I receive every day from my family. I want to thank my Mum and Dad for everything they have done for me over the years that has brought me to this point.

And to my wife, Victoria, who has given me unending love, encouragement and not inconsiderable patience, I offer my most heartfelt thanks. Without her constant support I would never have gotten this far.

LIST OF ABBREVIATIONS

Analogue to Digital Converter	ADC
Atomic Force Microscopy	AFM
Accelerators and Lasers In Combined Experiments	ALICE
Apertureless Scanning Near-field Optical Microscope	a-SNOM
Attenuated Total Reflectance	ATR
Electromagnetic	EM
Extended Multiplicative Signal Correction	EMSC
Edge Response	ER
Free Electron Laser	FEL
Focal Plane Array	FPA
Fourier Transform Infrared	FTIR
Fourier Transform Spectroscopy	FTS
Full Width at Half Maximum	FWHM
Hierarchical Cluster Analysis	HCA
Hyperspectral Imaging	HSI
Infrared	IR
k-Means Cluster Analysis	KCA
Line Spread Function	LSF
Metric Analysis	MA
Mercury-Cadmium-Telluride	MCT
Modulation Transfer Function	MTF
Numerical Aperture	NA
Negative Predictive Value	NPV
Principal Component	PC
Principal Component Analysis	PCA
Path Length In Air	PLIA
Positive Predictive Value	PPV
Point Spread Function	PSF
Quantum Cascade Laser	QCL
Resonant Mie Scattering	RMieS
Scanning Capacitance Microscopy	SCM
Scanning Electron Microscope	SEM
Scanning Near-field Optical Microscopy	SNOM
Signal to Noise Ratio	SNR
Scanning Probe Microscopy	SPM

CONTENTS

Scattering Scanning Near-field Optical Microscope	s-SNOM
Scanning Tunnelling Microscope	STM
Transmission Electron Microscope	TEM
Tip Enhanced Raman Spectroscopy	TERS
Undulator Gap Scan	UGS
Adjacent Tissue Myofibroblasts	ATM
Cancer-Associated Myofibroblasts	CAM
Deoxyribonucleic Acid	DNA
Gastro-Oesophageal Reflux Disease	GORD
Hematoxylin and Eosin	H&E
Oesophageal Adenocarcinoma	OAC
Oesophago-Gastro-Duodenoscopy	OGD
Oesophageal Squamous Cell Carcinoma	OSCC

Advances in modern medicine have extended life expectancy and increased survival rates for many previously deadly diseases. With the resulting increasingly ageing population, coupled with modern lifestyles, one of the major medical challenges faced in modern times is the increasing incidence of cancers.

The cancer with one of the fastest rising incidences in the western world is oesophageal cancer [1], which, though it represents only 3.2% of global malignancies [2], is often only diagnosed after the cancer has spread, usually becoming fatal. The life and death decision of diagnosing cancers is typically dependent on time-consuming, qualitative histological interpretations of stained sections of biopsies endoscopically retrieved from the affected tissue. Such interpretations are prone to both inter- and intra-observer variability [3] with life-changing outcomes from incorrect diagnoses.

Infrared (IR) techniques are well known to have the potential to provide better, more reliable diagnoses of cancerous tissue than the traditional methods [4] but are limited in their spatial resolution by diffraction effects to super-cellular length scales and Mie scattering of the radiation. There is great interest, therefore, in near-field imaging techniques to give spectroscopic images at sub-diffraction limited spatial resolutions.

In order to probe the sub-cellular behaviour of cancerous tissues a high intensity, high spectral resolution IR light source is required in order to give images combining high spectral and high spatial resolution at a low spectral density. IR free electron lasers (IR-FEL) are ideal to provide this type of output, giving very high output powers over a continuously tunable range of wavelengths.

Thesis Structure

This thesis gives, to the author's knowledge, the first application of fibre-based infrared scanning near-field optical microscopy (IR-SNOM) with an IR-FEL to the study of cancer. Initial experimental investigations into the tissue samples and image analysis techniques using Fourier transform infrared (FTIR) spectroscopy are presented in chapter 4, which led to the development of possible tissue classification methods that could be used for SNOM images. As with any new methodology there were unforeseen problems with the SNOM instrument that needed to be tackled sequentially as they arose, some of which were known, and some of which arose as a consequence of the development and refinement of the instrumentation and imaging methods. This thesis is concerned with the development of the instrumentation for SNOM studies on an IR-FEL and describes sequentially how these problems were discovered and solved in chapter 5. As a result of this, a major part is concerned with instrument development but this does lead to a viable experimental methodology for obtaining images of cancerous tissue and cells with a required combination of high spatial and spectral resolution, as demonstrated in chapter 6.

To clarify the different stages of development, the various experimental and technological hurdles encountered, as well as how different elements of this work impact on the others, figure 1.1 gives a roadmap of the events described in this work. Experimental steps are given as rectangles, experimental hurdles are rounded rectangles and ellipses give the experimental adaptations and developments that took place.

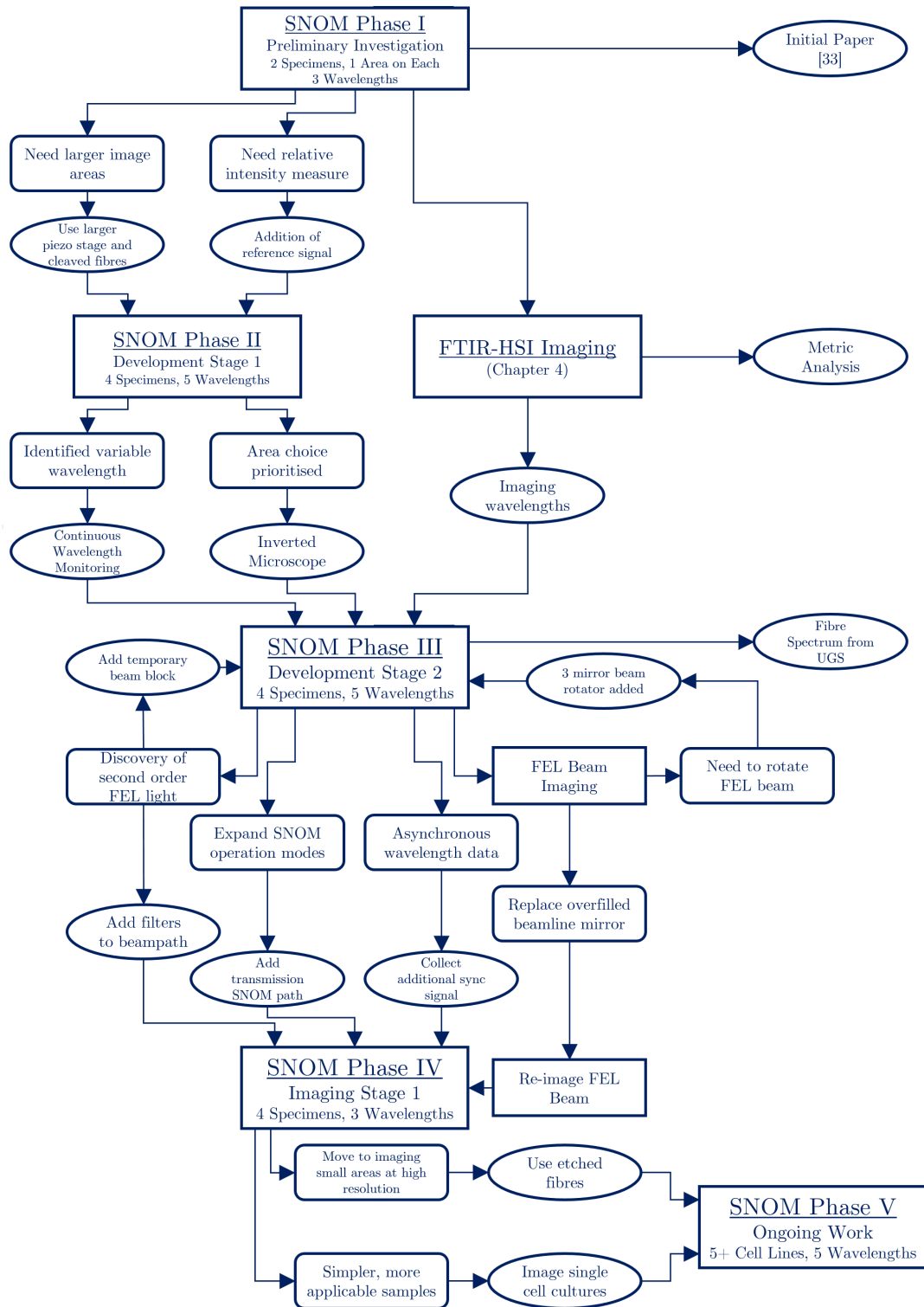


Figure 1.1: A schematic roadmap of the experimental work (rectangles), problems encountered (rounded rectangles) and developmental changes as a result (ellipses) during this work, with arrows indicating influence and consequences.

CHAPTER 2

INFRARED MICROSCOPY AND SPECTROSCOPY

Contents

2.1	Microscopy	4
2.2	Interaction of Light with an Object	5
2.2.1	Reflection and Transmission	6
2.2.2	Absorption	6
2.3	Spectroscopy	7
2.3.1	IR Microscopy and Spectroscopy	7
2.3.2	Fourier Transform Spectroscopy	8
2.3.3	Microspectroscopy: Hyperspectral Imaging	9
2.4	The Diffraction Limit	10
2.4.1	Defining Resolution	10
2.4.2	Diffraction Limited Microscopy	10
2.4.3	Pushing the Diffraction Limit	11
2.5	Breaking the Diffraction Limit	13
2.5.1	Scanning Near-Field Optical Microscopy	13
2.5.2	Applications of SNOM	14
2.5.3	Infrared SNOM	16
2.6	Oesophageal Cancer	17
2.6.1	Barrett's Oesophagus	17
2.6.2	Diagnosis and Treatment of Oesophageal Adenocarcinoma	18
2.6.3	Oesophageal Tissue Samples	19
2.6.4	Application of IR Spectroscopy to Tissue Characterisation	20

2.1 Microscopy

Optical microscopy is arguably the most widely used imaging technique, employed across many fields of research. Its popularity may be attributed to its speed, non-destructiveness

and flexibility, as well as the intuitive nature of the imaging method and information it gathers. Attributing the invention of the microscope to an individual is virtually impossible, as many different definitions of what constitutes a microscope exist. Certainly the first instrument to be called a ‘microscope’ was a two lens system consisting of a concave and a convex lens secured inside a hollow tube, created by Galileo Galilei in the mid 1620s, around the time of the first compound telescopes [5]. A principle aim of microscopy is to create images of objects on much smaller length scales than otherwise attainable, which is generally achieved through the use of magnifying optics, like the lens system employed by Galileo.

2.2 Interaction of Light with an Object

The interaction of an electromagnetic (EM) wave with an object is governed by the object’s complex refractive index $\underline{n} = n + i\kappa$. The real (n) and imaginary (κ) components of this index lead to the processes of reflection, transmission and absorption, demonstrated in figure 2.1.

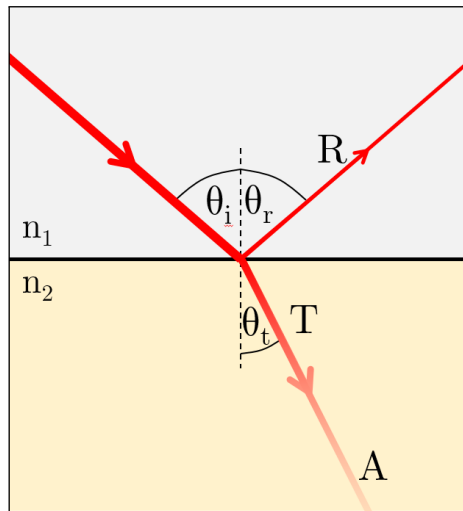


Figure 2.1: The interaction of EM waves with the bulk and boundary between different materials. The complex refractive indices $\underline{n} = n + i\kappa$ lead to three processes: reflection (R) and transimssion (T) at the boundary between two different media, and absorption (A) within the bulk of each medium. R and T are determined by the real component of \underline{n} while absorption is given by the imaginary component.

The portion of a beam that is transmitted through a boundary undergoes a change in direction, called refraction, due to the difference in the speed of light. The angle of refraction,

θ_t in figure 2.1, is governed by Snell's Law:

$$n_1 \sin(\theta_i) = n_2 \sin(\theta_t) \quad (2.1)$$

where n_1 and n_2 are the real components of the refractive indices of the two media and θ_i is the angle of incidence at the boundary.

2.2.1 Reflection and Transmission

The proportion of the EM wave reflected or transmitted from a boundary between two media, the reflectance R and transmittance T , are determined by the value of the real part of the refractive indices of the two media, labelled n , which is given by the relative speed of light in the medium compared to a vacuum: $n = c_{vac}/c_{medium}$. The reflectance of a surface is polarisation dependent and is given by the Fresnel Equations [6]:

$$R_s = \left(\frac{n_1 \cos(\theta_i) - n_2 \cos(\theta_t)}{n_1 \cos(\theta_i) + n_2 \cos(\theta_t)} \right)^2 \quad R_p = \left(\frac{n_1 \cos(\theta_t) - n_2 \cos(\theta_i)}{n_1 \cos(\theta_t) + n_2 \cos(\theta_i)} \right)^2 \quad (2.2)$$

where R_s and R_p are the reflectances for s- and p-polarised light at the boundary. For normal incidence this simplifies to give

$$R = \left(\frac{n_1 - n_2}{n_1 + n_2} \right)^2 \quad (2.3)$$

The transmittance of the boundary is given by conservation of energy such that $T = 1 - R$.

2.2.2 Absorption

As an EM wave propagates through a medium, it undergoes an exponential decay in amplitude determined by the absorbance, A , of the material. The absorbance is governed by the imaginary component of the material's refractive index, κ , according to:

$$\alpha = \frac{4\pi\kappa}{\lambda} \quad (2.4)$$

where α is the attenuation coefficient of the medium and λ is the wavelength of the EM wave. The absorbance of a medium is a function of the path length through the medium, l and is given by

$$A = \alpha l \quad (2.5)$$

To measure the absorbance of a material, a sample's transmittance is usually measured, comparing the intensity transmitted through the sample with the original intensity, and the absorbance calculated using the Beer-Lambert Law:

$$T = 10^{-A} \tag{2.6}$$

2.3 Spectroscopy

In general, the real and imaginary components of the complex refractive index are not constant, but can vary dramatically with wavelength. Spectroscopy is a complimentary technique to microscopy where the focus is on probing the varying properties of a sample at different wavelengths. The ability to measure the dependence of the reflection, transmission, absorption, fluorescence or other optical effects of a sample on the wavelength of the incident radiation can characterise many different properties of the sample and has led to much of our understanding of the physical world.

2.3.1 IR Microscopy and Spectroscopy

The mid-Infrared (IR) regime of EM radiation, with wavelengths between 1 and 10 μm is of particular interest for spectroscopy as the energies of IR wavelengths, given by $E = hc/\lambda$ where h is Planck's Constant and c is the speed of light in a vacuum, correspond to the energy gaps between many different molecular vibrational states. IR spectroscopy therefore probes the chemical properties of a sample, via its transmission and reflection properties.

Chemical bonds with a significant difference in electronegativity between the two bonded atoms produce a molecular electric dipole due to the distortion in the electron clouds of the two atoms [7]. IR photons can interact with these oscillating molecular electric dipole moments if the energy of the IR photon is equal to the energy gap between the molecule's current vibrational state and another, higher energy vibrational state. By absorbing the photon the molecule can be excited to this higher state and the photon is lost, leading to a measurable decrease in the transmittance of the sample at that wavelength. The exact energy, and therefore wavelength, that the photon requires depends not only on the two bonded atoms but also on the specific chemical environment of the bond.

IR microscopy and spectroscopy are therefore able to give the fingerprint of the chemical

species present within a sample based on this absorption mechanism. IR microscopy involves illuminating a sample with a single wavelength and imaging the spatial dependence of the absorption at the corresponding energy. IR spectroscopy uses either a broadband or tunable source to measure the dependence of the absorption on wavelength, giving a spectrum of absorbance against wavelength, and determine the different bonds present within a sample. The most widely used IR spectroscopy technique is Fourier transform infrared spectroscopy (FTIR), a type of Fourier transform spectroscopy (FTS).

2.3.2 Fourier Transform Spectroscopy

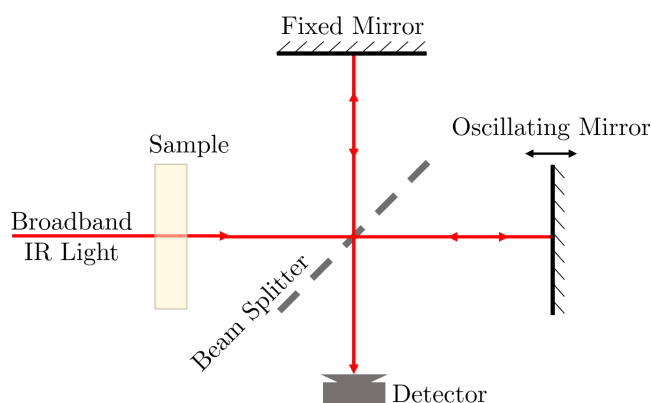


Figure 2.2: Schematic representation of a FTIR Spectrometer. A sample is irradiated with a broadband beam of IR light which then passes into a Michelson interferometer where one half of the beam is incident on a fixed mirror while another is incident on an oscillating mirror of known position with time. The recombined beams encode the spectral information of the sample absorbance in the time domain as each wavelength constructively and destructively interferes with the varying mirror position.

FTS is a powerful spectroscopic technique that uses a broadband source and a Michelson interferometer to measure the absorbance spectrum at a wide range of wavelengths simultaneously. The schematic for FTS is shown in figure 2.2. A broadband source of IR radiation, typically a GloBar blackbody source, is used to irradiate a sample and the resulting transmitted light passes into a Michelson interferometer, where the beam is split in two, with one half incident on a fixed mirror and the other on a mirror oscillating at a known frequency and known position over time. When the two beams recombine they interfere constructively or destructively to different degrees for different wavelengths in the beam, giving the spectral information of the constituent wavelengths of the beam in a time-domain signal called an interferogram, $f(t)$, collected by a detector. To represent this information in the frequency-domain, $F(\tilde{\nu})$ where $\tilde{\nu}$ is the spectroscopic wavenumber $\tilde{\nu} = 1/\lambda$, a Fourier transform is

applied:

$$F(\tilde{\nu}) = \int_{-\infty}^{\infty} f(t)e^{2\pi i\tilde{\nu}t} dt \quad (2.7)$$

FTS can be performed with a wide area of irradiance of the sample, giving an average spectrum over that area, or with a small aperture to restrict the area that is probed.

2.3.3 Microspectroscopy: Hyperspectral Imaging

By combining the spatial resolving power of microscopy with the spectral measurement of spectroscopy, microspectroscopy, also known as hyperspectral imaging (HSI), acquires spectroscopic data over an image area. The intention of HSI is to give the information in the spectral values a spatial component of variation as well, making it a powerful technique. In order to acquire such data, a focussing lens is used with an array of detectors in its focal plane. Often called a focal plane array (FPA), the series of detectors defines pixels of the image area, with the pixel size determined by the focusing optics.

The advantage of this technique over point spectrum acquisition FTIR is obvious in that it acquires a whole image area simultaneously, rather than requiring many separate measurements to obtain a similar type of image. In either case, it is important to consider the resolution of the images - the smallest length scale over which two objects can be distinguished. The first restriction of the resolution is the magnifying lens for the FPA: if a more powerful lens is used, the FPA has a smaller field of view for the same number of detectors and hence a smaller pixel size. The quality of the optics used is also a key factor, as the field of view of the FPA will depend on the numerical aperture (NA) of the lens, the range of angles over which the lens can successfully focus. By using stronger optics and better quality optics both of these factors can be reduced, giving increasingly smaller pixel sizes and thus probing smaller and smaller length scales in the sample. A third restriction on the resolution, however, comes from a hard physical limit placed on every focussing optic: the diffraction limit.

2.4 The Diffraction Limit

2.4.1 Defining Resolution

The resolution of a system is governed by the spatial frequencies that it can measure. A system with a high resolution is able to image small objects with sufficiently high spatial frequencies to construct the image. The smaller the object, the higher the spatial frequency required. This idea is encapsulated by the point spread function (PSF) [8], which describes the signal measured for a point-like signal. The width of the PSF for a given system gives a measure of its resolution, often by using the full width at half maximum (FWHM). The difficulty with using this method of determining the resolution is that the PSF is impossible to measure. An easier measure to determine can be derived from the edge response (ER), the signal measured by the system over a line discontinuity. It is possible to determine the resolution of a system via the ER by taking the range over which the signal changes from 10–90% of the maximum but, for noisy signals especially, this can be unreliable and difficult to determine [8].

A more appropriate method of determining the resolution of an imaging system is to use the system's frequency response [8]. From the ER the one-dimensional line spread function (LSF), similar to the PSF, can be found by taking the derivative with respect to distance:

$$LSF = \frac{\partial ER}{\partial x} \quad (2.8)$$

Applying a Fourier transform to the LSF gives the modulation transfer function (MTF) of the system. The MTF describes how well the system responds to increasing spatial frequency, and by taking the spatial frequency at which the system response has decayed to 10% another, more reliable measure of resolution can be obtained from the corresponding spatial period. Signals on this length scale are detected with a threshold 10% sensitivity.

2.4.2 Diffraction Limited Microscopy

The resolution of an instrument is determined not only experimentally by the quality of the optics used, but also fundamentally by the so-called 'diffraction limit' imposed upon all optical systems [9]. The discovery of the diffraction limit is often attributed to Ernst Abbe [9, 10] who, in 1873, discussed the resolution limit for visible light microscopy, describing it

as half the wavelength of blue light. This can be generalised for any wavelength, λ , of the EM spectrum using equation 2.9a:

$$\Delta d_{limit} = \frac{\lambda}{2n \sin \theta} \quad (2.9a)$$

where Δd_{limit} is the smallest resolvable length scale, n is the real component of the refractive index of the ambient medium (~ 1 for air) and θ is the objective lens half aperture angle. For an ideal lens ($\theta = \frac{\pi}{2}$) this simplifies to

$$\Delta d_{limit} = \frac{\lambda}{2} \quad (2.9b)$$

It is crucial to note the distinction between the limit imposed by the imperfection in the lenses, which can be improved upon, and the intrinsic physical limit placed upon the resolution by the imaging method itself.

For visible light the diffraction limit defines a minimum length scale of ~ 200 nm, sufficiently small to image the nuclei of cells (on average for human cells ≈ 6000 nm [11]), and even mitochondria (typically > 500 nm [12]) though smaller structures become difficult to resolve.

2.4.3 Pushing the Diffraction Limit

There have been several methods proposed to decrease, overcome or bypass the diffraction limit placed upon resolution. The first and simplest solution is to merely image using a shorter wavelength, giving a smaller minimum length scale. This has an obvious advantage in that the technique used is identical in principle to the original method employed, and so carries many of the above benefits, but introduces the difficulty of manufacturing the necessary optics to focus the light, a task that increases in difficulty the shorter the wavelength used. In addition to these considerations, imaging with different wavelengths (and therefore energies) of light is likely to change the origin of image contrast as new absorption mechanisms and energy regimes (such as infrared vibrational bands of organic molecules) are accessed; on one hand this increases the possible information that can be obtained by microscopy, but on the other hand the images produced at invisible wavelengths may be harder to interpret, and may not even contain the desired information at all.

A related approach is to use the same wavelength of radiation, but perform the measure-

ment inside a medium with a much higher refractive index, thus reducing the wavelength without altering the energy of the radiation and thus the information accessed. Attenuated total reflectance (ATR) is a spectroscopy technique that uses a prism of high refractive index, typically germanium or zinc selenide [13], on which the sample is mounted to perform the measurement. Total internal reflection at the prism-sample interface creates an evanescent field within the sample which undergoes absorption and influences the reflected beam.

In addition to imaging using shorter wavelengths of electromagnetic radiation, it is possible to use a different form of radiation for which it is easier to achieve a shorter wavelength, such as electrons in a transmission electron microscope (TEM) or scanning electron microscope (SEM). By using a beam of electrons, the wavelength of the incident radiation can be easily controlled: their de Broglie wavelength is given by the accelerating energy E applied to the beam. Applying a relativistic correction to the de Broglie condition gives [14]:

$$\lambda \approx \frac{h}{\sqrt{2m_0E \left(1 + \frac{E}{2m_0c^2}\right)}} \quad (2.10)$$

where m_0 is the rest mass of the electrons, h is Planck's constant and c is the speed of light in vacuum. Such techniques therefore give a diffraction limit on the order of 1 pm for an accelerating voltage of 100 kV but this exceeds the ability of the focussing components, so this cannot be utilised. More typical resolutions are around 1 nm. Despite the huge increase in spatial resolution, these techniques lose a significant amount of the intuitiveness and ease of use that conventional microscopy possesses, due to the often restricted conditions required for imaging and the change in contrast mechanism.

While the above methods improve the possible resolution by essentially reducing the size of the diffraction limit by using shorter wavelength radiation, they are still diffraction limited. In order to circumvent the diffraction limit entirely, a modified microscopy technique must be used. A metamaterial lens was proposed by JB Pendry [15] which uses negative refraction to form a non-diffraction-limited image by focusing all the Fourier components of the object. This has been demonstrated for microwave radiation [16] but the engineering difficulties in producing metamaterials makes refining this a significant challenge. Imaging in, or using, the near-field, that is the non-propagating component of the electromagnetic field at a distance from the object $z \ll \lambda$, is a more achievable technique that allows the non-propagating evanescent waves, which are not subject to the diffraction limit, to be accessed without the

need for the diffraction limiting lens systems of conventional microscopes, forming images with much higher spatial resolution [17].

2.5 Breaking the Diffraction Limit

The concept of near-field imaging was appreciated as early as 1928 [17], despite this, the first demonstration was not until 1972, by Ash and Nicholls [18] using an illuminating beam shone through a small hole in a screen, modulated at a fixed frequency by oscillating the sample such that the aperture was periodically closed by the sample. This was done at a wavelength of ≈ 3 cm as the constraints were then easier to meet than at visible wavelengths by a factor of several hundred, but the spatial resolution obtained, $\frac{\lambda}{60}$, significantly exceeded that given by the diffraction limit.

2.5.1 Scanning Near-Field Optical Microscopy

The technique of SNOM uses a small aperture ($a < \lambda$), typically an optical fibre with some form of tip, brought close ($z \ll \lambda$) to a sample to either illuminate or collect light from the surface. The tip and sample are then scanned laterally with respect to each other, and a constant tip-sample distance maintained through some feedback mechanism, usually by maintaining a constant shear force at the tip as in atomic force microscopy (AFM) [19] as this places the least constraints on the tip/sample materials and geometry, though electron tunnelling [20] and capacitance [21] can be used for conductive samples and tips. By monitoring the height of the tip, simultaneous optical and topographical images are recorded across the scan area. SNOM has a further advantage in that no special conditions, such as ultra high vacuum (UHV) or low temperatures, are required.

It was some time after its first demonstration that SNOM was achieved at visible wavelengths by Pohl *et al.* in 1984 [22]. The delay was chiefly due to the technological advancements required to control the lateral scanning of the sample on the nanometric scale required for visible light. This advancement came in the form of the piezoelectric technology employed by Binnig and Rohrer in their new scanning tunnelling microscope (STM) in 1982 [23] and allowed the development of a whole new range of techniques, given the general label SPM, which consist of a small probe brought close to a sample surface and scanned laterally over it, with a feedback mechanism maintaining the separation between tip and

sample, using piezoelectric drivers to reach nano-scale resolution. In addition to SNOM and STM are AFM [24], scanning capacitance microscopy (SCM) [19] and many others. Possibly the closest SPM technique to SNOM is non-contact AFM, where an oscillating metal probe interacts with the nearby surface via Van der Waals forces, damping the oscillation of the probe and leading to a reduction in the amplitude. The AFM feeds back on this reduction, driving the tip closer or further away from the sample surface using a piezoelectric driver to maintain a constant deviation from the natural frequency and keep a constant tip-sample separation. By reading the z-position of the tip, the height and other parameters of the surface can be measured.

SNOM does have several drawbacks that are a consequence of the method of acquisition of the images. The main drawback is that the imaging is much slower than conventional microscopy or microspectroscopy, taking pixels one at a time can take many minutes to take even a small image. There are many experimental difficulties associated with SNOM derived from its SPM nature, especially the dependence of imaging on the quality of the tips and reliability of the feedback mechanisms used. Despite the technical difficulties, SNOM still retains the flexibility and non-destructive nature of far-field microscopy that made it the powerful technique it is.

2.5.2 Applications of SNOM

Since its development, SNOM has been applied to a wide range of sample types and in a variety of different configurations. Initially SNOM was used to image metal surfaces [22, 25, 26] as these provide a large optical contrast, but has also extensively been applied to thin films and layered structures [27, 28], and semiconductors [29]. More recently the focus has shifted to imaging biological samples, specifically: cells and biological thin films [30, 31], neurons [32], and cancerous tissue [33].

There are four principal configurations (see figure 2.3) which fall into two categories: using the tip for illuminating in the near-field and collecting at a far-field detector (*illumination mode*), or illuminating in the far-field and using the tip to collect in the near-field (*collection mode*). In addition to these modes, the light that is collected can either be transmitted through the sample (*transmission mode*) or reflected from the surface (*reflection mode*).

Each configuration has advantages and limitations, for example transmission mode bears much more resemblance to conventional microscopy in its geometry, and so the images pro-

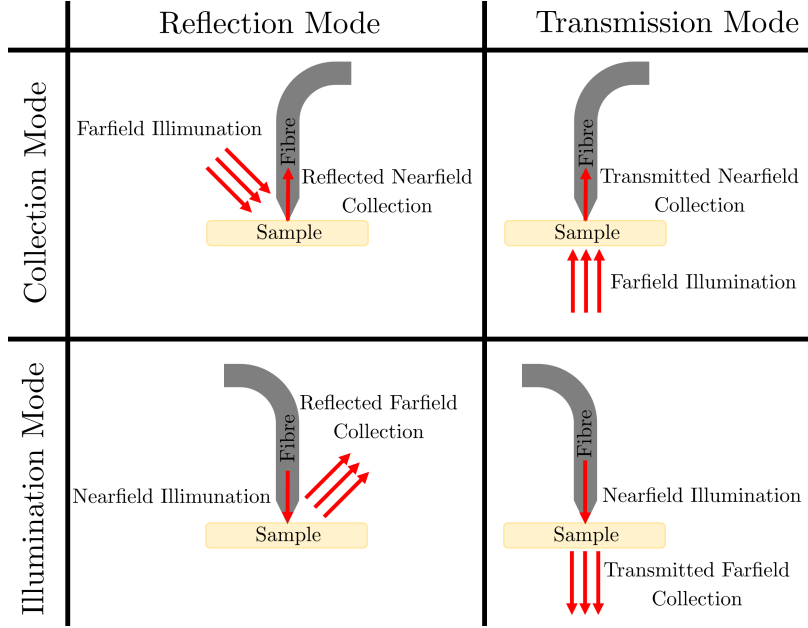


Figure 2.3: The four general configurations of SNOM. Images can be collected either in Illumination, where the tip transmits light to the sample in the near-field to be collected in the far-field, or Collection mode, where the tip collects far-field radiation from a source in the near-field. Both of these modes may be operated in transmission or reflection with the sample, making SNOM very adaptable to a wide variety of different sample types and experimental geometries.

duced are often more intuitive to interpret, while for opaque samples, reflection SNOM is necessary [19]. Most initial SNOM experiments were done in illumination mode [22, 26, 27, 34] possibly due to the difficulty in coupling the fibre to a detector, and mainly in transmission, meaning that the most common configuration in past literature is *transmission-illumination*, with *reflection-collection* also relatively common [32, 35].

There are additional modes of operation beyond the basic four shown in figure 2.3 including *illumination-collection* mode [29] in which the tip acts as both source and detector in the near-field. A family of similar techniques use a metal tip in the near-field of the sample to influence the far-field, apertureless-SNOM (a-SNOM) or scattering-SNOM (s-SNOM) [36, 37, 38] scatters the near-field component of a sample illuminated and imaged in the far-field. Atomic force microscopy infrared (AFM-IR) uses the tip to measure the local thermal expansion of the sample when irradiated with pulses of IR light [39]. The collection of all of these techniques represent a combination of spectroscopy with sub-diffraction limit imaging. A similar technique to a-SNOM is tip enhanced Raman spectroscopy (TERS) [40] which used the same principle of interacting in the sample near-field to enhance the resolution of Raman spectroscopy. The drawback of using Raman spectroscopy is that the spatial resolution that can be obtained is limited by the inefficiency of generating the Raman signal,

necessitating such a high illuminating power density to obtain sufficient resolution that the sample is likely to suffer thermal damage [41].

As mentioned above, there are significant technological hurdles associated with SNOM, not least of which is the fine motor control required to scan the tip close to the sample surface on a nanometric scale. The structure and creation of tips is another difficulty that has received considerable attention. In general, SNOM tips comprise an optical fibre, brought to a tapered end either by chemical etching [42] or thermal pulling [43], and then coating with an optically opaque layer, such as aluminium, leaving a sub-wavelength aperture at the tip. Another difficulty is the weak signal strength; evanescent waves are by their nature weak, and coupling these with the fibre is an intrinsically high-loss process, meaning that a very intense light source is required.

By using a tunable light source, it is possible to use SNOM for spectroscopic measurements, either by imaging the same area at several wavelengths [30, 33], or by sweeping the wavelength at a single point [44, 29]. This is one of the most powerful applications of SNOM; because it has the ability to take spectroscopic information on a local scale at sub-diffraction-limit resolution, it is able to provide a much richer source of information than conventional spectroscopic techniques.

2.5.3 Infrared SNOM

While significant work with SNOM is performed at visible wavelengths, the application of SNOM to IR wavelengths is particularly powerful, because for many samples of interest, especially tissues and cells, in the IR the length scales involved are on the order of the size of the wavelength. By circumventing the diffraction limit, sub wavelength imaging can give a much deeper insight into many different types of samples.

IR-SNOM has been applied to organic thin films [44] and keratinocyte cells from human skin [35] showing successful imaging at length scales much less than the wavelength of IR light. By imaging oesophageal tissue biopsy samples with IR-SNOM the subcellular development of oesophageal cancer can be investigated without the need for stains or fluorophores and with the potential to provide more quantitative measures of the samples.

IR-SNOM presents several additional challenges compared to visible SNOM. The necessity for an intense, tunable source is more challenging at IR wavelengths. Perhaps the best type of light source, in terms of both intensity and tunability, is a free electron laser (FEL)

[45] which uses synchrotron radiation emitted from an oscillated beam of electrons in a laser cavity as the lasing mechanism, are capable of very high powers and are continuously tunable over a range of wavelengths. This gives a high degree of flexibility and easily provides the intensity of light required [33, 46]. In recent years the development of the quantum cascade laser (QCL) has provided another potentially viable option [38] though the pulse structure of a FEL, giving a higher peak power and lower average power, is advantageous when imaging tissue samples to avoid damage to the sample. Another particular challenge for IR-SNOM is the use of IR transmitting optical fibres. The chalcogenide glasses As_2Se_3 and As_2S_3 are the best candidates for making these fibres with, but they are extremely fragile materials, making the creation of tips and sample imaging much more difficult.

2.6 Oesophageal Cancer

Oesophageal adenocarcinoma (OAC) is a cancer with one of the fastest rising incidences in the western world [1] and with a particularly asymptomatic clinical presentation. It is more often than not diagnosed too late for effective treatment [47]. In the UK the crude incidence and mortality rates of oesophageal cancer were found to be 14 and 12.6 per 100,000 population respectively by the GLOBOCAN 2012 project [2]. The prevalence of Barrett's Oesophagus in the general population is difficult to quantify, with many cases being asymptomatic, but is likely higher than 376 per 100,000 [48]. Many factors can contribute to the development of OAC, particularly drinking, smoking and obesity, and in particular, people with a condition called Barrett's oesophagus are 30-40 times as likely to develop OAC as the general public [49] with around 0.5% of people with Barrett's Oesophagus developing OAC per year [48]. Due to this significant effect, Barrett's oesophagus is considered a precursor condition to OAC and patients with Barrett's oesophagus attend regular endoscopies where biopsies of the affected areas of the oesophagus are taken. These biopsy samples are then examined by a histologist to assess the state of disease.

2.6.1 Barrett's Oesophagus

Barrett's oesophagus is characterised by the *metaplasia* (where mature cells of one type are replaced with those of another) for the normal stratified squamous epithelium (figure 2.4a) that lines the oesophagus into a columnar epithelium that more closely resembles

the lining of the stomach (figure 2.4b) [50]. Barrett's oesophagus is most often caused by gastro-oesophageal reflux disease (GORD) which leads to chronic acid reflux into the oesophagus. The cells at the junction between the oesophagus and the stomach respond to the change in their environment, adapting to more closely match the stomach lining. The columnar epithelium is a glandular tissue and creates deep, rounded pits called crypts in the normally smooth lining. At the bottom of these crypts, the glycoprotein mucin is created in specialised cells known as goblet cells. The metaplastic tissue can then become *dysplastic* (abnormally developed) which is considered a pre-cancerous stage (figure 2.4c). There are many definitions of how dysplasia presents. In general it is a term used to describe the morphological changes that occur in the tissue and comprises many changes such as deformations of the glandular crypt structures and larger, more disordered and irregular nuclei. Montgomery et al. [47] found that 'High Grade' dysplasia was strongly indicative of the development of cancerous tissue, and thus should be the stage at which the patient undergoes treatment. This final stage of development is known as *neoplasia*, an abnormal growth of new cells invasive to the surrounding tissues (figure 2.4d). The form of the cancer can vary dramatically from patient to patient, leading to a grading that represents how well *differentiated* the tumour cells are, or how closely they resemble the microscopic appearance and structure of the original cells they developed from. Poorly differentiated cancers bear little resemblance to the original tissue, with the cells appearing immature and unstructured, more closely resembling, and expressing more characteristics of, embryonic stem cells [51]. As such, poorly differentiated cancers tend to be more aggressive and have a poorer prognosis.

2.6.2 Diagnosis and Treatment of Oesophageal Adenocarcinoma

The chief aim of the routine biopsies that Barrett's oesophagus patients undergo is to assess the presence and progression of any dysplasia within the Barrett's tissue. The assessment is performed by taking a thin section of the biopsy and staining it with a suitable tissue stain to reveal the underlying structures of the tissue, which is otherwise transparent and colourless. One such stain that is frequently used is Hematoxylin and Eosin (H&E) which highlights the Deoxyribonucleic Acid (DNA) and protein components of the tissue, as shown in figure 2.5. This stained section is then examined under an optical microscope by a trained histologist who must then gauge the grade of the tissue based on a loose collection of guidelines. This evaluation is highly subjective and qualitative and as such is prone to inter-

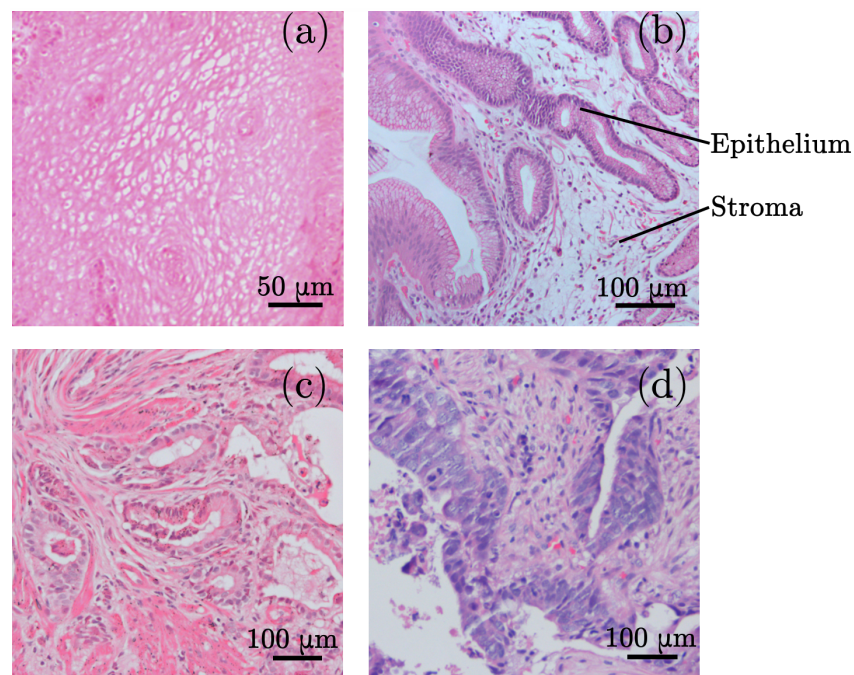


Figure 2.4: Microscope images of tissue samples, stained with a Hematoxylin and Eosin stain showing the stages of Barrett's oesophagus and oesophageal adenocarcinoma from (a), stratified squamous epithelium, through (b), metaplasia to Barrett's oesophagus, and (c), dysplasia, to (d) oesophageal adenocarcinoma. While the initial and final states are easily distinguished, the task of determining which samples will become cancerous, before they have already fully transitioned, is much harder. Labelled in (b) are the two principal tissue components, the epithelium and stroma.

and intra-observer variability [3]. A study in [47] found that for 138 patients, a group of 12 histologists reached a majority conclusion in only 99 cases (72%). The difficulty in reaching a reliable diagnosis is particularly problematic given the serious implications of misdiagnosis: a false positive leads to unnecessary and potentially dangerous surgery, while a false negative leads to a patient that potentially has an invasive carcinoma going unnoticed and delaying treatment. Any delay in treatment for any cancer has serious consequences, and so reliably grading and diagnosing the presence of dysplasia and adenocarcinoma of the oesophagus is of vital importance.

2.6.3 Oesophageal Tissue Samples

The oesophageal samples used in this work were biopsy samples taken during routine endoscopy from patients with Barrett's oesophagus and OAC, a procedure called an oesophago-gastro-duodenoscopy (OGD). Several biopsies were taken in the procedure and each sample consists of a number of biopsies. Sample information, including ethical approval and prepa-

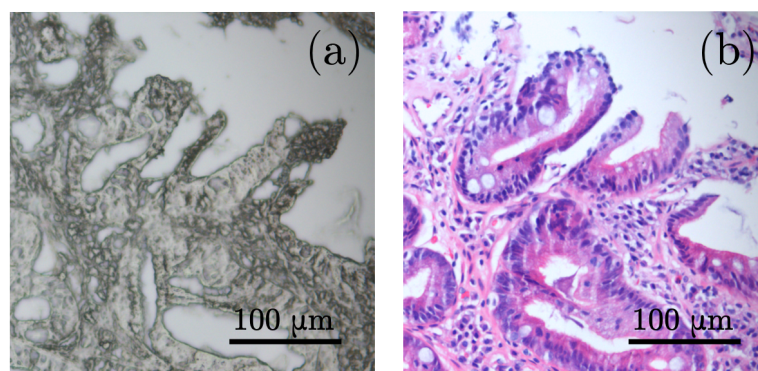


Figure 2.5: An example of Hematoxylin and Eosin (H&E) stain with two serial sections of a biopsy, (a) unstained and (b) stained with H&E to highlight the DNA (blue) and protein (red). This and other such stains can reveal the chemical information in the sample, but only lend themselves to qualitative analysis using a microscope.

ration are given in appendix A ¹. Before imaging the wax was removed from the samples using Xylene and the disks were allowed to air dry for two hours (see appendix B.1 for the dewaxing protocol used). This procedure also removed the lipids (fatty compounds) from the sample as they are also soluble in xylene, but left the rest of the tissue intact.

2.6.4 Application of IR Spectroscopy to Tissue Characterisation

The use of IR spectroscopy to study biological samples is well established. The various organic molecules that comprise the tissues and cells imaged in this work express characteristic absorption bands that can be used to explore the structures and concentrations of different biological components. Previous IR studies in both far- and near-field directed at the understanding and diagnosis of cancer tissues have included investigations of breast cancer [52], colon cancer [53], prostate cancer [54], melanoma [55], brain cancer [56] and many others. The wealth of information provided by IR spectroscopic techniques such as FTIR and Raman spectroscopy has made them a staple of biomedical research.

Figure 2.6 shows a typical spectrum obtained on a Barrett's oesophagus sample, displaying two spectral regions. The functional group region contains relatively few absorption bands, typically consisting of stretching modes with the strongest from C–H, O–H and N–H bonds. The fingerprint region contains many absorption bands mostly corresponding to various bending modes of different molecular species.

A common approach towards the interpretation of the fingerprint region is through the

¹All sample staining and sectioning was performed by Mr David Berry, Institute of Translational Medicine, University of Liverpool

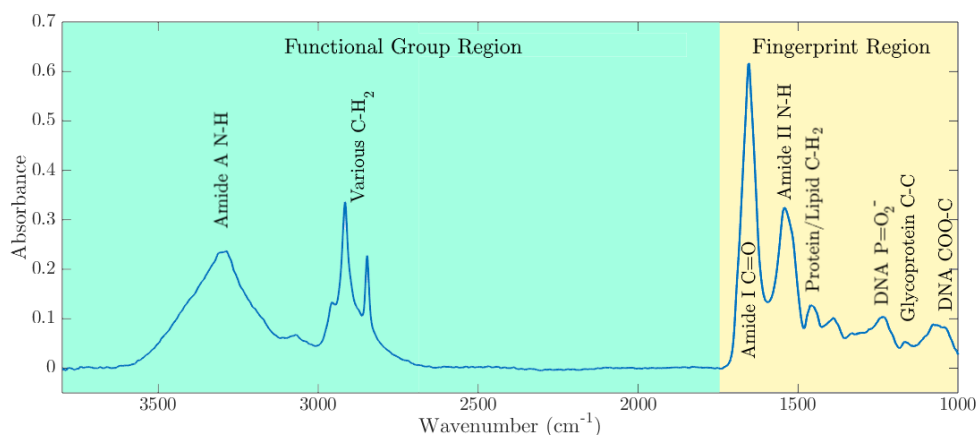


Figure 2.6: The IR absorbance spectrum from a point on a Barrett's oesophagus tissue sample. The spectrum can be divided into two regions, the functional group region and the fingerprint region. The latter region contains many characteristic absorption bands corresponding to bending modes of many biologically relevant molecules. Key biological bands are labelled with the principle biomarker and chemical bond responsible.

use of a minimalistic model, based on the identification of simple absorbance bands that are assigned to a small number of classes of biologically important chemical species, or biomarkers [57]. The principal bands in the fingerprint region are given in table 2.1, identified using references [55, 58, 59]. The exact peak location depends on the chemical environment of the relevant bonds, and varies slightly in different types of tissue [58], thus the wavelength or wavenumber of the absorption band differs slightly between different reference sources. The wavelengths and wavenumbers given in the table are for the Barrett's oesophagus tissue, and are given a corresponding biomarker tissue component that is the principal source of the absorption band.

Wavenumber (cm^{-1})	Wavelength (μm)	Vibrational Mode	Assigned Biomarker
1051	9.51	COO–C Stretch	DNA
1081	9.25	P=O ₂ ⁻ Stretch	Glycoprotein / DNA
1164	8.60	C–C Stretch	Glycoprotein
1237	8.08	P=O ₂ ⁻ Stretch	DNA
1455	6.87	C–H ₂ Bend	Protein / Lipid
1545	6.47	C–N Stretch / N–H Bend	Protein (Amide II)
1650	6.06	C=O Stretch	Protein (Amide I)
2924	3.42	C–H ₂ Stretch	Lipids
2955	3.38	C–H ₂ Stretch	Lipids
3285	3.04	N–H Stretch	Protein (Amide A)

Table 2.1: The main biological vibrational bands present in the IR spectrum of tissue. Each wavenumber and wavelength have the main vibrational mode associated with the peak and the corresponding biological molecule that can be assigned to them. It is important to note that the assigned biomarkers are not the only source of these bands, simply the strongest.

Contents

3.1	Software	23
3.2	FTIR Preprocessing	24
3.2.1	Mie Scattering Correction	24
3.2.2	Integral Normalisation	25
3.2.3	Principal Component Analysis	25
3.3	Cluster Analyses	27
3.3.1	Hierarchical Cluster Analysis	28
3.3.2	k-Means Cluster Analysis	29
3.4	SNOM Preprocessing	29
3.4.1	FEL Intensity Correction	31
3.4.2	Piezo Correction	31
3.4.3	Alignment	36
3.4.4	Image Filtering	37

This chapter describes the numerical methods used during this work, including data preprocessing and techniques used for data analysis.

The data analysed during the course of this work vary significantly in structure, size and type, such that several different preprocessing and analysis techniques were employed. The following section details the mathematical techniques and software that were used to perform the various analyses in this work.

3.1 Software

The software used to process the data collected during this work was MATLAB, an interactive programming environment that can be used for numerical analysis and data

visualisation and processing [60]. This work made use of many of MATLAB's useful built-in functions, as well as a large amount of self-built functions and graphical user interfaces to process the various data as required. Further details of each of some of the MATLAB functions used for this work are given in appendix C.

3.2 FTIR Preprocessing

The FTIR images obtained during this work were in the form of three dimensional cubes of data, with the first two dimensions representing the values of a 128×128 pixel array, and the third dimension giving values at 1479 wavenumbers, giving a spectrum at each pixel location. The images were subjected to three stages of preprocessing: (i) a numerical correction for the effect of Mie scattering in the sample [61], (ii) normalisation of each spectrum by its total integral absorbance, and (iii) dimensionality reduction using principal component analysis.

3.2.1 Mie Scattering Correction

Mie scattering is the name given to the solution to Maxwell's equations that governs the interaction of light with homogeneous spherical scatterers. The solution of these equations can be greatly simplified using approximations in the cases where the wavelength $\lambda \not\approx a$ where a is the diameter of the scattering spheres, in particular Rayleigh scattering for $\lambda \gg a$ describes how light interacting with the Earth's atmosphere gives a scattered intensity $I \propto \frac{a^6}{\lambda^4}$ and so blue light is scattered much more strongly than red, leading to a blue day-time sky and a red sunset. For IR spectroscopy of tissue, the typical length scales are around $5-20 \mu\text{m}$, so the Mie Scattering solution does not have a simple approximation, and a more direct accurate approach is required. So-called resonant Mie scattering (RMieS) results in a suppression of the higher wavenumber side of absorption band peaks in the spectrum and thus a shift in the observed position of the peaks towards lower wavenumbers [62]. In this work, the FTIR spectra were all corrected for the effects of RMieS using an algorithm developed by Bassan *et al.* described in [61, 63] as an extension of the extended multiplicative signal correction (EMSC) described in [64, 65]. The parameters used for the algorithm are given in appendix C. The corrected spectra have a slightly reduced range, giving 1453 spectral values each. The results of applying the correction to an example spectrum are shown in figure 3.1a-b

below.

3.2.2 Integral Normalisation

The samples were dewaxed prior to imaging, removing the spectral and physical influence of the wax, but leading to variable sample thickness, particularly at the edges of the tissue and within the areas of stroma, fibrous areas of connective tissue. To compensate for the variable thickness, which leads to variable absorbance, the integral intensity recorded at each pixel, representing the total absorbance over the spectral range of the image, was normalised:

$$\alpha_{norm}(x, y, k) = \frac{\alpha(x, y, k)}{\int_{range} \alpha(x, y, k) dk} \quad (3.1)$$

Although this compensates for the sample thickness, any particularly transparent sections of tissue, or especially thin areas, will have enhanced spectral features as a result of the normalisation. To compensate for this, an additional quality control was placed on each spectrum: if the total absorbance of a pixel fell outside of the range 80 – 520 (arb. units) the pixel was discarded. In such a manner, any pixels corresponding to gaps in the tissue or particularly highly scattering or absorbing debris were removed from the data.

3.2.3 Principal Component Analysis

In the analysis of large data sets there is often a need for data compression, usually in the interests of processing and analysis time. The spectra produced by the FTIR spectrometer comprise 1453 points (after the Mie scattering correction) and therefore the 128×128 hyperspectral cube contains a large quantity of data. As each peak has an associated width that spans several wavenumbers of the spectrum, adjacent points are likely to behave similarly, leading to a linearly dependent set of spectral points. The result of such linear dependence is that some parts of the spectral information are redundant, and the dimensionality of the data can be reduced without losing a significant amount of the information they contain.

Principal component analysis (PCA) can be used to reduce the dimensionality of the data while preserving the principal variations between them, as well as identifying key patterns within the data set [66]. The original 1453 spectral points can be taken to represent a 1453-dimensional space in which each pixel is located according to the absorbance at each wavenumber of its spectrum. PCA creates a new, linearly independent set of orthogonal axes

3.2. FTIR PREPROCESSING

for the data, called principal components (PC). These axes are ordered such that the first PC is aligned along the direction with the strongest variance in the original data set, essentially plotting a line of best fit through the data. The second PC is then defined orthogonal to the first in the direction with the next highest variance. This process is repeated until the total dimensionality is reproduced. Because the new dimensions are ordered in terms of variance in the data set, if there is a strong linear dependence a significant number of the later dimensions will provide very little variation across the data set, and so can be discarded, reducing the total size of the sample data, but retaining the information contained within it. The details of the usage of PCA in this work are given in appendix C.

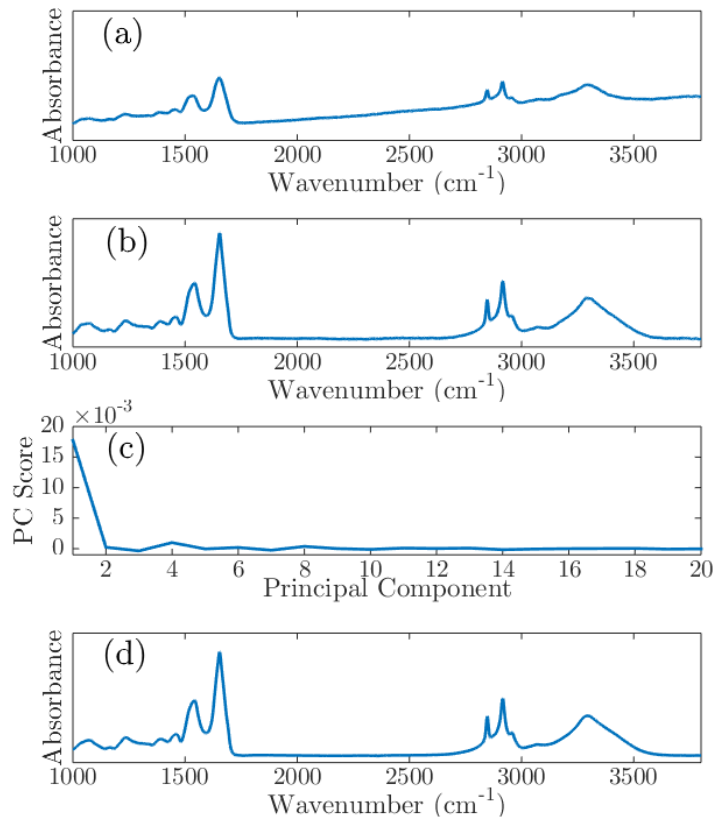


Figure 3.1: The spectrum of a pixel taken from one of the FTIR images. (a) the original spectrum prior to processing; (b) the same spectrum after correcting for Mie scattering; (c) the spectrum in terms of the 20 calculated PC of the whole combined data set; (d) the same processed spectrum projected back onto the original set of wavenumbers. The Mie scattering correction gives a big improvement to the spectrum. The PCA does not remove any visible structures from the spectrum when projected back, and most of the structure of the spectra after PCA are given by the first PC.

The information contained within the FTIR data set was found to be very well preserved

by retaining even only the first 20 PC. Figure 3.1 shows a pixel before and after a PCA to only 20 components. These PCs describe 99.83% of the variance of two combined images, and as such was taken to be a good approximation to the original image, while reducing the number of data values needed to describe each pixel by a factor of approximately 73. The first 10 PCs still described 99.6% of the image variance, but the difference in processing time for the most part between 10 and 20 components was considered minimal. To highlight the redundancy of the majority of the spectral data when considering inter-pixel variation, the first principle component accounts for 91.7% of the total variation in the two images, which implies that to describe the data using simply a modulation in amplitude of an average spectrum would retain 91.7% of the information contained within the images. It is important to note that PCA was not used for the SNOM image data as the dimensionality was much lower.

3.3 Cluster Analyses

Cluster analysis is a technique for algorithmically assigning data to groups, or clusters, according to some relational parameter between them [67]. The parameter used in this work was the Euclidean distance between the data in the n-dimensional space in which it is described. For the FTIR data this space is given by the first 20 PC, so the Euclidean distance is given by:

$$\delta_{ij} = \sqrt{\sum_{p=1}^{20} (\alpha_i(p) - \alpha_j(p))^2} \quad (3.2)$$

where δ_{ij} is the distance between the i^{th} and j^{th} points and $\alpha_i(p)$ is the PCA resultant “absorbance” of the i^{th} point at PC number p . The cluster position within the 20-dimensional space is given by the *Centroid*, calculated by taking the average position of the cluster’s data, calculated using the same distance measure.

The power of cluster analysis is that it is able to group data according to their relative similarity or difference without needing any user input. It is therefore an entirely unguided, automated technique which is able to distinguish patterns in data which would be impossible to perceive by the human eye. The only effect the user has on the outcome of the analysis is in deciding how many clusters to create, although it can be possible to procedurally decide this parameter [68]. There are two types of clustering algorithm considered here: hierarchical

cluster analysis (HCA) and k-means cluster analysis (KCA).

3.3.1 Hierarchical Cluster Analysis

HCA, as the name suggests, creates a hierarchy of clusters, each time the cluster number increases, one of the clusters is split into two, while the others remain unchanged. The method for determining the hierarchy begins by assigning a cluster to each observation in the data set. The two clusters that are closest, as measured by the chosen distance measure, are combined to form one larger cluster, a process that is repeated until the data is all in one cluster, recording the cluster contents and distances at each stage. It is easy to see that for larger data sets this task becomes increasingly demanding in terms of both processing power and memory load.

HCA is performed via a chain of processes to produce the hierarchical tree, or dendrogram, that displays how the clusters join: which clusters are joined (represented by the numbered 'leaves' of the diagram), in what order and at what distance (represented by the position and length of each branch on the x -axis). In a dendrogram the links and distances between each of the joined clusters are shown as a series of brackets, the position of which give the distances between the centroids of each of the clusters being agglomerated. The dendrogram is a very useful tool in visualising how the data is arranged and what sort of clustering the data displays. It also allows the most appropriate number of clusters to be determined, either visually or numerically.

The most appropriate number of clusters can be loosely defined as the number at which the distances between the closest two of the remaining clusters is inconsistent with the distances between the clusters joined in the previous iterations. Clearly if the clusters are at a dramatically larger distance than their components were from each other, then the link is joining two distinct groups of data together, rather than joining similarly spaced, neighbouring data. This can be seen visually in the dendrogram by simply looking for unusually long brackets, or numerically during the clustering process by specifying an inconsistency coefficient cut-off value. The FTIR data set, even after dimensionality reduction with PCA, is a large enough data set that running the MATLAB functions takes a significant amount of time. The number of clusters that is most appropriate can be determined by examining the dendrogram of the cluster distances.

3.3.2 k-Means Cluster Analysis

In contrast to HCA where the number of clusters is determined after the majority of the data processing, KCA requires the number of clusters to be specified at the beginning. The specified number of clusters is created randomly at first by distributing the centroids at random locations within the data. The data points closest to each centroid, as determined by the chosen distance measure, are assigned to its cluster, and new centroids are determined from the average positions of each cluster's contents. The process is repeated - reassigning clusters based upon the new centroid locations and recalculating new centroids - until the cluster assignments converge on a solution. Depending on the initial placement of the centroids, there may be several stable solutions and so the clustering process can be repeated and the optimal solution identified. The optimal solution is that which minimises the total distance of every point to its centroid.

This method of clustering is simpler to visualise and easier to use than HCA; it is, however, limited by requiring the number of clusters as a user input. While HCA is able to determine the most appropriate number of clusters based upon the link distances compared to the links below it in the tree, for KCA the only way to determine the appropriate number of clusters is to try repeated clusterings with varying number of clusters and select the one which seems to fit the data better. These two different methods of clustering are considered due to the differences in how they dissect the data: they approach the task of assigning clusters from dramatically different directions, and so they may reveal different aspects of the data structure.

3.4 SNOM Preprocessing

Data acquired by SNOM primarily takes the form of individual images at a fixed wavelength. By maintaining a scan area over several images at different wavelengths, a comparable structure to the FTIR-HSI data can be obtained, but must be checked for pixel registry. The resulting data cube is much smaller than the FTIR-HSI data in the spectral dimension, typically comprising only 3-5 images. In addition to the SNOM signal images that were measured, the simultaneously acquired topographic measurement also provides an image, along with the various additional channels that were added during the development of the SNOM instrument (see chapter 5).

The images produced by the SNOM generally possess a much lower signal to noise level than FTIR images, chiefly arising from the very low levels of light that were collected. As detailed in chapter 5 much effort is taken to minimise the noise contribution of both the FEL and the electronic equipment, but the images can be improved further through a small amount of preprocessing, similar to the steps taken for the FTIR images detailed above. The SNOM signal images are first corrected by reference to a simultaneously acquired background signal image to account for slow variation in the FEL intensity line-by-line. Following this ‘normalisation’ a correction for the non-linearity of the piezo $x - y$ stage is applied to aid comparisons between forwards- and backwards-directed images as well as optical microscope images for analysis. Sequential images in a series at different wavelengths are then aligned for pixel registry and cropped to their common area, accounting for any drift in the position of the scan over time. The final stage in the preprocessing is then a minimal Fourier transform filtering of the images to remove ‘streaky’ vertical noise due to FEL intensity variation over a single line. These stages are summarised in figure 3.2.

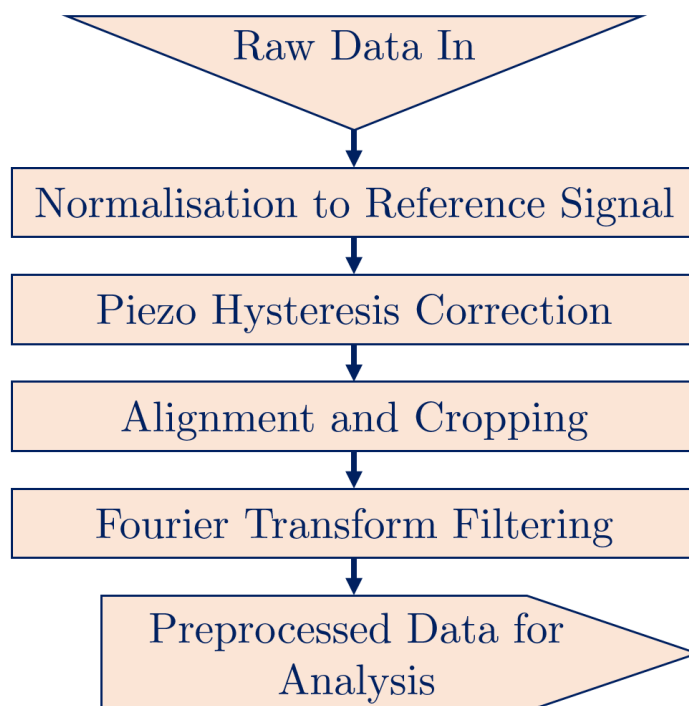


Figure 3.2: The stages of preprocessing applied to the raw SNOM data. The individual processes are described in detail below.

3.4.1 FEL Intensity Correction

Normalisation of an IR spectrum with respect to a reference signal or background is standard procedure [69]. With the SNOM images, however, doing this is not strictly appropriate. The SNOM aperture collects only a very small part of the total illuminating IR beam or spot, even approaching the ideal beam focus dictated by the diffraction limit, a SNOM is designed to collect significantly less than the entirety of the total spot size simply by its operating parameters. Thus any spatial structure within the beam, or indeed positional jitter or drift, will lead to a variation in the SNOM signal, without necessarily showing a correlated variation in a reference signal collecting the whole beam. It might be possible to use a second SNOM to measure a more comparable reference, but it would be next to impossible to ensure that the two are sampling the same part of the beam. Despite this, referencing the SNOM signal to a background variation by dividing corresponding pixels in each image can remove the effect of gross variation in the FEL intensity and did sometimes improve signal to noise. This process can just as easily introduce more noise into the image if there is a lack of good correlation between the SNOM signal and the total beam intensity.

Nevertheless, some form of correction must be applied as the FEL output is variable over the time scale of a few seconds. Due to acquiring bi-directional scans, where the SNOM scans were collected in both the forward and backward direction of tip scanning, with the backwards-direction line acquired after the corresponding forwards-direction line, each line in the image is acquired independently from the previous one and can therefore be subject to variations and drifts in the average light observed across the line. An effective solution for this variation was to correct for long time scale variations in FEL intensity without attempting to compensate pixel-by-pixel: each line of the SNOM image was divided by the median value of the corresponding reference image line. The reference line median was used as it is less sensitive to the occasional dips in the FEL output that occur, and so will produce a more appropriate average value for the line.

3.4.2 Piezo Correction

The $x-y$ piezo translation stage employed in the inverted microscope SNOM (see section 5.5) was found to have an inherent non-linearity across the scan area and asymmetry in the forward- and backward-directed scans. This is most noticeable in topographic images acquired on a calibration sample consisting of islands of gold deposited on a silicon substrate,

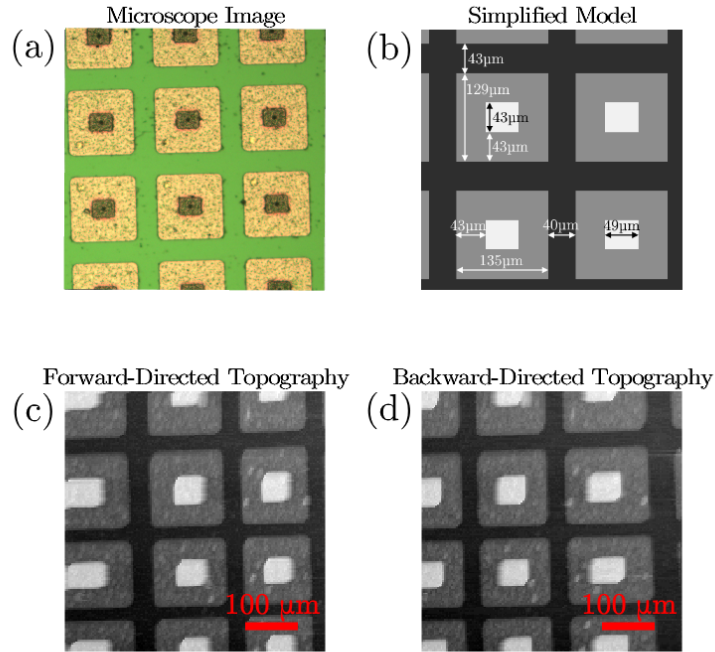


Figure 3.3: (a) A visible light optical microscope image of the calibration Au/Si sample showing the islands of gold deposited on a silicon substrate. (b) a simplified schematic of this sample showing the true sizes of its features. (c, d) Forward- and backward-directed topographic images acquired using the SNOM with a sharp cut metal wire tip in place of the usual optical fibre, showing the non-linearity and offset between the two images.

denoted Au/Si hereafter. The true dimensions of this sample were obtained from a calibrated optical microscope. The microscope image, along with a simplified schematic are shown in figure 3.3a,b. Shown in figure 3.3c,d are the true forward and backward scans over a nominally $500 \mu\text{m}$ square area acquired using a cut wire tip. The observed images are significantly different from expectation.

The first distortion to note is that there is a marked stretch produced over one side of each image. The stretch is approximately reversed for the backward-directed image compared to that seen for the forward-directed image acquired in the same SNOM scan. The forward image pixels are acquired left to right over the course of the scan line, while the backward image pixels are acquired right to left after the piezo has reversed direction. Given this directionality it is the case that both directions begin stepping over the corresponding stretched region of travel in that direction and approach a linear step size toward the end of each line. This observed hysteresis is a common problem with piezoelectric drives [70].

The second distortion is the slight offset between the forward and backward images; this

is in part due to built-in software compensation for non-linearities in the piezo. A further observation from these images is the rectangular, rather than square, nature of the scan area. Using the known sizes of the islands on the calibration sample, the y -range is approximately $516 \mu\text{m}$ while the x -range is only $482 \mu\text{m}$. In general none of these distortions present a serious problem, but to aid analysis and comparison with optical microscope images of the samples it is necessary to correct the SNOM images for the observed non-linearity and asymmetry. This would also potentially allow forward and backward images to be averaged and therefore improve the signal to noise ratio (SNR) for each image.

In order to correct for these effects, the apparent relative location of each boundary on the calibration sample within the $500 \mu\text{m}$ image was plotted against the true relative position on the sample. By taking a third order polynomial fit to the curve the relationship between the true and apparent pixel location as a function of piezo position within the $500 \times 500 \mu\text{m}$ scan range of the stage can be determined and the curve produced used to correct the images. This approach should compensate for any process that affects the pixel size or aspect ratio in both x and y . The curves produced from the forward and backward images are shown in figure 3.4c

The curves can be used to interpolate a true pixel (x_{true}, y_{true}) based on the observed values in the (x_{obs}, y_{obs}) -plane, returning an image with the pixel size given by the estimated pixel size of the original image ($1.6 \mu\text{m}$ for an image over nominally $500 \mu\text{m}$ in 150 pixels). Figure 3.4d shows the effect of correcting such a $500 \mu\text{m}$ forward-directed image taken on the Au/Si calibration sample: the resultant image is more rectangular as the x -axis is contracted to match the expected sizes, and shows a much more uniform size of feature across the image compared to the original version shown in figure 3.4a.

A comparison of the processed forward- and backward-directed images is necessary to determine if the final curves are suitable for use as a standard calibration procedure. If the curves compensate for the non-linearity seen in the piezo drives then the two directions should become essentially identical, with the exception of any artefacts originating from the direction of motion of the tip. Figure 3.5 gives the image difference of the two corrected images using the final curves. The only features that stand out are imaging artefacts from the direction of motion. Based on these results the SNOM images can be corrected for the non-linearity to produce images that should be closer to the optical microscope images. As the topography, SNOM signal and reference images are acquired simultaneously, the same

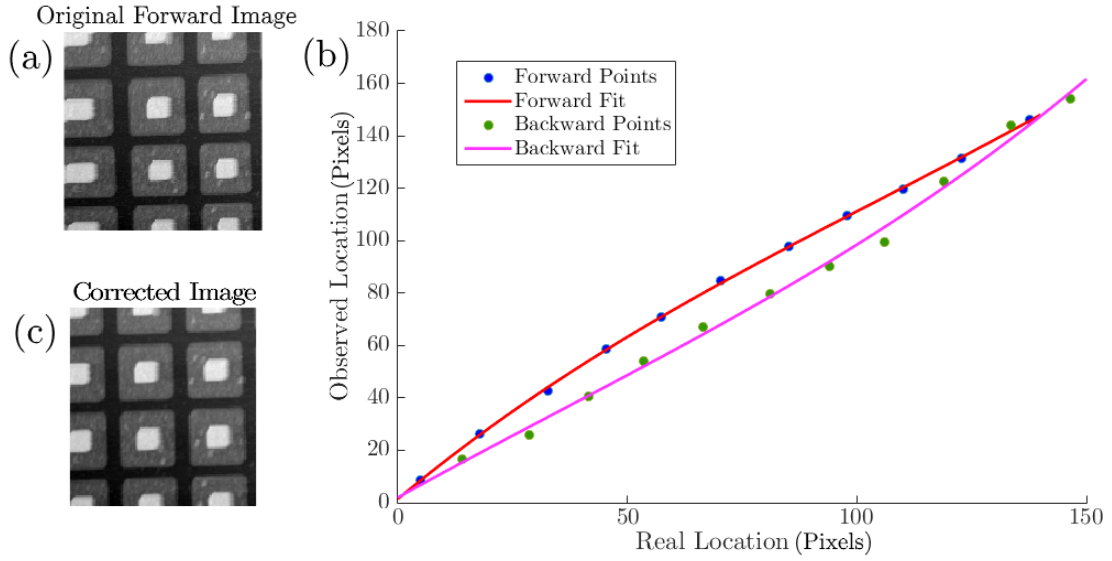


Figure 3.4: (a) a $500 \times 500 \mu\text{m}$, 150×150 pixel forward-directed topographic image of the Au/Si calibration sample acquired using a cut tantalum wire tip and the x, y piezo stage. (b) the apparent pixel location plotted against the true spacing of step features along a single line in the horizontal (x) dimension (blue circles) and the third order polynomial fitted to this line (red line), with the same data in the backward direction (green circles and magenta line) showing the hysteresis in the scanning of the piezos. (c) The corrected image given by the red correction curve in (b) which closely resembles the expected dimensions seen in figure 3.3. The discrepancies between the optical and topographic images can be attributed to a topographic tip artefact resulting from the finite size and non-ideal shape of the tip. The resultant image is 151×142 pixels and thus $503 \times 473 \mu\text{m}$ in size.

correction can be applied to all three, though because the reference image contains no spatial information it is not necessarily appropriate to use this image after the correction has been applied. Thus this stage in the image preprocessing had to be performed after the FEL intensity correction above was applied.

The same non-linearity curves should be reproduced by each $500 \times 500 \mu\text{m}$ image but when considering smaller scan areas within the $500 \mu\text{m}$ travel of the piezo drives it became apparent that while the full-size images are approximately the same size in each direction, for smaller images this isn't necessarily the case. This is demonstrated by the $250 \times 250 \mu\text{m}$ topographic images in figure 3.6, where the origin is still $(-250, -250) \mu\text{m}$ but the images are nominally $250 \times 250 \mu\text{m}$. Although the apparent range of the x -piezo is the same in both the forward- and backward-directed images the true size of each is slightly different. In the forward direction the area lies in the most non-linear range of the corresponding curve giving an image that is stretched, while the backward direction is in the linear part of the piezo curve and the image appears as such. Some method of correcting smaller images must be devised in order to accurately process the smaller scan sizes, and in general one might

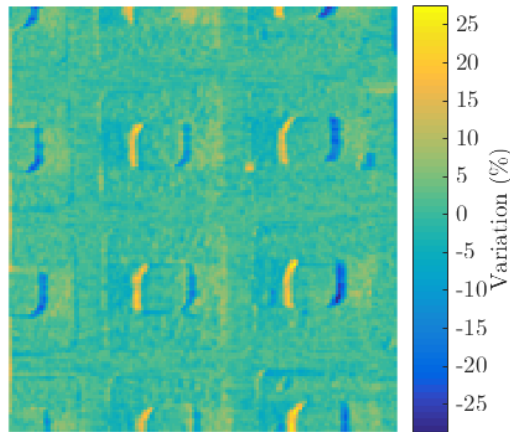


Figure 3.5: The difference between the forward- and backward-directed topographic images of the Au/Si calibration sample after correcting for the piezo non-linearity. The only features that stand out are the topographic artefacts at edges of the islands where the sample steps down along the direction of motion, and thus on opposite edges in each image.

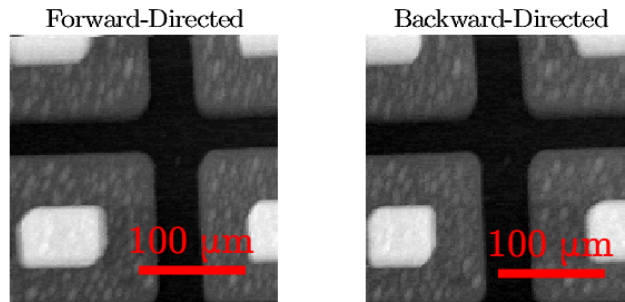


Figure 3.6: The forward- and backward-directed scans for a smaller $250 \times 250 \mu\text{m}$ image of 150×150 pixels with the same origin of $(-250, -250) \mu\text{m}$. The smaller scan range results in slightly different real sizes for the two directions as each is over a different part of the curves seen in figure 3.4b

hope that for a section of the $500 \mu\text{m}$ area, the corresponding section of the correction curves should apply.

Assuming that the smaller areas are indeed represented by sections of the full-range curves and correcting the forward and backward topographic images from two $250 \times 250 \mu\text{m}$ areas, one with an origin of $(-250, -250) \mu\text{m}$ the other with an origin of $(0, 0) \mu\text{m}$ as estimated by the SNOM software, gives images that are different in size, as expected, and are closer to the optical microscope, but which do not show enough similarity to allow the images to be averaged together. Some remaining element of their non-linearity is preserved, suggesting that for smaller scan ranges the curves representing the necessary correction are slightly different to the relevant section of the $500 \mu\text{m}$ curve. After applying the correction,

however, the images are much more similar to each other and to the true sample topography, meaning that the approximation can be used as a partial correction. As a general protocol the SNOM image series were corrected using this approximation, but if a more accurate representation of the sample was required, or to allow image averaging, it was possible to use the bidirectional topographic images to adjust the curves to provide the optimum similarity between the two images. This latter method is, however, time consuming and only allows the x -direction to be properly corrected.

3.4.3 Alignment

The 75 minute approximate time scale required to acquire a 150×150 pixel SNOM image means that there was a potential for physical drifts in the sample, thermal or otherwise, to affect the sampled area in sequential images. While it was impossible to completely eliminate the sample drift, the typical distance that a sample drifted over several hours was not more than $5 - 10 \mu\text{m}$, and often much less than the pixel resolution of the images. To compensate for any offset between images across a set of wavelengths, the set of images was aligned to the first image in that set. The alignment was performed using the topographic images for each wavelength. The ideal registry of each image to the first image in the series was determined using their two dimensional cross-correlation:

$$XC(p, q) = \sum_{y=0}^{n_{y_1}-1} \sum_{x=0}^{n_{x_1}-1} I_1(x, y) I_2(x - p, y - q), \quad \begin{aligned} &-(n_{x_2} - 1) \leq p \leq (n_{x_1} - 1) \\ &-(n_{y_2} - 1) \leq q \leq (n_{y_1} - 1) \end{aligned} \quad (3.3)$$

which measures the total product of the two images at different shifts $\binom{p}{q}$ from each other, recording the value in $XC(p, q)$. When the two images are optimally aligned the corresponding pixel of XC is a maximum, thus the required shift of the image can be determined by the location of this maximum. This is the only stage of the preprocessing that was performed using the topography images, as the details seen in the light image are variable with wavelength, whereas the topographies should be essentially identical. Having performed the alignment by shifting each image by the required amount, the image set was cropped to its common area.

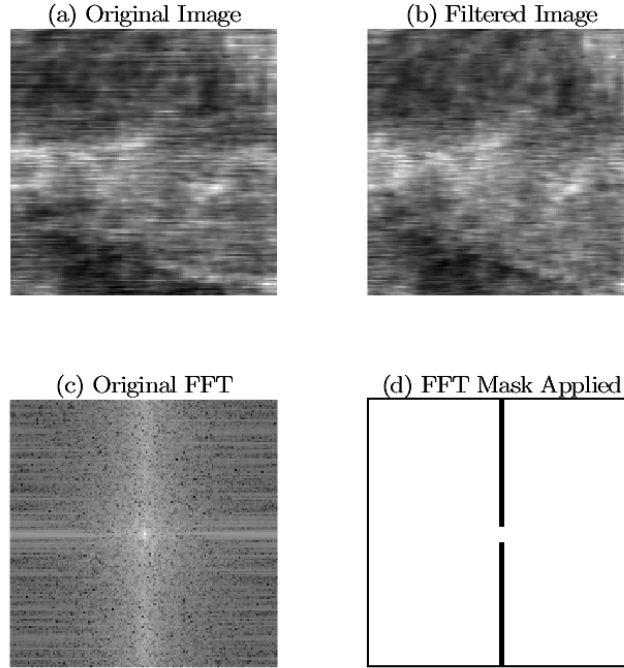


Figure 3.7: (a) A 150×150 pixel ($250 \times 250 \mu m$) SNOM image at a wavelength of $6.50 \mu m$ after applying a median correction. The correction has levelled the image successfully but there is still a significant vertical line-to-line noise contribution. (b) The resulting image after the standard FT filtering, showing a much reduced impact from the ‘streakiness’ but little loss of other information. (c) The two dimensional FT of (a) with the $f_x, f_y = 0$ pixel at the centre. The image signal is present over the whole FT range, but the brighter vertical stripe up the centre of the FT is due to the ‘streakiness’ seen in the image. (d) The mask applied to the FT. Pixels corresponding to black in the mask are set to zero in the FT and the result is then transformed back to produce (b).

3.4.4 Image Filtering

To further minimise line-to-line noise each SNOM light image was filtered by taking the two-dimensional discrete FT, which transforms the spatial signal $I(x, y)$ of an $(n_x \times n_y)$ image into spatial frequencies $\hat{I}(f_x, f_y)$ using the discrete analogue of the continuous FT given in equation 2.7 in section 2.3.2:

$$\hat{I}(f_x, f_y) = \sum_{y=0}^{n_y-1} e^{-\frac{2\pi i y f_y}{n_y}} \left(\sum_{x=0}^{n_x-1} e^{-\frac{2\pi i x f_x}{n_x}} I(x, y) \right) \quad (3.4)$$

with the spatial frequencies f_x and f_y in each dimension given by $0, \frac{1}{n}, \frac{2}{n}, \dots, \frac{n-2}{n}, \frac{n-1}{n}$ and the inverse function defined as:

$$I(x, y) = \sum_{f_y=0}^{n_y-1} e^{\frac{2\pi i y f_y}{n_y}} \left(\sum_{f_x=0}^{n_x-1} e^{\frac{2\pi i x f_x}{n_x}} \hat{I}(f_x, f_y) \right) \quad (3.5)$$

By taking the FT of an image it is possible to remove particular frequency contributions that are adding noise to the image by removing the corresponding frequency components from the FT image and transforming back to the image. Particularly for the SNOM light images the variation in FEL intensity from line-to-line can be mostly compensated for by dividing by the median of the reference signal line as detailed above, but any slow variation across a single line leads to a horizontal ‘streakiness’ when considering vertically adjacent lines. This vertical noise in the image can be significant and was easily removed using a mask applied to the image FT then applying the inverse transform. An example image, its FT and the mask used on all the images, as well as the resultant filtered image is shown in figure 3.7. The mask was chosen to remove the strong vertical bar of noise in the FT without removing too much of the desired signal, although this technique removed some detail, the effect of the filtering was deemed to be a net gain in the quality of the image.

CHAPTER 4

FTIR HYPERSPECTRAL IMAGING OF OESOPHAGEAL TISSUE

Contents

4.1	Introduction	40
4.2	FTIR-HSI Experimental Details	40
4.3	Image Data	41
4.3.1	Sample Labelling	41
4.4	Hierarchical Cluster Analysis	43
4.4.1	Discussion of HCA	48
4.5	k-Means Cluster Analysis	49
4.5.1	2 Cluster KCA	49
4.5.2	3 Cluster KCA	50
4.5.3	4 and 5 Cluster KCA	51
4.5.4	6, 7 and 8 Cluster KCA	52
4.5.5	Discussion of KCA	53
4.6	Metric Analysis	59
4.6.1	Labelling Method	61
4.6.2	KCA-Inspired Absorbance Metrics	65
4.6.3	Automated Metric Optimisation	68
4.6.4	Optimised Absorbance Ratio MA	72
4.6.5	Discussion of MA results	76
4.7	Conclusions	78

In this chapter IR absorption experiments on human oesophageal tissue of both benign and malignant nature are presented. A detailed assessment of the different analysis techniques is presented and the results of several different methods of spectrum discrimination are shown to have varying degrees of success at producing a map of the tissue types present in the image areas.

4.1 Introduction

The standard method of histological examination uses chemical stains to highlight particular chemical components within a sample which can then be viewed under a microscope to be graded according to the structure and presentation of the tissues that comprise it. The subjective and inaccurate nature of this grading presents a significant problem for the patient as well as the histologist(s) performing the procedure. By using IR spectroscopy, the chemical information within the sample can be extracted without the need for histological stains, and in a much more quantitative manner, opening the way for robust numerical and computer-driven grading of tissues.

The chief aim of this work is to develop a more reliable method of investigating and diagnosing the state of oesophageal tissue using spectral information, and as FTIR hyperspectral imaging provides a large amount of spectral information very quickly it presents an ideal candidate for automated tissue labelling analyses where the spectra are grouped by some method into categories, revealing the structure of the tissues without the need for external input. There are many ways to allocate data into groups, and three are explored here: HCA, KCA and MA. The aim of the work presented in this chapter was to assess and develop an analysis procedure that could be used as a more quantitative and reliable method of histological assessment, using a detailed analysis of two specimens, denoted A and B. The details of the analysis methods used here are given in chapter 3.

4.2 FTIR-HSI Experimental Details

The FTIR spectrometer used for this work was a Varian 670-FTIR spectrometer in conjunction with a Varian 620-FTIR imaging microscope produced by Varian (now Agilent Technologies, Santa Clara CA, USA) with a 128×128 pixel mercury cadmium telluride (MCT) FPA. Images were acquired with a spectral range from 950 to 3800 cm^{-1} with a resolution of 4 cm^{-1} , co-adding 256 scans. This instrument belongs to Professor Peter Gardner's group at the Manchester Institute of Biotechnology and access to this instrument was part of the collaborative *Spectrochemical Analysis of Cancer* (SCAnCan) grant. A description of the preprocessing and analyses used for the FTIR-HSI data is given in section 3 above.

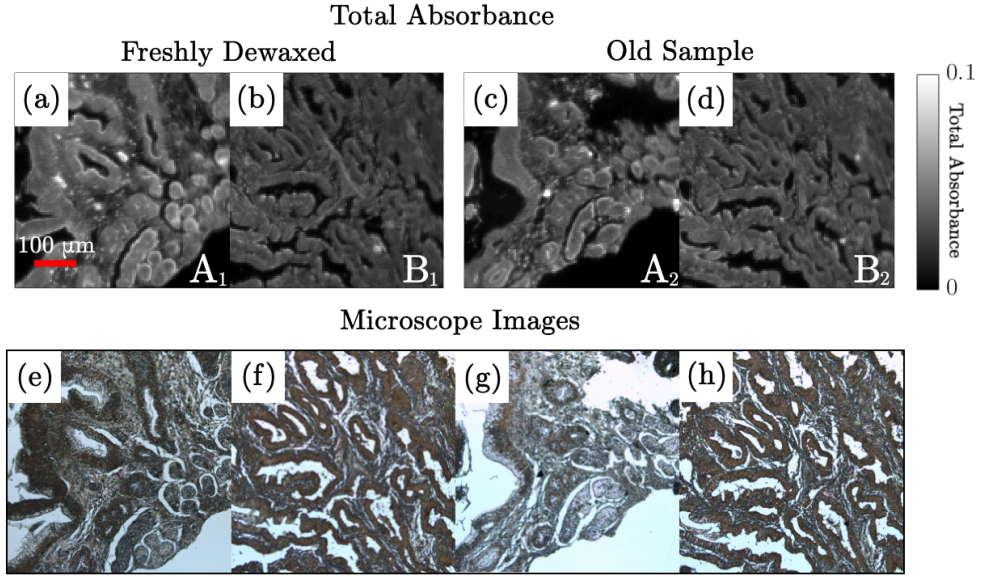


Figure 4.1: Total absorbance maps of the raw image data and matched optical microscope images. (a) – (d) the pilot group - two serial sections from two biopsy samples dewaxed at different times: (a) and (b) are freshly dewaxed samples of Barrett’s oesophagus (A_1) and OAC (B_1) respectively, while (c) and (d) are serial sections of the same samples dewaxed approximately 6 months prior to imaging (A_2 and B_2). (e) – (h) are the corresponding optical microscope images of the four image areas.

4.3 Image Data

The unprocessed images and corresponding optical microscope images are shown in figure 4.1. To assess the chemical stability of the samples with time, the pilot group consisted of two serial sections from each of two biopsy samples. One was benign Barrett’s oesophagus and the other OAC. The first section of each sample was freshly dewaxed within two hours of imaging, while the other had been dewaxed approximately six months earlier. The purpose of these secondary sections was to assess the effect of age on the samples after dewaxing, which is largely unknown. The raw image data is calculated from the data by summing each pixel along the spectral dimension to produce a map of total absorbance over the range of the spectrum:

$$\alpha_{total}(x, y) = \sum_{n=1}^{1453} \alpha_n(x, y) \quad (4.1)$$

4.3.1 Sample Labelling

The sample areas A_1 and B_1 shown in figure 4.1a,c were labelled, pixel by pixel, with the aid of an experienced pathologist¹ to give maps of the tissue type at each tissue. These maps are shown in figure 4.2. The first pair of images, (a), is a detailed labelling of the specific

¹Dr Olivier Giger, Institute of Translational Medicine, University of Liverpool

tissue classifications, while the second pair of images, (b), describes a simplified model, with classification into four tissue types: Barrett's epithelium, benign stroma, cancerous epithelium, and cancerous stroma. In the second pair of images, the pixels corresponding to tissues that do not fall into these loose classifications - nerve cell, debris, smooth muscle, collagen fibres and gaps in the sample - were removed from the model.

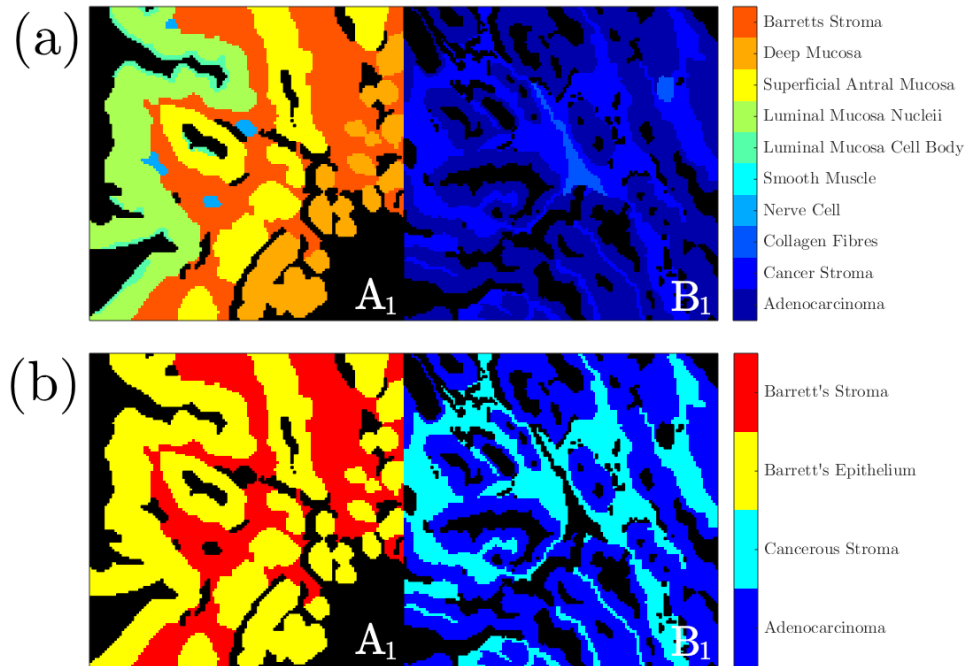


Figure 4.2: Tissue maps corresponding to the sample areas in figure 4.1a,b: samples A₁ and B₁. These labelled maps can be used to compare the results of pixel labelling to the underlying tissue architecture of these sample areas. The first pair of images (a) represent a detailed characterisation of ten different tissue types, with unknown debris and gaps in the samples coloured black. The second pair of images (b) gives a simplified labelling of the four main tissue classifications, a more basic model that facilitates easier comparisons to labellings produced through cluster analyses.

These labelled images allow a direct comparison between the clusters produced by the cluster analyses below and the true tissue classifications within the two freshly dewaxed sample image areas A₁ and B₁. Comparisons were drawn between the groupings given by each of the analyses considered in this chapter using the well known statistical quantities of sensitivity, specificity, positive predictive value (PPV) and negative predictive value (NPV). These terms are used here in the context of labelling success, rather than in the outcome of a clinical trial: sensitivity is defined as the percentage of the relevant tissue class that is identified as such by the grouping method (equation 4.2), and specificity is the percentage of the other tissue classes that are not identified incorrectly by the grouping method (equation 4.3). In essence they quantify the ability of a classification method to correctly identify the

right pixels and to correctly exclude the wrong pixels from each grouping. PPV and NPV are defined as the number of pixels correctly included and excluded from the cluster respectively as a proportion of the total number included/excluded (equations 4.4 and 4.5). A perfect labelling method would include all pixels of the correct class and exclude all the pixels of any other class, thereby giving a sensitivity and specificity of 100%, Also identifying only, and all of, the correct pixels giving a PPV and NPV of 100%.

$$\textit{Sensitivity} = \frac{\textit{Number of Correct Positives}}{\textit{Number of Real Positives}} \quad (4.2)$$

$$\textit{Specificity} = \frac{\textit{Number of Correct Negatives}}{\textit{Number of Real Negatives}} \quad (4.3)$$

$$\textit{PPV} = \frac{\textit{Number of Correct Positives}}{\textit{Total Positives}} \quad (4.4)$$

$$\textit{NPV} = \frac{\textit{Number of Correct Negatives}}{\textit{Total Negatives}} \quad (4.5)$$

In all of these quantities the ‘real’ and ‘correct’ assignments are determined relative to the labelled images given in figure 4.2b. For example, if a pixel labelled as cancerous epithelium in figure 4.2 is grouped with the other cancerous epithelium pixels, it is deemed a correct positive for the cancerous epithelium group and also a correct negative for the other three groups; conversely if the cancerous epithelium pixel is grouped with the cancerous stroma pixels then it is a false negative for cancerous epithelium, a false positive for cancerous stroma, but still a correct negative for Barrett’s epithelium and benign stroma. The difference between the measures of sensitivity/specificity and PPV/NPV is that the former two are judging the success of the grouping with respect to the ‘correct’ tissue classifications, while the latter are with respect to the pixels included or excluded from the grouping of pixels itself.

4.4 Hierarchical Cluster Analysis

The four FTIR images shown in 4.1 were subjected to a combined agglomerative HCA which not only groups the data, but can suggest the most appropriate number of clusters to

4.4. HIERARCHICAL CLUSTER ANALYSIS

represent the sample structure based upon the inconsistency measure, as detailed in section 3.3.1. HCA aims to group data based on iteratively grouping the closest pair of clusters within the data cloud. Every pixel is initially in an individual cluster on its own, and the algorithm is applied successively until only one cluster remains. The distance between each pair of clusters as they are joined is recorded in a dendrogram, with longer links representing larger distances between the centers of the two clusters.

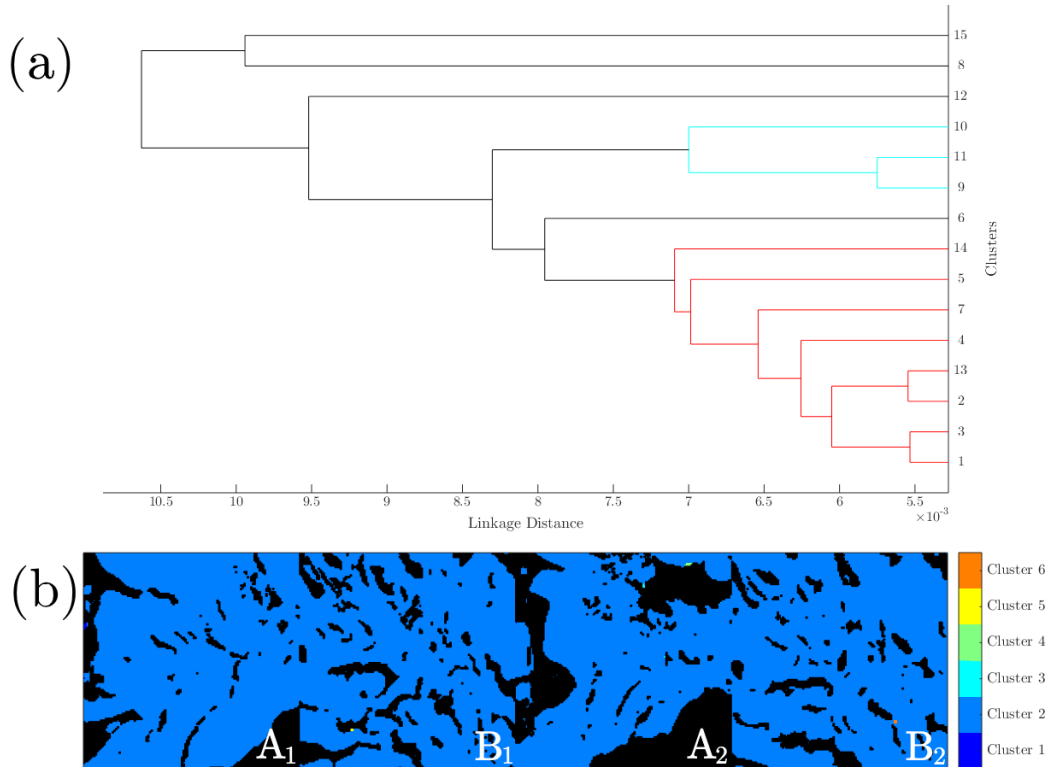


Figure 4.3: Initial HCA results. (a) The dendrogram produced by the original pre-processed data, plotted to 15 clusters with unique colours for branches whose next links give an inconsistency value $I \geq 0.7$; (b) the cluster identifications with the data clustered by the dendrogram cut to the recommended number of clusters given by the inconsistency value.

The dendrogram produced from the data is shown in figure 4.3a plotted to 15 clusters. The branches are coloured with unique colours below links in the dendrogram showing inconsistency values of 0.7 or higher, essentially determining those links that do not represent a consistent grouping. This measure of inconsistency gives the optimum number of clusters to be six. Figure 4.3b displays the cluster identifications when cut to the recommended level of six clusters, but clearly this clustering does not represent the tissue structure of the samples seen in figure 4.2.

Exploring higher numbers of clusters shows that thirteen of the top fifteen clusters contain

very few pixels. Figure 4.4 has plotted the same HCA to fifteen clusters, with the majority (99.7%) of the pixels in the four image areas being assigned to only two of the resulting clusters. Thirteen of the top fifteen clusters represent pixels that lie significantly outside of the normal scatter of the data, possibly pixels that have been adversely affected by the image processing stages (particularly normalisation) and so represent outliers from the group. HCA is particularly sensitive to such outliers as the clusters are formed by joining the two closest clusters together: any point or group of points that is significantly distant from the majority of the data will be distinct until the final few clusters, while the remaining data is clustered together.

The two substantial clusters in figure 4.4, those that are not merely isolated pixels, seem to represent a splitting of the epithelium tissue in samples A_1 and A_2 from the other tissue classes, the first true differentiation in tissue class in the dendrogram. This suggests that this epithelial tissue is most distinct from the others, and that the adenocarcinoma tissue is closer to the presentation of the two stroma tissues. Unfortunately the differentiation of further classes is hidden by the anomalous pixels.

The dendrogram branch below the two significantly populated clusters was isolated to further investigate its structure in an effort to identify whether further sample regions could be identified using HCA. The resulting dendrogram is shown in figure 4.5. This dendrogram now shows no inconsistent clusters, even with a reduced inconsistency value of 0.6 and further reductions of the inconsistency cut-off produces either no inconsistent links or hundreds of them. The HCA is simply unable to determine the true groupings of tissue clusters, either due to problems resulting from the preprocessing or by being too susceptible to the natural variation in chemistry present in tissue samples. Thus automatically determining the appropriate number of clusters becomes impossible and the only course of action is to

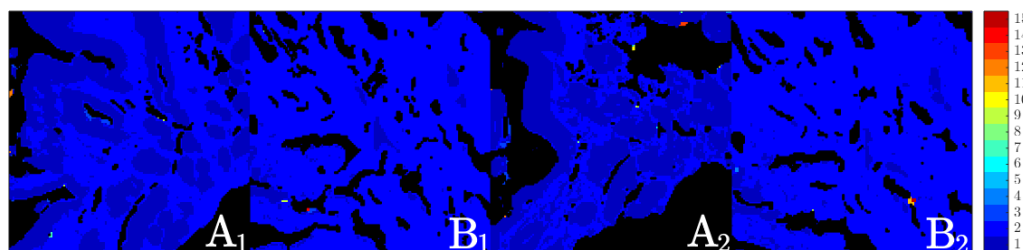


Figure 4.4: The cluster identifications given by cutting the dendrogram in figure 4.3 to 15 clusters. at this point 13 of the clusters are still made up of only a few pixels, but there are now two principle clusters representing true areas of tissue.

4.4. HIERARCHICAL CLUSTER ANALYSIS

Tissue Class	Cluster	Sensitivity (%)	Specificity (%)	PPV (%)	NPV (%)
Barrett's epithelium	1	79.0	95.7	85.3	93.5
Benign stroma	2	90.8	43.5	20.0	96.8
Cancerous epithelium	2	96.6	51.1	40.6	97.8
Cancerous stroma	2	92.4	43.6	20.1	97.4

Table 4.1: Cluster-Tissue assignments for two cluster HCA shown in figure 4.5, assigning the tissue classifications to the cluster with the maximum sensitivity to it. These statistics are derived only from the first two images, A_1 and B_1 , of the image set.

manually investigate the cluster splitting to determine subjectively where best to cut the dendrogram. Cutting the new dendrogram at two clusters reproduces the splitting of the data seen in Clusters 1 and 2 in figure 4.3, an expected result as the data has not been modified.

The tissue classification of each pixel, as determined by figure 4.2 was compared directly with the clusters produced by the HCA for samples A_1 and B_1 . The sensitivity, specificity, PPV and NPV values, as defined in section 4.3.1, for the grouping of the four general tissue classifications were calculated. The values of these statistics for the two clusters are shown

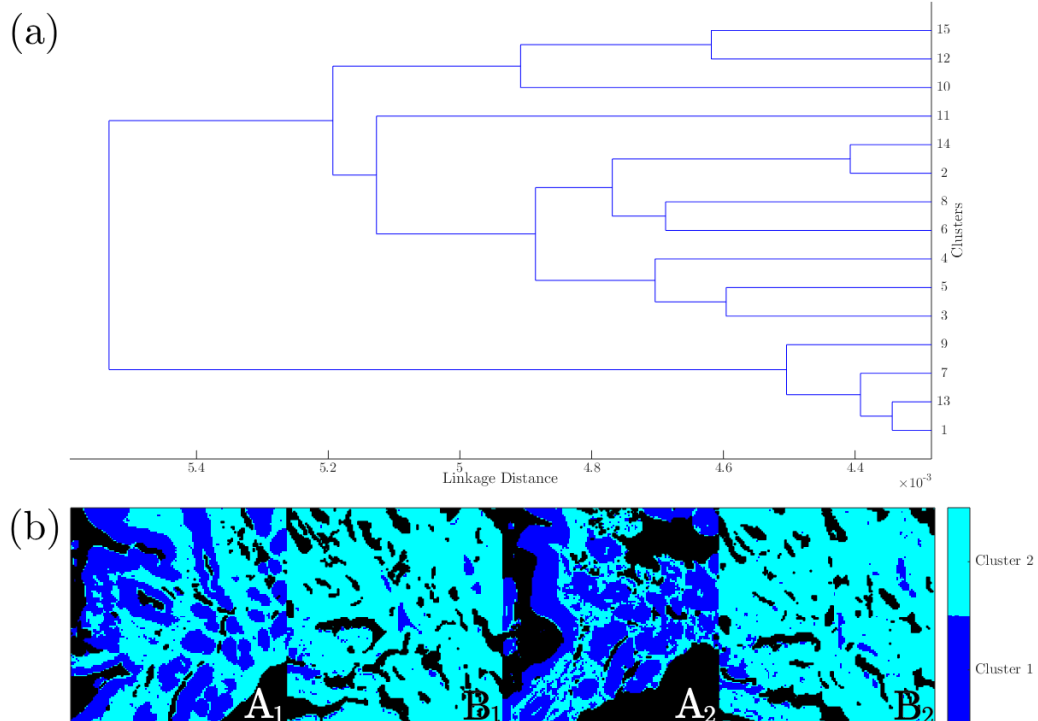


Figure 4.5: The structure and clustering of the two significant clusters produced by the HCA. (a) The dendrogram produced by only the two significantly populated clusters, plotted to fifteen branches with unique colours for branches whose next links give an inconsistency value $I \geq 0.6$, showing no inconsistent links; (b) the cluster identifications for this dendrogram plotted at two clusters, producing the same labelling as given by the first two clusters in figure 4.3b without the thirteen potentially anomalous clusters

in table 4.1 with the four tissue types from the simplified labelling each assigned to a cluster according to which has the highest sensitivity to it. As observed in figure 4.4, the values in the table show that the Barrett's epithelium was clustered separately from the rest of the tissues, with a fairly high sensitivity and specificity. The sensitivity values given by the grouping of the other three tissues are all very high, but because they are grouped together the corresponding specificities are low: the number of correct negatives is relatively low as there are many of the pixels that should be labelled as different tissues included in the cluster. This behaviour is even more evident in the PPV values for the cancerous epithelium, cancerous stroma and Barrett's epithelium tissues, as the number of correct positives is low compared to the total positives due to the combination with the other two tissues. The NPV values are very high for each tissue type, as the clustering differentiates between the Barrett's epithelium and other tissues reliably, giving a high proportion of correct negatives or, inversely, a low number of false negatives.

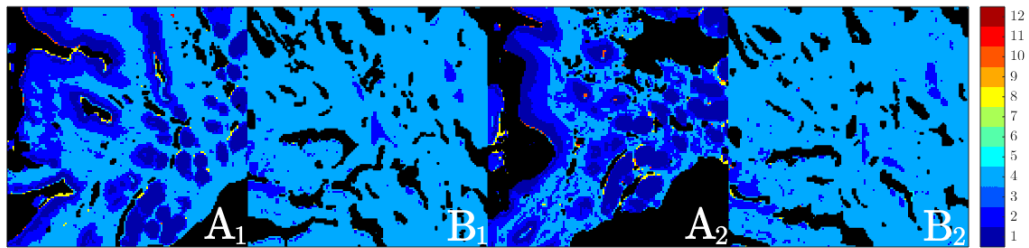


Figure 4.6: The image data displayed with twelve hierarchical clusters formed from the two significantly populated clusters isolated in figure 4.5b. There are three main clusters containing the majority of the pixels in the image, with 9 small clusters around the edges of these main clusters. Focussing on the significant three clusters, the Barrett's epithelium cluster (Cluster 1 in figure 4.5) has split to form two separate clusters with different regions of the epithelium in each.

Cutting the dendrogram at a higher number of clusters gives further problems arising from small groups of outlying pixels: three and four clusters splits Cluster 2 by separating off clusters of 19 pixels and then a further 4 pixels respectively. It is not until plotting twelve clusters that a significant division occurs. The previous nine clusters that are produced are located around the edges of the regions defined by the first two clusters, these are again regions of outlying data possibly resulting from thinner areas of tissue, or perhaps pixels that contain elements of multiple tissue classes. The cluster identification image for twelve clusters in figure 4.6 shows that the significant change in the labelling of the sample (aside, that is, from the small boundary clusters) is that the Barrett's epithelium cluster has now split to form two distinct regions.

4.4.1 Discussion of HCA

The sensitivity of the clustering produced by HCA to any outlying or anomalous pixels significantly diminishes the suitability of applying this analysis technique with respect to this FTIR-HSI tissue data. There are several effects that may lead to individual pixel values lying outside the normal scatter that arises from purely chemical variations within the tissue. Any regions of tissue that have minimal absorbance, through either thickness or natural transparency, which are not eliminated by the quality testing that is performed in the preprocessing, could be artificially enhanced by the integral normalisation. As these pixels have the lowest signal to noise, the enhancement to the noise inherent to the data is a much more significant effect than for pixels with stronger absorbance, and could lead to spurious spectral values.

The inverse situation, where a pixel has an unusually high absorbance, could also lead to an outlying point. This could occur due to a piece of debris on the sample surface, or from damage to the sample itself, and will lead to an essentially opposite effect to the low absorbance anomaly with the integral normalisation artificially reducing the values in the spectrum intensity due to an isolated extreme absorption feature. Although the preprocessing does attempt to eliminate the majority of the pixels that have either extreme of total absorbance, it is also important to retain as much of the useful data from the images, resulting in a compromise between eliminating as many outliers as possible and keeping the useful data. The imperfect nature of the resulting spectra means that HCA will usually identify anomalous pixels before truly separate clusters.

Despite the difficulty in discerning the true clusters in the data from the outlier scatter, HCA was able to establish a consistent difference between the pixels consisting of Barrett's epithelium and those representing other tissues in figure 4.5, meaning that while HCA cannot give enough reliability, there are consistent differences that can be found between the tissue classifications. Considering a different clustering method, KCA, which is much less sensitive to the outliers present in the data than HCA could, by essentially ignoring outlying data in favour of general structures, give access to the structure of the data to a greater degree and allow more differences to be examined.

4.5 k-Means Cluster Analysis

In the same manner as for HCA the four FTIR images in figure 4.1 were subjected to KCA. KCA provides a grouping of data, similar to HCA, by collecting together pixels of the data into clusters, but instead of iteratively building the clusters, a pre-defined number are randomly assigned and an iterative process adjusts them to give an optimum grouping, as detailed in section 3.3.2. To ensure the reliability of the clusterings produced, the KCA was repeated 5 times (replicates) and the solution with the lowest total sum distance from each cluster centroid to the pixels in that cluster, that is the most tightly clustered solution, was taken as the final clustering. In the same way as for HCA the groupings produced at each cluster number were compared to the labelled images in figure 4.2 to give an idea of how well the clustering represents the tissue structure and which number of clusters is most appropriate. The only way to determine what number of clusters is appropriate is to specify each value individually and investigate the structures grouped in each case. Furthermore, while the HCA method simply splits one of the higher clusters each time the cluster number is increased, the KCA method creates an entirely new clustering. This difference means that changing the cluster number in KCA can have a dramatic effect on the regions picked out by the analysis: each clustering is essentially independent.

4.5.1 2 Cluster KCA

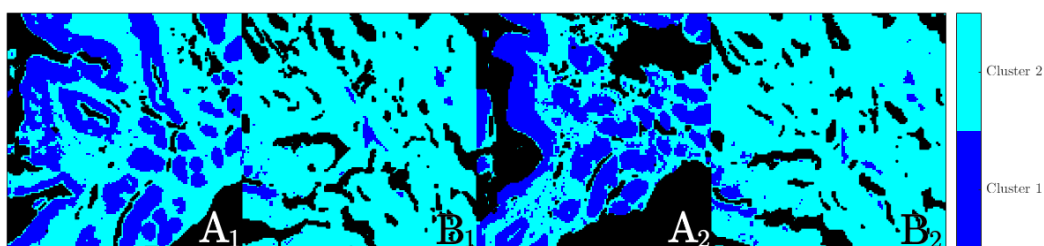


Figure 4.7: The clustering results for KCA with two clusters. The identification map produced is very similar to that seen for the first splitting of clusters using HCA above (figure 4.5b), producing a cluster, predominantly consisting of Barrett's epithelium tissue, separated from the other tissue classifications. This is very similar to the clustering given by the HCA in figure 4.5.

Specifying a grouping into two clusters gives the image shown in figure 4.7, this image is very similar to the first significant cluster splitting seen in the HCA above, specifically in figure 4.5b. The KCA performed here has retained the majority of the image data in a primary cluster, whilst separating the regions of Barrett's epithelium tissue into another. There are

a few small areas of mislabelling of this Barrett’s epithelium cluster in the B samples which are approximately co-located in the serial sections, implying that the mislabelling is due to a true similarity between the spectra in the Barrett’s epithelium tissue and this region of tissue.

Tissue Class	Cluster	Sensitivity (%)	Specificity (%)	PPV (%)	NPV (%)
Barrett’s epithelium	1	72.2	97.8	91.1	50.7
Benign stroma	2	93.8	39.9	19.6	97.6
Cancerous epithelium	2	98.4	47.0	39.1	98.8
Cancerous stroma	2	93.6	39.8	19.3	97.6

Table 4.2: Cluster-Tissue assignments for two cluster KCA, assigning the tissue classifications to the cluster with the maximum sensitivity to it. As with the HCA above, the statistic values are calculated only using the images for samples A_1 and B_1

The sensitivity, specificity, PPV and NPV values were again calculated for the images of A_1 and B_1 in table 4.2 and show very similar quantities to the values given by the HCA in table 4.1. The clustering of Barrett’s epithelium is less sensitive in this KCA, resulting in a much lower NPV as well, but the specificity is higher.

4.5.2 3 Cluster KCA

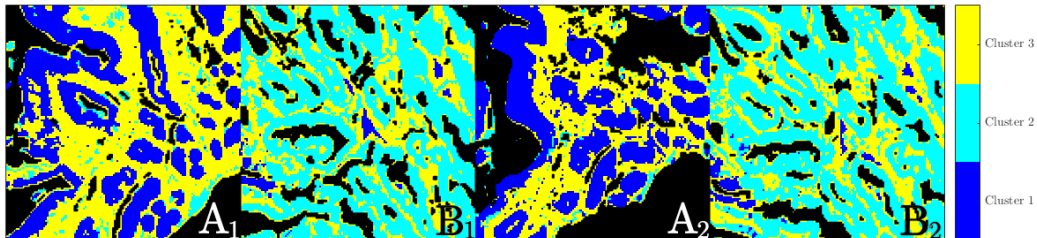


Figure 4.8: The clustering results for KCA with three clusters. This has clustered the stroma tissues from the samples together, grouping the two different types of epithelium into clusters of their own.

The cluster map given by the three cluster KCA for the combined image data is shown in figure 4.8. The use of three clusters, as with two, distinguishes Barrett’s epithelium tissue as a cluster separate from other areas of tissue. In addition to this, another cluster contains pixels mostly corresponding to cancerous epithelium, with both stroma types combined together into the remaining cluster. It can be seen that the areas of the OAC samples that were mislabelled at 2 clusters are also mislabelled as Barrett’s epithelium when three clusters are used, and a few regions of the Barrett’s oesophagus samples have been mislabelled as the cancerous epithelium cluster.

Tissue Class	Cluster	Sensitivity (%)	Specificity (%)	PPV (%)	NPV (%)
Barrett's epithelium	1	69.2	98.1	92.2	90.9
Benign stroma	3	89.0	71.2	32.5	97.7
Cancerous epithelium	2	79.8	89.0	71.4	92.7
Cancerous stroma	3	54.6	65.8	19.7	90.4

Table 4.3: Cluster-Tissue assignments for three cluster KCA, assigning the tissue classifications to the cluster with the maximum sensitivity to it.

Tissue Class	Cluster	Sensitivity (%)	Specificity (%)	PPV (%)	NPV (%)
Barrett's epithelium	1/3	46.0/42.3	89.3/99.7	57.8/97.7	83.9/84.5
Benign stroma	4	71.4	81.0	36.9	94.8
Cancerous epithelium	2	77.9	89.3	71.5	92.1
Cancerous stroma	4/2	41.6/40.9	76.3/74.0	21.2/19.4	89.5/89.1

Table 4.4: Cluster-Tissue assignments for four cluster KCA, assigning the tissue classifications to the cluster with the maximum sensitivity to it.

4.5.3 4 and 5 Cluster KCA

Increasing the clusters from two to three allowed two of the four general tissue groups (Barrett's epithelium, benign stroma, cancerous epithelium, cancerous stroma) in figure 4.2 to be clustered independently. From this it might be hoped that at four clusters, each of the four types are separately identified. The clustering produced with four clusters in figure 4.9 shows that this is not the case: instead of finding two stroma clusters, one for each classification, the Barrett's epithelium tissue is now divided between two clusters, generally able to be described as the optically more and less dark components of the tissue.

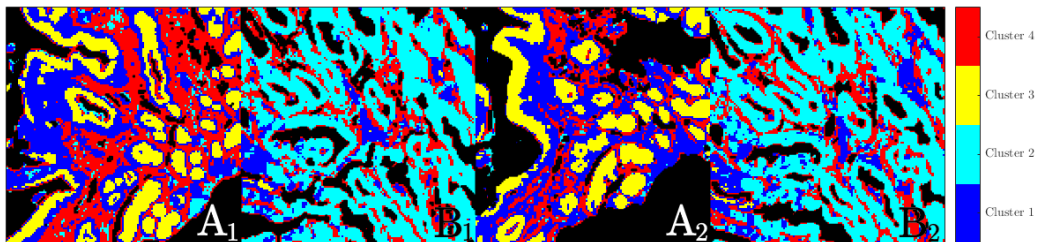


Figure 4.9: The clustering results for KCA with four clusters. The addition of another cluster has still maintained the cancerous epithelium cluster

At five clusters the Barrett's epithelium and cancerous epithelium tissues are still mostly clustered separately, but rather than each of the two stroma being clustered independently, the two clusters are split almost evenly between both samples. This division here suggests that the model for the stroma is too general. It is known to be a complex tissue comprising several types of cell with variable density and composition, especially in this sample

sections. The variability can be seen in the optical images in figure 4.1e-f as a variation in the optical density of the sample, but the chemical variations resulting from this could potentially be much more significant. As shown in figure 4.10 at five clusters there is a blurring of the clusters, that is the clusters are less sensitive to any one class, and three of the four classes (Barrett's epithelium, benign stroma, cancerous epithelium and cancerous stroma) are grouped across several clusters to a greater degree, creating clusters with a mix of classifications.

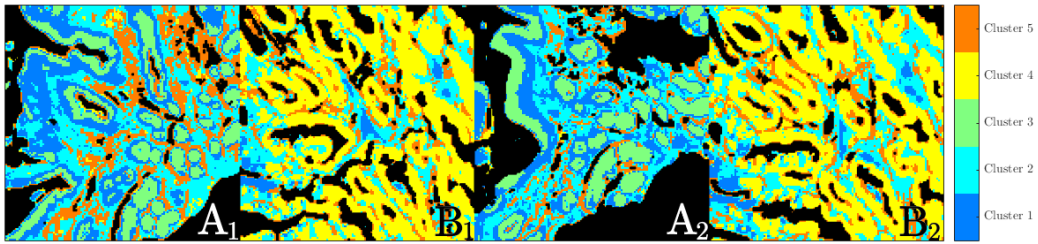


Figure 4.10: The clustering results for KCA with five clusters. While there are now two clusters containing predominately stroma pixels, they are not specific for either type of sample. The definition between the clusters is also decreased when compared to the results for fewer clusters.

4.5.4 6, 7 and 8 Cluster KCA

Extending the number of clusters further further decreases the level of success in differentiating between the tissues, as shown in figure 4.11. The degradation is somewhat to be expected from the fact that there are four groups of tissues that are being compared to clustering of 6 or more groups of spectra. If the data is naturally grouped into 4 or 5 clusters, adding further clusters into the analysis will obscure this structure by adding clusters in between the true clusters, bringing spectra from each group together and ‘blurring’ the differentiation. If considering the full 13 classifications of tissue, it is important to note that the grouped classifications were made by combining similar tissue classes together, thus the lack of differentiation will persist into the sub-classes that make up each group.

From the cluster images in figure 4.11 it can be seen that, while the Barrett's epithelium cluster splits further into several sub clusters, the cancerous epithelium tissue class is consistently assignable to a single majority cluster, and until eight clusters there is no significant secondary cluster of cancerous epithelium tissue.

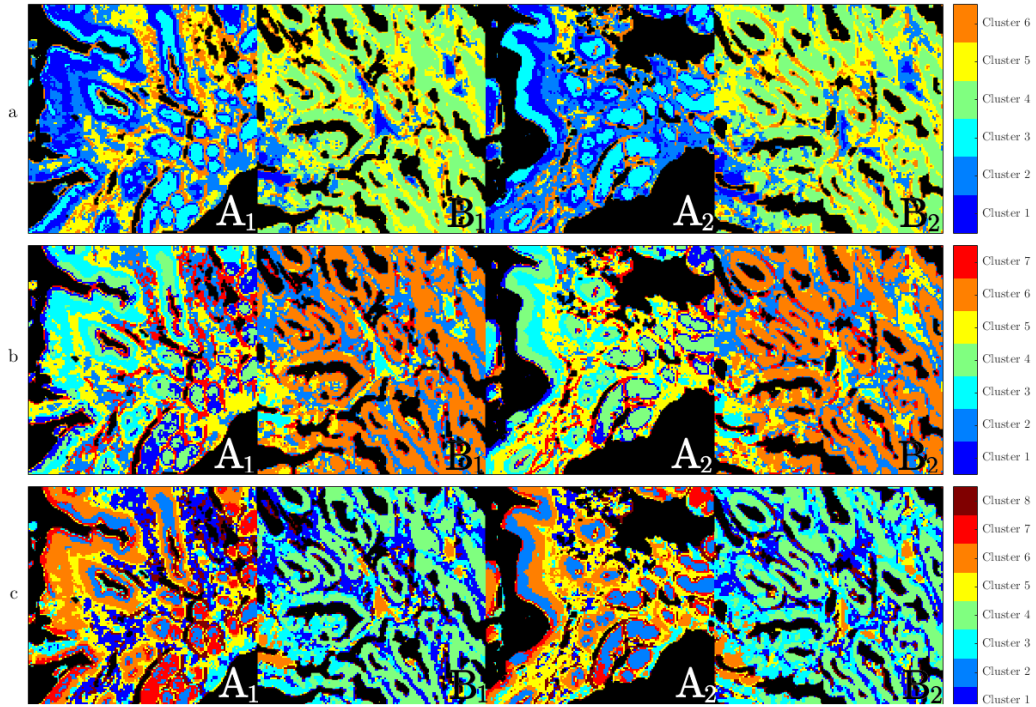


Figure 4.11: The clustering results for KCA with six (*a*), seven (*b*) and eight (*c*) clusters. The differentiation between tissue classifications further degrades with increasing cluster number. The cancerous epithelium tissue retains a single majority cluster throughout which only starts to degrade at eight clusters.

4.5.5 Discussion of KCA

Comparison with HCA

The cluster images produced by KCA are a significant improvement upon those from the HCA. KCA is much less sensitive to outlying data points and so is able to look more precisely at the structure of the data. The agreement for two clusters between HCA and KCA is a strong indicator that the structure observed is not through chance, but rather is a feature of the data. The ability of the three cluster KCA to essentially cluster together the stroma, the Barrett's epithelium and the cancerous epithelium separately shows that while the stroma tissues are too similar to distinguish at this level, the epithelial tissues in the Barrett's oesophagus and adenocarcinoma are significantly different both from each other and from the stroma tissue.

The similarity between the cancerous and benign stroma tissues is demonstrated further by the lack of individuality within the clusters, even up to eight: in each analysis the cluster(s) that correspond to the areas of stroma tissue are always a mixture of both cancerous and benign. While one may possess a majority of Barrett's epithelium or cancerous

epithelium, neither is specific enough to truly label one tissue classification.

Ability to Identify Cancerous Tissue

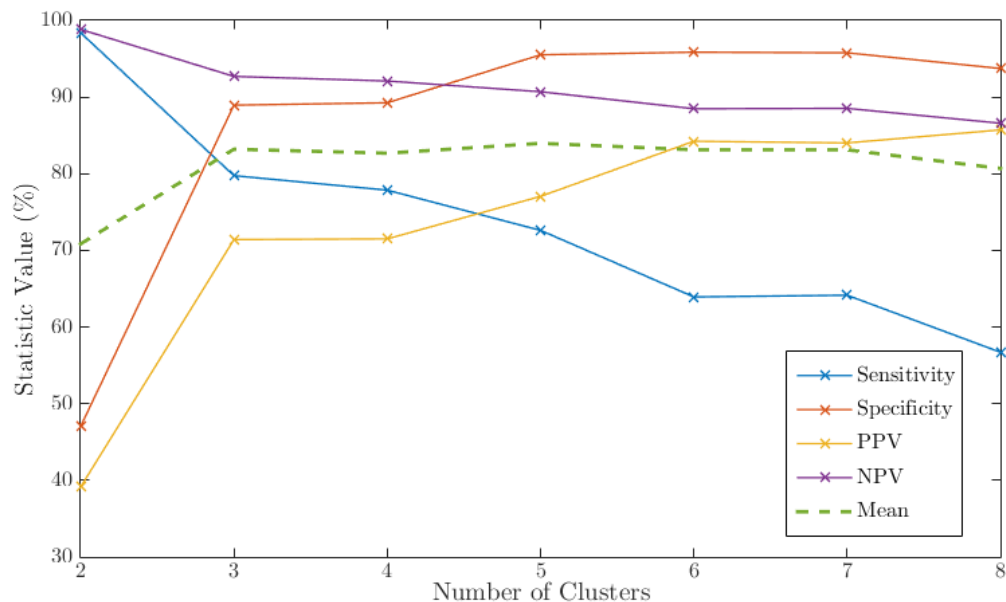


Figure 4.12: The four statistics for the classification of the cancerous epithelium tissue plotted for varying number of clusters. Also plotted is the mean value of the four quantities. This is maximised at the optimum number of clusters, in this case 5 clusters, with three clusters giving a slightly lower value.

The aim of these analyses was to determine the ability of HCA and KCA to identify the presence of different tissues within a sample imaged using FTIR-HSI. In terms of this aim the results of KCA were a success in that even up to 7 clusters this approach is able to maintain a single ‘Cancer’ cluster corresponding to the cancerous epithelium tissue regions. This cluster gives access to a quantitative measure of how successful each clustering is with respect to identifying cancerous epithelium: the sensitivity, specificity, PPV and NPV calculated

Cluster	Sensitivity (%)	Specificity (%)	PPV (%)	NPV (%)
2	98.4	47.0	39.1	98.8
3	79.8	89.0	71.4	92.7
4	77.9	89.3	71.5	92.1
5	72.6	95.5	77.1	90.7
6	63.9	95.9	84.2	88.5
7	64.2	95.8	84.0	88.5
8	56.7	93.7	85.7	86.6

Table 4.5: The statistic values for samples A_1 and B_1 differentiating the cancerous epithelium tissue class for varying cluster number. In each case the identified cluster is the one with the highest sensitivity to cancerous epithelium.

at each cluster number for the cluster representing the cancerous epithelium tissue. The clustering that maximises all four of these for the cancerous epithelium cluster should be the optimum number to use to identify this tissue classification. Table 4.5 shows the trends in these four quantities with varying cluster number. The sensitivity and NPV both decrease for higher numbers of clusters, with the decrease in sensitivity far outstripping the decrease in NPV, while the specificity and PPV both increase markedly with increasing number of clusters. These trends, along with the mean of the four values at each cluster number, are plotted in figure 4.12. The average value shows a surprisingly flat trend after the initial jump from two to three clusters, and has a maximum value at 5 clusters, with three clusters a close second.

Finding the optimum value to be five clusters suggests that this is the best representation of the tissue structure. At five clusters the areas identified roughly correspond to the optically lighter and darker Barrett's epithelium areas, two stroma clusters shared between the two types of sample, and a single cancerous epithelium cluster. As stated above the two stroma components are likely to correspond to different densities of stroma tissue, which is fibrous and contains many gaps and thinner sections after dewaxing. Thus this five-cluster representation is an appropriate way of grouping the tissues.

The maximum sensitivity of 72.61% is far from ideal: the cluster analysis only identifies 72.61% of the cancerous pixels. However, the specificity is good, showing that the cancerous epithelium cluster is 95.52% accurate in excluding the other tissue types. The PPV and NPV give similar statistics, but with respect to the contents of the cluster: for five clusters the cancerous epithelium cluster is 77% cancerous epithelium tissue (a PPV of 77.05%) and only 9.3% of the other tissue types were included (a NPV of 90.7%).

Discussion on Sample Morphology

The results of the KCA highlight some details of the tissue morphology that are a product of the type of samples being imaged. At four and five clusters the Barrett's epithelium and stroma respectively are successively separated into two clusters. In the case of the Barrett's epithelium clusters the two clusters label the optically darker and lighter regions of the Barrett's epithelium tissue. The former correspond to areas with a high density of nuclei while the latter are regions of particularly low nuclear density. These different areas are produced by the relative orientation of the columnar epithelial cells and the cut across the

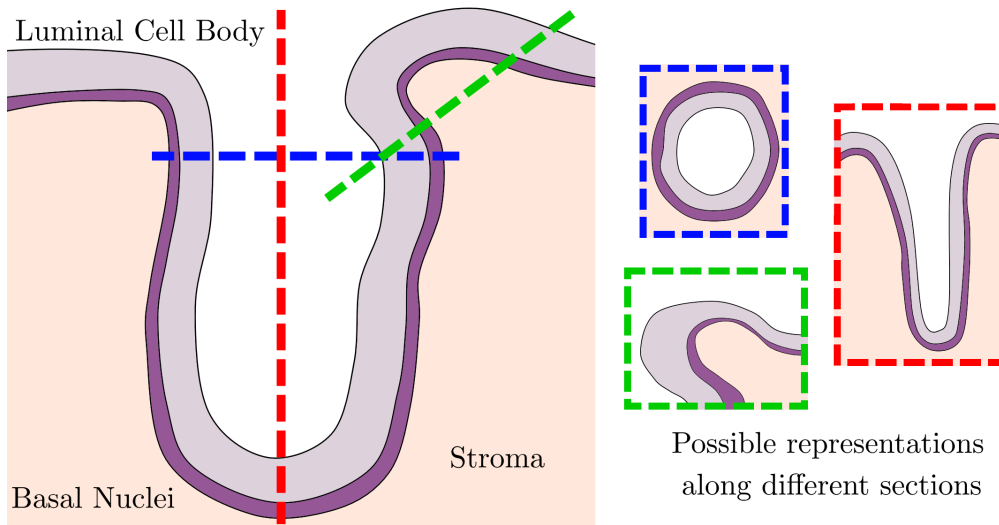


Figure 4.13: An illustration of how different cuts through the three-dimensional crypt shape in a sample of Barrett's oesophagus tissue can lead to very different two-dimensional cross-sections.

sample to produce the section. The epithelial cells in Barrett's oesophagus are columnar, and as such have a major axis that points towards the lumen (inside) of the crypt it is part of. The nuclei of these cells are typically located at the base, away from the lumen. If the epithelial cells are orientated with their major axis parallel to the direction of the section cut, the cross-section of the cells will have two regions: the bases of the cells forming a dark layer of nuclei and the upper portion of the cells forming a layer comprising of mainly cell walls and cytoplasm. Alternatively if instead the cut is perpendicular to the cell major axis entire regions of the cut tissue can be only nuclei or only cytoplasm, leading to much larger 'patches' of a single component of the epithelial tissue. By varying the cut angle, or more appropriately, as the orientation of the cells varies across the image area, different profiles of cells are created, leading to a complex picture of the tissue. Some simple examples of this variability are shown in figure 4.13, though the true samples are more complicated than this, the general principle that different cuts through the sample give dramatically different shapes of tissue is demonstrated.

These different presentations of the same tissue have all been grouped together for the generalised tissue classifications, but when subjected to KCA the clusters pick out the differences. Furthermore, depending on the depth of a cell in a crypt, its presentation and composition can also vary [3]. The full thirteen classification image attempts to capture some of this complication by labelling each different type of region but, as stated above,

when clustering to higher cluster numbers the KCA does not pick up on the subtler differences.

Effect of Age

A secondary aim of this investigation was to assess the effect that the time elapsed between the removal of the wax and imaging of the samples had on the quality of the spectral information obtained. This is important to characterise, as the SNOM imaging of the same type of samples took a considerably longer time than the FTIR-HSI, with a dewaxed sample being imaged over several days. To that end, the second pair of FTIR-HSI images, A₂ and B₂, were acquired in approximately the same area of serial sections of the same samples but dewaxed approximately six months before imaging. Despite this difference in age, the samples show little variation in terms of the way that areas are labelled (other than those expected from the variation between serial sections) after the preprocessing stages detailed in section 3.2.

Since the secondary samples were not labelled as the primary samples were in figure 4.2, chiefly because of the time taken to perform this step, the accurate labelling statistics are unknown, but it can be seen from a comparison with the optical images of the scan areas in figure 4.1g,h that the clustering is selecting the same types of areas in both primary and secondary samples. Furthermore, if a significant difference between the fresh and older samples was present, they would be likely to cluster independently. This result implies that the FTIR-HSI data of older samples is still comparable to that of new samples, something that was previously unknown.

The general medical practice with fixed and wax-embedded biopsy samples is to use dewaxed specimens as soon as possible after removing the paraffin wax due to worries that the sample will degrade. It is important to note that the samples used in this work were not stored in any particularly preservative manner, simply being stored at room temperature in a closed, but not airtight, petri dish. Knowing that the samples are at least qualitatively the same after six months implies that after two or three days there should be no discernible degradation of the chemical signals in the samples. It is important to note that this does not rule out other types of degradation that the FTIR-HSI is not sensitive to.

Applicability to a Generalised Case

Any analysis aimed at determining if an oesophageal tissue sample is benign or cancerous needs to be applicable to any appropriate sample image data. Cluster analysis is a good initial approach as it requires very few user inputs: it is an essentially unguided analysis technique. This type of analysis also has its downsides. While it is able to identify these tissue types in one pair of samples, it does not follow that it will produce the same results on another pair of samples. For example, simply setting the KCA algorithm to find 5 clusters in a single image corresponds to over-clustering like that seen for the higher cluster numbers in figure 4.11, an individual sample could contain up to 4 of the five types of cluster seen here, but should not contain more according to the simplified model in figure 4.2b. Plotting five clusters would obscure the tissue structure in the same way as plotting six or seven clusters does in the above analysis. Most important of all is that in both HCA and KCA what is returned is simply a map of clusters, with no knowledge of what they correspond to. It is only by comparing the maps produced with a previously determined map that the knowledge of which cluster corresponds to which tissue classifications becomes evident.

The above reservations do not obviate the value of KCA as an investigative tool. The results obtained demonstrate that it is possible to distinguish between the different tissue types based on their spectra and that the differences are consistent enough to group the majority of each tissue type. In addition to this it can also be seen that the loose classifications of the four tissue types: Barrett's epithelium, benign stroma, cancerous epithelium and cancerous stroma are successful but are also, as mentioned above, a simplification of the actual tissue structure, giving two clusters for both the Barrett's epithelium and stroma classifications.

The KCA was especially good at reliably identifying the cancerous epithelial tissue from the other tissues. This could be used as a diagnostic if the analysis used on the data is aimed toward specifically selecting this tissue. To identify the wavenumbers best at differentiating between the cancerous epithelium and other tissues, the result of clustering to 5 clusters were taken as the optimal clustering. The average spectra of the cancerous epithelium cluster and the combination of the other clusters were compared by taking the square of the difference between them, shown in figure 4.14, given by:

$$\alpha_{diff} = (\alpha_{4 \text{ mean}} - \alpha_{1,2,3,5 \text{ mean}})^2 \quad (4.6)$$

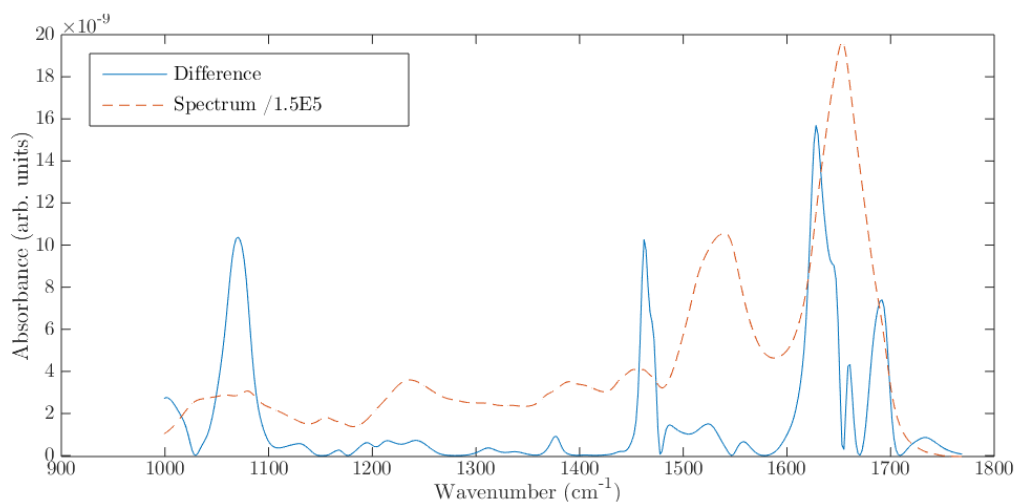


Figure 4.14: The spectral square difference between the average spectrum of the cancerous epithelium cluster and the other four clusters combined, calculated for 5 clusters. There are four principal peaks that give a difference between the averages: 1071, 1462, 1628 and 1692 cm^{-1}

The four largest peaks are found at 1071, 1462, 1628 and 1692 cm^{-1} (9.31, 6.84, 6.14 and 5.91 μm respectively). There is no guarantee that the differences between the average spectra are consistent over the whole of the sample, but it provides a start point to progress analysis further.

While KCA can identify differences in the data, those differences are not necessarily due only to the chemical variations in the sample and the approach could find entirely independent types of clustering for different sample data. In order to provide a method of differentiating between spectral data that is not dependent only on any self-consistent variation within the set being tested, a more guided or directed approach must be used, to label these spectra in a manner that can be relied upon across multiple sets of independently acquired data. With this aim, a method of analysis that learns the signature of several classifications from a training set and applies that knowledge to label another, unknown set of data was developed.

4.6 Metric Analysis

The use of different techniques to label IR spectra from biological samples is a large area of active research. There are many examples of the use of both HCA and KCA as well as other types of unsupervised clustering techniques (for example [67][71][72]) applied to classification of cancerous cells and tissues. The application of unsupervised techniques like

these remains a popular and intuitive method for accessing complex information patterns within a spectroscopic data set.

With the advance in recent decades of increasingly powerful computers the development of machine learning techniques has been possible. Machine learning aims to use an *a priori* knowledge of the classifications or behaviour of a small set of data to teach an algorithm to be able to statistically predict the classifications of another, larger set of data, such as FTIR spectra acquired over a candidate biopsy sample, in order to label the different regions of the sample. Many variants of machine learning exist, all of which tend to provide a probabilistic measure of the classification of each tested spectrum. discriminant function analysis (DFA) [54] and linear discriminant analysis (LDA) [73] aim to define functions of the sample spectra that discriminate between them. artificial neural networking (ANN) models the learning algorithm in a similar structure as a brain [74].

These approaches to automated labelling of sample spectra according to common behaviours is similar in nature to the cluster analyses considered above, but by sacrificing the unsupervised analysis in order to gain the ability to direct the analysis towards desired differentiations.

While machine learning algorithms are well established in analysing FTIR spectroscopic data from tissue for cancer diagnosis, the application of such techniques to SNOM images requires an approach that is as flexible and accessible as possible. For this reason, a variant of the above machine learning techniques was developed specifically for this work.

The principle applied in this MA is that of a basic machine learning algorithm: a small set of known data is used as a training set to quantify the response of the different tissue classifications to a given quantitative measure, or metric. Once the outcome of the metric has been calculated for each classification, it can then be used to label unknown data based upon its response to the same metric. This method represents a significant advantage over cluster analysis by identifying data in a directed way, classifying pixels according to the behaviour expected by each tissue class, rather than simply classifying groups by the strongest differences between them. In addition this approach is very flexible, as any test to the candidate data that produces a quantitative outcome can potentially be used as a metric. The disadvantage of MA lies in the requirement of an adequate training set. The classification can only be as accurate as the training set given to the MA, and the same data may be slightly differently labelled with a different training set. Therefore an effective MA

requires not only a suitable metric - or set of metrics - to be defined, but also a high quality training set of sufficient size to ensure that the labelling is robust and reliable.

4.6.1 Labelling Method

The following section provides the procedural details and mathematics used in the MA. The general principle can be broken into two stages: training the algorithm and applying the learned discriminator metrics to the unlabelled data.

Training the Analysis

The MA is trained with a set of j groups of data with known classification, $(\zeta_1, \zeta_2, \zeta_3, \dots, \zeta_j)$, with each group of data containing n spectra corresponding to a specific classification:

$$\zeta_i = [\alpha_1, \alpha_2, \alpha_3, \dots, \alpha_n] \quad (4.7)$$

There is no requirement that all classification groups be the same size, but a larger number of spectra in the training set group will lead to a more accurate analysis. For this FTIR-HSI data the training set consisted of 200 randomly selected spectra of each of the four simplified tissue classifications shown in figure 4.2. This number was chosen to represent sufficient data to reliably model the characteristics of the tissue classes without relying on too much of the original data set: the 200 pixels correspond to less than 5% of each class. Potentially any quantitative measure produced from these spectra can be used as a metric, providing that it has different values for each tissue classification.

Having defined a metric $f(\alpha)$, it is evaluated for each of the training set classes producing a vector of n values for each classification

$$[x_1, x_2, \dots, x_n] = [f(\alpha_1), f(\alpha_2), \dots, f(\alpha_n)] \quad (4.8)$$

where n is the number of spectra in the relevant class of the training set. Realistically any given metric will produce a distribution of values for each tissue class, which needs to be sufficiently distinct from those produced by the other classes to produce a reliable labelling method. The metric values are used to form a histogram, with 50 bins over their range, which is then fitted with an appropriate function to model their distribution, $M_i(x)$. Each classification produces a distribution for a given metric, which is then compiled with the

distributions produced by the other classes in order to be used in the labelling stage.

In this work the distributions of metric values were often very close to a Gaussian distribution:

$$M_i(x) = Ae^{-\frac{(x-\mu)^2}{2\sigma^2}} \quad (4.9)$$

where A is the amplitude of the Gaussian curve, μ is the mean of the classification's metric values and σ is their standard deviation from the mean. MATLAB was used to fit the distributions with Gaussian functions over an initial range of $\mu \pm 2\sigma$ defined by the `average` and `stdev` functions for the whole data set. As these functions are sensitive to outlying data, the fit produced over that range was used to generate new values for the mean and standard deviations as defined by the functional form and these were compared to the original values from the full data set. If the standard deviation of the fit was less than half that of the original data then the fitting procedure was repeated over the new $\mu \pm 4\sigma$ range defined by the first fit result. This is effective at removing any outlying data that might otherwise skew the fit produced by MATLAB and ensures that the modelled distribution is as accurate as possible.

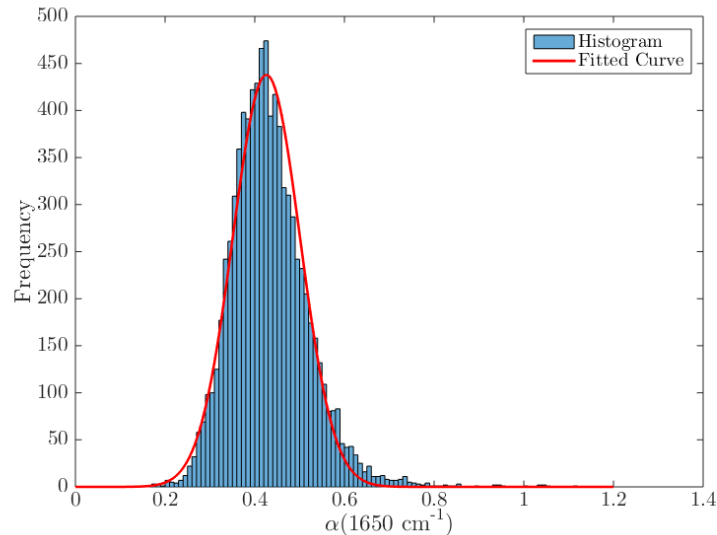


Figure 4.15: A histogram produced by the labelled cancerous epithelium tissue spectra at the Amide I peak at 1650 cm^{-1} and the fitted Gaussian distribution. It can be seen that the histogram is very Gaussian in nature, making this approximation a good one, but does have an element of positive skew.

Fitting a Gaussian curve to the histograms produced by a metric is clearly not always appropriate. With this work it was used as an approximation to simplify the analysis, and was found to be a relatively good approximation for simple metrics. An example of a

histogram produced from the FTIR data and the corresponding fit to it is shown in figure 4.15. The metric values used to produce the histogram are simply the values of absorbance from a single tissue type, cancerous epithelium, at a single wavelength, 1650 cm^{-1} . The fitted histogram closely resembles a Gaussian profile, but does have a slight positive skew. Despite this, the approximation was deemed to be appropriate for the majority of metrics.

To increase the reliability and accuracy of the analysis, multiple metrics may be employed. While a single metric could allow each classification to be successfully labelled if the distributions are well separated from each other, the reality of the data being analysed here is that the differences between the tissues are small. From any given metric it is unlikely that the FTIR-HSI data will give narrow, well-separated distributions for each classification and thus it is necessary to use several different metrics to distinguish between even two tissue classifications.

If the metrics and training set are unchanged, the training stage of the MA needs to be done only once, and can be applied to multiple labelling stages, giving a much faster labelling method than HCA and a comparable speed to KCA.

Applying the Labelling

Having identified the distributions $M_i(x)$ that describes the behaviour of each class with respect to a given metric from a training set of known data, the MA applies this knowledge to a set of unknown data, in this case the FTIR-HSI data cube. As in the two cluster analyses above, each spectrum is considered independently from its spatial location, and the classification label is tracked back to the spatial location after it has been labelled.

An initial check on each spectrum is performed to eliminate those spectra that correspond to areas of low absorbance, essentially removing the spectra of gaps in the samples, similar to the check performed in the original preprocessing stages for the FTIR-HSI data. Any spectrum with an integral intensity less than 12% of the maximum integral intensity observed for the data being labelled are excluded from the labelling process.

Each test spectrum $\alpha_{test}(k)$ gives an associated metric value

$$x_{test} = f(\alpha_{test}) \tag{4.10}$$

that needs to be compared to the distributions given by the training set. The metric dis-

tributions from the different classes can potentially be dramatically different in width and height and so the method for comparing the value of a metric to the distributions must compensate for this. The Gaussian distributions $M(x)$ are area-normalised such that they have an integral over all x of 1:

$$\int M_{i,norm}(x)dx = 1; M_{i,norm}(x) = \frac{M_i(x)}{\int M_i(x)dx} \quad (4.11)$$

This produces a probability density function for the classification as a function of metric value, but to obtain a true probability from this distribution requires an area of the curve: a range of x to integrate over. It is not clear what this range would represent for complex metric forms, but in general the uncertainty in the value of the metric, Δx gives a quantity that not only provides the suitable range $x \pm \Delta x$ but also provides a way of compensating for the variable distribution width. For a metric value that lies within an overlapping region of a narrow and a broad curve the area found for the narrow distribution, and therefore the corresponding probability, will appropriately be much higher than for the broad curve, representing the specific nature of a narrow distribution of metric values and therefore its increased ability to identify that classification. The probability that a given spectrum belongs to the class ζ_i is evaluated by the *confidence coefficient* c_i given by:

$$c_i = \int_{x_{test}-\delta x}^{x_{test}+\delta x} M_{i,norm}(x_{test})dx \quad (4.12)$$

If multiple metrics $x_{test,j} = f_j(\alpha_{test})$ are used, the confidence coefficients in equation 4.12 are generalised to

$$c_{i,j} = \int_{x_{test,j}-\delta x}^{x_{test,j}+\delta x} M_{i,j,norm}(x_{test,j})dx \quad (4.13)$$

calculated for each metric j and for each classification i , and the combined confidence coefficients for each classification are found by summing the individual values for each metric:

$$c_i = \sum_j c_{i,j} \quad (4.14)$$

The total confidence values, χ_i , for each spectrum across each possible classification are sum-normalised:

$$\chi_i = \frac{c_i}{\sum_i c_i} \quad (4.15)$$

to meet the requirement that the sum of probability over the classes is 1. After testing each metric against each class the spectrum is assigned to the class for which it has the highest confidence.

The MA produces an image of classification identifications in the same way as the cluster analyses do, with unique colours representing each tissue classification. In addition to the colour, the pixels are also varied in intensity according to the confidence in the assigned class: brighter pixels are more confident.

4.6.2 KCA-Inspired Absorbance Metrics

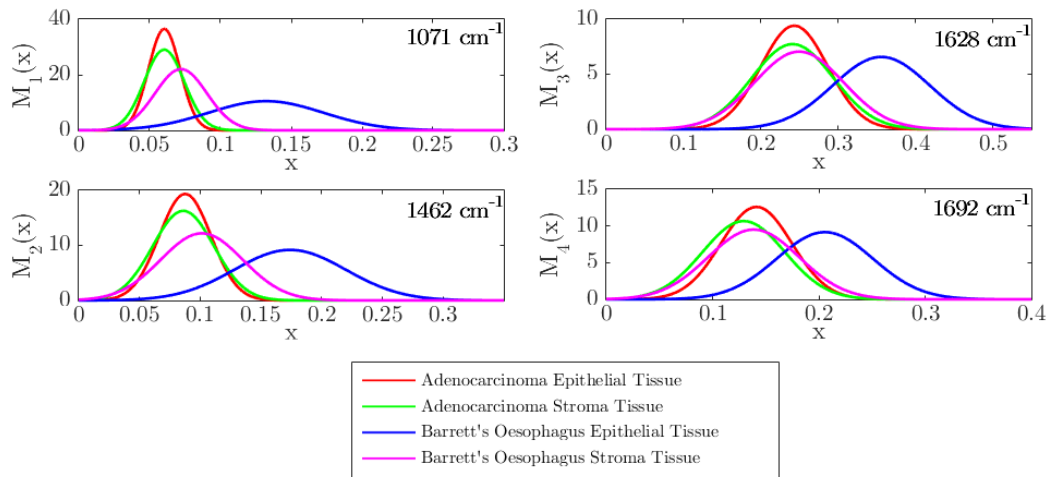


Figure 4.16: The distributions produced by the four distinguishing wavenumbers that were identified by the five cluster KCA results evaluated over the four training sets for the MA. Each training set was formed from 200 random spectra of one of the simplified classifications. Although these wavenumbers were identified to classify the cancerous epithelium tissue the distributions for Barrett's epithelium are by far the most distinct.

One of the most basic forms of metric that could be applied to the FTIR-HSI data is the values of absorbance at specific wavenumbers. Those wavenumbers identified in figure 4.14 (1071, 1462, 1628 and 1692 cm^{-1}) were taken as four metrics to label the sample, as these should be able to provide a good separation of the cancerous epithelium data, thus giving a diagnostic for that tissue. In order to provide a training set, 200 spectra from each of the four simplified classifications given in figure 4.2 were selected at random to give the most unbiased training set. These spectra were taken only from the first two images, but were used to label all four images.

The metric distributions produced for the four tissue types are displayed in figure 4.16. The distributions are far from an ideal situation of a minimal overlapping area between,

but even with a large overlap, it should be possible to produce a map of the sample tissues. The wavenumbers were chosen to distinguish the cancerous epithelium tissue, but instead of finding clearly separated distributions for the cancerous epithelium tissue by which it could be easily labelled, it is the the Barrett's epithelium tissue distributions that are all by far the most distinct, with peaks at comparatively much higher metric values than the other three types. Interestingly the cancerous epithelium and stroma sets give very similar distributions, while the benign stroma set is more distinct from the cancerous stroma, in contrast to the combined cancerous/benign stroma clusters and distinct cancerous stroma/epithelium clustering seen in most of the KCA clusterings shown above.

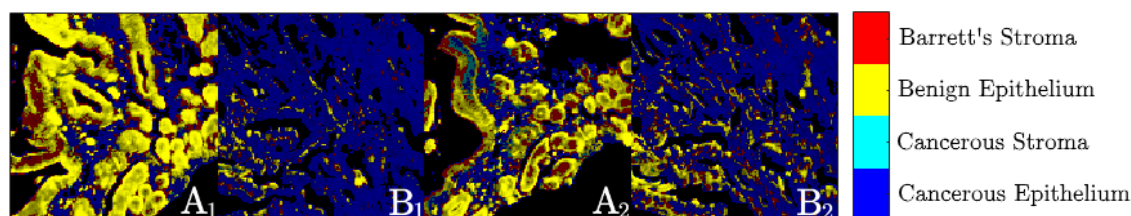


Figure 4.17: The map of labeling produced by the MA using the absorbance values at four wavenumbers as the metrics used to distinguish between the tissue types. In the same way as for the cluster analyses above the tissue classifications are given by colours, with the added intensity scale to represent the confidence value for each pixel: brightly coloured pixels are high confidence, darkly coloured pixels are low confidence. The Barrett's epithelium tissue has been confidently labelled, while the cancerous epithelium and stroma are mainly grouped together under the cancerous epithelium label and the Barrett's epithelium tissue is not confidently labelled, though it does mainly exist in the Barrett's-containing sample areas it is also labelled in the cancerous tissues significantly as well, along with the Barrett's epithelium tissue.

Applying the labelling to the whole set of image data produces the mapping in figure 4.17. Rather than mapping the cancerous epithelium tissue confidently, the Barrett's epithelium tissue is the most confidently and accurately labelled. The cancerous epithelium and stroma tissues have been mainly grouped together under the cancerous epithelium label, and the benign stroma tissue is also significantly included in that label. A large portion of both cancerous samples have also been labelled using the two Barrett's labels. In the same way as for the cluster analyses above the sensitivity, specificity, PPV and NPV were calculated for this mapping and shown in table 4.6.

The cancerous epithelium and Barrett's epithelium labels give relatively high sensitivities, though the sensitivity for Barrett's epithelium is much higher. The general ability of the Barrett's epithelium label is similar to, and slightly better than, the labelling achieved by the three cluster KCA above, but the cancerous epithelium label does not reach the level of

Tissue Label	Sensitivity (%)	Specificity (%)	PPV (%)	NPV (%)	Number Labelled
Barrett's epithelium	81.61	90.94	74.09	93.97	8696
Benign stroma	17.71	93.02	28.36	87.88	2761
Cancerous epithelium	86.65	69.76	49.79	93.79	14661
Cancerous stroma	0.37	99.49	9.88	86.67	162

Table 4.6: Tissue assignments for the labels given by the first MA, using the first two images A_1 and B_1 only and comparing to the labelled images above as before. The two epithelial clusters are labelled with relatively high sensitivities, and the Barrett's epithelium tissue label is also very specific. The other two classifications, having been grouped together, show very low sensitivity. The cancerous stroma tissue in particular has a sensitivity of only 0.37% simply because most of the corresponding spectra have been labelled as cancerous epithelium while only 162 spectra were labelled as cancerous stroma.

success achieved by the KCA. The Barrett's epithelium tissue label is also very specific. The other two classifications, having been grouped together, show very low sensitivity, and poor PPV. The cancerous stroma tissue in particular has a sensitivity of only 0.4% simply because most of the corresponding spectra (only 162 spectra were labelled as cancerous stroma) have been labelled as cancerous epithelium.

The mapping obtained by the procedure described above is in line with the behaviour of the distributions given by the metrics in figure 4.14: the Barrett's epithelium mapping is more reliable as it is removed from the other three distributions in all five metrics, while there is a large overlap between the other three classes such that they are not easily differentiated. The cancerous epithelium distribution is slightly narrower than the other two distributions with which it has a significant overlap, therefore having a higher distribution value and thus will give larger areas, and correspondingly larger confidence values, for the cancerous epithelium, cancerous stroma and benign stroma spectra over a relatively large range of each metric.

This labelling displays some merits but it is not as successful as the KCA method described earlier at recognising which tissue samples are benign or cancerous as all four image areas here have significant amounts of each of the tissue labels present within them. The low success of this labelling stems from three sources. The first shortfall is the number of metrics used. Increasing the number of metrics should give increased information about each spectrum that is tested, and the labelling should be better able to distinguish each classification. The second potential issue is that the labelling produced by MA will only ever be as good as the training set used. Selection bias is minimised by randomly selecting

a training set from the labelled data, though this bias is still present to some degree in the accuracy of the original labelling itself. The quality of the randomly selected spectra may also be lower than could be necessary to produce a good labelling of the test data. A third effect that could be a cause of difficulty in labelling the spectra is seen in the metric distributions in figure 4.14 where the general trend of the four tissues is similar across all four metrics. The peaks are all in the same order: cancerous stroma, cancerous epithelium, benign stroma, Barrett's epithelium with similar relative widths. This correlated behaviour across the fingerprint region could be due to the intrinsic behaviour of the tissue, but could also be due to different components of the tissue having consistently variable thickness.

While the tissue samples were cut to a uniform thickness before dewaxing, after the paraffin wax was removed the samples will have relaxed to account for the volume removed by this process. The different tissue components will relax to differing degrees due to the amounts of their structural components that are unaffected by dewaxing. The thicker areas of tissue will give increased absorbance across the spectrum and so will lead to higher values for each metric used here, as observed for the Barrett's epithelium tissue. The Barrett's epithelium tissue is also non-uniform, as discussed in the KCA discussion above in section 4.5.5, which will lead to a larger variation in absorbance over the tissue, which is seen in the corresponding distributions of metric values above.

To mitigate these effects, more and better metrics had to be found, which took into account the variable thickness and other spatial effects that could interfere with the application of the MA. One such metric is the ratio of the absorbances at two different wavenumbers. This is only a slightly more complicated metric than taking the absorbance at a single wavenumber, but by taking the ratio any multiplicative factors affecting the spectrum as a whole will cancel from the final metric values. To increase the number of metrics, it becomes necessary, especially with a more complex metric form, to find a method of identifying the metrics that will produce the most reliable labelling method.

4.6.3 Automated Metric Optimisation

To develop the MA further, a self-optimisation metric-finding routine was implemented to identify and use the optimum metrics for discriminating between specific pairs of classifications in the training set. The following is a description of the implementation and outcome when applied to the FTIR-HSI above.

Optimisation Method

The training set for the MA essentially already contains information on how to distinguish its component classifications. By providing separate groups of spectra that are already labelled as distinct, it simply becomes a task of identifying consistent differences between the two groups. By choosing a general metric form based upon combinations of spectral values and evaluating a range of specific metrics based on permutations of the general form, the optimum combination can be identified for a given comparison.

In this work the general form of metric used was a ratio of one absorbance value against another at a different wavenumber:

$$f(\alpha_{test}(k)) = \frac{\alpha_{test}(k_1)}{\alpha_{test}(k_2)} \quad (4.16)$$

which provides several advantages over more complex discriminants. Firstly it is simple to understand in terms of the spectrum; it gives the absorbance at a particular wavenumber, as in section 4.6.2 with raw wavenumber values, but references them against another value in the spectrum to give a comparison between the two. Secondly it allows several potentially confounding effects to be removed, or at least reduced, from the final value produced. The main effect that is eliminated is the variable thickness of the sample leading to a variation in total absorbance from pixel to pixel, essentially changing the amplitude of the spectrum. By taking the ratio of two values, this amplitude cancels. A side effect of this cancellation is that it removes the need to normalise the spectra in the preprocessing stages, and the use of wavenumbers directly means that it is also unnecessary to perform the PCA to the data. It is also the case that the MA should be able to directly identify the gaps in the sample, and so the integral limit exclusion imposed on the data is also unnecessary. As a result, the only preprocessing stage that needs to be applied to the data is the Mie scattering correction, which is now especially important as any discrepancies in peak locations will have large effects on the outcome of ratios based on those peaks.

Rather than evaluating a metric for every classification in the training set and using those distributions to distinguish between all classifications, an optimised set of four metrics is found for each potential comparison pair of classifications. For example if a training set of three classifications, A, B and C, is used, then the comparison pairs A-B, A-C and B-C will each have four specific metrics found to be the best at discriminating between the two

classifications involved, without using those metrics to compare either of the classes in each pair with the one not in the pair. This produces a set of metrics:

$$f_{A-B;j}(\alpha) \quad (4.17)$$

$$f_{A-C;j}(\alpha) \quad (4.18)$$

$$f_{B-C;j}(\alpha) \quad (4.19)$$

$$j = 1 \dots 5 \quad (4.20)$$

which give each classification eight confidence coefficients. These are processed in the same way as above to give the confidence values for each classification.

In order to identify the optimum metrics for each discrimination, the general metric must be calculated for every wavenumber combination k_1, k_2 , for each individual spectrum within both classifications in the comparison pair. This is a significant computation, increasing with the squares of both the number of spectral points and the number of classifications and linearly with the number of spectra in each classification in the training set. The output of this calculation is a set of pairs of distributions, in this case Gaussian functions characterised by equation 4.9, fitted using the histograms of the values of each permutation of the general metric for both classifications:

$$M_{A,A-B}(x_{k_1,k_2}) \text{ and } M_{B,A-B}(x_{k_1,k_2}) \quad (4.21)$$

Continuing the simplified example with three classifications, A,B and C, if each classification contains 10 spectra where each has 10 spectral values, the computation above produces 270 pairs of Gaussian distributions based on 10 metric values. For a general number of classifications n_ζ and number of spectral points n_k there are:

$$N_{pairs} = \frac{1}{2} n_\zeta (n_\zeta - 1) n_k (n_k - 1) \quad (4.22)$$

pairs of distributions to be evaluated for success in distinguishing the relevant classifications. For the FTIR-HSI data using the four simplified classifications and one for the gaps in the sample, and using each of the 1453 spectral values, $N_{pairs} = 21.1 \times 10^6$. Reducing the number of spectral points used in the comparisons will have the biggest effect on the number of calculations required. As shown by the PCA performed in the preprocessing (see

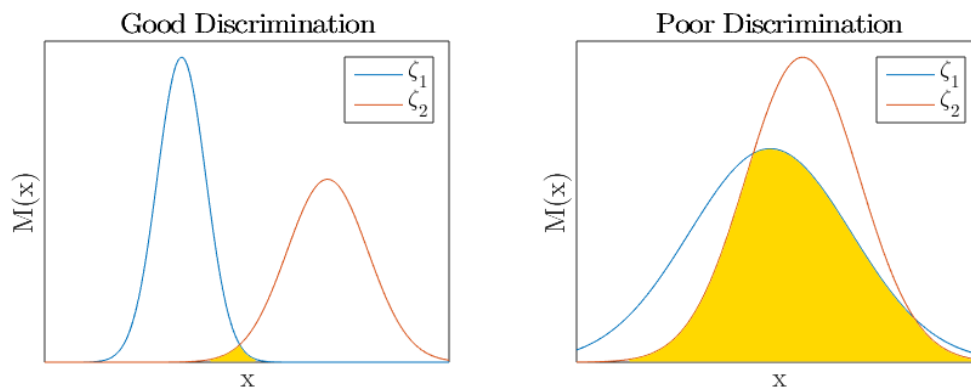


Figure 4.18: Examples of distributions produced by metrics that are either good or bad discriminators for the two classes ζ_1, ζ_2 . The overlap regions have been shaded. The good discriminator curves only overlap by 1.7% while the poor discriminator curves have a 77% overlap.

section 3.2) there is a large amount of redundancy in the spectral information. This is to be expected, as most of the tissue contains very similar chemical components. By using every fifth spectral value, rather than every one, the number of distribution pairs drops to 8.4×10^5 without significantly impacting the generalisation of the metrics. An additional reduction can be obtained by removing the gaps between tissues as a class. It is very unlikely that the low absorbance values produced by these pixels will produce similar values for the metrics for other tissues, and so will generally be labelled as random classes with very low confidence values, and appear black in the labelled images. This gives a total number of comparisons of 5.0×10^5 .

It is impossible to compare each of these pairs of distributions by hand to see which ones show the best distinction from each other, so a computer-guided method must be used. A particular metric is judged to be a good discriminator for a pair of classes if the distributions for the metric evaluated for the two classes have only a small overlapping area. Examples of a good and a bad discriminator are shown in figure 4.18, where the good discriminator produces distributions that are well separated and narrow with respect to the gap between them, while the poor discriminator has a substantial overlapping region of the two distributions and is much less able to define the two classes distinctly. Based on this, each metric distribution pair is evaluated based upon the overlapping area between the two curves, giving a measure of how well it discriminates the two classes. For this area to make a useful quantity, both curves need to be area normalised (see equation 4.11) before computing the overlap. The four metrics that produce the best (smallest) overlap are recorded as the optimum metrics for the pair of classes they have been calculated for, and are then used to label the unknown data in

the same way as above. The ability of the general metric to discriminate between different classes as a function of the spectral values used can be plotted in a *butterfly diagram* with the two axes plotting k_1 and k_2 and the colour scale giving $1 - A(k_1, k_2)$, where $A(k_1/k_2)$ is the area of overlap of the two metric distributions in that pair at the corresponding wavenumber ratio, making good pairs a brighter colour. These diagrams can aid different analyses, and were used to guide imaging wavelengths for the SNOM (see section 5.5.1)

4.6.4 Optimised Absorbance Ratio MA

Using the same randomly sampled training set as used for the KCA inspired absorbance value metrics in section 4.6.2, an optimised set of absorbance ratio metrics was found. As discussed above, by using absorbance ratios the need for most of the preprocessing that was performed on the data before applying KCA was removed and only the Mie Scattering Correction needed to be applied. The best five absorbance ratio metrics that distinguished between each pair of tissue classifications were found and used to label the four images as before. The wavenumbers used for each metric were found using the method given above, sampling every 10 cm^{-1} over the range $1010 - 1700 \text{ cm}^{-1}$. This range covers the reliable portion of the fingerprint region of the IR spectrum, and was chosen as this region contains many different vibrational signatures which represent a large amount of information about the sample. The fingerprint region also spans the operation range of the ALICE-FEL/SNOM, meaning that the results of the optimisation and labelling can also be applied to the SNOM data.

In order to obtain a general understanding of the ability of these four tissue classifications to be distinguished by the ratio values the butterfly diagrams for each comparison pair of classifications are shown in figure 4.19. While some show similar patterns, each butterfly diagram is different, meaning that different pairs of wavenumbers will give better results for each pair of tissue classifications. The colourbars on the right of each diagram shows that for Barrett's epithelium in particular there seems to be a larger maximum value, giving metrics with less overlap and thus better discrimination.

The results of the labelling are shown in figure 4.20. The map produced by the MA is again very different from those obtained previously. A complete reversal from the previous success in labelling Barrett's epithelium tissue using the 'raw' absorbance values found from the KCA is observed. Here the Barrett's epithelium tissue is very poorly labelled, while the

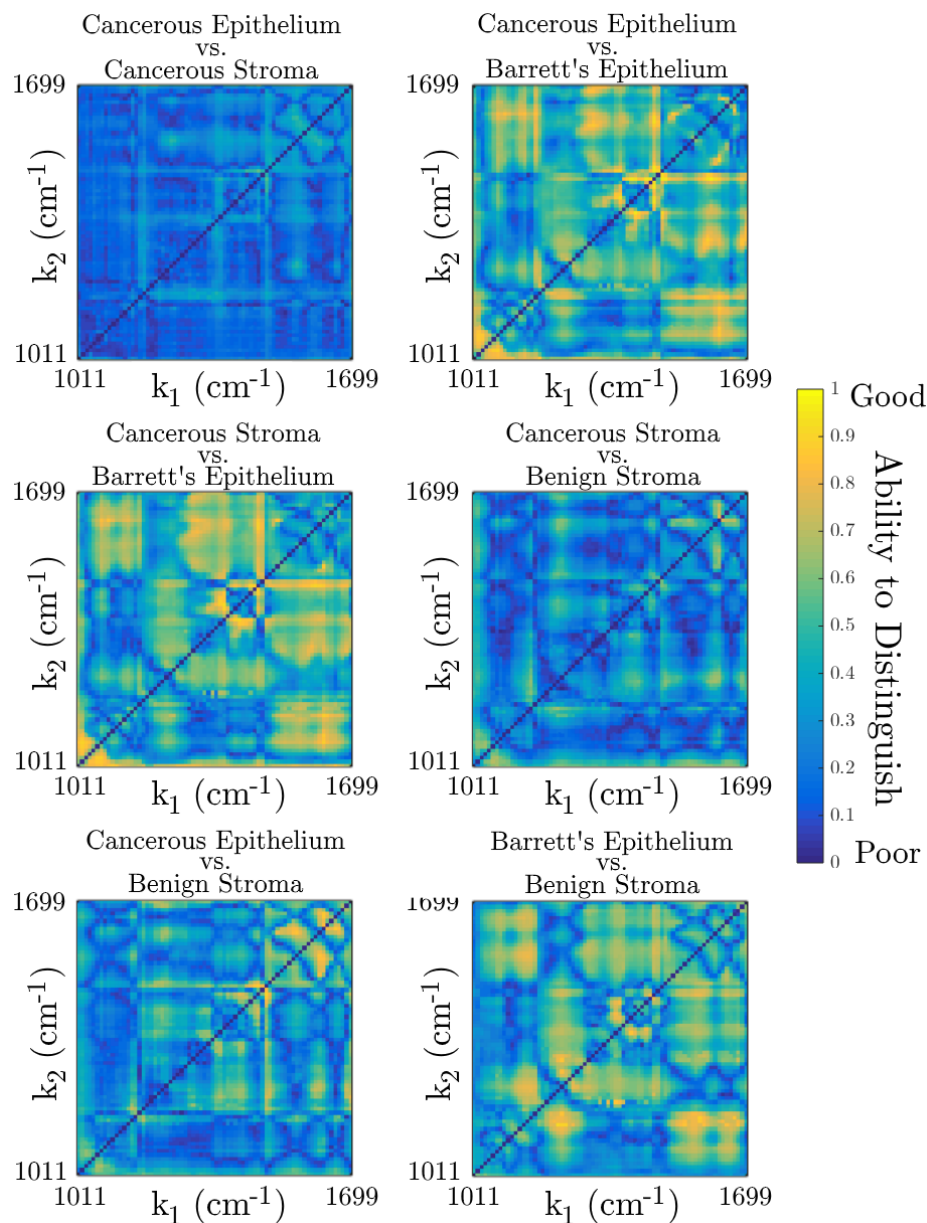


Figure 4.19: Butterfly diagrams for each comparison pair of tissue classifications, using the same randomly sampled training set as used for the KCA inspired MA. The plots show the ability of each wavelength pair (k_1, k_2) to distinguish that particular tissue pair by giving a value equal to $1 - A$ where A is the area of overlap between the two corresponding metric distributions $M(\frac{k_1}{k_2})$. All six images are scaled to a common colourmap to demonstrate the differing ability for each pair of classifications to be distinguished between.

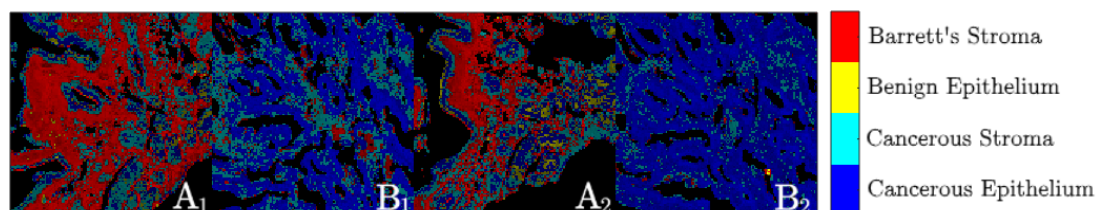


Figure 4.20: The labelling produced by the optimised absorbance ratio metrics, using the same training set as the KCA-inspired MA above.

Tissue Label	Sensitivity (%)	Specificity (%)	PPV (%)	NPV (%)	Number Labelled
Barrett's epithelium	4.32	99.83	88.80	76.67	384
Benign stroma	70.09	80.37	35.76	94.52	8663
Cancerous epithelium	70.69	83.10	59.15	89.12	10070
Cancerous stroma	36.32	80.36	22.11	89.15	7163

Table 4.7: Statistics for the MA labelling using the 5 best optimised ratio metrics for each classification comparison pair. Again, these values were calculated using only samples zA_1 and B_1 .

cancerous epithelium tissue is much more reliably identified.

The statistics for the labelling are given in table 4.7. The failure to label the Barrett's epithelium tissue is shown by the 4% sensitivity, but by labelling so few spectra the sensitivity, PPV and NPV are all relatively reasonable values for the Barrett's epithelium label. Generally these statistical quantities are not as high as seen for the KCA above, and for the most important label in terms of a diagnostic - the cancerous epithelium label - the sensitivity is dramatically lower than observed even for the KCA-inspired MA (see table 4.6).

From the classification image produced it can be seen that the Barrett's epithelium tissue has been labelled as benign stroma in some regions and as a combination of cancerous epithelium and cancerous stroma in others. As seen in all of the labelling and clustering above, the two stroma labels are somewhat mixed between the two types of sample, though clearly here the cancerous stroma label is more confined to the cancerous samples and the benign stroma to the Barrett's samples. The cancerous epithelium label is applied fairly well to the areas of cancerous epithelium tissue identified in the images in figure 4.2, with a clear difference again arising between these two pairs of samples.

In order to provide a useful tool the labelling must be as reliable as possible. The MA labelling will only be successful if the training set used to define the behaviour of each classification is representative and consistent. While it could be the case that the training set used here is somehow unrepresentative of the tissues this is unlikely as the set was randomly generated from the whole image. It is the case here that the training set size is more likely to be an important factor in the consistency and reliability of the modelled behaviour. An optimum situation can therefore be attained by using the whole image area as the training set.

The MA was repeated with the training set expanded to include every pixel possible but

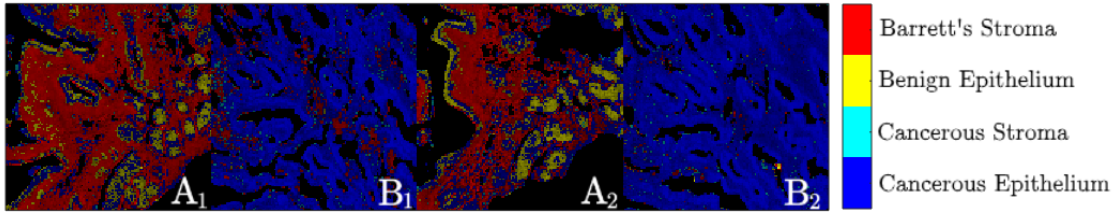


Figure 4.21: The labelling produced by the optimised absorbance ratio metrics, using a training set comprising the whole of the labelled images to give as reliable a labelling as possible based on training set consistency and representation of the tissues' behaviour

Tissue Label	Sensitivity (%)	Specificity (%)	PPV (%)	NPV (%)	Number Labelled
Barrett's epithelium	23.98 ↑	99.40 ↓	92.70 ↑	80.47 ↑	2042 ↑
Benign stroma	75.54 ↑	79.05 ↑	35.99 ↑	95.40 ↑	9278 ↑
Cancerous epithelium	89.80 ↑	71.75 ↓	52.39 ↑	95.31 ↑	14442 ↑
Cancerous stroma	4.13 ↓	98.81 ↑	35.75 ↑	87.04 ↓	518 ↓

Table 4.8: Statistics for the MA labelling using the 5 best optimised ratio metrics for each classification comparison pair calculated for samples A_1 and B_1 , based on using the whole labelled image as a training set and comparing. Arrows are added to indicate the change from the previous labelling using 200 randomly selected spectra from each tissue classification.

with the other parameters unchanged. The classification image produced, shown in figure 4.21 with statistics in table 4.8, does improve with respect to the labelling of the cancerous epithelium and Barrett's epithelium tissues, but the cancerous stroma tissue labelling deteriorates significantly such that only 518 pixels are labelled as cancerous stroma, giving a sensitivity of 4%. Arrows have been added to the table to show the change from the smaller training set to the larger. The principal effect of increasing the number of spectra used in training the MA is an increase in the statistics of the labelling produced. However, this is not universal. Because of the difficulty in labelling the cancerous stroma tissue, the corresponding sensitivity and NPV are dramatically reduced, and the specificity of the cancerous epithelium label also decreases as it includes most of the cancerous stroma tissue.

The amount of Barrett's epithelium tissue that is labelled by the new training set is greatly increased, increasing the sensitivity of the labelling to 23%, but following the same pattern as seen in the previous MA there are regions of Barrett's epithelium that are incorrectly labelled as cancerous epithelium. The pattern of regions successfully identified, and those mislabelled as other tissues, is echoed in the second pair of images, suggesting that the difficulty in distinguishing between the cancerous epithelium and Barrett's epithelium tissues is a result of the metrics used and the characteristics of the tissue, rather than another

indirect effect. In general the extension of the training set does increase the accuracy of the MA in these four images, but the outcome is still not as definitive as the KCA results.

4.6.5 Discussion of MA results

In all three cases above, the results of the MA show the ability to identify the different tissue classifications based upon a limited amount of information from the tissue spectra, some with better success than others. Taking optimised absorbance ratios, rather than using individual values, gave a more accurate tissue map, but saw a move from easily distinguishing the Barrett's epithelium tissue to struggling to identify it, contrary to the observation of more distinguishable metric distributions from the butterfly diagrams. The reason for this could lie in the fact that the Barrett's epithelium tissue in the simplified mapping in figure 4.2 comprises several different classifications of tissue, displaying slightly different characteristics, and therefore expressing more variability. Figure 4.14 shows that for the Barrett's epithelium class the distributions are consistently broader than those for the other classes and that the ease of labelling it came from the fact that the Barrett's epithelium distributions all lie at higher absorbance values and thus are separated well from the others. When moving to ratios of absorbance values this 'amplitude offset' is cancelled out, but the variation within the class will remain.

By extending the training set to the entire labelled image an additional increase in accuracy was achieved for the Barrett's epithelium and cancerous epithelium classes, but at the expense of the labelling of the stroma classes. In order to elucidate the efficacy of the labelling, the four-dimensional 'distance' can be calculated for each mapping from the ideal situation of sensitivity, specificity, PPV and NPV all giving 100%:

$$d_4 = \frac{\sqrt{(100\% - Sens.)^2 + (100\% - Spec.)^2 + (100\% - PPV)^2 + (100\% - NPV)^2}}{2} \quad (4.23)$$

for which values have been given in table 4.9 columns 1 and 2. The division by two compensates for the length of the diagonal from (0,0,0,0) to (1,1,1,1). It is clear from these values that the 5 cluster KCA gave the best representation of the tissues in the image area, but of the three directed labellings using MA the full image training set gave an increased ability to label the cancerous epithelium tissue, while the Barrett's epithelium tissue was not as accurately labelled, though better labelled than using only a small, partial training set.

Analysis Type	Cancerous epithelium d_4 (%)	Barrett's epithelium d_4 (%)	Cancerous epithelium d_2 (%)	Barrett's epithelium d_2 (%)
5 Cluster KCA	18.60	17.63	19.63	18.01
KCA-Inspired MA	30.22	16.79	23.38	14.50
Absorbance Ratio MA	27.07	49.56	23.92	67.66
Full Image Ratio MA	28.24	39.41	21.24	53.76

Table 4.9: Measures of success for the different labelling methods used for the FTIR-HSI data. The first two columns give the four-dimensional euclidean distance of the labelling from the ideal outcome of 100% for all four measures calculated, the second two give a more appropriate measure using only the Sensitivity and Specificity values, in two dimensions.

Using the four values together is perhaps not the best measure of labelling success, as they are interrelated, so instead considering only the sensitivity and specificity gives a two-dimensional distance:

$$d_2 = \sqrt{\frac{(100\% - Sens.)^2 + (100\% - Spec.)^2}{2}} \quad (4.24)$$

The general trend seen in this second measure is similar to the four-dimensional distance, but the shorter distances for the cancerous epithelium labelling have shortened further, while the longer distances for the Barrett's epithelium have increased. This measure is more sensitive to the low sensitivity values of the Barrett's epithelium labelling in the ratio MA.

The KCA does give a better mapping of the sample tissue structure. This is likely to be a result of using the entire spectrum of the data being labelled, after PCA, to find differences between them. The amount of information available to determine the clustering is significantly larger than the limited information given to the MA, meaning that the labelling given by the MA could be expected to be less accurate. Unlike the KCA, however, for the MA this information is processed in a controlled and directed way, meaning that specific differences are used, rather than some other effect that may or may not represent the tissue structure. While the KCA labelled this image area more accurately there is no reason that it would label another area in the same way. Even re-clustering this same area would give different cluster numbers to the same groups of pixels. The MA will assign the same label, with the given tissue association, to pixels in the same or another image area consistently, giving it a much better ability to convey information about the sample.

The MA training sets used here are all from simplified tissue classifications. By using a less complicated model of the sample the ability of the MA can be tested and evaluated, but

in order to develop the analysis further requires a more appropriate model of the sample, like that seen in the first pair of images in figure 4.2. As discussed above increasing the number of classifications increases the computation time of both the training and the labelling processes as the square of this number, but a further restriction comes from the diminutive sample sizes that some of these tissues have represented in these two fully labelled images. In order to get a more generalised and reliable training set and to further develop the MA algorithm additional FTIR-HSI need to be taken of different samples showing different types of tissue and presentations of disease, with a training set taken from many different patients and sample areas. Other types of metrics could also be explored, given that the strength of MA is the flexibility in terms of what measures of pixel behaviour can be used. The ratio values used here, and particularly the optimisation method, could also be improved with further checks on the goodness of fit, perhaps taking different forms of fit to provide a more accurate representation of the probability distribution of each classification. Nevertheless the MA applied here shows great potential as a complimentary tool to histological review of biopsy samples. As a technique to be applied to SNOM imaging results, the MA shows promise. By optimising the choice of wavelengths ratioed in the MA, the hope is that the best possible results from the SNOM data can be achieved.

4.7 Conclusions

FTIR-HSI is a technique that provides a large amount of spectral information over a relatively large image area. As such it can lead to the ability to group pixels in the image according to similar behaviour or characteristics. This analysis shows the success in reproducing the labelling of two areas imaged on one benign and one cancerous sample using several techniques, each one also producing the same sort of labelling in serial sections of both biopsy samples.

The initial agglomerative HCA tested on the data showed that the tendency to have outliers in the spectral data, due to small scatterers or imperfections in optics or detection, rendered the analysis impossible to apply routinely. Instead, a round of outlier removal and a second round of analysis was required, which was still affected by small clusters of spurious pixels. The KCA results showed that this analysis was much better suited to clustering the data, and the cluster maps reproduced very accurately the structure of the simplified model

of the tissues in each sample. By using the sensitivity, specificity, PPV and NPV of each clustering the results for 5 clusters was determined to give the most accurate map of the tissues.

Despite the accuracy of KCA, the analysis was not directed enough to be used as a tool for histological labelling, giving no indication as to the reason for clustering each group together, and having no control over the differences found. To remedy this the MA was developed to use a much more directed approach, training the algorithm with a subset of the data of known classification and using the knowledge gained of the behaviours to label the whole of the image areas. The initial use of absorbance values as the metrics gave promising results in terms of labelling the Barrett's epithelium and cancerous epithelium tissues, but with some significant overlap between the two images and little success in labelling the stroma tissues. By using absorbance ratios the effect of variable total absorbance in different tissues and at different locations was mitigated.

The results produced by the MA, while not as accurate as the KCA are much more useful in terms of determining the tissues present within each sample, rather than simply finding the corresponding structures with no knowledge of the tissue components producing them. With the data available the MA can give a labelling of the tissues with a sensitivity and specificity for cancerous epithelium of 89.9% and 71.8% respectively.

An important conclusion to be drawn from each of these analyses is that the data from the samples that had been dewaxed many months before imaging were, qualitatively at least, comparable to the data from the freshly dewaxed samples. The lengthy time scale of SNOM imaging requires that the samples be stable for several days. The results in this chapter show that, chemically, the samples are stable for several months, meaning that a few days will not pose a risk of degradation to the samples.

The establishment of the MA machine learning technique described in this chapter led to an analysis with the potential to be applied to SNOM imaging results. In order to make use of MA, SNOM images need to be acquired that will give a reliable training set. The development of the SNOM instrument and direction of experimental technique, described in chapter 5 was directed to make the results more reliable and able to be analysed using this technique.

CHAPTER 5

ALICE-SNOM INSTRUMENT DEVELOPMENT

Contents

5.1	Instrumentation	81
5.1.1	The ALICE Accelerator	81
5.1.2	SNOM Instrumentation	82
5.2	Characterisation and Principal Developmental Hurdles	90
5.2.1	ALICE Beam Imaging	90
5.2.2	FEL Second Order Light	101
5.2.3	Undulator Gap Scans and the Spectral Properties of the Fibres	102
5.2.4	Resolution: Optical and Topographic	110
5.2.5	Imaging and Analysis Considerations	113
5.3	Phase I SNOM: Preliminary Investigation	121
5.3.1	Phase I Set-up	121
5.3.2	Phase I Development	122
5.4	Phase II SNOM: FEL Reference	124
5.4.1	Phase II Set-up	125
5.4.2	Phase II Development	126
5.5	Phase III SNOM: Inverted Microscope	130
5.5.1	Phase III Set-up	131
5.5.2	Phase III Development	133
5.6	Phase IV SNOM: Accelerator Development and Transmission Path	138
5.6.1	Phase IV Set-Up	139
5.6.2	Discussion of Phase IV	141

This chapter describes the details of the characterisation, developments and improvements made to the SNOM instrument and ALICE accelerator performed as a significant part of this work. The instrument, layout, electronics and approach to imaging were all adapted substantially over the course of this work and merit discussion on the reasoning

behind the adaptations and of the outcomes of each phase of experimentation with respect to both the imaging results and understanding obtained of the instrument and source. The initial two sections describe the standard instrumentation common throughout the development of the instrument, as well as the significant technological and experimental hurdles encountered. The later sections describe the development over time, split into five phases. These sections display simplified layout and electronic schematics which represent the generalised approaches used in each phase of SNOM imaging experimental time, but do not necessarily include all of the Au plane mirrors used to steer the IR-FEL beam between the other components. The chronology of the SNOM development is outlined in the introduction in figure 1.1.

5.1 Instrumentation

5.1.1 The ALICE Accelerator

The ALICE accelerator (Accelerators and Lasers In Combined Experiments) is a fourth generation light source based at Science and Technology Facilities Council (STFC) Daresbury Laboratory in the North West of England. It is an energy recovery linear accelerator with several sources, of particular interest here is the IR-FEL light source. A schematic diagram of ALICE is shown in figure 5.1.

ALICE accelerates short intense bunches of electrons to 35 MeV using two superconducting linac modules. The electron bunches are temporally compressed in a chicane before entering an undulator, where alternating dipole magnets cause the beam to undulate. The undulation of the electrons causes the release of synchrotron radiation, and by placing the undulator between two cavity mirrors, the radiation from one pulse to the next is synchronised, causing the radiation to be emitted coherently and amplification occurs. Because the lasing medium is bunches of electrons in free space, this source is called a free electron laser. The wavelength of the FEL is tuned using the gap between the magnets in the undulator, but was also dependent on many other parameters of the accelerator. As such, it was found part way through the SNOM experimental development that the calibration of the wavelength that was produced for a given gap was not consistent, and so continuous monitoring of the output wavelength was implemented. The average calibration curve for the wavelength produced for different gaps, with the variability observed over the many measurements of

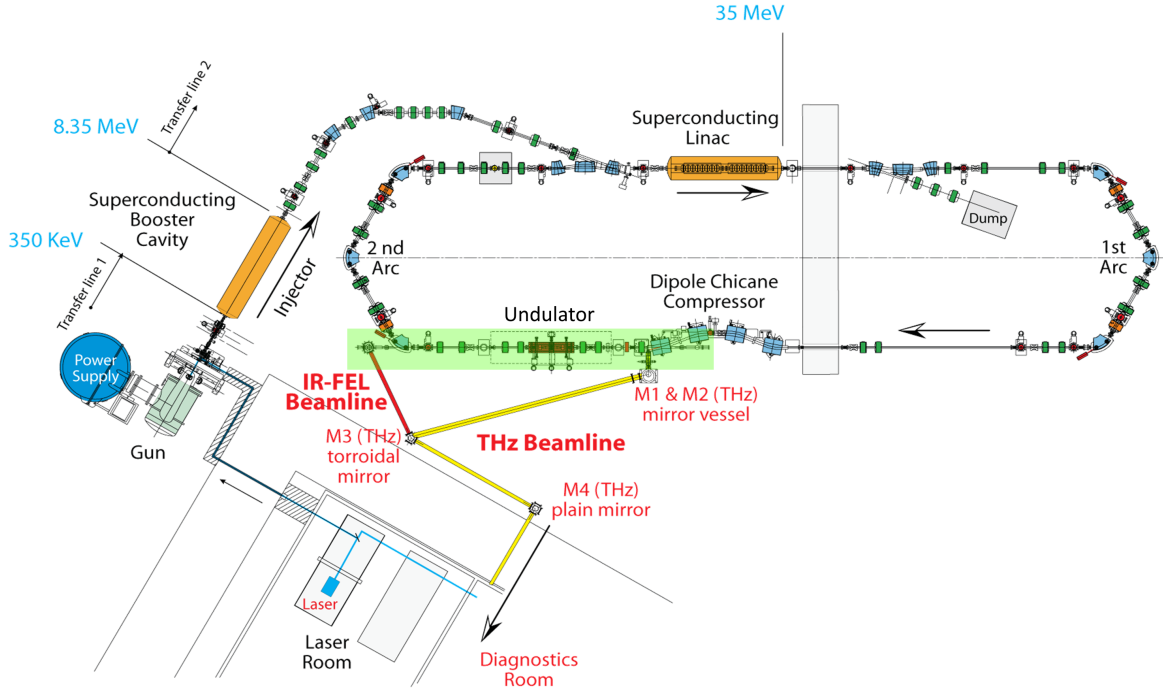


Figure 5.1: A schematic diagram of the ALICE accelerator [75]. The electron bunch energies are written in blue at each point of acceleration, and the green indicated area shows the FEL cavity containing the undulator.

the calibration during the work presented here displayed as error bars on the curve, is shown in figure 5.2.

The IR-FEL produces short, intense pulses of IR light, with a wavelength continuously tunable over a range from 5.5 to $9 \mu\text{m}$. The bandwidth of the emission from the FEL was typically $0.1 \mu\text{m}$ FWHM. The pulse structure consists of a $\sim 75 \mu\text{s}$ macropulse at a 10 Hz repetition frequency, each of which consist of 1 ps micropulses at a frequency of 16.25 MHz . The typical power measured at the FEL output was $\sim 15 \text{ mW}$, but given the very small duty cycle of the FEL ($\sim 0.000012\%$) the peak power was very high, making the ALICE IR-FEL ideal for SNOM.

5.1.2 SNOM Instrumentation

The optical and technological components used throughout the development of the SNOM instrumentation, and the rationale for using them, are detailed below.

Optical Components

The optical components used in this work for the transport of ALICE IR-FEL beam from the FEL itself to the sample were chosen to have good optical properties over the range

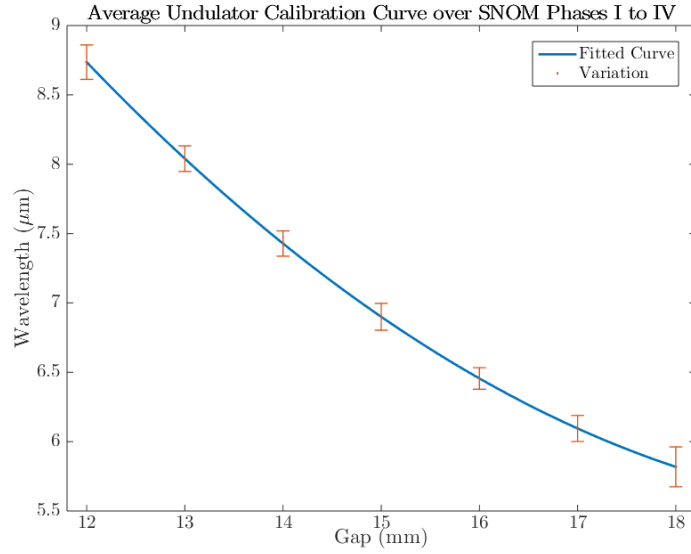


Figure 5.2: The average calibration curve for the wavelength produced at different undulator gaps. The error bars were determined from the range of the variation at each point on the curve and are almost one full width at half maximum FWHM large in places.

of output wavelengths the FEL could produce. The mirrors used were either Au, Al or Ag metal mirrors protected by an overcoat of SiO_2 , all of which possess a high reflectance over the FEL tunable range. The addition of a dielectric coating protects the mirrors from both damage, especially the soft Au, and corrosion for the Ag and Al. At the typical angle of incidence of 45° the Au mirrors used at the SNOM end station have a reflectance of over 94% for $\lambda = 1 - 10 \mu\text{m}$, the Al mirrors have reflectance $> 90\%$ and Ag mirrors have a reflectance of $> 93.5\%$ over the same range [76]. Of these, the Au mirrors give the flattest optical response with variable wavelength and so were the ones used for most applications, but are the most susceptible to damage and are more expensive so for the larger mirrors Ag and Al were used.

The IR-transparent components - beam pipe windows, beam splitters and lenses - were made from a variety of different materials. CaF_2 and BaF_2 are excellent transmitters of the IR wavelengths used for this work, and also possess high visible transparency and so make very good components where this visible transparency is useful, such as beam pipe windows. CaF_2 was used here in preference to BaF_2 as it is less fragile than BaF_2 and significantly less expensive. CaF_2 was used here for the beam pipe exit windows and for short focal length lenses to focus the beam onto the single element reference detector, but the lenses used for the SNOM light paths were ZnSe which had longer focal lengths.

Piezo Drivers

The development of piezoelectric drivers by Binnig *et al.* [23] revolutionised microscopy by allowing an entirely new branch of SPM imaging techniques. These drivers use materials exhibiting the piezoelectric effect, where a mechanical deformation of the crystal structure generates a voltage across it in a similar way as the pyroelectric effect produces a voltage from the thermal stress on the sample. In order to produce a motor-like effect piezo stages take advantage of the inverse piezoelectric effect also expressed by these materials: by applying a high voltage across a piezoelectric material a small physical deformation is induced. This deformation can be used to precisely control the position of a sample or the height of a tip in SPM techniques, giving very precise motors on a nanometric scale. The piezo stage used for the SNOM after phase I was a Piezosystem Jena PXY 500 AP dual axis translation stage, chosen for its large scan range of $500 \times 500 \mu\text{m}^2$ and the $100 \times 100 \text{mm}^2$ central aperture.

SNOM Feedback

The SNOM feedback was controlled using a bimorph, a device with two piezoelectric materials joined together with a passive layer between. Lateral oscillations can be created by applying opposite alternating voltages to each side of the bimorph, causing one to expand and the other to contract, demonstrated in figure 5.3. By varying the frequency of the voltages, the bimorph can be made to resonate at its natural frequency. This device can be used to maintain the tip-sample separation by monitoring the amplitude of the resulting oscillation using a second bimorph layer on the back of the first. The oscillation of the first bimorph pair flexes the second pair and a response voltage is produced, with an amplitude proportional to the amplitude of the oscillation of the bimorph.

If a fibre is glued to the first bimorph layer and brought close enough to a sample to interact via Van der Waals forces the resulting drag on the tip dampens the oscillation and the amplitude decreases, giving a reduced voltage amplitude from the second bimorph layer. To maintain a constant distance from a sample, a feedback loop is used that maintains the measured amplitude at a certain set point that is less than the response away from the sample, ensuring that the tip is engaged with the sample and well controlled.

The resonant frequency and amplitude of bimorph oscillation were both parameters that needed to be set for the SNOM instrument used in this work. Depending on how much glue was used, the tension on the fibre and how far the fibre protruded from the end of the

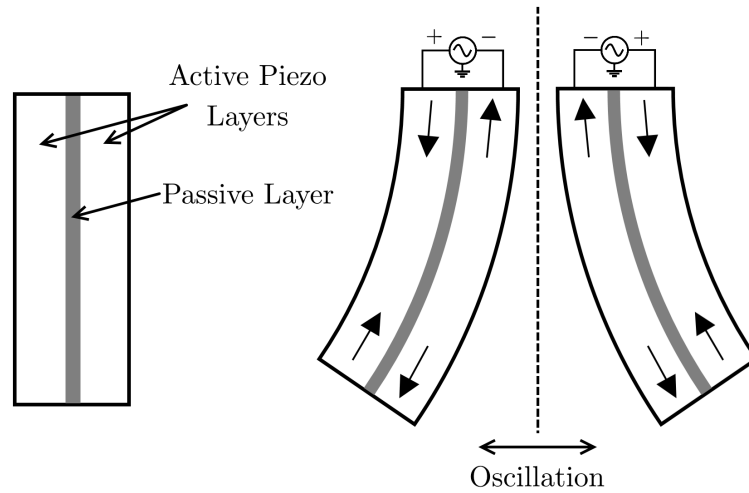


Figure 5.3: The principle of operation of a bimorph device. Two joined piezoelectric strips are given opposite alternating voltages, causing them to oppositely expand and contract. This expansion and contraction causes the bimorph to alternately flex to either side (exaggerated in the above diagram) and therefore oscillate at the frequency of the alternating voltage. If the voltage frequency is equal to the natural frequency of the bimorph, resonance occurs, leading to a greatly increased amplitude of oscillation.

bimorph, the resonant frequency and resulting amplitude for a given driving voltage would vary. Typically the resonant frequency was between 3.5 and 3.8 kHz and the driving voltage amplitude was varied to give a resulting voltage amplitude measured by the second bimorph of between 15 and 20 mV. The set point for the feedback loop was then set to approximately 5 – 10% lower than the resultant voltage to give a reliable distance without approaching too close to the sample.

IR Fibres

Optical fibres utilise the property of total internal reflection to guide rays of light down the fibre with minimal loss of intensity, allowing a curved path to detectors or from sources to samples. A core of refractive index n_{core} is surrounded by a cladding material of refractive index $n_{cladding} < n_{core}$. The difference in refractive index means that rays of light in the core that are incident on the boundary between the core and cladding at an angle to the normal greater than the critical angle for that interface are reflected back into the core. The critical angle, θ_c , is the one that gives an angle of refraction of 90° :

$$\sin(\theta_c) = \frac{n_{cladding}}{n_{core}} \quad (5.1)$$

If the core and cladding have very similar refractive indices the critical angle becomes larger and the fibre is more selective in terms of the maximum angle from the axis of the fibre that transmits light, the angle of acceptance.

Fibres with large core diameters with respect to the wavelength of light used, so called multimode fibres, are subject to *multimode dispersion* where the different possible optical paths at greater than the critical angle have significantly different path length and so the collected light is temporally distorted by the fibre. Singlemode fibres, those with core diameters similar to the wavelength of light used, are not affected by this process as the angle of acceptance is very small.

The fibres used in this work were singlemode fibres with a core size of 6 μm , with the exception of one 100 μm fibre used during the investigation of the spectral behaviour of the fibres described in section 5.2.3. This avoided spreading out the weak signal from the SNOM both temporally and spatially. Using cleaved fibres required that the core size be as small as possible in order to achieve a small resolvable length scale.

The material used for the core and cladding of these fibres was As_2Se_3 , a material with excellent mid-IR transmitting properties but that is, as mentioned previously, very fragile. The core was 6 μm in diameter, with a total core and cladding diameter of 170 μm . To protect the fragile core and cladding, the fibres are coated with an acrylate protective coating. In the later phases of SNOM imaging (see section 5.5) the distance from the sample to the detector had to be significantly increased to accommodate the inverted microscope, and so longer fibres were used from CorActive [77] which had an additional protective jacket and sleeve around the fibre.

There were two different types of fibre aperture used during this work: (i) cleaved fibres and (ii) etched and gold-coated tips. The preliminary work performed in phase I was done using etched tips in order to achieve a high spatial resolution over a small scan area. The implementation of a larger piezo stage translation range and the desire to image more representative areas of the tissue samples necessitated that cleaved fibres be used, improving reliability and strength when performing larger step sizes and taking many images. The ongoing phase of imaging, phase V (section 6.4), is using etched and gold coated tips once again to give the higher spatial resolution that SNOM is able to achieve.

The cleaving process was very simple, the fibre end was simply cleaved using a sharp blade perpendicular to the fibre axis. The fragility of the chalcogenide core and cladding

material meant that a clean cleave could be achieved, sometimes requiring repeated cleaves until this was the case. The etching process was much more time consuming, requiring that the outer layers of the fibre be removed and the fibre etched in a concentrated solution of hydrogen peroxide and sulphuric acid, known as “piranha” solution, which etched the fibre into a tip using convection currents to shape the tip profile [42]. Etched tips then needed to be coated with a thin layer of gold in an evaporation chamber at an angle to the fibre axis. The etching and gold coating procedures are described in appendix B.2. This process made the sides of the tip opaque to IR light while leaving an aperture clear at the point. A similar process was described in reference [42]. For both tip types the true aperture size obtained was, within the scope of work described here, impossible to obtain prior to imaging, where the aperture could be inferred from the resolution obtained. In order to have a prior knowledge of the aperture size, a SEM could be used to image the end of the fibre.

Detectors, Electronics and Signal Processing

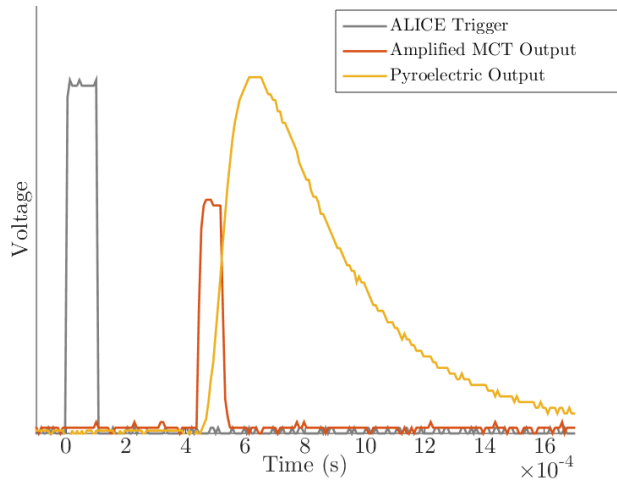


Figure 5.4: The output voltage curves of the two detectors used for the SNOM instrument. The MCT detector responds very quickly to the FEL radiation, but the pyroelectric detector has a much slower response and takes much more time to return to zero. The ALICE trigger pulse produced by the accelerator was used to synchronise the electronics.

There were two types of IR detector used in this work, for two levels of sensitivity. The very low level of light collected by the SNOM necessitates the use of a highly sensitive detector. The material HgCdTe (MCT) can be used to create detectors with very high sensitivity to IR light because it has a tunable bandgap in the IR range. The detector operates by measuring the excitation of a valence band electron to the conduction band upon

absorption of an IR photon. A small bias current applied to the detector allows the electrons to be detected. Because IR photons have energies on the order of thermal excitations at room temperature, the detector must be cooled using liquid N₂ and suspended in a vacuum. MCT detectors have a high sensitivity which allows the low signal levels for the SNOM to be measured and subsequently amplified for data collection. The response of MCT detectors is very fast, as shown in figure 5.4, so they can be used to measure much shorter pulses than the 75 μ s, 10 Hz FEL macropulses, but are not fast enough to measure the 1 ps micropulses within each macropulse.

For direct measurements of the FEL beam, pyroelectric detectors were used as their lower sensitivity (their voltage output per Watt of incident power) was appropriate for the power typically delivered by the portion of the FEL beam reflected by the CaF₂ beam splitters, giving a large but not saturated response. The pyroelectric detectors were also sufficiently fast in recovering from each FEL pulse. The general principle of operation of pyroelectric detectors is that they sense the temperature change in a detection element resulting from absorption of IR radiation. These detectors consist of one or more elements of a crystal with pyroelectric properties, that is that their polarisation changes with changes in temperature, which give a voltage output proportional to that change. Crystals with this property are non-centrosymmetric, possessing a net dipole within the unit cell such that when the temperature of the crystal is changed the distortion in the lattice structure changes the net polarisation of the crystal and thus a measurable voltage across it. The resultant output voltage gives the smooth curve shown in figure 5.4 which peaks quickly and then slowly decays back to zero in a time scale of tenths of a *ms*.

The electronic control and data collection was performed by a central SNOM control module based on the system described in reference [78]. This module, linked to a desktop PC which used customised software, controlled the position of the three piezo axes and the feedback on the *z*-axis, as well as collection of the various data channels and synchronisation to the ALICE accelerator. The data values were sequentially read into analogue to digital converter (ADC) cards and passed on to the software to be processed and recorded. The ALICE accelerator ran at a macropulse repetition rate of 10 Hz, which corresponds to a period of 100 ms. A synchronisation signal given to the SNOM controller linked the timing of the FEL pulses to the measurement of the ADC channels, a graph of the typical timing is shown in figure 5.5.

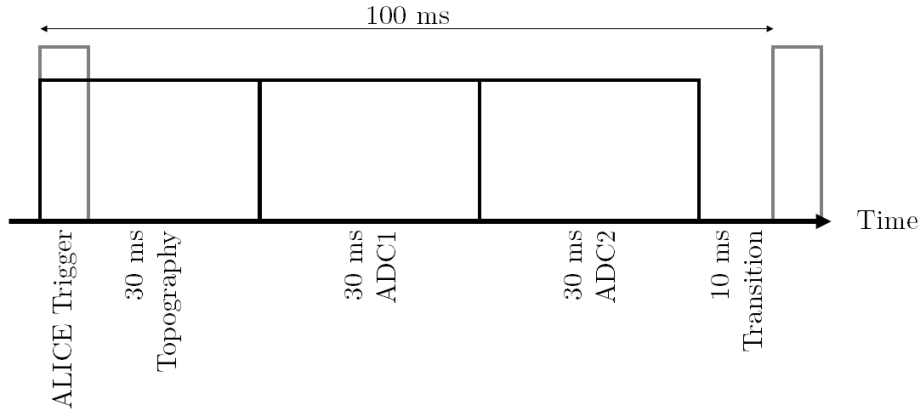


Figure 5.5: A representation of the timing of SNOM data collection channels relative to the ALICE IR-FEL pulses. Each ADC was read sequentially over the 100 ms period, averaging over the timing window, and allowing 10 ms for the SNOM to move the sample and settle at the new location after the values were recorded. With a variable number of ADC channels being read in each of the phases below, the time over which the values were read was varied to maintain this overall behaviour.

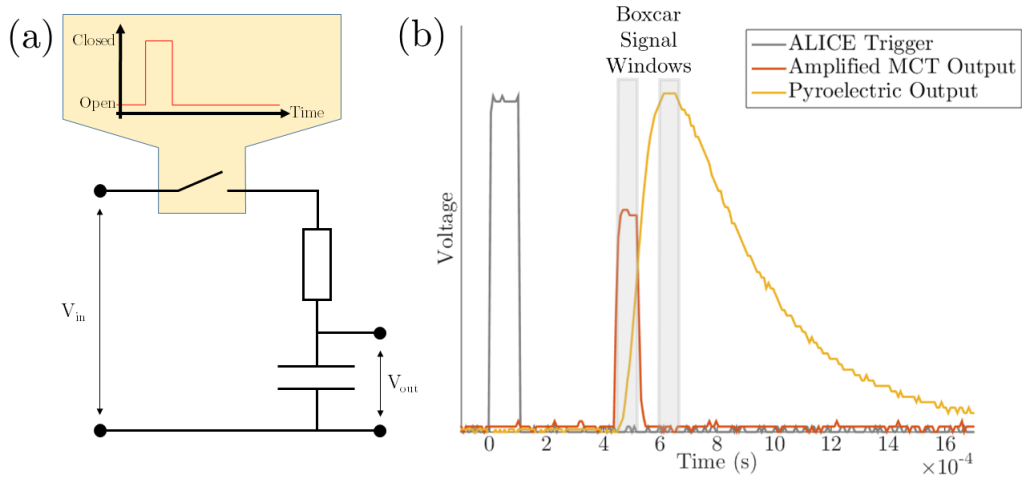


Figure 5.6: (a) The boxcar integrator can be thought of as a switched low-pass filter, while the signal window is on the boxcar integrator integrates the signal V_{in} by charging a capacitor, giving V_{out} . A second circuit was used to measure a background value in the same way which was subtracted from the value of V_{out} . (b) The voltage curves for the ALICE trigger pulse, MCT output and reference pyroelectric detector output. By using a trigger pulse from the ALICE accelerator the boxcar integrator and SNOM electronics were synchronised to the FEL pulses. The signal windows for the boxcar integrators were set to include the peak of the two different detector curves.

The two types of detectors used in these experiments are described in section 5.1.2 and produce very different output voltage profiles. Consequently these curves needed to be processed in a manner that would give comparable measures of the IR light intensity or power measured by each detector. As the IR-FEL output has such a low duty cycle averaging the detector over time will not give an accurate measurement of intensity, and include a much higher proportion of noise than signal. Thus the voltage pulses from each

detector needed to be averaged in some way over only the length of the pulse. To this end the two signals were processed using a boxcar integrator to give stability, noise reduction and amplification. A boxcar integrator is essentially a switched low-pass filter, where the switch is controlled by an adjustable boxcar function as shown in figure 5.6. The input signal is electronically integrated over the signal window, which was set such that it contained the peak of the detector response. A second window was set to integrate, over the same length of time, a background value containing no signal, which was then subtracted from the signal window integral and the final value converted into an analogue voltage output which was proportional to the area of the detector signal. By carefully positioning the signal and background windows the effect of noise in the system can be greatly reduced. Boxcar integrators also give the possibility of averaging over several pulses, though this was undesired for the slow repetition rate of the ALICE IR-FEL.

The Boxcar integrators used in this work were Delta Developments Boxcar Integrators and the earlier model called chopped signal integrators. As the MCT detector had a fast response time, the output signal shape was able to be entirely captured in the signal window with the background window just afterwards, but the slow response of the pyroelectric detector used for the reference signal had too large a temporal extent to measure fully, instead the window was placed over the peak of the curve and the background window was placed before the response rather than afterwards due to the long tail on the curve. The gains on the boxcar integrators ($\times 1$, $\times 10$, $\times 100$) were adjusted for each image to give a voltage in the region of 0.2 – 1.5 V.

5.2 Characterisation and Principal Developmental Hurdles

5.2.1 ALICE Beam Imaging

When the SNOM was adapted to be mounted on an inverted microscope in phase III (see section 5.5), the z -piezo control was placed on the SNOM head itself. As such the aperture of the SNOM was no longer fixed throughout the scan at a constant position within the beam focus. If the topography of the sample surface increased in height, the tip would move up to accommodate it, translating vertically in the beam and therefore being susceptible to variations in the local intensity. The total range of the z -piezo on the tip was 20 μm which is roughly 10% of the achieved focal size for the FEL. If the focussed beam was completely

uniform this would not represent a problem. However, from a report on the ALICE IR-FEL beamline [79] there was expected to be significant diffraction-based structure in the beam arising from a sub-optimal sized outcoupling hole for the FEL cavity and a subsequently over-filled toroidal mirror in the beamline. Due to the motion of the aperture in the beam focus, the potential impact of structure in the beam needed to be ascertained, where previously it was deemed to be of little impact.

The 1.5 mm outcoupling hole of the FEL was smaller than optimal for beam transport, resulting in a small but measurable diffraction from the hole, which was approximately 15 m from the SNOM end station, leading to a spreading of the beam and a slight diffraction pattern propagating down the beam pipe. This structure on its own would not have caused issues with the light collected by the SNOM as the variation in observed intensity over this range of translation in the focus would have been negligible if the tip was positioned at the maximum intensity. The main effect was expected to come from a 17.5° grazing incidence toroidal mirror with a diameter of 75 mm that was used to steer the IR-FEL beam through the radiation shielding labyrinth. The mirror was being overfilled by this diffracted beam by almost 60% horizontally by a beam of 50 mm meeting a mirror aperture of 22 mm, which would have resulted in a large diffractive effect from the aperture of the mirror and lead to sharp fringes across the beam in one direction. To assess the structure in the beam at the SNOM, and what effect it might have on the SNOM measurements, the beam was imaged using a PyroCamIII two-dimensional pyroelectric array detector [80] with a 12.8 mm, 160×160 pixel array ($80 \mu\text{m}$ pixel size) at different gaps/wavelengths, both at the focus and with a partially defocussed beam. A secondary investigation was also carried out by maintaining the wavelength and imaging the partially defocussed beam at the limits of the variable parameters of the accelerator that would still give an IR-FEL output. This was performed in order to determine what effect, if any, the parameters other than the undulator gap would have on the beam structure.

The detector was placed in the SNOM beampath with a path length in air of approximately 750 mm. A 300 mm focal length ZnSe lens was used to focus the IR-FEL beam onto the detector array and could be translated in order to defocus the beam. The intensity of the IR-FEL was modulated by using a single KRS5 holographic wire grid polariser, as the detector was saturated by the full intensity of the focussed beam. For the focussed beam images the detector was placed such that the angle of incidence of the beam from the

horizontal was $\sim 15^\circ$ to emulate the intensity distribution over the tissue samples and to spread the vertical axis of the beam out to highlight the relevant structure. This gave an anisotropy to the focus, with two principle axes: the longer axis orientated essentially along the x -direction of the SNOM scans, vertical in the beam cross-section, and the shorter axis along the y -direction, horizontal in the cross-section. For the defocussed beam, the intensity was much lower, so the polariser was removed to give a stronger image, and the detector was orientated to give normal incidence.

Beam Structure and Variation

The images taken at the focal length of the lens, $f = 300$ mm are shown in figure 5.7. The line profiles across the center of the focus are included, and display the different shapes in the two orthogonal directions. The y -axis is elongated by positioning the detector so that the beam is incident on the detector array at the same 15° grazing angle used for SNOM imaging.

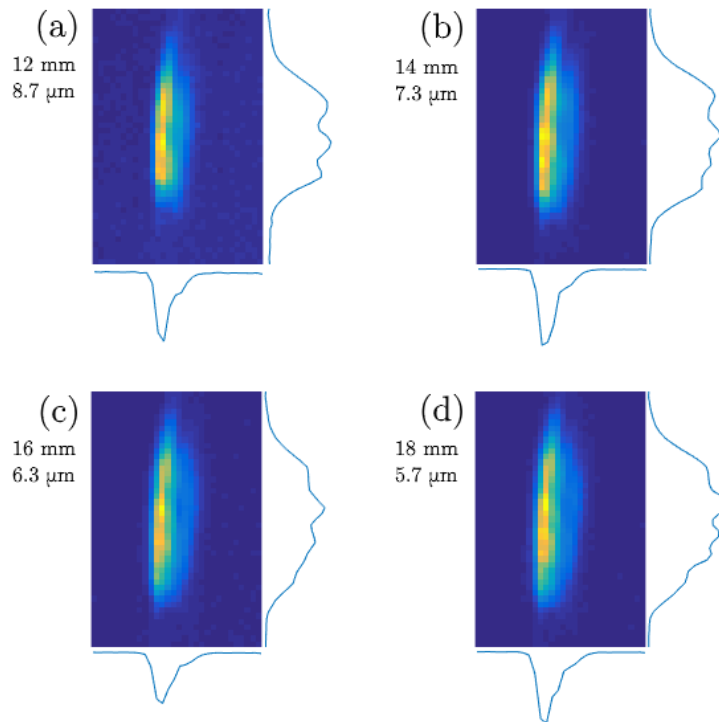


Figure 5.7: Images of the FEL beam focus elongated in the y -axis by setting the PyroCamIII detector at an angle to the beam to reproduce the intensity profile at the SNOM aperture. The images were taken at four different undulator gaps, 12, 14, 16 and 18 mm, covering the main FEL operating range. The approximate wavelengths for the gaps are given for each one. The structures in the focus at each of these gaps are similar to those at the others, but with subtle variation in the y -axis.

Given the expected diffraction structure in the beam, the comb-like peaks measured along the y -axis of these images is not surprising. There seems to be only a small variation in the focus with gap/wavelength, though the Full Width at Half Maximum (FWHM) of the focus in both directions increases slightly with increasing gap (decreasing wavelength) and the shape and position of the peaks along the y -axis do change slightly. The x -axis profiles all show a small shoulder on the right of the beam, visible in the images as a smudging to the right. The origin of this shoulder is unknown.

The average size of the focus in these images is $260 \pm 30 \mu\text{m} \times 1750 \pm 80 \mu\text{m}$. Correcting for the vertical elongation gives a perpendicular cross-section size of $260 \pm 30 \mu\text{m} \times 450 \pm 20 \mu\text{m}$, showing that the beam is not of a uniform size, but rather has spread much more in the vertical direction than in the horizontal direction.

Having measured the variation of the focus structure with the undulator gap, a constant undulator gap of 14 mm ($\lambda \sim 7.3 \mu\text{m}$) was selected and the many other accelerator parameters used to adjust the lasing condition of the ALICE IR-FEL were varied to their upper and lower limits which were still able to produce a measurable FEL beam. It was not possible to acquire images at two extreme values for every parameter if the optimal value was already at one of the extremes. Images were taken of the defocussed beam at the initial optimised state, and successively at each extreme with each parameter being re-optimised before changing the next, and a further image was taken of the final re-optimised beam. The set of parameters that were investigated represented any and all adjustments that were routinely varied during the normal operation of ALICE to maximise the power and stability of the IR-FEL beam, and are listed in figure 5.8 along with the corresponding pair of beam images.

The variation of the structure in the beam over the course of the changes seems negligible, certainly the most significant effect that is seen is the fluctuations in the total intensity arising from different lasing conditions within the FEL cavity. In order to accurately assess the differences between the beam cross-sections over the experiment, two approaches were used. Firstly PCA was used to see the principal variations within the structure, picking out the largest effects across the data. The first four PC images are shown in figure 5.9 with the corresponding variances, Δ , of each PC given as a percentage of the total variance of the images. Secondly the images were sorted by their intensity at the central peak (row 62) and the central vertical line profiles were extracted (column 59) These line profiles can be used

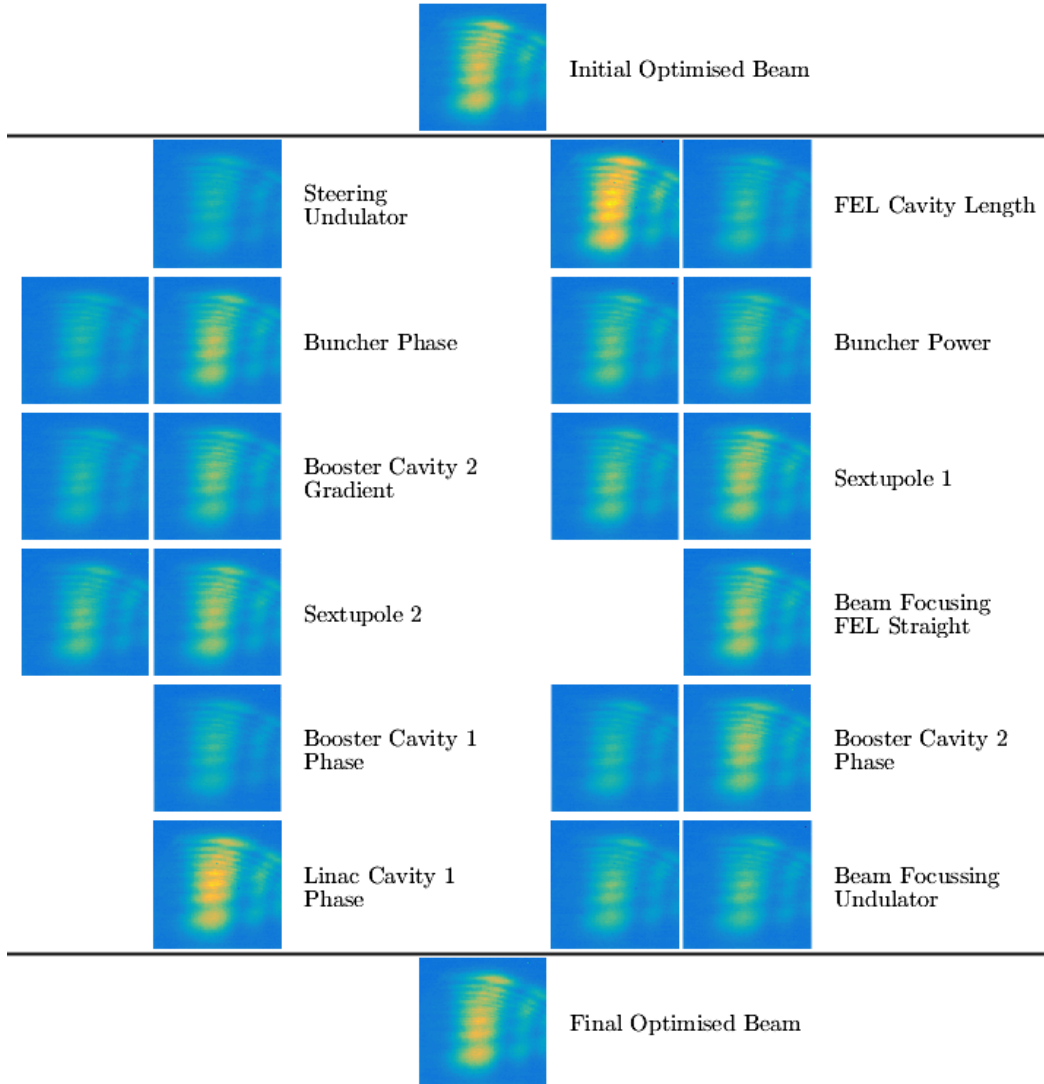


Figure 5.8: Images taken at approximately $f/2$ of the partially defocussed FEL beam at the fixed gap of 14 mm. There is a large amount of visible structure. The gap was kept constant and different parameters that are routinely adjusted as part of the normal accelerator tuning were changed to maximum and minimum values that would still provide a measurable FEL beam. The images taken at each extreme are shown, with the corresponding parameter that was varied. All images were plotted with the same colourmap to show the variation in intensity. There is little visible variation between the images in terms of structure within the beam, simply an intensity modulation depending upon the lasing conditions of the FEL. The FEL was re-optimised at the end, giving a final image that differs from the initial optimised state by $< 2.8\%$ on a pixel-by-pixel basis.

to visualise the structural changes using the waterfall plots in figure 5.10.

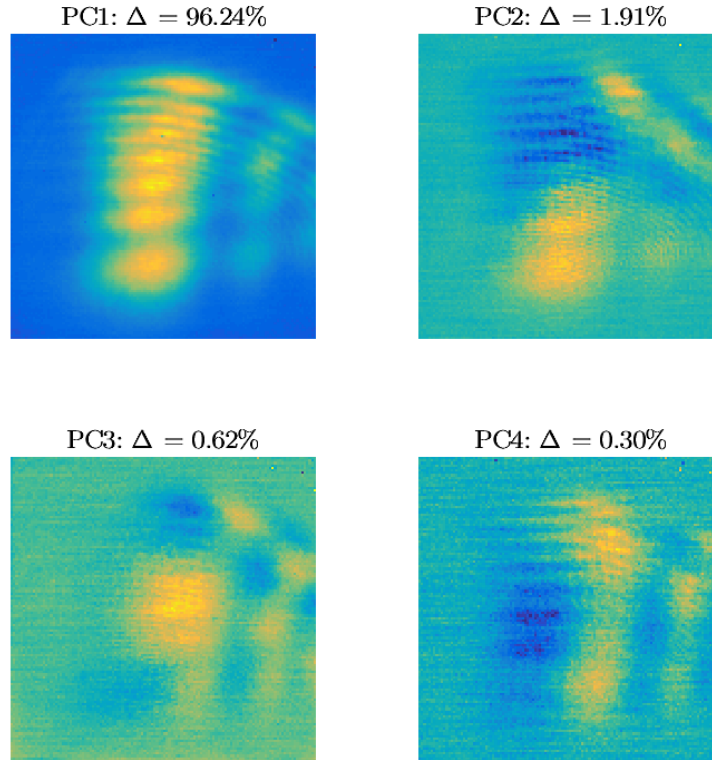


Figure 5.9: The first four PC images given by applying PCA to the images taken of the defocused ALICE beam under varying accelerator parameters, with the variances, Δ , of each PC given as percentages of the total variance. These four PCs account for $> 99\%$ of the total variance. PC1 shows that the majority ($\Delta > 96\%$) of the total variance is change in the intensity of a general beam profile. The next three PCs account for variations within that general beam shape: PC2 gives a modulation between the upper and lower parts of the beam, PC3 gives a central modulation and PC4 gives a left-right modulation. All three of these are over significantly larger length scales than the structure in the general profile, and represent much lower variations in intensity

The first four PCs given by the PCA account for over 99% of the total variance. The first PC confirms that the majority of the variance of the images is accounted for by a simple intensity variation. PC1 is the average beam profile that is varying in amplitude over the course of the accelerator changes, accounting for over 96% of the total variance. The three other PCs give modulations within the beam profile in three different ways: relative modulations between the top and bottom, middle and outer, and left and right parts of the beam profile in that order. These modulations provide a relatively good basis set to give beam profiles for which any region can be made to be more intense. Over the images taken the second, third and fourth PCs only correspond to a total of $\sim 3\%$ of the total variance,

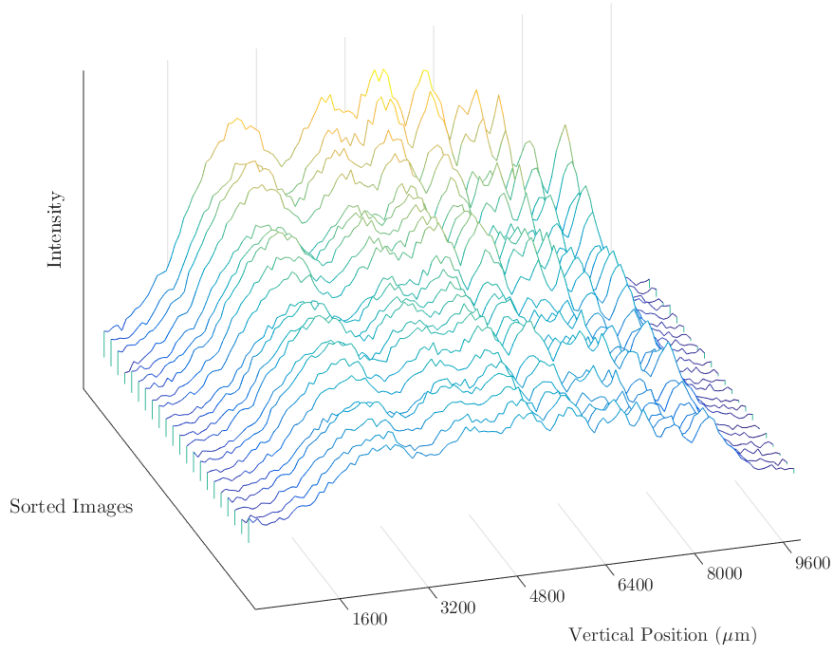


Figure 5.10: A waterfall plot of the central beam profile of the images at varying accelerator parameters, sorted by the central peak intensity. The line profiles are mainly uniform, but with small relative variations that can be seen as inconsistencies in the visible offset between the lines.

meaning that the beam shape and structure was very stable. Furthermore the length scales of these modulations are much greater than the significant structure in the general profile shown in PC1 so should give a very insignificant contribution to any variation in the signal recorded by the SNOM.

Another interesting feature of these PC images is that the lower PCs highlight the many diffraction patterns present in the beam, especially PC2. At least 4 different sets of diffraction rings are visible in the PC2 image, probably resulting from slightly misaligned optics in the beam path. This shows that although there is a significant and preventable contribution from the overfilled toroidal mirror, care needed to be taken to align the optical components to the beam as accurately as possible and to reduce the number of under-sized apertures that the beam passed through. The general form of PC2 is also very similar to the difference between the initial and final optimised states of the FEL beam in figure 5.8 suggesting that this variation is most likely to be a time-based drift in the general shape of the beam.

The small variations demonstrated by the PCA are confirmed by the waterfall plot showing small peak-to-peak variations down the central line profile. To an approximation this is the translation direction of the SNOM aperture, so variation along this axis could potentially

lead to further variation of the signal measured by the SNOM that does not correlate with the total FEL intensity. The variations between these images due to changes in the intensity distribution, rather than the total intensity, are significantly smaller than the spatial variations peak-to-peak along the line, which therefore poses a greater problem.

Outcome of Initial Beam Imaging

The two cross-sectional axes of the FEL beam show very different profiles: the horizontal axis is a relatively smooth, broad single peak with a slight shoulder, but the vertical axis is split into multiple peaks, which vary in number, position and shape with gap/wavelength. This is in close agreement with the expected structure given in [79] with deviations that can be attributed to the additional optical components in the remainder of the beam path and their limited apertures.

Since the SNOM aperture was moving along one axis of this anisotropic beam profile, there were two possible scenarios: the aperture could either be moving in the smoothly varying axis, or the one with the multiple peaks. From the orientation of the detector and the images obtained, it was seen that the motion of the tip in the beam due to the z -piezo positioning at the SNOM head was along the vertical y -axis. Thus the SNOM aperture was moving through the multiple-peak diffraction pattern seen in the beam images, giving a potentially large variation in intensity with sample topography, independent of the FEL intensity.

It was reasoned that by rotating the beam by 90° the aperture could be made to move along the more smoothly varying axis and thus give a much lessened effect from the topography. This principle is demonstrated in figure 5.11, where the two situations are demonstrated pictorially. For comparison the range of motion ($\sim 80 \mu\text{m}$) of the aperture within the scaled focus is also shown. The perpendicular focal size is not uniform; by rotating the beam, the elongation that results from the grazing incidence at the sample produces a much rounder focus than seen in the images above, though the area is the same and so the overall average intensity is maintained.

As described above, the structure in the beam is further complicated by small variations in the distribution of intensity with varying accelerator parameters. These fluctuations were small compared to the general beam structure however, and represented the maximum possible range of the possible changes, thus over the course of a SNOM image the varia-

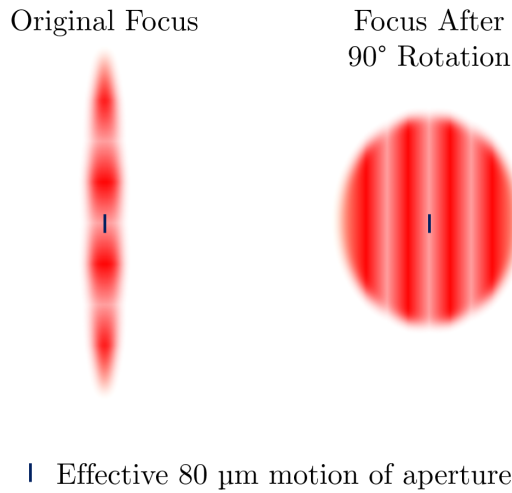


Figure 5.11: A diagrammatic representation of the motion of the SNOM aperture through the beam structure resulting from the vertical translation with varying topography. By rotating the beam by 90° the motion becomes aligned with the structure and will therefore produce a much smaller effect. The $80 \mu\text{m}$ travel of the aperture is calculated from the $20 \mu\text{m}$ z -piezo range elongated by the grazing incidence of 15° from horizontal.

tions should remain roughly constant and only change with retuning of the accelerator for subsequent images.

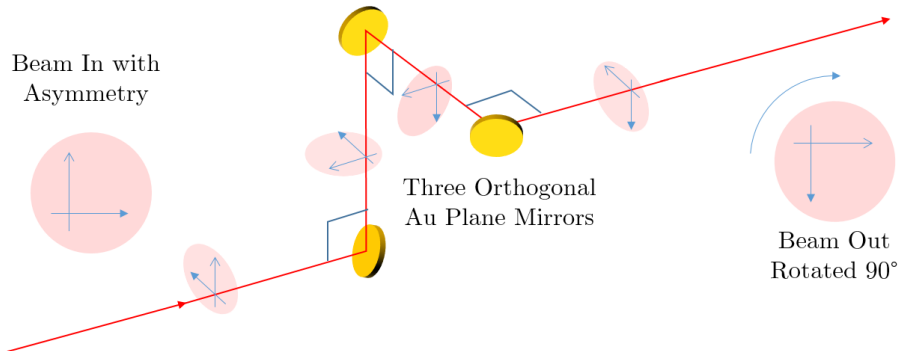


Figure 5.12: To rotate the FEL beam by 90° three mirrors were arranged to give three different orthogonal reflections to map the axes $(x, y) \rightarrow (-y, x)$. This total rotation was achieved through three reflections: $(x, y) \rightarrow (x, -z) \rightarrow (-y, -z) \rightarrow (-y, x)$.

The effect of varying the accelerator parameters was therefore judged to be insignificant compared to the inherent structure of the beam. As a short term solution, a three-mirror beam rotator demonstrated in figure 5.12 was added to the beam path, with a long-term goal of replacing the overfilled toroidal mirror with a larger one to reduce the diffraction effects.

When the mirror was replaced between phases III and IV the beam was imaged again to ascertain the changes that had resulted from the beamline upgrades. The imaging was done using the same PyroCamIII detector as was used in the first set of beam imaging and approximately the same set-up, and though the path length and detector placement were not necessarily the same as for the earlier results the two sets of data can still be compared in a qualitative manner.

Impact of Beamline Improvements on Beam Structure

As before images were taken of the beam at the focus, though here the detector was not placed at an angle to the beam to emulate the reflection mode geometry, but perpendicular to it as in the transmission imaging mode. With the addition of the wavelength measurement performed using the multi-element pyroelectric detector array, the images could be taken at the wavelengths used for imaging: 6.50 , 7.30 and $8.05 \mu\text{m}$ which are shown in figure 5.13. To avoid saturating the detector with the increased intensity of the FEL the electron bunch train length in the accelerator had to be reduced to $50\mu\text{s}$, half its usual value, which had the effect of halving the intensity.

The focus achieved for these images was noticeably better than previously measured, with a FWHM that was at least as small as, and mostly smaller than, the previous results, with an average FWHM of $270 \pm 20 \mu\text{m} \times 350 \pm 60 \mu\text{m}$. The focus shape is also better, showing a much flatter peak and smoother variation than before the mirror upgrade. The

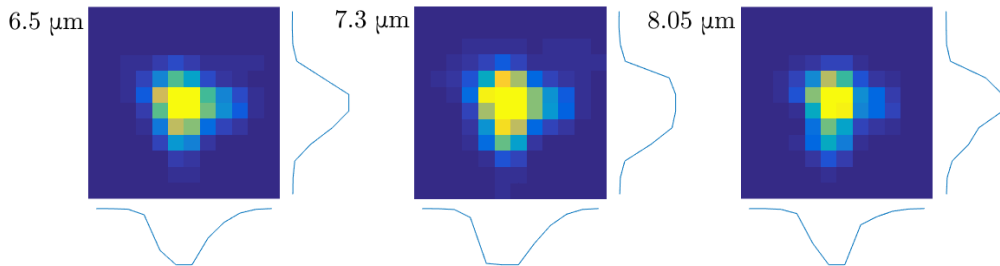


Figure 5.13: Images of the focussed FEL beam after upgrades to the ALICE IR-FEL beamline with vertical (y) and horizontal (x) line profiles over the center of the foci. These images were taken at the imaging wavelengths of 6.5 , 7.3 and $8.05 \mu\text{m}$ with the PyroCamIII detector perpendicular to the FEL beam. The cross-section profiles show a high level of similarity to each other, and are similar in shape and size in the x direction to the profiles seen in figure 5.7. The y direction profiles show a much better shape than the previous images, due in part to the normal incidence at the detector, but are smaller than the extrapolated size that could be achieved previously, with no visible sub-structure.

beam cross-section is still far from uniform, but given the large number of optical components and large distance from source, the resultant shape is not surprising.

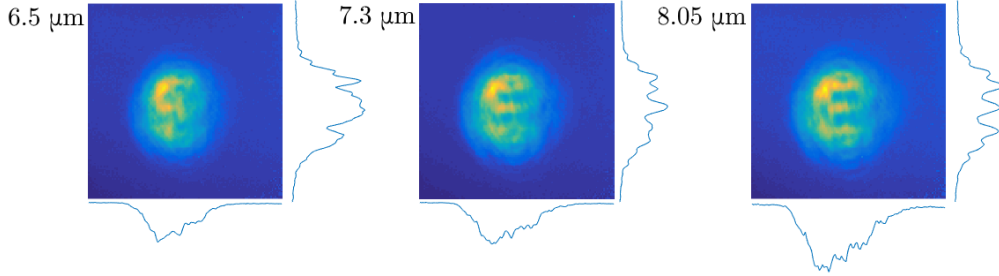


Figure 5.14: Images of the defocussed ($\sim 0.75 f$) beam taken with the PyroCamIII detector. The beam appears much more uniform, with less obvious structure, but plotting vertical and horizontal profiles through the center of the image shows clear structure of two principal types: coarse vertical diffraction peaks from the beamline with a spatial period of $\sim 80 \mu\text{m}$ when extrapolated to the focus size, and smaller diagonal diffraction patterns. The coarser pattern is consistent with a reduced overfilling of the toroidal mirror, while the finer patterns could be the result of further optics in the beamline. Both features are a much lessened effect than those seen in the previous beam imaging.

The detector was then moved closer to the lens to approximately $0.75 f$ and the recording of the images repeated, this time with the full $100 \mu\text{s}$ train length to give clear images. The defocussed images, showing the remaining structure of the beam cross-section are shown in figure 5.14. The difference from the previously observed structure (in figure 5.8) is remarkable, although the structure is not completely removed, it is significantly reduced. The mirror is still comparable in size to the beam incident upon it, and as such will still impart diffraction effects to the reflected beam, but by reducing the overfilling the mirror the diffraction effects are lessened. Rather than many slightly curved and separated local maxima in the y -direction, there is now a generally cohesive beam shape, though with a disordered maximum and still several fringes of higher intensity. The size of these fringes is much larger than the previous ones: extrapolating to the size of the focus gives these sub-peaks a period of approximately $80 \mu\text{m}$, compared to the previous sub-peak period of roughly $55 \mu\text{m}$.

There is a clear improvement between the beams for phase III and phase IV but some structure is still seen in the defocussed beam on length scales similar to the motion of the aperture in the beam. One reassurance that the effect on the SNOM signal was minimised by the improvements was that the focus size of the FEL beam was decreased, and showed no sub-structure on the PyroCamIII detector. A secondary observation can be made from the defocussed images: high spatial frequency diagonal striping can be seen in most of the

images, similar to the diffraction patterns seen in PC2 in figure 5.9. The striping can be ascribed to further optics in the beam path being overfilled or slightly mis-aligned with respect to the beam. In the x -direction line profiles this pattern seems to be a contributor to a small amount of structure.

5.2.2 FEL Second Order Light

During the course of phase III (see section 5.5) it was also discovered, by accident, that the SNOM was detecting a surprisingly unexpectedly high signal resulting from second order emission from the FEL. The discovery was made when a signal was still observed from the MCT detector while a silica glass (SiO_2) shutter was closed in the FEL beamline. This shutter has a transmittance $T < 3\%$ above $4.4 \mu\text{m}$ which increases sharply for wavelengths between $2.8 < \lambda < 4.2 \mu\text{m}$ [81] which is almost exactly the range of second harmonic light that the ALICE IR-FEL could produce:

$$\frac{5.70 \mu\text{m}}{2} = 2.85 \mu\text{m} \quad (5.2)$$

$$\frac{8.60 \mu\text{m}}{2} = 4.30 \mu\text{m} \quad (5.3)$$

The FEL light should have only contained a very small fraction of the second order wavelength ($\lambda/2$) yet it was contributing up to 50% of the observed SNOM signal. The disparity between expectations and measurements made of the quantity detected by the SNOM could be explained by two contributing factors. Firstly the $6 \mu\text{m}$ core of the fibres will have had a much greater transport efficiency for shorter wavelengths of light, so while the first order wavelengths are very close to the cut-off for transmission down the fibres, the second order wavelengths are not, giving an increased relative intensity. Secondly the diffraction of the second order light at the outcoupling hole of the FEL and the subsequent diffraction from the overfilled mirror was expected to be significantly less than that for the first order wavelengths, giving a much smaller and more ideal cross-sectional profile which should have been concentrated at the center of the main beam. If the location of the SNOM aperture was placed at the point of maximum intensity in the focussed beam, then it would measure a greater proportion of the second order beam, as it was focussed much more tightly. These two effects together could explain the large proportion of second order light.

For the upper half of the second order range there are no strong features in the IR

spectrum of the tissue, thus the second order light will not have contributed to the contrast seen in the SNOM images at the higher wavelengths, but below $3.75 \mu\text{m}$ there are strong peaks associated with C–H stretches which will lead to additional, undesired contrast. A short-term solution was employed to eliminate as much of the second order light as possible, without impacting on limited experimental time by inserting a partial beam-block at the center of the beam. Because the second order light was expected to be concentrated into a smaller cross-section at the center of the main FEL beam, this beam block simply removed the second order light, with the downside that it also blocked the most intense region of the first order light.

As a more robust method of removing the second order light from the FEL, a high-pass filter $> 4.5 \mu\text{m}$ was placed just after the beam pipe exit window for phase IV of imaging, described in section 5.6. The beamline upgrades resulted in a much larger FEL intensity at the SNOM resulting from a decrease in the loss at the mirror that was replaced. The increase in intensity resulting from these modifications gave much more reliable imaging conditions, indeed the operators controlling the accelerator noted a correlation between the increased intensity of the FEL and the increased stability of the output. The focus was, however, intense enough to both saturate the MCT detector and also damage the samples. Consequently crossed polarisers were also employed to modulate the intensity in a controllable and predictable way.

5.2.3 Undulator Gap Scans and the Spectral Properties of the Fibres

One of the advantages of using the ALICE IR-FEL as a source was the continuous tunability of the FEL output wavelength through varying the undulator gap size. With the addition of real-time wavelength monitoring in phase III using the multi-element pyroelectric detector array, spectra could be measured using the SNOM by sweeping the gap size over a range, leading to a varying wavelength over a corresponding range, and measuring the SNOM signal on a sample. This gave the opportunity to essentially perform local, near-field spectroscopic measurements at a point on a sample using the SNOM. In order to utilise this approach, however, the transmission properties of the SNOM fibre needed to be characterised.

The data measured during such an undulator gap scan (UGS) had several channels recorded in parallel, with the outputs giving spectra of the FEL intensity from the spec-

trometer given by the integral of the fitted curve from the multi-element array detector, the FEL intensity on the SNOM table from the reference detector and the intensity measured by the SNOM aperture via the MCT detector, each taken with respect to both the undulator gap and the fitted wavelength of the FEL. To reduce the impact of noise five measurements were recorded at each value of the undulator gap and the signals from the other channels (wavelength, FEL intensity, reference signal and SNOM signal) were averaged. Because the fitting of the FEL wavelength required a sufficient FEL intensity to give a reliable fit, any transitory dips in the output could lead to a spurious fit and an anomalous wavelength. Such wavelength readings were removed during the averaging process. A further noise reduction was performed using a three point moving local regression smoothing, ignoring outliers at deviations of $> 6\sigma$. While this has the potential to hide important data, the spacing of the wavelengths was much less than the bandwidth of the FEL output and so adjacent points were expected to be largely similar. The uncertainty on each averaged measurement was calculated using the error on the mean $\Delta\bar{x} = \sigma_{N-1}/\sqrt{N}$, though the uncertainty on the final values was generally very small.

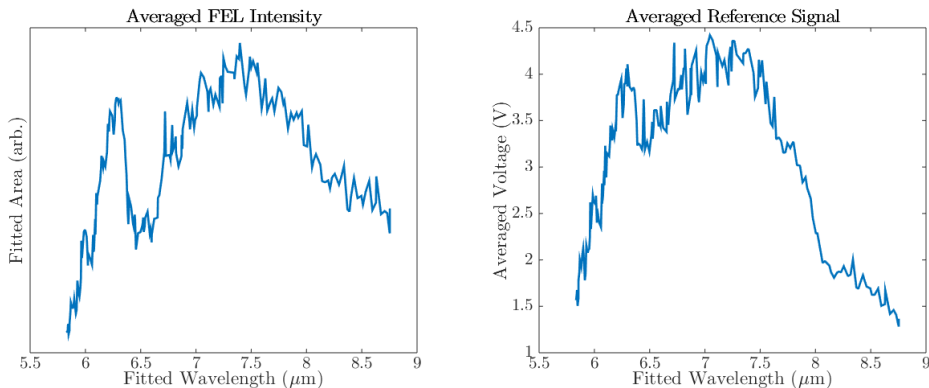


Figure 5.15: Averaged UGS curves of the two measurements of FEL output plotted against the determination of the FEL wavelength by fitting the output of the multi-element detector array in the spectrometer. The FEL intensity measurement was derived from the area of the curve fitted to the multi-element pyroelectric detector array in the spectrometer used to monitor the FEL wavelength. The reference signal that was measured to give a method of normalising the SNOM images was also recorded in the UGS and was much more successful at compensating for the variations in FEL output.

Typical examples of the two measurements of FEL intensity - the fitted area measured at the spectrometer and the reference detector boxcar output - produced by this UGS are displayed in figure 5.15, showing similar but distinct behaviour. The area of the curve fitted to the multi-element detector array output was uncalibrated with respect to true FEL

intensity, giving a rough approximation to the variation in intensity more than the actual value. Due to the way in which the fit area was calculated, when the FEL intensity was lower at either end of the range of the undulator gap, the area given by the fit was less reliable than the value found by the reference detector. This is shown by the much more prominent low values at the extremes of the reference signal curve rather than the FEL intensity curve which suppresses the effect of the lower intensities. The longer PLIA in the spectrometer can also be seen by the enhanced dip at $\sim 6.5 \mu\text{m}$ due to water absorption along the light path; the dip is also seen in the reference signal but is not as pronounced. The reference signal, as when used with the SNOM imaging, gave a much better normalisation for the variation in the FEL intensity than the spectrometer-derived value, and so was used to compensate for this variation when possible.

UGS of Calibration Samples

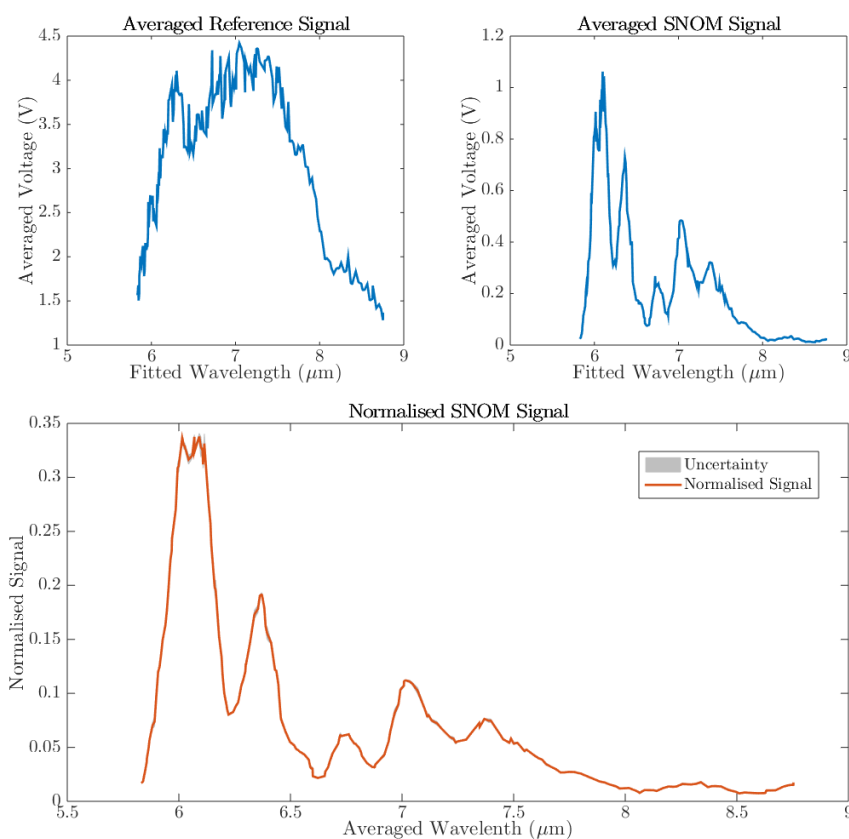


Figure 5.16: The results of an UGS taken on a Au mirror surface using a $6 \mu\text{m}$ core diameter fibre. The averaged SNOM signal was divided by the averaged reference signal to give the normalised red curve underneath. This normalisation was very successful at removing the majority of the noise from the spectrum. The resulting curve is not the flat response that could have been expected from a Au mirror, instead a number of prominent peaks are seen.

In order to characterise the signal recorded by the SNOM many UGS were taken on a Au mirror surface which, as detailed in section 5.1.2, has a very flat optical response over the wavelength range of the ALICE IR-FEL. The reason for this was to limit the variation in response of the sample with wavelength and measure only the wavelength variation of the optical set-up itself. These UGS were performed as a significant part of phase III of SNOM imaging. The SNOM signal measured using a 6 μm core diameter CorActive fibre on the Au mirror is shown in figure 5.16, along with the normalised SNOM signal found by simply dividing the SNOM signal by the reference signal. The uncertainty in the final value, plotted as a grey area around the line is very small and can only be seen clearly in a few places. Normalisation to the reference signal was very successful at removing the majority of the noise in the spectrum.

The normalised curve that was produced by the UGS is not the flat response of a Au mirror: five prominent peaks can be seen. Given that the sample was clean and relatively spectrally uniform, and that these peaks are not seen in the FEL intensity variations, the spectral features must be originating either in the tip-sample interaction, the fibre itself, or at the MCT detector.

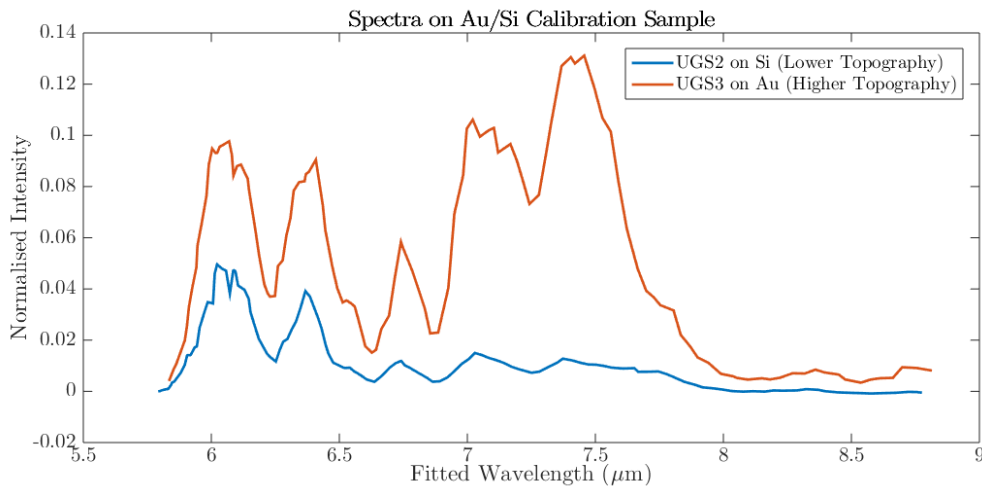


Figure 5.17: The results of an UGS taken on the Au/Si calibration sample. Similar peak positions to those seen on the Au mirror in figure 5.16 are visible, but saturation of the detector during the Au UGS means that it was not possible to normalise and peak locations and intensity for all but the central peak are not accurate.

Further evidence of the origin of these peaks being associated with the fibre or aperture is given by figure 5.17. These two UGS were measured over two different points on the Au/Si calibration sample, one on an area of Si and the other on one of the Au islands. The same line shape is seen in these two spectra, though the relative intensities of the peaks

have dramatically changed. Partly this was due to saturation of the detector during the Au UGS resulting from the significantly higher reflectance of Au compared to Si, but while the two peaks at longer wavelengths saturated the detector, the peak at approximately $6.8 \mu\text{m}$, which was a larger peak in figure 5.16, does not saturate. From this it can be demonstrated that the relative intensity of each of the peaks was variable across different UGS but, as seen in figure 5.17 taking two UGS scans in different places gave peaks in approximately the same locations. This finding suggests that the fibre is giving the structure seen in figures 5.17 and 5.16 as it is less likely that the tip-sample interaction was the same on both regions of the sample.

Understanding the Spectrum

To give a quantitative comparison of the two spectra obtained on the Au/Si sample, the reliable peak at approximately $6.75 \mu\text{m}$ in the two UGS spectra in figure 5.17 were fitted with Gaussian curves. From these fits it was possible to measure the location and size of each and compare between the two spectra to check for consistency and assess if these peaks were variable with the tip location. The calculated peak locations were $6.74 \pm 0.01 \mu\text{m}$ and $6.76 \pm 0.01 \mu\text{m}$ for the Si and Au peaks respectively, with the uncertainties given by 95% confidence bounds of the fit parameters. These two peaks are consistent with each other within these bounds, giving no evidence of variation in the peak location either over time or with the location of the tip.

To characterise the entire spectrum, more accurate fits of all of the peaks in the Si spectrum in figure 5.17 were calculated, first with individual peak fittings to provide approximate locations and the appropriate number of peaks and then with a combination of eight Gaussians simultaneously, determined to be an adequate number to accurately reproduce the shape observed in the UGS spectra. The peak locations, 95% confidence bounds, and the general assignment of each of these eight peaks are given in table 5.1 and the corresponding fit produced is shown in figure 5.18.

The fitted curve in figure 5.18 was compared to the Au mirror spectrum in figure 5.16, showing a very similar line shape with peak locations within the 95% confidence bounds determined for the fit. The relative peak heights are slightly different between the fit and Au mirror spectrum, but are much closer than the variation seen on the Au spectrum from figure 5.17. With the spectra being so similar while being acquired on different days, with

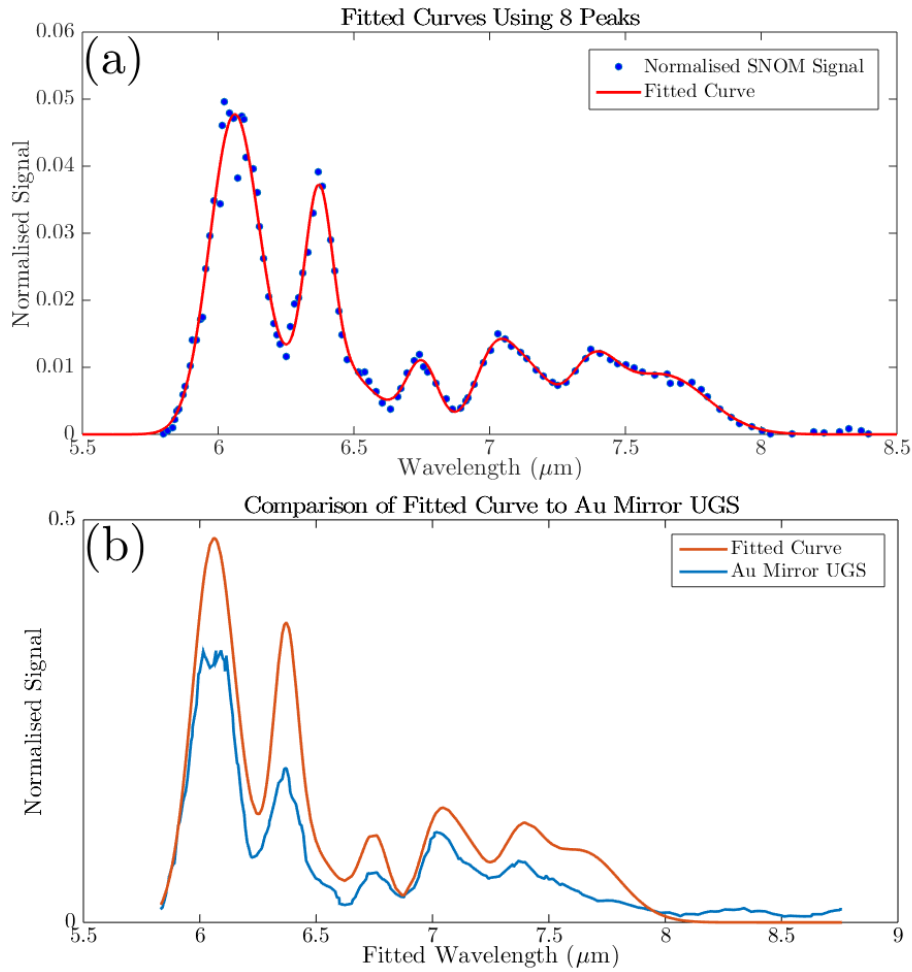


Figure 5.18: (a) The fitted curve plotted with the points of the Si spectrum from figure 5.17. The eight peaks used to fit the curve give a good fit. (b) This fit is compared with the spectrum measured over the Au mirror, showing a very similar shape, and consistent peak positions with relatively similar peak heights.

different fibres and on different types of sample, the most likely origin of the structure is the transmission properties of fibre itself.

Fibre Spectrum

To understand the origin of the spectral features resulting from the transmission through the IR fibre, an UGS was taken where, instead of measuring the SNOM signal in reflection, a 100 μm core diameter fibre, also from CorActive and with the same composition, was placed at the focus of a 50 mm focal length CaF_2 lens and the ALICE IR-FEL beam directly coupled into the fibre. The measured spectrum is given in figure 5.19 with the same fitted curve produced using the Si spectrum produced above. Due to the much larger signal level that could be transmitted down the larger core, the MCT detector saturated too easily and the pyroelectric reference detector had to be used instead. This set-up has the advantage of

Peak Description	Center (μm)	95% Confidence Bounds (μm)
Peak 1	6.06	6.05 - 6.07
Peak 2	6.37	6.36 - 6.38
Peak 2 Shoulder	6.41	6.35 - 6.46
Peak 3	6.75	6.73 - 6.77
Peak 4	7.03	6.83 - 7.23
Peak 4 Shoulder	7.17	6.91 - 7.43
Peak 5	7.38	7.31 - 7.45
Peak 5 Shoulder	7.64	7.47 - 7.81

Table 5.1: Peak descriptions and locations for the fit given in figure 5.18. The smaller peaks show a correspondingly greater uncertainty in location, but these peaks give a very good fit to the measured spectrum.

removing the effects of the MCT detector and tip-sample interaction from the measurement and only contains the signatures of the lens, fibre and reference detector. The lens and reference detector signals were both included in the reference signal measurements (see figure 5.15) which did not show the peaks seen previously in figures 5.16 and 5.17, and are also present in this measurement in figure 5.19.

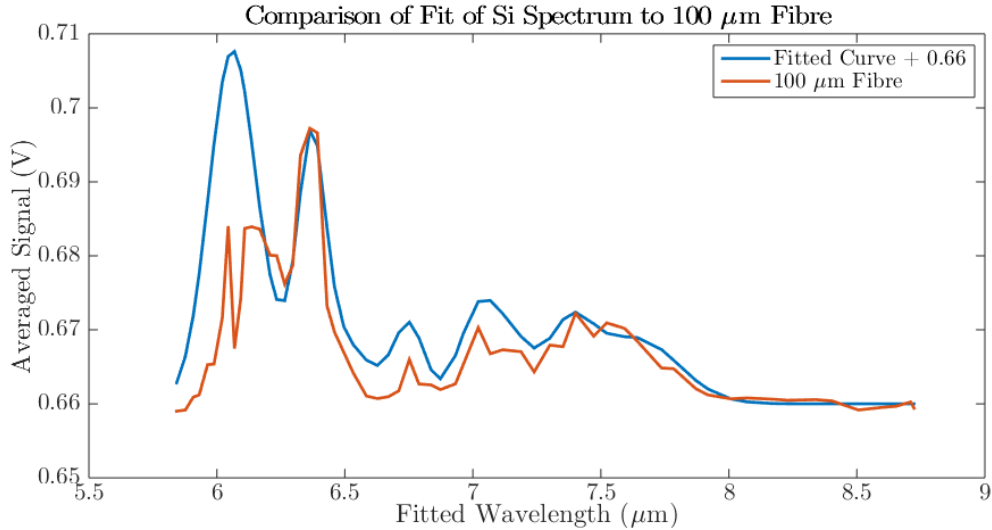


Figure 5.19: The spectrum measured by an UGS with the FEL beam directly coupled into a $100 \mu\text{m}$ core diameter fibre. Also plotted is the same curve fitted to the Si spectrum in figure 5.18. The $100 \mu\text{m}$ fibre spectrum is noisier than previous spectra because it could not be normalised, as the reference detector was used to measure the signal transmitted through the fibre. The shape of the spectrum is very similar to the shape of the fitted curve from previous UGS but the variation is on a large pedestal value of $\sim 0.66 \text{ V}$ rather than 0 V .

The disadvantage of using the reference detector is that there was no usable reference signal for normalisation, and so the spectrum produced was noisy. The shape produced by this UGS, however, very closely resembles the shape produced in the previous UGS taken with the $6 \mu\text{m}$ core diameter fibres, but with a large pedestal value of 0.66 V , giving a

5% peak-to-peak variation over the spectrum. Comparing this variation to the 50 – 100% peak-to-peak variation for the 6 μm core diameter fibre shows that the size of the core plays an important role in the modulation of the spectrum - further evidence that the fibre itself is the source of the structure seen in these UGS.

A final piece of information comes from the transmission spectrum of the fibre, given in the datasheet from CorActive for these fibres [77]. The spectrum, shown inset in figure 5.20, shows the relatively flat transmission properties of the As_2Se_3 over the FEL tunable range, but the small fluctuations in the spectrum do correspond closely to the features seen in the UGS spectra, with the comparison shown in the main graph in figure 5.20.

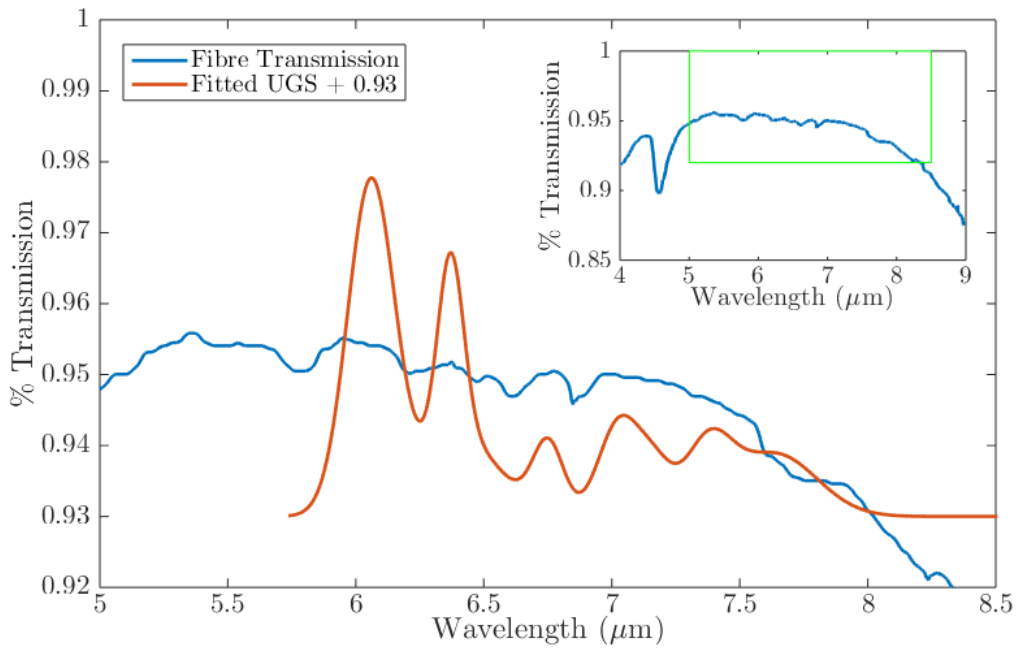


Figure 5.20: The spectrum of the fibres from the datasheet provided by CorActive [77] compared with the shape of the spectra from the UGS above. Inset is the full spectrum with the indicated region enlarged for the main graph. The shape of the UGS spectra closely resembles the peaks and troughs of this fibre spectrum, suggesting that the structures seen are resulting from absorption within the fibre.

The peaks and troughs of the fibre spectrum match very closely the shape of the UGS curve and suggests that absorption within the fibre material is causing the UGS profile shape. There remain two additional effects, however, that require consideration. The first is the size of the features seen in the spectrum. The variation in the fibre transmission spectrum provided by CorActive is only $\sim 0.5\%$ peak-to-peak on a value of 95%. For the 100 μm core diameter fibre, however, the modulation was roughly 5% of the signal strength, while for 6 μm core diameter fibres the modulation was up to 95%. The absorption by the fibre

must be enhanced beyond that predicted for the material by the manufacturer. The 6 μm core diameter size fibre will act as a single mode fibre, with the transmitted mode extending significantly into the cladding material [82]. The cladding material, therefore, will also be contributing to absorption, and no spectrum is known for this material, although it is still As_2Se_3 and so should have similar spectral features at roughly the same wavelengths. The larger core size fibre will be multimode and so represents an intermediate situation that is much closer to the ideal case given in the fibre datasheet.

The second effect needing to be understood is the variable relative peak intensity, even post-normalisation. It could be the case that the FEL intensity variations did not normalise well, though the curve produced in figure 5.16 shows a much cleaner spectrum than pre-normalisation. Another possible source of this variation in intensity at different wavelengths is the structure known to have existed in the beam at the time that these UGS were taken. Any change in the aperture position in the beam could have led to a slightly different part of the wavelength-dependent beam structure being sampled by the SNOM aperture and so a different signal strength at the same wavelength.

UGS Conclusions

The spectra produced by these UGS show a significant amount of structure originating from absorption in the fibre itself. The spectral features of the fibre are also compounded with the FEL intensity variations and different detector response curves, which make normalisation more difficult, though some success was had. The beam structure and this normalisation difficulty together contributed to peak height and position variations between UGS, that could not be compensated for, on a scale at least as large as the expected variations that a biological sample would give at different sampling points. Because of these difficulties UGS were not performed during phase IV and stricter monitoring of scan wavelength was implemented for phase IV to avoid the fibre spectrum affecting the fixed-wavelength SNOM images.

5.2.4 Resolution: Optical and Topographic

The SNOM technique obtains images in the near-field of a sample to circumvent the diffraction limit on the resolution placed upon conventional far-field microscopy. The spatial resolution obtained by SNOM imaging is one of its main advantages over other techniques.

There have been many different reported findings for resolutions obtained in other work and any resolution below λ can be considered to be below the diffraction limit. In the experiments conducted during this work the principal focus was the development of understanding with regards to both the SNOM equipment and oesophageal cancer, rather than in obtaining high resolution images. This was the main driving force behind the choice to use cleaved fibres rather than etched fibres, since although the resolution becomes limited by the size of the fibre core, the cleaved fibre is much more stable, does not require such careful handling and can image larger areas with more extreme topographic variation.

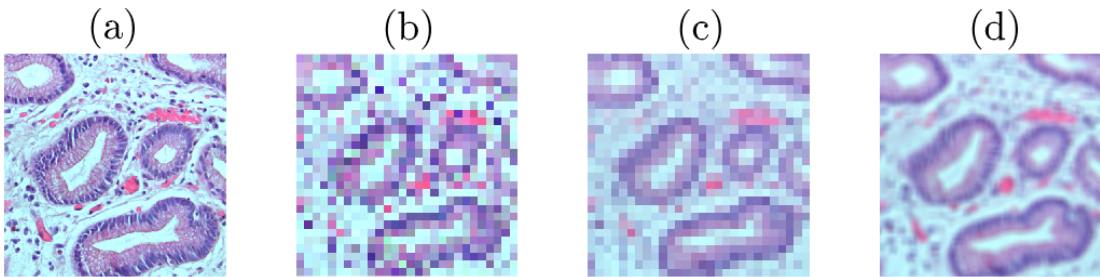


Figure 5.21: The effect of varying the pixel size with different true resolutions for an image area of $280 \times 280 \mu\text{m}$. (a) An image of a stained tissue section showing clear, crisp detail in the sample, with a pixel size of $0.5 \mu\text{m}$ and a matched resolution of $0.5 \mu\text{m}$. (b) An under-sampled version of the same image area at $0.5 \mu\text{m}$ true resolution but with a pixel size of $10 \mu\text{m}$, essentially taking every 20th pixel; the image is much less recognisable in terms of the structures seen. (c) An appropriately sampled image, with a resolution and pixel size of $10 \mu\text{m}$; although the number of pixels is the same as in (b) the image appears much clearer and the structures are recognisable. (d) An over-sampled image where the resolution is still $10 \mu\text{m}$ but the pixel size is $0.5 \mu\text{m}$; the image shows more detail than is seen in (c) despite having the same true resolution of $10 \mu\text{m}$ but has 400 times as many pixels so would take 400 times as long to acquire with the SNOM. A compromise should be used between (c) and (d) that maximises detail while minimising the acquisition time.

It is important to know the spatial resolution that each ‘tip’ is capable of achieving in order to vary the pixel size so as to avoid excessive under- or over-sampling of the image, as demonstrated in figure 5.21. Under-sampling, that is collecting pixels at a spacing larger than the resolution of the fibre, leads to loss of information [8] and a resulting image that is hard to interpret, and while over-sampling, collecting pixels at a spacing less than the resolution of the fibre, gives a higher level of detail in the image, it takes longer to acquire the image. By over-sampling the image only slightly, a good level of quality can be achieved without dramatically increasing the time taken. However, in order to determine the optimum pixel size a knowledge of the typical resolution obtained by the SNOM is required. The cleaved fibres used in this work had a core size of $6 \mu\text{m}$ which should give a maximum

resolution on the order of $6 - 10 \mu\text{m}$ in the transmission imaging mode, but can give smaller resolutions in reflection due to the geometry of the tip and sample, where the SNOM aperture effectively includes the gap between the tissue and sample, which is nominally on the order of $\sim 50 - 100 \text{ nm}$.

To test the resolution of the fibres a calibration sample consisting of Au islands deposited onto a Si substrate, the same sample used to calibrate the piezo hysteresis in section 3.4.2. SNOM images were taken over the edge of one of the islands at two different sizes, shown in figure 5.22. The topography and SNOM signal images show a well defined edge where the sample steps up to a Au island and the reflectivity of the surface changes. Although the SNOM image is noisy the difference is clear between the two regions. Examining the response of both the topographic and optical signals to the sharp edge on the sample provides a measure of the resolution for each.

The ER of both the topography and SNOM signal over the sharp step edge of one of the

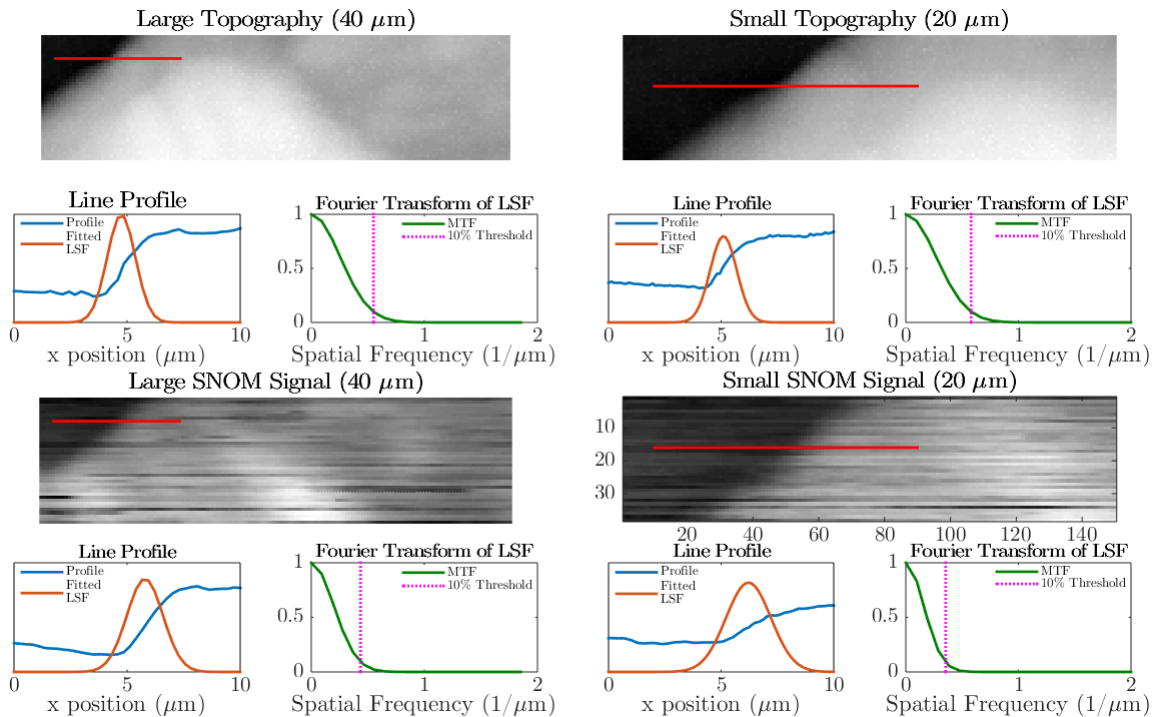


Figure 5.22: Extracted line profiles from two pairs of images taken on a calibration sample with a sharp step edge were used to estimate the resolution of the SNOM measurements. One pair of images (topography and SNOM signal) were taken over a $40 \mu\text{m}$ square scan area with 150 pixels in each dimension and the other pair were at the same number of pixels but only scanning half the size ($20 \mu\text{m}$) and so at half the pixel size. Each line profile was essentially differentiated, by taking the difference between adjacent points, and fitted with a Gaussian curve. The fitted LSF was Fourier transformed to give the MTF and an estimate for the resolution of each of the images at the 10% threshold level of the MTF.

Au islands was used to calculate the MTF as detailed in section 2.4.1. Figure 5.22 shows the ER profiles extracted from the indicated lines in each of the four images along the scan direction of the SNOM. The first difference of each of these profiles was taken to give the LSF which was fitted with a Gaussian to reduce the impact of the noise present in the signal. The FT of these fitted LSF were plotted and the 10% level determined for each one. The resolution of each image was determined by taking the reciprocal of the spatial frequency to give topographic spatial resolutions of 1.81 μm and 1.73 μm for the 40 and 20 μm images respectively and corresponding optical spatial resolutions of 2.30 μm and 2.83 μm .

The two images give very similar results, leading to an average optical spatial resolution of 2.57 μm which, for an imaging wavelength of $\lambda = 6.75 \mu\text{m}$, gives a resolution in terms of the wavelength of almost $\lambda/3$, demonstrating that the optical resolution of the SNOM was indeed below the diffraction limit.

The spatial resolutions of the topography images were significantly smaller than those found for the optical images. This can be understood by the different nature by which the topography is measured compared to the SNOM signal. The resolution of the topography will be determined by the shape and size of the lowest point on the fibre. Not only is this potentially independent of the SNOM aperture when using cleaved fibres, but it is also subject to change if the fibre either sustains damage or picks up some sort of debris, without necessarily impacting the optical resolution in the same way. The effective SNOM aperture is also likely to vary to some extent depending on the tip-sample interaction and geometry of the fibre tip, so the results obtained here can only give an approximate value resolution that was obtained on tissue samples

Based upon these resolution measurements, the SNOM images taken with cleaved fibres were acquired with a pixel size smaller than 2.6 μm in order to obtain an appropriate match to the typical resolution expected.

5.2.5 Imaging and Analysis Considerations

When analysing images, it is important to be aware of the different types of information they contain, and to interpret them appropriately. For SNOM, there are many variables that can affect the signal measured at a given pixel that can be both desired or undesired depending on the type of imaging being performed. In any analysis of images where noise can be a problem, SNR is often used to give a measure of the impact of the noise relative

to the signal level. As the signal levels measured by the SNOM are typically very small, the impact from different sources of noise can be great. Generally image analysis of this data would therefore seek to distinguish signal from noise, but which effects classify as ‘noise’ depends on how the images are taken and what effects are of interest. A simple definition of ‘noise’ is used here: any sort of undesired contrast mechanism within the SNOM images. Further to this, the noise in the data acquired by the SNOM can be of two main forms: pixel-to-pixel variations and image-to-image variations.

In microscopy there are many different effects that contribute to the observed contrast in a given pixel, the principal and most desirable is absorption or reflection by the sample. Additional information can come from added chemical stains [83] or fluorophores [84], as with H&E stain used to label DNA and protein in tissue samples. The extension to SNOM adds a number of further contrast mechanisms associated with the near-field. Any changes in the refractive index at or near the sample surface, either from a chemical or structural change, will produce variations in the signal propagated down the SNOM fibre [85]. Although this makes SNOM a powerful tool for imaging in many different ways it also means that it is sensitive to additional undesirable effects. The evanescent field at the sample surface decays exponentially with distance, so any variation in tip-sample distance will exponentially affect the SNOM signal measured. Vibrational noise is therefore a potentially significant problem, as is any perturbation to, or breakdown of, the feedback used to maintain the tip-sample separation.

Other undesired pixel-to-pixel contrast mechanisms can arise from variations in the radiation incident upon the sample, such as fluctuations in the source intensity or wavelength or, as discussed above, relative motion of the beam and aperture. Image-to-image contrast changes could also arise from these variations in wavelength, intensity or beam position, albeit on a longer time scale, making the separation of these effects very difficult. An additional source of variation of apparent source intensity is absorption of the radiation in the ambient atmosphere. For IR wavelengths the main contributor to absorption in air is the presence of H₂O. The amount of absorption in the air is very sensitive to wavelength, and also may vary with time as the ambient humidity varies.

A further effect on any SPM technique is the shape and geometry of the tip and sample [86]. Again both of these can change image-to-image, but can also be strongly dependent on position within a scan area.

In order to be able to minimise the impact of these different types of contrast mechanisms and to recognise or mitigate them, those sources that are undesired need to be identified and characterised. The development of the SNOM instrument detailed above contained many occasions where the improvements made to the equipment and set-up were driven by a desire to mitigate these effects.

Informative Contrast Mechanisms

For SNOM, there are many different potential sources of desired contrast, depending on the approach taken to imaging, the mode of operation and the type and wavelength of illumination. Effects that, in the far-field, are easy to understand such as absorption and reflection, become more complicated in the near-field [85]. As with far-field imaging, however, the signal contained within the evanescent waves at the surface of a sample are related to variations in the complex refractive index at the surface, giving analogous types of effect, but with potentially less intuitive responses at different wavelengths. This contrast was the desired contrast mechanism investigated in this work, relating the SNOM signal measured to the sample chemistry. By measuring in reflection imaging mode, the resolution was better than in transmission with the cleaved fibres used, but the SNOM signal was much more surface sensitive. The reflection images therefore do not give information for the whole thickness of the samples, further complicating the interpretation of the contrast seen: the comparison between the SNOM images and visible light-based information could only be performed with stained and unstained images of the whole sample thickness, with no way of isolating only the chemistry of the surface.

Another source of contrast that can be informative, and is often used in conventional far-field microscopy, is the polarisation of the illuminating source and how it interacts with the sample geometry [25]. The polarisation of the ALICE IR-FEL was fixed by the plane of the undulator, giving a strong polarisation to the FEL beam. Using a single polariser to modulate the beam intensity delivered to the SNOM would have changed the plane of polarisation incident on the sample, but using crossed polarisers with the second polariser's plane of polarisation fixed with respect to the sample removed this problem, and the effect of polarisation was not investigated in this work.

Air Absorption

The PLIA was varied significantly during the development of the ALICE-SNOM instrument. The effect this had on the impact of absorption by water vapour and CO_2 along this path was modelled using data from the high-resolution transmission molecular absorption (HITRAN) database and the National Institute of Standards and Technology (NIST) [87, 88] modelling a path length of 1 m, the maximum used in this work, at an ambient temperature of 295 K and relative humidity of 80%. The resulting transmittance spectrum is shown in figure 5.23a, along with the convolution of this spectrum with the spectral shape and bandwidth of the FEL beam to model the typical transmittance of the FEL beam along a PLIA of 1 m. A rough approximation to the corresponding FEL intensity that could be measured is shown in figure 5.23b, found by approximating the output curve of the FEL with

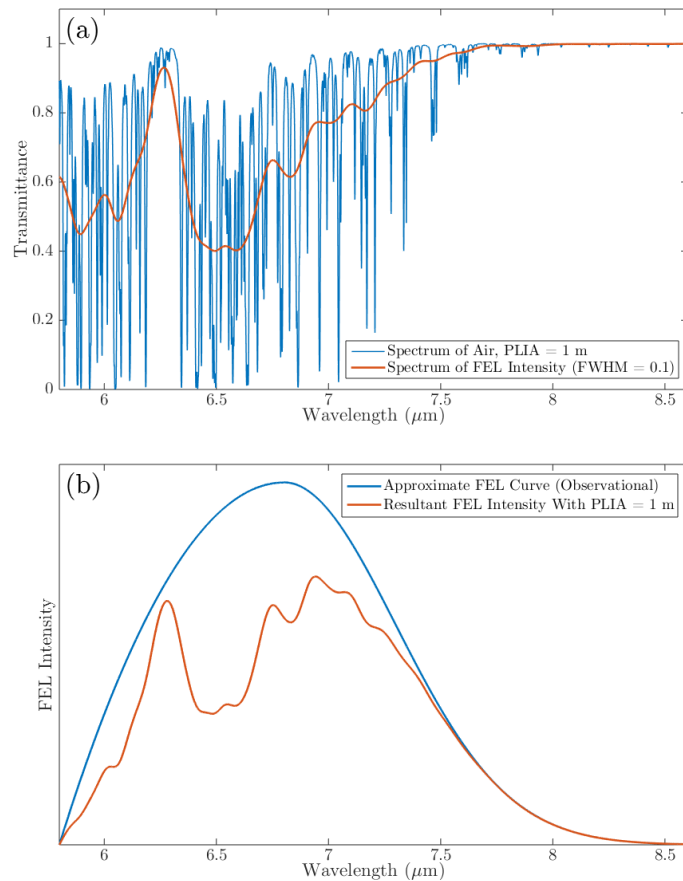


Figure 5.23: A model of the absorption due to the absorption by H_2O and CO_2 along a 1 m PLIA. (a) The transmittance of the PLIA derived using data acquired from NIST and HITRAN [87, 88]. (b) An approximate model of the FEL output intensity with wavelength based on observations of peak wavelengths and the FEL range, using this the approximate resultant FEL intensity profile can be obtained. This is consistent with the profile recorded during undulator gap scans.

wavelength and multiplying this by the transmittance of the PLIA. This curve shape is very similar to the reference signal and FEL Intensity measured when scanning the wavelength during UGS, as detailed in section 5.2.3.

The variation of transmittance with wavelength for this PLIA shows the very sharp and intense absorption bands of H₂O. The absorption due to CO₂ gives only a very small effect. By considering that the ALICE IR-FEL is not truly monochromatic, but instead has a bandwidth with a FWHM of $\sim 0.1 \mu\text{m}$, the transmittance experienced at a particular central wavelength can be derived by the convolution by a Gaussian with a FWHM of $0.1 \mu\text{m}$. The transmittance resulting from this gives a much smoother profile. While this should give the intensity measured by the SNOM, the particular wavelengths corresponding to the absorption by water vapour will still be removed from the FEL beam. The absorption features are so sharp, though, that it should still be possible to access the biomarker vibrational bands. Increasing the PLIA further gives an exponential increase to the absorption along the length and will begin to have more detrimental effects to the intensity that is measured at the SNOM.

Source-Related Effects

The most intuitive and understandable type of the undesired sources of contrast in SNOM arise from effects linked to the light source. Here the ALICE accelerator IR-FEL gives the high peak power and relatively low average power that was required in order to successfully image these samples without damaging them. Using a FEL as the source does, however, come with several potential issues that had to be understood and mitigated. As detailed above the FEL beam had significant structure over its cross-section, leading to potential issues when the tip was translated vertically in the beam for the inverted microscope SNOM. By replacing the over-filled mirror that was known to produce much of this structure, its impact was reduced to a manageable level.

An additional effect that was also compounded by the beam structure is the spatial motion of the beam. The FEL was tens of metres away from the SNOM along an evacuated beam pipe. Any small vibrational motion at the FEL would have been essentially amplified by this long distance. To avoid this effect the FEL was vibrationally isolated and the beam observed to ensure that no problem arose. This vibrational motion could have resulted in pixel-to-pixel noise in the SNOM images, but slower motions, such as thermal expan-

sion/contraction of components over the course of hours will also affect the image-to-image values, by varying the portion of the beam focus being sampled by the SNOM aperture. Beam motion of both types is hard to compensate for, as any change in focal point affects the pedestal value that the image variation sits upon, but attempting to re-maximise the SNOM signal for each new SNOM image will change this value anyway.

Perhaps the most expected source of noise present in the FEL intensity was the variation in intensity over time. This effect manifested in several different ways, affecting both pixel-to-pixel and image-to-image values. The shot-to-shot noise on the FEL, simply the variation in intensity or wavelength from one macropulse to the next, was able to be maintained at a reasonably low level. The peak to peak noise level of the intensity variation was used to adjust the accelerator parameters to give a value of $< 5\%$ over 1 minute. Additional instabilities in the accelerator could also lead to momentary drops in lasing, giving a few pixels with no FEL beam in the SNOM images, as well as occasional ‘wobbles’ in intensity, often linked to the cryogenics in the superconducting linear accelerator modules. These effects, other than drop-outs, should have been able to be normalised using the reference signal but, as discussed above, this was not always successful. Further thermal effects in the accelerator hall could also lead to much slower effects, such as a slow variation in the cavity length of the FEL, leading to a shift in wavelength and intensity that could not be compensated for, and instead had to be monitored over the course of the imaging, facilitated by the addition of real-time wavelength monitoring during scanning in phase III.

Tip-Related Effects

SNOM is a technique that relies upon having an aperture close to a sample surface. If some external influence affects the manner in which the tip engages with the sample then not only is the topographic image adversely affected, but the SNOM signal can also deteriorate.

One of the most commonly seen effects on the topographic images during this work was the production of artefacts from large or misshapen tips. The topographic image measured during a SNOM scan is, as with other SPM techniques [86], a convolution of the sample surface topography and the tip shape. If the end of the SNOM fibre has a large area, then only the highest point of topography under that area is sensed by the feedback mechanism, leading to repeated ‘stamps’ of the tip shape over the image, obscuring the fine detail. In some cases this ‘tip artefact’ made accurate matching of the image to corresponding

microscope images impossible.

The samples that were under investigation in this work were complicated tissue sections with many small pieces and debris. This gave the possibility of influencing the topographic feedback mechanism by colliding with some piece of detritus on the sample surface or lifting the sample edge during scanning. In doing so the feedback mechanism would retract the tip suddenly while scanning and then re-approach the sample, leading to a high streak in the topographic image. In the most extreme cases the fibre was damaged leading to a very different topographic response, with a higher chance of tip artefacts.

In all of the cases above the topographic measurement of the sample, used to maintain the distance between the sample and SNOM aperture, is disrupted or unreliable. This does affect the topographic image in undesirable ways, but perhaps more significantly the optical measurement is also affected by the variation in the height of the aperture in the evanescent field at the sample surface. Images with significant topographic effects, therefore, were considered much less reliable than those without and, in the case of an isolated topographic effect, that region was cropped from the image.

By using cleaved fibres for phases II - IV the possibility of damaging the tip was greatly reduced, leading to the ability to perform larger, faster scans. The likelihood of colliding with the sample or debris and the chance of tip artefacts were increased, however, due to a larger area moving near to the sample surface. Etched fibres, conversely, have a much weaker interaction with the sample and so are less likely to pick up debris and will have much smaller tip sizes, reducing the chance of problematic tip artefacts, but are much more fragile. An unforeseen problem that also arose with cleaved fibres was a significant spatial offset between the SNOM aperture and the lowest point on the tip, where the topography was sensed. The aperture, in this case, was therefore at a much less controlled distance from the sample surface, essentially randomly varied over the course of the image independent of the actual area that was optically sampled. Again, using etched fibres would minimise this problem.

Sample-Related Effects

The third source of additional, potentially undesired contrast is the sample itself. This may seem counter-intuitive, as the contrast arising from the sample is desired and allows an understanding of the sample chemistry to be obtained. Any changes to the sample during

the acquisition of a set of SNOM images, or damage after a tip collision, will change the contrast seen in the later images. The images each took typically 1-1.5 hours to acquire, so care had to be taken to ensure that the sample was undamaged and undisturbed between or during scans.

The potential impact for an extra, undesired chemical species to be present on the sample should also be considered, as these will clearly affect the IR signal observed. The most likely contaminants to a biopsy sample such as the ones imaged in this work is residual wax remaining after the dewaxing process. Every effort was taken to ensure that the dewaxing process was successful in removing the wax, with several stages of increasing cleanliness of Xylene and rinsing in isopropyl alcohol. Additional effects may also come from the aging of the samples, especially the potential for microbial contaminants growing on the specimens after they have been dewaxed. To avoid this the samples were typically only imaged for approximately a week after removing the wax, and the evidence given by the FTIR labelling in chapter 4 that even after a period of months there was no significant change observed implies that this was not a serious issue with these samples.

Additionally the geometry of the sample relative to the plane of polarisation is known to have an effect on the signal measured [25]. Other structural effects, such as shadowing of lower-lying areas of sample by raised portions, will also have an effect. Separating these sources of contrast from the information that is of interest is very difficult, polarisation effects could be observed by measuring with several different planes of polarisation and observing the difference but time constraints and potential damage to the sample made this infeasible. Instead of compensating for these effects, an appreciation that these could impact the images should allow analyses to be applied and conclusions drawn.

Image Ratios

Many of the above effects are spatially dependent within a given scan area, but should stay relatively constant over the course of several scans. By taking ratios of images, many of these effects should cancel or be reduced. The pixel-to-pixel noise that is not spatially determined but rather is temporal in nature, such as the FEL intensity variations, will not cancel, but by developing a more appropriate reference signal the work above moved towards being able to eliminate much of this noise. The noise that is varying image-to-image will also not cancel by taking ratios, but should give more of a constant offset in image value,

rather than influencing individual pixels.

5.3 Phase I SNOM: Preliminary Investigation

An early pilot study using the SNOM on the ALICE IR-FEL facility [33] used a pilot group of two samples of oesophageal tissue, one adenocarcinoma and one benign Barrett's oesophagus, to measure high resolution images using a simple set-up as a proof of concept and starting point for this project. The diagnosis of each sample was unknown at the time of imaging and analysis, to avoid bias.

The images obtained were very small, $40 \times 40 \mu\text{m}$ with a pixel size of $0.2 \times 0.2 \mu\text{m}$, and unguided in location: the tip was simply positioned over an area of the tissue. These small areas are therefore not necessarily representative of the samples they were taken from, which limits the conclusions that can be drawn from qualitative arguments, but the published analysis of the imaging results shows that there is a clear discrimination between the two images based upon differences in the distributions of the $8.05 \mu\text{m}$ phosphate stretch signal associated with DNA. One sample was measured to have regions of DNA extended over $\approx 20 \mu\text{m}^2$ while the other had much smaller areas of $< 10 \mu\text{m}^2$. This was in-line with the findings in previous work [58, 89] that the amount of DNA is vastly larger in cancerous tissue than in benign tissue, leading to an identification of the first sample as cancerous and the second as benign.

5.3.1 Phase I Set-up

The set-up for acquiring these first images is shown in figure 5.24. The ALICE IR-FEL beam exited the CaF_2 window at the end of the beam pipe and was focussed onto the sample using a ZnSe lens of focal length $f = 300 \text{ mm}$. By placing the lens just after the beam pipe exit window, the path length in air (PLIA) was just over 300 mm giving minimal absorption by water vapour and CO_2 in the air. A purged container could not be used as the air disturbance caused by the flow of gas could have interfered with the topographic feedback of the SNOM. For a discussion of the effect of the PLIA see section 5.2.5. A camera was used to monitor the approach of the fibre to the surface, but was not used to guide the sample area beyond placing it on the piece of tissue on the disk. The fibres used to take these preliminary images were etched and gold coated As_2Se_3 fibres, which have been described

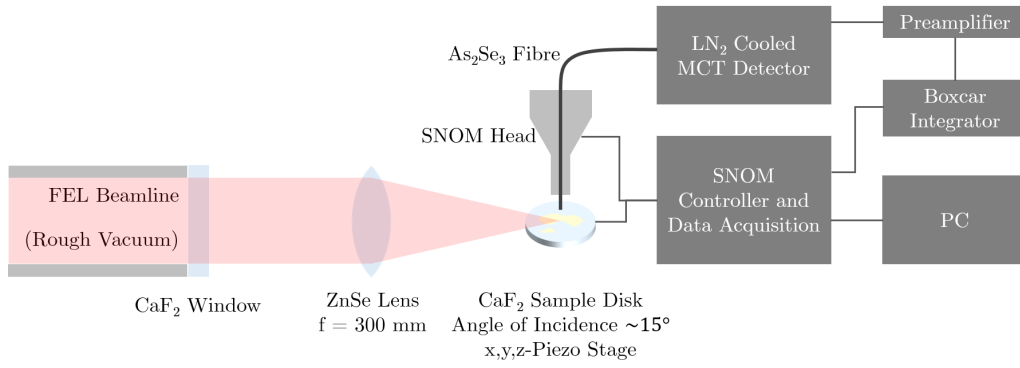


Figure 5.24: Simplified schematic for the first phase of SNOM imaging. The IR-FEL beam was delivered to the end-station of the beamline in an evacuated beam pipe with a CaF₂ exit window. Immediately after this window, a 300 mm focal length Zn₂Se₃ lens was used to focus the FEL beam onto the tissue sample. The sample was mounted on a three axis piezo stage to control the scanning plane (x, y) and to maintain the tip sample height (z). A single electronics module was used to control the piezos and collect the two data channels, the topography and the integrated SNOM signal from the boxcar.

in section 5.1.2.

The choice of initial wavelengths with which to image the samples was based on the spectra in the second figure in reference [58] where absorption peaks are shown for the different biological components. The wavelengths chosen had to lie within the range of the ALICE IR-FEL and give peaks that were sufficiently distinct from others for identification of that particular biomarker: 7.00 μm was chosen as a general ‘blank’ background, with no strong spectral features, 7.30 μm was assigned to protein/glycoprotein corresponding to the CH₃ bend around 1360 – 1390 cm^{-1} and 8.05 μm was assigned to DNA giving the PO₂⁻ stretch between 1200 cm^{-1} and 1250 cm^{-1} . The intention behind this choice of imaging wavelengths was to produce a chemical map of these different biological components of the tissue, each of which are expected to differ in cancerous tissue from their physical arrangements or concentrations in benign Barrett’s oesophagus or healthy tissue [90].

5.3.2 Phase I Development

This phase of SNOM imaging was designed to allow a small data set to be collected to form a pilot study. Due to restrictions in imaging time and available resources the set-up was deliberately made simple and basic, but to give enough information about the samples and areas imaged to prove the concept of using IR-SNOM to investigate oesophageal tissue. There were two data channels recorded simultaneously for these images: the light intensity measured by the MCT detector, amplified and then converted to an analogue voltage by

a boxcar integrator, hereafter referred to as the SNOM signal, I_{SNOM} , and the z -piezo position giving the topography of the sample surface. An example set of images acquired during phase I shown in figure 5.25.

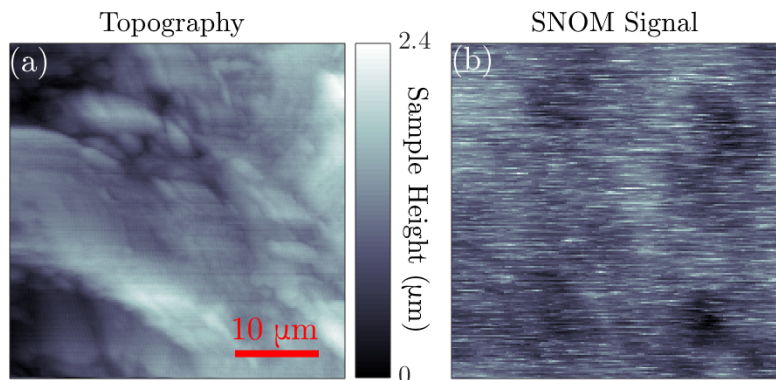


Figure 5.25: Sample images acquired during phase 1. The images are $40 \times 40 \mu\text{m}$ with a pixel size of $0.2 \times 0.2 \mu\text{m}$, and the SNOM signal image (b) has been filtered using a FT filter as described in section 3.4.4, but without some sort of reference value for the variable IR-FEL intensity the images cannot be cleaned up further. Features on the order of $\sim 1 \mu\text{m}$ can be seen in the SNOM Signal image in (b), setting this as an upper limit on the resolution obtained in these images. This image, along with the other two wavelengths, allowed cluster analysis to demonstrate the larger area of DNA signal observed in this specimen, leading to the conclusion that it was cancerous.

Figure 5.25 shows the forward-directed images, where the image is constructed sequentially pixel-by-pixel left to right along a given line and then scanning bottom to top from line to line. The image set shown in figure 5.25 was taken at $8.05 \mu\text{m}$ to represent a map of DNA in the sample, based upon the associated phosphate stretch in DNA at that energy. From this SNOM image and the image on the other sample at the same wavelength, cluster analysis and contour plotting showed that the areas of high DNA signal were significantly larger in this sample, suggesting a diagnosis of cancer.

The SNOM signal itself was sufficient to determine which of the two samples was cancerous, but for a more detailed investigation the relative intensity of the light source was needed in order to quantify the corresponding variation in the signal and possibly to normalise the image. In addition, an increased number of sample areas needed to be imaged to give a better understanding of both inter- and intra-patient variability/consistency and the repeatability of the results. Because tissue varies on a scale of tens of microns, the exact placement of a single $40 \mu\text{m}$ area within a large (several mm) biopsy sample can have a strong effect on the information captured in each image. It was therefore clear that an important consideration should be the location of the image within the tissue sample, specifically with regards to

its composition, so that a more representative and applicable area could be studied, and to facilitate matching to microscope images the areas should contain identifiable topographic markers.

5.4 Phase II SNOM: FEL Reference

The second phase of experiments expanded the number of channels recorded by the SNOM software to three, with the addition of a relative background intensity channel, the reference signal I_0 . This channel read an analogue voltage from a second boxcar integrator in the same way as the I_{SNOM} data, but the voltage was generated from the output of a single-element pyroelectric detector which was receiving a small portion of the FEL light reflected by a CaF_2 beam splitter. This channel recorded the variation in the FEL power over time, with no spatial information, but was still recorded in image format, analogous to the I_{SNOM} images. The aim of measuring the reference signal was to facilitate normalisation of the SNOM signal with respect to the source variation over time in order to produce an image that was independent of the FEL intensity, a step that is standard practice in spectroscopic measurements.

An effort was also made to image in locations of interest. Not every biopsy piece on a sample was of the same type or presentation of the tissue, having been taken from several locations around a suspicious lesion and embedded in the same block of paraffin wax. For this reason it was important to choose a biopsy region that would give results consistent with the experimental aims, specifically regions containing the epithelium and stroma of the tissue, and not regions containing large quantities of debris or other tissues. The goal was to guide area placement by using stained serial sections of the same sample, giving an indication of the expected sample morphology. Both phase I and phase II were limited in how accurately the image areas could be defined and located by the quality and geometry of the approach camera images. The sample piezo stages for both phases were three-axis stages, with x , y , and z control. As such it was impossible to obtain images from a camera perpendicular to the sample as it would have been blocked from above by the SNOM head assembly and from below by the sample stage. The approach camera for phases I and II provided an image at approximately 30° from the surface normal and so gave a limited field of view that was in focus, and the true scan location was blocked by the fibre itself. This

geometry of image was able to ensure that the approximate location of the fibre was within an area of interest, but a precise location was impossible.

5.4.1 Phase II Set-up

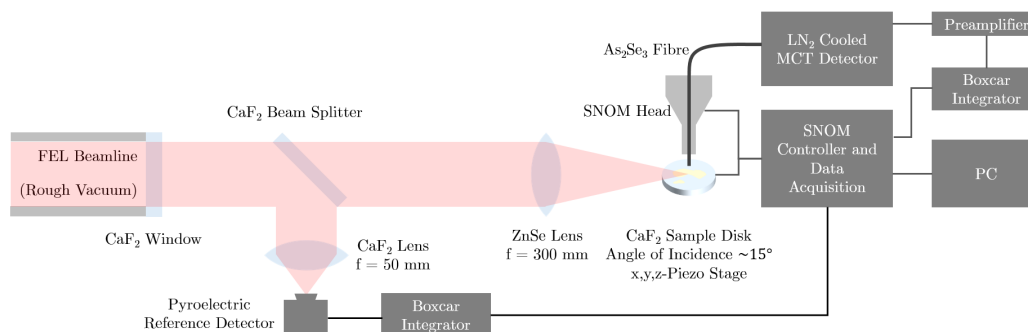


Figure 5.26: Simplified Schematic for phase II of the SNOM imaging. A CaF_2 beam splitter was added to the beam path, which reflected $\sim 5\%$ of the IR-FEL beam to a pyroelectric detector to measure the relative intensity variations of the beam power. The FEL beam was focussed onto the detector element using a 50 mm focal length CaF_2 lens, thus the detector measured the relative intensity of the whole FEL beam. The signal from this detector was processed using another boxcar integrator to give values comparable to the SNOM signal.

A schematic diagram of the phase II set-up is shown in figure 5.26. The addition of a CaF_2 beam splitter to the optical path of the FEL beam after it exited the beam pipe allowed a small portion ($\sim 5\%$) of the beam to be measured by a single element pyroelectric detector, having been focussed onto the element using a 50 mm focal length CaF_2 lens. The voltage signal from this detector was then processed using the same type of boxcar integrator as was used for the SNOM signal, to give an analogue voltage signal. The analogue voltage was then recorded as an additional data channel.

The choice of imaging wavelengths for phase II experiments was again based upon the FTIR data of biological components given in [58, 89], and expanded to five wavelengths:

- $6.00 \mu\text{m}$ was assigned to protein (amide I C=O stretch at around 1670 cm^{-1})
- $6.50 \mu\text{m}$ was assigned to protein (amide II N–H bend / $\text{C}\equiv\text{N}$ stretch at around 1540 cm^{-1})
- $7.30 \mu\text{m}$ was assigned to protein/glycoprotein (CH_3 bend around $1360 - 1390 \text{ cm}^{-1}$)
- $8.05 \mu\text{m}$ was assigned to DNA (PO_2^- stretch between 1200 cm^{-1} and 1250 cm^{-1})
- $8.60 \mu\text{m}$ was assigned to glycogen (CO-O-C asymmetric stretch at around 1160 cm^{-1})

5.4.2 Phase II Development

This phase of SNOM imaging had several advantages over the initial experimental set-up, the main one of which was the recorded variation in the output power of the FEL. The increased knowledge of scan location based upon the camera images was another significant improvement that led to much more successful image collection through choosing areas that were of interest and could be matched up to visible light microscope images after imaging with the SNOM. The size of the image areas was increased to an approximate size of $250 \times 250 \mu\text{m}$ giving a further increase to the chance of obtaining pertinent images. The exact location of the image, as discussed above, was impossible to predict due to the location and geometry of the camera used to approach the tip and look at the sample. Despite much effort to ensure that the appropriate areas of tissue were investigated, the success rate at selecting a scan area that was over the intended target was low. The larger scan areas did, however, allow the SNOM topographic scans to be matched up to standard visible light microscope images (as in figure 5.27d) to aid analysis and to quality test the areas imaged.

Fibres

A further change to the set-up from phase I was the move from etched and gold-coated fibres to cleaved fibres. This was in part necessitated by the larger image area size, but also gave several advantages over the use of etched fibres. The larger scan size required a larger step size on the piezo scan in order to maintain a reasonable time for each scan to be completed (≈ 1 hour), and the etched fibres are extremely fragile. The variations in topography that are measured on tissue samples could easily damage the tip if the piezo is scanned too fast for the feedback to react to a rising edge, damaging not only the tip but also the sample itself. Cleaved fibres are much more robust to crashing, and also give a much more reliable feedback response as the damping force between the tip and sample is much higher as the end of the fibre is larger. The cleaved fibres therefore give more robust and less variable imaging conditions for larger scan sizes.

A further advantage of using cleaved fibres is that the time taken to etch the fibres and coat the tips with gold is significant, whereas the time taken to cleave the fibres can be essentially insignificant compared to the time required to acquire even one SNOM image. The corresponding reduction in lost time between scans where the fibre had to be replaced was a large bonus to the limited time available for experiments. The principal downside to

using cleaved fibres instead of etched tips is the decreased optical resolution that results from having a larger aperture on the fibre. The aperture on etched As_2Se fibres can be as small as $0.1 \mu\text{m}$ [91] while the aperture on the cleaved fibre is at least as large as the core of the fibre, in this case $6 \mu\text{m}$. The true sizes of aperture achieved during SNOM imaging varied significantly, and could only be determined after imaging with the individual fibres and the above figures are only an indicator of typical sizes. The larger aperture will have given an increased resolution size and so allow larger images to be taken. A further advantage of using cleaved fibres was the increase in the quantity of light collected by the cleaved SNOM fibre over the etched tips, improving the signal quality.

Imaging

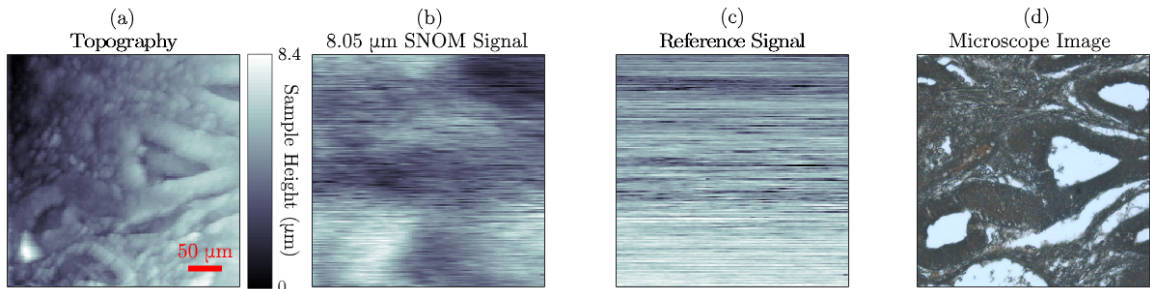


Figure 5.27: An example set of simultaneously acquired images from the second phase of SNOM imaging. Three data channels ($a - c$) were measured, the first two being the same topographic and SNOM signal channels measured in phase I. The third channel was the reference signal given by the pyroelectric detector. (d) The corresponding image area captured using a traditional visible light microscope. These images are $340 \times 340 \mu\text{m}$ with a pixel size of $2 \mu\text{m}$. Although the topographic image shows a clear resemblance of the image area, there is little in the SNOM image that correlates with any feature seen in the microscope images, and the smallest features visible in the image that could correspond to real structures within the sample are no smaller than $10 \mu\text{m}$.

The topographic images for phase II were generally of good quality, and were mostly able to be matched up to optical microscope images after acquisition. There was little, however, in the optical images that could be correlated with any visible features of samples, and the resolution of the images were typically very poor compared to expectations. This is demonstrated in the image series shown in figure 5.27, the topography (a) and corresponding optical microscope image (d) show a very good agreement, but the SNOM signal image (b) has no features that matches with anything in the image area. The SNOM signal should not necessarily correlate with the topography, in fact this could be a sign of imaging problems (see section 5.2.5), but there should be some spatial variations that are linked to the transition

from sample to slide and so be spatially located at such locations. It is not clear why the details seen in the images, such as those here, seem to be impossible to reconcile with the sample area. Further to this difficulty the optical resolution of the image seems to be no better than $10\ \mu\text{m}$ in the images above, certainly due in part to using cleaved fibres with larger apertures, but possibly a result of relatively large variations in FEL intensity that were difficult to normalise reliably.

Normalisation

Efforts at using the reference signal images to correct the SNOM signal images met with mixed success. Often large qualitative correlations were seen between the two images but when attempting a numerical normalisation:

$$I_{normalised} = \frac{I_{SNOM}}{I_0} \quad (5.4)$$

it was found that the variations within the two images were not necessarily proportional to each other and the resulting normalised images were sometimes worse than the un-normalised images. An example of an image set that does not normalise using this method is shown in figure 5.28, the reference signal (b) seems to contain similar stripes of variable FEL power that the SNOM signal (a) is affected by, but applying the pixel-by pixel normalisation (c) does not compensate for them. Even simply normalising by the line-by-line median reference signal value (d) according to

$$I_{normalised}(x, y) = \frac{I_{SNOM}(x, y)}{\text{median}(I_0(x_1, y) \dots I_0(x_n, y))} \quad (5.5)$$

does not improve the image significantly beyond the pixel-based normalisation. By dividing each line of the SNOM signal image by its mean value, ‘line-levelling’ it, the detail in the image is made much clearer (e), but the variation in FEL intensity along the lines themselves is still a major factor in the contrast seen.

The large amount of noise, compared to the small variations in signal arising from the sample chemistry, was highlighted by the addition of the reference signal image. While gross variation across the image area is seen, smaller details are not visible, and little can be correlated with the sample area given by the topography. It was impossible to obtain a reliable or usable signal that could be used to investigate the tissues themselves without

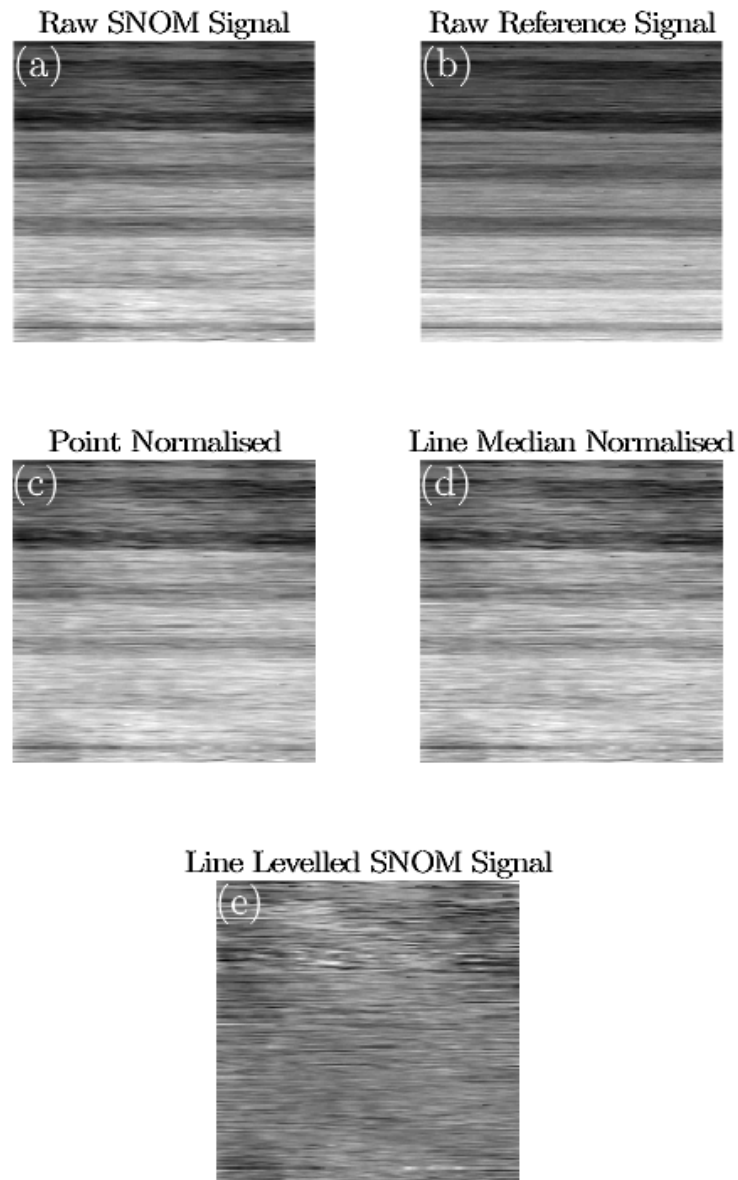


Figure 5.28: An example SNOM signal (a) and reference signal (b) pair of images showing a large amount of noise associated with a long time scale variation of FEL intensity between two different lasing states. Neither point-to-point (c) nor line-median based normalisations (d) significantly improve the image. Only by dividing each line of the SNOM signal image by its median value (e) can the stripes be removed, though this does not account for FEL intensity variations along each line.

reducing the general noise level in the images. Possibly the largest source of noise within most of the images obtained in phase II was the variation in the output of the IR-FEL over time. With the complication of unreliable normalisation with respect to the reference signal, the images were mostly found to be too noisy to allow reliable conclusions to be drawn from them.

A potential secondary effect that could contribute to the normalisation difficulties was the variable wavelength output of the FEL. Over the course of the long SNOM scans the FEL cavity length can vary due to shifts in beam energy and cavity length, both of which affect the energy taken from the beam in the FEL undulator and thus the wavelength of radiation produced. The variation in wavelength during each SNOM scan was not known during phase II, only the starting wavelength, so the SNOM signal data could not be relied upon. Because of this unreliability, measures had to be put in place to monitor and record the spectrum of the FEL over time. This problem was compounded by the difficulty in locating a suitable image area and identifying the location of the scan within the sample tissue afterwards. The outcome of the phase II experiments was therefore the necessity for further development of both the accelerator as a source and the SNOM set-up in order to minimise these effects.

5.5 Phase III SNOM: Inverted Microscope

Phase III of the SNOM work represented a significant change in the general set-up as well as a shift in the approach taken towards SNOM imaging. The SNOM was adapted to be mounted on an inverted optical microscope to facilitate accurate placement of scan areas and understanding of imaging conditions. An inverted microscope illuminates a sample from above and places the focussing optics underneath the specimen, which allows the SNOM head to be mounted in a headstock above the sample whilst maintaining the ability to observe the sample itself from underneath. Given that the small thickness and semi-transparency of the samples mean that the top surface is visible from the underside, this approach enabled the scan areas to be positioned and imaged to a much more accurate degree than achieved previously and the fibre and sample could also be monitored for any damage.

The addition of the microscope optics underneath the sample necessitated the use of a piezo stage with a clear optical path to the underside of the sample. A Piezosystem Jena

PXY AP 500 μm two-axis x,y piezoelectric actuator was used for this reason, and the z -piezo had to be moved to the headstock, where the head of the SNOM was now moved in z (height) and the sample scanned in the x,y plane. The new x,y stage allowed for much larger image sizes to be taken if required, as well as more flexibility in positioning the SNOM scan origin. Longer fibres from CorActive with full protective jackets described in section 5.1.2 were used in phase III due to the increased distance from the SNOM head to the MCT detector.

The FEL beamline included a beam splitter, earlier in the line than the SNOM itself, which diverted another $\sim 5\%$ of the FEL beam to a spectrometer for diagnostic purposes. The spectrometer used a diffraction grating and single element pyroelectric detector to ascertain the peak wavelength of the FEL output. The diffraction grating produces an angular separation as a function of wavelength, $\theta(\lambda)$ according to:

$$\theta(\lambda) = \sin^{-1} \left(\frac{\lambda}{d} \right) \quad (5.6)$$

where d is the grid separation of the grating. Rather than moving the detector relative to the grating, the grating was rotated to vary the wavelength incident on the detector. With the addition of a multi-element pyroelectric array the spectral distribution could be measured instead, essentially converting $\theta(\lambda)$ into $x(\lambda)$ using the known distance to the detector array, and the spectrum of the IR-FEL was monitored over time. This gave a large advantage over the previous phase of experiments where the lack of knowledge of the wavelength during the scan meant that little could be made of the data from longer time scale images, and the SNOM scanning could be paused and the accelerator parameters adjusted if sufficient deviation was measured. The spectrum was also integrated to give another measure of the FEL power, but had the same limitations of the reference signal in that it was not representative of the signal collected by the fibre, with the addition of the fact that the detector was not accurately calibrated and significantly removed spatially, and in terms of optical components, from the beam at the SNOM.

5.5.1 Phase III Set-up

As a result of the studies of the beam images reported above, the apparatus was modified during phase III. The schematic diagram shown in figure 5.29 for phase III, after the beam

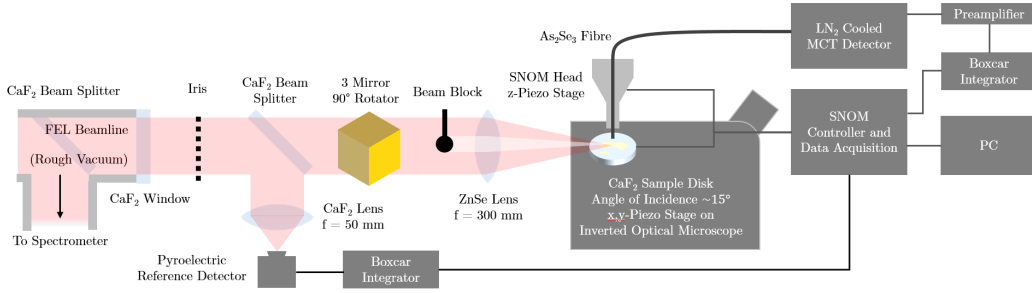


Figure 5.29: Schematic for phase III of the SNOM experiments. Significant changes were implemented between phases II and III, the biggest of which was the change to an inverted microscope with a rearrangement of the piezoelectric drives to allow a clear optical path through the sample for the microscope objective. To mitigate the effect of the structure in the beam measured in section 5.2.1 the beam was rotated using a three mirror rotator, and a beam block had to be installed in the center of the beam after the lens to remove the second order FEL light that was more concentrated there. Data was acquired on a multi-element pyroelectric detector in the spectrometer to monitor the wavelength during the SNOM images, with another CaF_2 beam splitter was used in the evacuated section of the FEL beamline to separate a small portion of the FEL beam to the spectrometer. To modulate the observed intensity of the FEL beam under the SNOM aperture, an iris was used that allowed the SNOM signal value to be set to approximate standardised values.

imaging results led to the introduction of a three mirror beam rotator, is very similar to that seen for phase II with the addition of the rotator and the spectrometer beam splitter. The beam splitter for the spectrometer was within the evacuated FEL beamline, and steered 5% of the FEL beam to the spectrometer through a separate CaF_2 window (not included in the schematic) to provide a record of the FEL wavelength and a secondary, more approximate) measure of the intensity both in total and at the desired wavelength, as well as providing continuous information on the FEL wavelength during each SNOM scan.

To rotate the ALICE IR-FEL beam, three Au mirrors were arranged to reflect in three orthogonal directions, which produces the end effect of rotating the beam by 90° clockwise as demonstrated in figure 5.12. This rotation is achieved by mapping the axes $(x, y, z) \rightarrow (-y, x, z)$ through the three reflections: $(x, y, z) \rightarrow (x, -z, y) \rightarrow (-y, -z, -x) \rightarrow (-y, x, z)$. The assembly of these mirrors was included in the beam path for the SNOM, which meant that the PLIA had to be increased to 850 mm to accommodate it, and thus the level of absorption due to water vapour along this path was increased.

To provide an element of standardisation for the SNOM signal values an iris was used to modulate the amount of FEL light reaching the SNOM aperture. While this will have contributed a small diffractive effect to the beam it was sometimes necessary to prevent the detectors from saturating.

Given the successes of applying the MA developed in section 4.6, the experiments in phase III aimed to extend its application to the SNOM. As in FTIR-HSI, many variables that are spatially dependent in SNOM images should cancel or reduce when taking ratios of images acquired in the same scan area. The type of metrics, as for the HSI data, was therefore taken to be ratios of the pixel intensity recorded by the SNOM at two different wavelengths.

The Butterfly Diagram (see section 4.6.3) for the FEL tunable range was calculated for the comparisons between the four basic tissue classifications from the FTIR-HSI data, and a set of wavelengths chosen to give a useful number of sufficiently reliable metrics, with the assumption that these would continue to be good metrics for the different imaging conditions of SNOM. Additional selection criteria were placed upon the wavelengths: they needed to be more separated in wavelength than the FEL bandwidth of $\sim 0.1 \mu\text{m}$; if possible they had to coincide with accepted biomarker signatures; the wavelengths also had to lie within the passband of the new fibres, which had a sharp cut-off at $8.5 \mu\text{m}$ but were able to transmit much shorter wavelengths than the FEL could produce. These criteria resulted in the previous wavelengths of 6.00 , 6.50 , 7.30 and $8.05 \mu\text{m}$ being retained and $8.60 \mu\text{m}$ being excluded, while $6.25 \mu\text{m}$ was added to provide a number of ratios with other wavelengths. Using the whole of the labelled FTIR-HSI images in figure 4.2 to produce a set of six butterfly diagrams allowed figure 5.30 to be generated by taking the maximum value for each wavelength pair across the six butterfly diagrams, to show the general ability of each wavelength pair to discriminate between the tissues. In this figure, the brightness of the pixel (k_1, k_2) represents the success of the ratio k_1/k_2 to distinguish between the four different tissues in the simplified model employed here. The wavelengths selected based upon the criteria above are shown on the axes. While a better set of wavelengths could be chosen, the set that was used still provides a sufficient number of good comparisons while also giving individual images that can be related to the biological components as before.

5.5.2 Phase III Development

With the insertion of the beam rotation assembly the problem presented by the structure seen in the beam was circumvented to some extent, but still required a more robust solution. Adding an extra three mirrors into the beam path not only increased the PLIA, lowering the achievable signal and increasing spectral artefacts from water absorption, but also increased

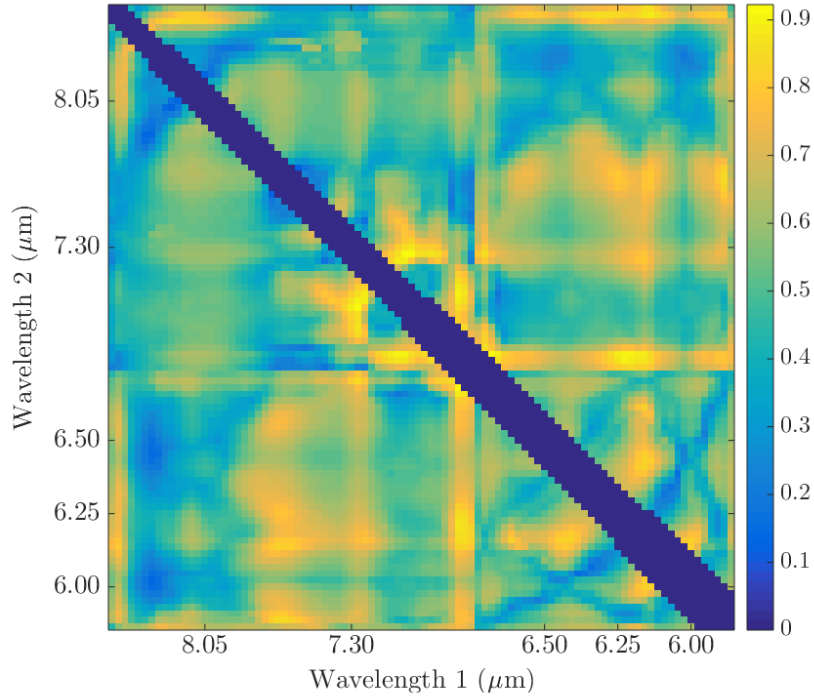


Figure 5.30: The map of tissue differentiation ability for wavelength pairs within the spectral window given by the FEL and the CorActive fibres. Using the labelled FTIR-HSI data in figure 4.2 the set of 6 butterfly diagrams were calculated using the whole of the data as a training set, to give the most reliable set of data possible. This map was produced by taking the maximum value for each wavelength pair across the six images. A central band of comparisons were excluded by being too similar to distinguish easily using the FEL due to its bandwidth of $\sim 0.1 \mu\text{m}$. The set of wavelengths that were adapted from the previous phases are labelled on the axes, showing many possible comparisons. Better comparison pairs exist, but would not be as usable as individual images.

the difficulty in aligning the SNOM aperture and the sample to the FEL beam. Concerns over the observed beam structure and that the potential motion of the beam could still have led to topography-based intensity variations necessitated a return to the phase II set-up for the majority of the available experimental time. This kept the aperture at a fixed position in the beam, and so would pose less of a potential problem.

Wavelength Monitoring

The spectroscopic data recorded using the multi-element pyroelectric detector monitoring the wavelength proved difficult to use. The SNOM does not necessarily measure every FEL 10 Hz macropulse, whereas the data measured by the spectrometer records continuously. The two sources of data were acquired independently, so with little ability to reconcile them the best that could be made of the spectrometer data was in ensuring that the wavelength

was approximately constant during each scan.

The FEL beam, as mentioned in section 5.1.1 is not strictly monochromatic, with a Gaussian distribution with FWHM dependent on many factors, including wavelength, but $\Delta\lambda \leq 0.1 \mu\text{m}$ was routinely attained. The wavelength of the FEL was identified as the mean wavelength of a Gaussian fit to the data measured by the spectrometer, and the maximum permissible deviation from the target wavelength was half of the fitted FWHM.

Area Identification

The aim at the onset of phase III was to have a more guided approach to the location of scan areas. The inverted microscope was a more appropriate tool with which to do this compared to the low magnification approach camera used for phases I and II. By developing a standard approach to identifying and positioning an area of interest on the samples the difficulties associated with the first two imaging phases were minimised and some success was had in placing the scan area in its intended location. The areas of interest were identified initially by examining the samples prior to the removal of the wax from the sample using another inverted microscope. This task was easily done in parallel with the SNOM imaging of a different sample, optimising the use of the available accelerator beam time. The same areas of the samples were also examined after removing the wax, as much more detail could be seen with the wax removed, whilst the sample was air-drying. Having identified the areas of interest, the first SNOM scans on the samples were performed without collecting the FEL light, and so could be done without synchronising to the 10 Hz repetition rate of ALICE and instead scan at a much faster rate and acquire large topographic images which were matched up to the microscope images of the samples acquired earlier. Areas were selected that possessed easily recognised topographic features, such as holes or islands that have an easily recognised shape and are of an appropriate size to be seen easily in the topographic images. This strategy allowed the interesting and appropriate areas of tissue to be found with the SNOM at a much higher success rate than previously, but at the expense of the lost experimental time while positioning the topographic images.

Signal Strength

The effect of both long and short time scale variations in the FEL power was still a significant issue with the images obtained during phase III. The differences between the

mean FTIR-derived absorbance values of the tissue components at $8.05 \mu\text{m}$ (1245 cm^{-1}) are on the order of 40 – 50% of the average absorbance at that wavelength. Assuming that the SNOM signal contrast variations were on the same order of magnitude, which is not necessarily the case but gives a usable approximation, then it is required that the noise level from other sources be below this level to get a signal to noise ratio of more than 1. The typical noise level arising from variations in the FEL intensity that was regularly achieved during this phase was 5% using the root mean square variation of the FEL power measured at the outcoupling hole of the FEL cavity. This value was dependent on many accelerator properties such as the undulator gap and cavity length and also with the time of day at which the images were taken, seemingly from variations in ambient temperature. Using this as a baseline, the contrast seen in the SNOM images should be easily distinguished from the noise associated with the FEL intensity, but within a single tissue type the expected typical signal variation at a fixed wavelength, based upon the FTIR-HSI spectra, is between 20 and 30%, while the shot-to-shot noise of the FEL was typically much larger than the 5% RMS noise level measured. Therefore the need for a reliable way of removing the FEL noise was evident. However, normalisation of pixel-to-pixel variation using the reference signal was unsuccessful in removing the majority of the noise in the image, though it did lessen it to a small extent.

Filtering the images using a FT based filter (see section 3.4.4) gave a much better noise reduction for the ‘streakiness’ seen in the images, represented as a broadband, mainly high spatial frequency, vertical band in the FT images. The danger of doing so was that information was lost from the image. To minimise the relevant information that was lost, the filter was limited to the minimal standard filter shown in section 3.4.4.

Phase III Example Images

A set of images acquired by the SNOM during phase III on a sample of OAC tissue at a wavelength of $8.05 \mu\text{m}$ is shown in figure 5.31. The scan area measured $140 \times 140 \mu\text{m}$ with $1 \times 1 \mu\text{m}$ pixel size. To give context to the information seen in the SNOM images, the optical microscope image of the corresponding scan area is included. The matching process for this was entirely manual, with only an approximate area known from images taken while approaching the tip to the sample. As discussed above the inverted microscope was only partially used due to concerns about the beam orientation and structure, thus these images

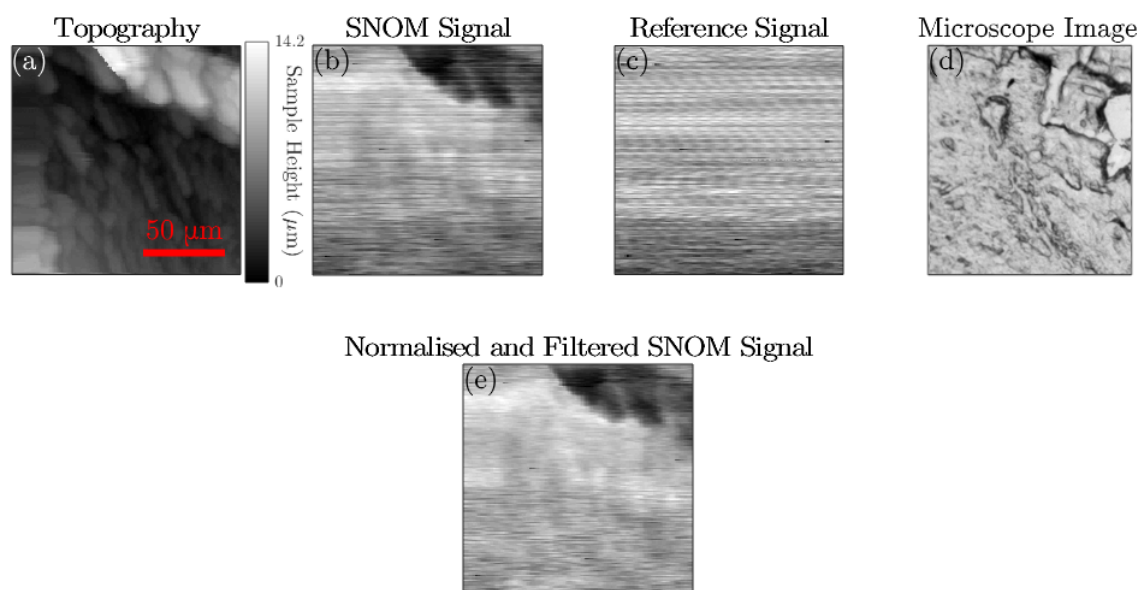


Figure 5.31: (a-c) An example set of images acquired by the SNOM in phase III. These images were taken on a cancerous sample using a cleaved fibre and measure $140 \times 140 \mu\text{m}$ with $1 \times 1 \mu\text{m}$ pixel size. The optical microscope image (d) is of the corresponding scan area, and (e) is the processed SNOM signal image that has been subjected to a line-by-line median normalisation and FFT filtering to remove as much of the noise from the image as possible. The clear feature in the top right of the topography (a) and SNOM signal (b) images is likely to be an artefact of the imaging conditions. In the top right of the optical microscope image (d) there is a small hole in the sample with large flaps of the tissue attached loosely to the edges. This will have resulted in a strong topographic response and a corresponding optical variation that is independent of the tissue under the aperture. More relevant and reliable detail can be seen away from this feature, with a stripe of rougher-looking stroma tissue in the optical image giving a corresponding band of contrast up the center of the SNOM signal image.

were acquired using the phase II instrument on the phase III beamline.

The reference signal image shows that the FEL beam reaching the SNOM end station was affected by a periodic modulation in intensity, evidenced by the obvious vertical stripes in the image. It is unclear, therefore, why this periodic variation is not seen in the SNOM signal. Attempting a point-by-point normalisation of the SNOM signal by the reference signal simply introduces this oscillation as additional noise without reducing the impact of slower variations in FEL power, so to process the image the processed SNOM signal image was subjected to a line-by-line median normalisation and subsequent FFT filtering to remove as much of the noise from the image as possible.

The SNOM signal image is dominated by a clear feature in its top right which is likely to be a topographic artefact. In the top right of the optical microscope image a small hole in the sample can be seen which has large flaps of the tissue attached loosely to the edges. This

will have resulted in a strong topographic response and a corresponding optical variation that is independent of the tissue at the aperture. Away from this feature there is a good level of reliable contrast which can be associated with different regions of tissue in the optical image. A stripe of rougher-looking stroma tissue in the optical image corresponds to a band of detailed contrast up the center of the SNOM signal image, which can be associated with the cancerous stroma regions showing much more variability in their composition compared with the regions of cancerous stroma.

Despite obtaining some useful images, it became clear during phase III that the best way to further improve the imaging results from the SNOM on ALICE required an upgrade to the ALICE IR-FEL beamline to reduce the impact of the structure in the beam and increase the intensity that was transported to the SNOM end station, thereby reducing the impact of noise. The crucial factor that was limiting the beam transport was the overfilled toroidal mirror. By replacing this mirror with a larger one, increasing its aperture and so reducing the overfilling of the mirror, there would be a corresponding reduction in the beam structure and also an increase in the amount of the beam transported on down the beamline.

5.6 Phase IV SNOM: Accelerator Development and Transmission Path

Following the beam imaging results in section 5.2.1, the ALICE IR-FEL beamline was upgraded to replace the overfilled mirror that was identified as the principal source of the structure [79] with a larger one. The SNOM end station was also modified to allow the imaging mode to be changed easily between transmission and reflection using a translatable mirror. The new optical path was also arranged to incorporate the three mirror beam rotator that was added in phase III into the main beam delivery mirror geometry, thus minimising the PLIA. To establish the improvement to the quality of the FEL beam in terms of structure, the beam was imaged again using the PyroCamIII as before. The focussed and defocussed beam was investigated as before and the change in structure assessed, discussed in section 5.2.1 above.

Despite the structure in the beam not being eliminated entirely, it was reduced by the beamline upgrades, and by incorporating the three-mirror rotation geometry into the standard beam delivery pathway at the SNOM end station the variation of the SNOM signal due

to motion in the beam focus was reduced to a minimum. To eliminate the variation entirely would require a different piezoelectric driver configuration, returning to the previously used x, y, z stage at the sample but with the clear vertical pathway. This was outside of the possibilities achievable during this work.

In order to improve the flexibility of the SNOM experiments a path for transmission SNOM, as shown in figure 5.32, was added. In this orientation the vertical movement of the SNOM aperture in the beam was eliminated as a significant source of contrast since any z -motion would then be aligned with the propagation vector of the FEL beam. While there is variation along this direction in the focussed beam, if a long focal length lens (600 mm here) is used then the variation in sample topography by $< 10 \mu\text{m}$ is negligible, and thus should not have a noticeable effect on the local intensity at the SNOM.

The focus of the beam in the transmission mode of operation was no longer spread out over a large area by a large angle of incidence, instead the minimal focus size achieved was approximately $270 \times 350 \mu\text{m}$. This reduction in focal size gives a corresponding increase in the intensity under the SNOM aperture, which in turn gives a significant improvement to the quality of the images obtained in this mode by reducing the effect of the various sources of noise in the system. The increase in intensity at the sample meant that crossed polarisers had to be used to reduce the amount of IR light reaching the surface, setting a standard MCT voltage value and ensuring that the sample did not get damaged.

5.6.1 Phase IV Set-Up

The SNOM set-up was dramatically changed for phase IV with the addition of a transmission pathway and a translatable mirror to select between the two imaging modes, shown in figure 5.32, as well as incorporating the three mirror rotator into the beam path. The exit window of the FEL beamline was moved to a position at the back and above the SNOM table, and one of the three mirrors was inside the evacuated beamline to steer the beam downward, with the other two used to bring the beam forward and to the right to place it back into the same position and direction as in the previous phases. These three reflections provide the 90° rotation of the beam as in figure 5.12 with the first reflection reversed. The PLIA for the reflection imaging mode was comparable to phase III, but for the transmission mode had to be much longer, at almost 1 m, to steer the beam to the underside of the sample. The electronics used for this phase were the same as those used previously, with one

5.6. PHASE IV SNOM: ACCELERATOR DEVELOPMENT AND TRANSMISSION PATH

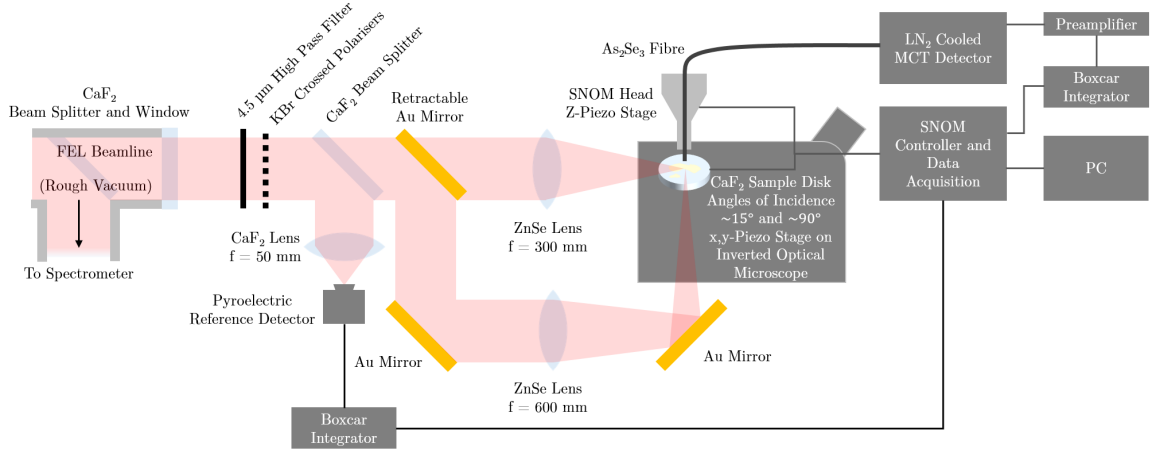


Figure 5.32: Schematic for phase IV of SNOM experiments. The set-up was expanded further to include a second mode of imaging, with the sample illuminated perpendicularly from below and the transmitted light collected by the SNOM, with a second, longer focal length lens. To set the intensity at the SNOM to a safe level, to avoid not only saturating the detectors but also to prevent the samples being damaged, crossed polarisers were used. A high pass filter with a cut-off at $4.5 \mu\text{m}$ removed the higher order FEL light much more effectively than the beam block that was utilised in phase III.

addition: a spectrometer synchronisation signal was also recorded by the SNOM controller electronics.

The reason for incorporating another ADC channel to the SNOM data collection was to reconcile the different measures of FEL intensity from the reference detector and the spectrometer. The data measured by the multi-element detector array on the spectrometer in phase III proved difficult to reconcile with the SNOM images, the data collection was entirely independent of the SNOM measurement and it was found that the SNOM occasionally skipped the measurement of a FEL pulse and instead waited for the next one to measure before moving to a new point. Although each FEL pulse was measured by the spectrometer, there was no mechanism by which to match the ones recorded by the SNOM to the correct FEL pulses at the spectrometer. In order to synchronise the two data sources, a National Instruments MyDAQ [92] was used to produce a DC voltage that incremented by a small amount with every FEL pulse and reset after 120 increments. The synchronisation voltage was recorded in both the spectroscopic data, by the spectrometer, and in a fourth data channel of the SNOM imaging software. This allowed the wavelength distribution of the FEL to be matched to each pixel in the SNOM images, and also provided a further means of normalisation for the SNOM signal.

By adding a second imaging mode, an assessment of the optimal number of wavelengths

and the amount of time available to collect the, determined that the number of imaging wavelengths had to be reduced to three, 6.50, 7.30 and 8.05 μm , to acquire sufficient data and still retain the ability to use the MA on the SNOM data.

5.6.2 Discussion of Phase IV

Over the course of the four phases discussed here many of the problems identified in the initial set-up were remedied or mitigated. Many of these were unknown during initial investigations which is often the case when a new methodology is introduced. The parallel development of the ALICE accelerator and SNOM instrument allowed the operating procedures of each to benefit from the development of the other. The beamline mirror upgrade gave a much greater intensity at the SNOM and so improved the image quality dramatically, while also minimising the beam structure. The SNOM electronics was expanded to four collection channels, two of which were collecting reference data to aid in normalisation and understand the accelerator output. Furthermore the inverted microscope allowed the image area to be much more easily identified, though some difficulties were still found due to the use of cleaved fibres.

The reliability of the optical contrast obtained in images during phase IV highlighted other potential problems that needed to be overcome. These issues arose mainly from the samples and fibres used, rather than the ALICE IR-FEL source or optical path, and were therefore difficult or impossible to circumvent, requiring instead that the conditions of the SNOM imaging be considered much more closely and images analysed in a way that the desired information was accessed, while compensating for any undesired effects where possible.

Although the number of imaging wavelengths was reduced for phase IV, the total number of images collected for each scan area was increased from five to six. The ease of adapting between the transmission and reflection imaging modes enabled both to be used successively at each wavelength, doubling the output from each chosen image area. The results obtained from this phase of imaging gave the first truly usable spectral data, allowing not only an investigation of the tissues, but a comparison between the information given by the reflection and transmission images and possible joint analyses. These are discussed in detail in chapter 6.

CHAPTER 6

IR-SNOM IMAGING OF OESOPHAGEAL TISSUE

Contents

6.1	Phases II and III: Sets A and B	143
6.1.1	Image Sets	143
6.1.2	Qualitative Description of Set A and B	146
6.2	Phase IV: Sets C and D	151
6.2.1	Image Sets	153
6.2.2	Tissue labelling of SNOM Image Sets	156
6.2.3	Other Approaches to Analysis	163
6.3	Conclusions to Phases I-IV	165
6.4	Phase V: Further SNOM Development	166
6.4.1	Phase V Image Set	167
6.5	Future Work	171

This chapter presents the results of SNOM imaging with the IR-FEL on the ALICE accelerator. As with the FTIR-HSI imaging analysis, the focus of this work is in the evaluation of the quality of the results obtained and in the analysis techniques applied.

Some of the best sets of images were selected to be analysed, with their quality being judged by the presence of recognisable contrast and higher SNR. Using the information known from the approach cameras and microscope camera, as well as the topographic and SNOM signal images, each set was matched with a corresponding area of a visible light microscope image taken on the same sample after SNOM imaging. This allows the structures seen in the images to be related to the sample morphology and tissue architecture of the scan area to aid analysis and understanding.

6.1 Phases II and III: Sets A and B

As discussed in chapter 5 during phases II and III of SNOM Imaging several obstacles and potential issues with the SNOM experimental setup were discovered and remedied. The images acquired during these phases of imaging are therefore less reliable, in particular with respect to wavelength stability and accuracy. As such, two image sets that showed good optical contrast were selected but only qualitative investigations could be relied upon.

6.1.1 Image Sets

Set A

SNOM set A is a set of images acquired during phase II of SNOM imaging, giving five imaging wavelengths at 6.50, 7.00, 7.30, 8.05 and 8.60 μm on an oesophageal tissue sample with a diagnosis of OAC. The images were taken over a nominal $340 \times 340 \mu\text{m}$ scan area with $2 \times 2 \mu\text{m}$ pixels. Figure 6.1 shows the images that make up set A. The topography image was the image acquired with the 6.50 μm SNOM signal image, and very little variation was observed between this and the other topographies over the course of these scans. The lower half of the figure displays the five SNOM signal images, with the corresponding wavelength of FEL light. The SNOM signal preprocessing was initially limited in these images to a line

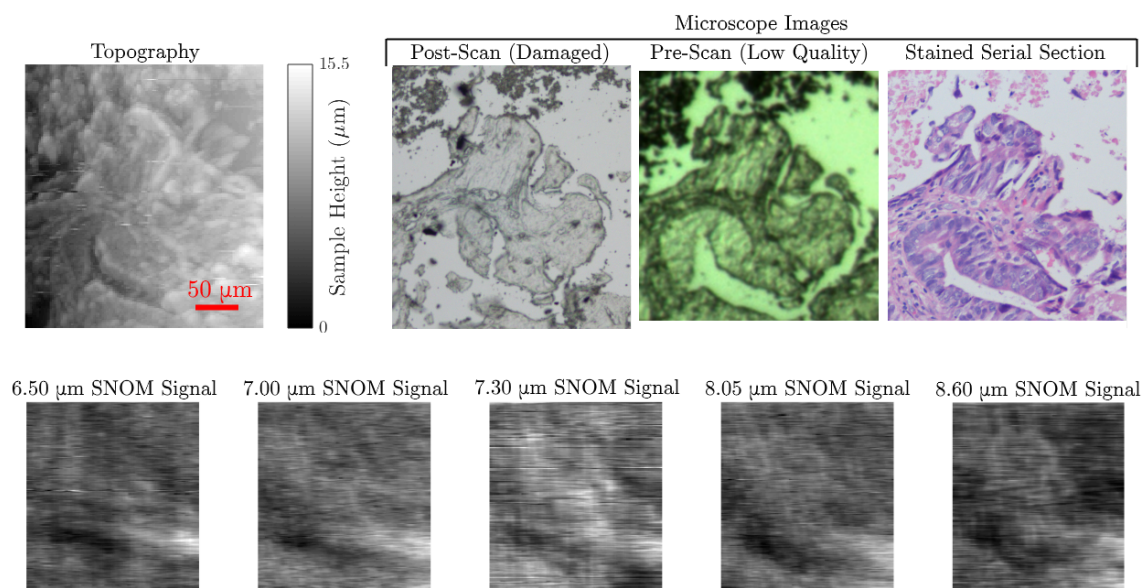


Figure 6.1: SNOM images set A, taken on a cancerous oesophageal tissue sample. The five SNOM signal images acquired of the area shown in the microscope images and topography. These images are $307 \times 275 \mu\text{m}$, (167×151 pixels) after alignment and cropping to a common area.

median normalisation to the reference signal, and for the 6.50 and 7.3 μm images a further line-levelling of the SNOM signal, again by the line median, to remove intensity variations that could not be normalised out. The images were then aligned with each other and cropped to give their common area. Using some of the clear features in the SNOM images it was clear that there was a slight misalignment of the SNOM signal relative to the topography images by an offset of $\begin{pmatrix} x \\ y \end{pmatrix} = \begin{pmatrix} -2 \\ +8 \end{pmatrix}$, and after this correction the final image set was 167×150 pixels. Using the known calibration of the visible light microscope the final area of the combined scans was found to be $307 \times 275 \mu\text{m}$.

Figure 6.1 also shows three microscope images taken with a visible light microscope. The first microscope image is the area after SNOM imaging, showing a large amount of damage due to a tip crash that occurred after these SNOM images were acquired. A low-quality image was acquired of the same sample after dewaxing and before imaging with the SNOM that shows the same image area without the damage. This image allows the scan area to be properly characterised in terms of its tissue structure, especially when used in conjunction with the third microscope image, the same area of a serial section that was stained with H&E stain.

In these microscope images there is a clear demarcation between two different types of tissue within the main area. The pre-scan image shows these as light and dark areas, while the stained image allows a more direct assignment of epithelium and stroma tissues respectively. This assignment comes from the presentation of cancerous epithelium tissue with H&E stain: a large quantity of DNA with poorly defined nuclei and a corresponding relatively uniform dark purple colour, while the cancerous stroma tissue is much paler and has more isolated nuclei in dark purple. There is also a significant amount of debris in the top third of the images, which is of unknown origin.

Set B

SNOM set B was acquired during phase III of SNOM imaging, though, as detailed in section 5.5.2, the inverted microscope SNOM was not used due to concerns over the influence of the structure in the FEL beam profile, meaning that the images in set B are comparable to set A in terms of how they were taken. This image set was processed in the same manner as set A, with line median normalisation relative to the reference signal images applied to each image. No line-levelling of SNOM images was required, as the ALICE IR-FEL stability

was improved for phase III relative to phase II.

After aligning and cropping the images the area could be matched to microscope images and it then became clear that the strong topographic feature in the upper right quadrant of the images was associated with a damaged area of the sample, possibly caused when approaching the fibre to the sample surface prior to imaging. The extreme topography resulted in a prominent topographic artefact in the SNOM signal images which was removed by masking the corner of each image, as shown in figure 6.2, which clarified the contrast seen in the images and removed the suspect data.

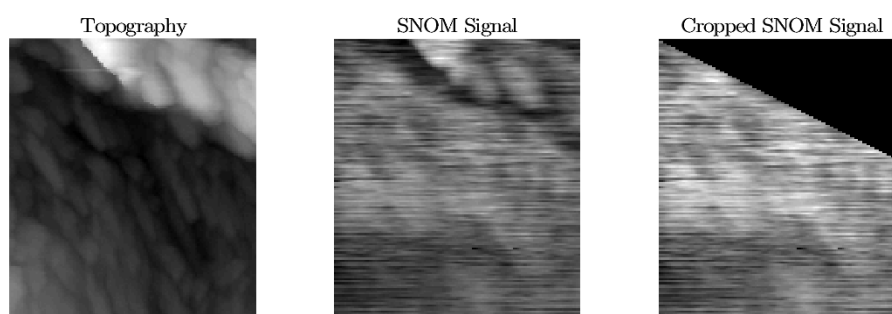


Figure 6.2: The images obtained at $\lambda = 7.30 \mu\text{m}$ as part of set B. The sample topography shows a strong feature in the upper right quadrant of the image which led to a prominent topographic artefact in the images, appearing at $7.30 \mu\text{m}$ as dark bands surrounding normal intensity regions. To remove this artefact a mask was applied to the images after alignment that removed the feature while retaining as much of the reliable image as possible.

The sample that was imaged for set B was a serial section of the same cancerous sample that was imaged in set A, but the scan area was located in a different biopsy specimen within the sample. The images were taken at four IR wavelengths: 6.25 , 6.50 , 7.30 and $8.05 \mu\text{m}$, shown in figure 6.3. The corresponding area of the sample was again imaged post-scan by a visible light microscope but no corresponding area of the stained section for this sample could be identified, as the tissue structure variation with depth was too great and the stained section was somewhat removed from the one imaged with the SNOM. Instead of an exact match, a representative area of the stained section is shown in figure 6.3 with similar tissue structure. Using these images in the same way as for set A the true scan size of $145 \times 128 \mu\text{m}$ with 137×121 pixels was determined.

The sample area shown by the microscope images for set B is much more disordered and less segregated into separate tissue regions than seen for set A. Nevertheless there are some visibly different patches of tissue: smoother regions where there is cancerous epithelial tissue

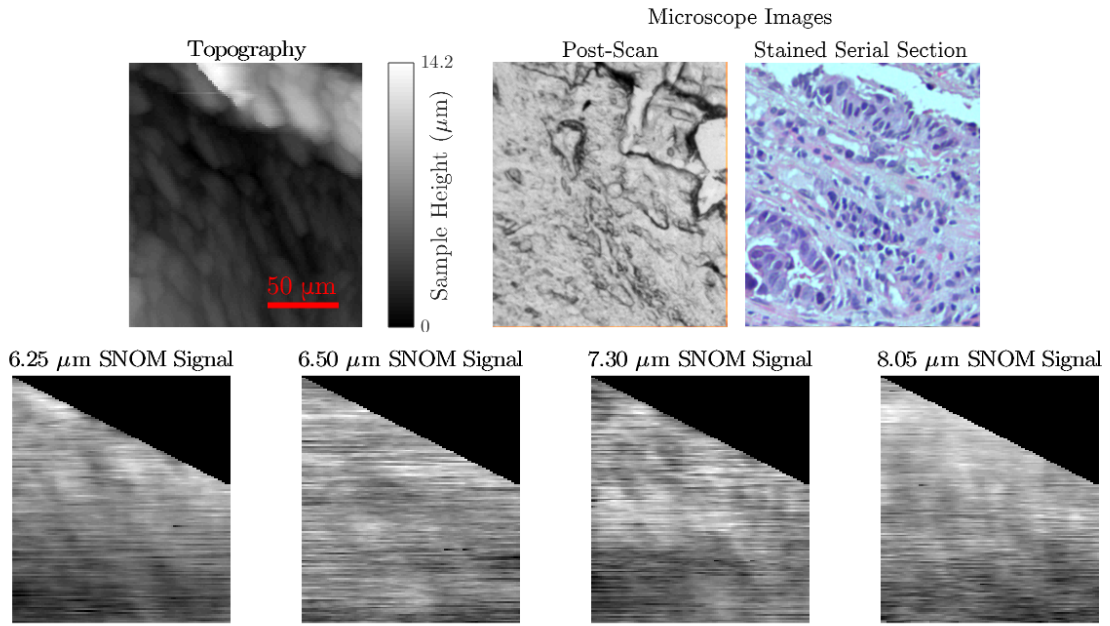


Figure 6.3: SNOM image set B, taken on a cancerous oesophageal tissue sample. The four SNOM signal images acquired of the area shown in the microscope images and topography. These images are $146 \times 128 \mu\text{m}$ (137×121 pixels) after alignment and cropping to a common area. Additionally, a mask was applied to the image area to remove a topographic artefact resulting from the extreme topography observed in the top right of the image area. This can be linked to damage that occurred to this area of the sample when approaching the SNOM fibre. The stained serial section microscope image is not an exact match to the area, which was not possible to obtain, but instead is representative of the tissue structures in the true image area.

and striated, less uniform regions of cancerous stroma tissue, though the boundaries between them are not clear. The damage to the area that resulted in the topographic artefact in the SNOM signal images can be seen in the upper right area of the post-scan microscope image in figure 6.3. The stained tissue section for this biopsy sample was significantly different from the section imaged by the SNOM, and as such a directly corresponding area could not be identified. Instead a representative area of this region of the sample is shown, displaying a similar structure to that seen in the unstained image.

6.1.2 Qualitative Description of Set A and B

The analysis of sets A and B was limited to a qualitative investigation of what consistencies and inconsistencies could be found, and how the response of the SNOM related to the areas of tissue imaged. The principal reason for this restriction was the variable nature of the wavelength of each image, meaning that the data is not as reliable as would ideally be the case for more numerical analysis. In addition to this, it was important to move towards

understanding the signal given by the SNOM in order to determine what effects may need to be remedied or mitigated in later phases, and in future experiments.

Topographic Images

The topographic images for these two sets differ greatly, not only in the type of area imaged, but also in terms of the quality of the image. The topography for set A shows a large amount of detail, and the area was easily matched to a microscope image, despite the damage to the area. Conversely the topography shown for set B suffers from a fairly strong tip artefact and no real detail can be seen in the sample area. The tip artefact results in a long, thin, diagonal shape reproduced across much of the detail in the topography, obscuring any features smaller than the tip. Because of this the scan area could only be identified using the contrast seen in the SNOM images.

The topography image for set A also allows a certain amount of tissue differentiation to be performed, as the areas of cancerous epithelium tissue that can be recognised from the stained microscope images show as much smoother regions of topography, while the cancerous stroma patches give a much rougher and slightly raised topography. Using this as a definitive measure of tissue type is not particularly reliable, but it does aid in recognising sources of contrast within the SNOM signal images.

Slide-Tissue Contrast

The image area for set A contains a large area of slide with a small amount of debris scattered across it. The only SNOM signal image that clearly shows a difference in signal level between the tissue and the slide, other than isolated features in other images, is the image at $8.60\ \mu\text{m}$. Despite this, in all five SNOM signal images in set A the gap in the sample in the lower left quadrant of the image area is consistently dark. There are no large gaps in set B to compare the observable contrast from set A with.

Another structural source of contrast that is also of note is the bright signal associated with the edges and boundaries between tissue regions. This is particularly clear in the 7.00 and $8.60\ \mu\text{m}$ images in set A, and the $6.25\ \mu\text{m}$ image in set B. The contrast could be a result of the discontinuity in the tissue resulting in increased scattering at the surface, but is clearly wavelength-dependent and sensitive to the particular structure of the tissue.

Effect of Different Wavelengths

A comparison of the images obtained at different wavelengths shows a degree of correlation between the signals, where some features of tissue lead to similar features in many of the images. For example the bright stripe in the set A images seen in the lower left corner corresponds to a rough area of tissue in the topography that seems to be a region of muscle tissue based upon the stained image. Importantly, however, the uncorrelated contrast given by varying the wavelength is significant.

The effect of increasing wavelength on the apparent optical resolution in these images is somewhat contrary to expectations. While the diffraction limit on resolution is proportional to wavelength, giving worsening resolution with increasing wavelength, in these images the reverse seems to be the case, with the detail seen in the images taken at longer wavelengths seemingly sharper and on smaller length scales. This is consistent with the expectation that near-field images are not diffraction-limited

General Structures

A few general structures with similar behaviour at certain wavelengths can be noted for each set. The regions of cancerous stroma in set A are brighter than the regions of cancerous epithelium, at wavelengths of 7.00, 7.30 and 8.05 μm in particular. These three wavelengths should provide images related to the distribution of protein and glycoprotein in the case of 7.30 μm and DNA for 8.05 μm while 7.00 μm was chosen as a 'blank' wavelength. The epithelial tissue should contain more nuclear matter than the stroma tissue, as evidenced by the large amount of dark purple seen in the stained section image, which should give stronger signal at 8.05 μm . A certain element of anti-correlation is expected between the DNA and protein, though the higher density of cellular matter in epithelial tissue in general could explain the lower signal seen from the 7.30 μm image. Certainly it is the case that the contrast seen across these images is not simply given by the arrangement of the chemical biomarkers within the sample tissues.

For set B the 'stringy' band of cancerous stroma running diagonally up through the center of the image area from the bottom edge can be distinguished in the four images from the cancerous epithelium regions around it, partially from the bright bands given by the boundary of the tissue as discussed above, but also from the corresponding disordered stripe of contrast in the 7.30 and 8.05 μm images. There is less differentiation between the areas

of stroma and the areas of epithelium in set B. The 6.25 and 6.50 μm images do not contain much contrast, while in the 7.30 and 8.05 μm images the contrast appears very detailed. However, despite being able to identify the band of cancerous stroma tissue in the center of the image there is little else that can be definitively identified in the rest of the image in relation to the scan area identified in the microscope image. There are several reasons why this could be the case. Firstly the scan area was very difficult to accurately match to a microscope image due to the tip artefact in the topographic images discussed above and the topographic artefact in the SNOM signal images that had to be masked out of the SNOM images. It is therefore possible that the area is not matched correctly to the optical microscope images. Secondly the area of the tissue that was imaged, as demonstrated by the stained microscope image in figure 6.3, was highly disordered and more difficult to divide into tissue classifications by eye. Thirdly the artefacts in the image add an additional and unwanted source of contrast to the image, as discussed in section 5.2.5, which could obfuscate the desirable contrast in the images.

Image Ratios for Set A

For phase II of SNOM imaging the 7.00 μm images were taken as a supposed ‘blank’ image that contained no strong biological sources of contrast but would be affected by the other unwanted contrast mechanisms and so could potentially be used to correct for these mechanisms in the other images. The 7.00 μm image in set A does indeed show some detailed contrast, unlike much of the other contrast seen in the images obtained at the other four wavelengths, but shares some similarities with the other images, especially in the effects of the edges and boundaries in the image area.

A rudimentary attempt to remove these effects is shown in figure 6.4 where the intensities of the pixels in each of the images is ratioed against the 7.00 μm image. Taking this approach does not, however, increase the details seen in the images. Dividing by the 7.00 μm image removes most of the contrast that was seen in the original images, and the FEL instability noise from both images in the ratio is carried forward to the resulting image, obscuring the contrast further. Particularly interesting here is that the 8.05 μm image, when divided by the 7.00 μm image, loses almost all of the recognisable information in the image. Due to the lack of success of this cancellation, the 7.00 μm imaging wavelength was dropped from future experiments.

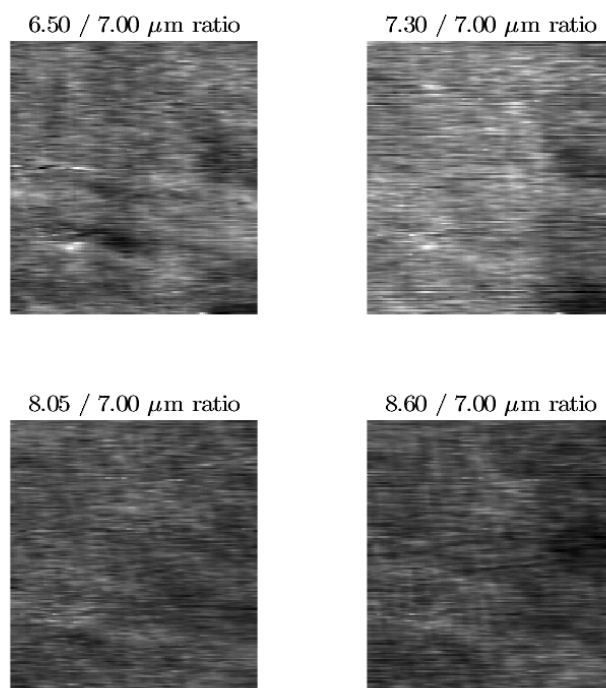


Figure 6.4: Image Ratios from set A against the 7.00 μm image. Taking the ratio of the images does not remove unwanted topographic sources of contrast and highlight the chemical contrast in the images. Instead the noise from both images compounds and obscures nearly all of the visible contrast from each image.

Conclusions from Sets A and B

These image sets highlight several potential issues and effects governing the contrast and information present in the images. Perhaps the strongest finding is the impact that the topographic information can have on the SNOM signal images. The topographic artefact in set B gave a large region of the image area where the contrast was dominated by the variation in tip height, and contained no information about the tissue under the tip. This is an extreme case, but the bright regions seen in set A at edges and boundaries between tissues is possibly an intermediate case of the same effect, where changes to the topography that are independent of the true sample height under the SNOM aperture will have a potentially strong effect on the SNOM signal measured. SNOM's sensitivity to the exponentially decaying evanescent field at the sample surface means that this effect cannot be avoided other than by ensuring that the topography is either very flat and smooth, or is being sensed at the SNOM aperture such that the aperture-sample distance is maintained truly constant.

A further topographic effect lies in the tip artefact also seen in set B, with little clear

topographic features due to a large and elongated tip shape (see section 5.2.5). This meant that, compared with set A, the scan area was very difficult to match with the area of the sample in the microscope images obtained post-scan. The difficulty was partly reduced by transitioning onto the inverted microscope SNOM for phase IV but an accurate topography image allows much more accurate registry to be obtained than would otherwise be possible, and aids in interpreting the images.

The imaging wavelengths that gave the best images in these sets were the longer wavelengths. The FEL power and stability falls dramatically for wavelength above $8.00\ \mu\text{m}$ so the $8.60\ \mu\text{m}$ imaging wavelength was dropped from future experiments. The wavelengths for set B, taken during phase III were identified from the Metric Analysis of FTIR-HSI data to give potential ratios that could be used as metrics in a numerical analysis. Across both sets, the clearest contrast was seen at 7.30 and $8.05\ \mu\text{m}$ so these wavelengths were retained for phase IV. Although the $6.50\ \mu\text{m}$ images are less clear, the correspondence to the Amide II band and therefore its potential use for protein labelling, was deemed important so it too was retained.

In terms of understanding the signal that each tissue component produces at these wavelengths, image sets A and B do not provide much information. In set A the areas of cancerous epithelium do seem to give a lower SNOM signal than the cancerous stroma, but this could also be due to the smoother topography at those locations, while in set B the contrast is difficult to link to the tissue structure due to the difficulty in matching the area up and the disordered nature of the sample area in terms of tissue distinction.

From these conclusions it was clear that further imaging needed to be performed to gain insight into the best way to image these samples with SNOM as well as characterise the behaviour of the sample.

6.2 Phase IV: Sets C and D

Phase IV of SNOM imaging added a second imaging mode to the SNOM instrumental set-up that enabled transmission images to be obtained as well as reflection. Each sample area was imaged at three wavelengths in both reflection and transmission modes, giving six images per set. The combination of forward- and backward-directed imaging gave two such sets per sample area that, despite correcting for the piezo-drive asymmetry, could not be

combined due to differences in pixel spacing and registry. Each of the images was subjected to the full preprocessing described in 3.4 to produce self-consistent, aligned and noise-reduced sets of images. The aim was to attempt to apply a MA, described in section 4.6, to each set in order to assess its application to SNOM images and further develop the understanding of the instrument and the samples. Two image sets are considered here, one from a cancerous OAC sample and one from a benign Barrett's oesophagus sample.

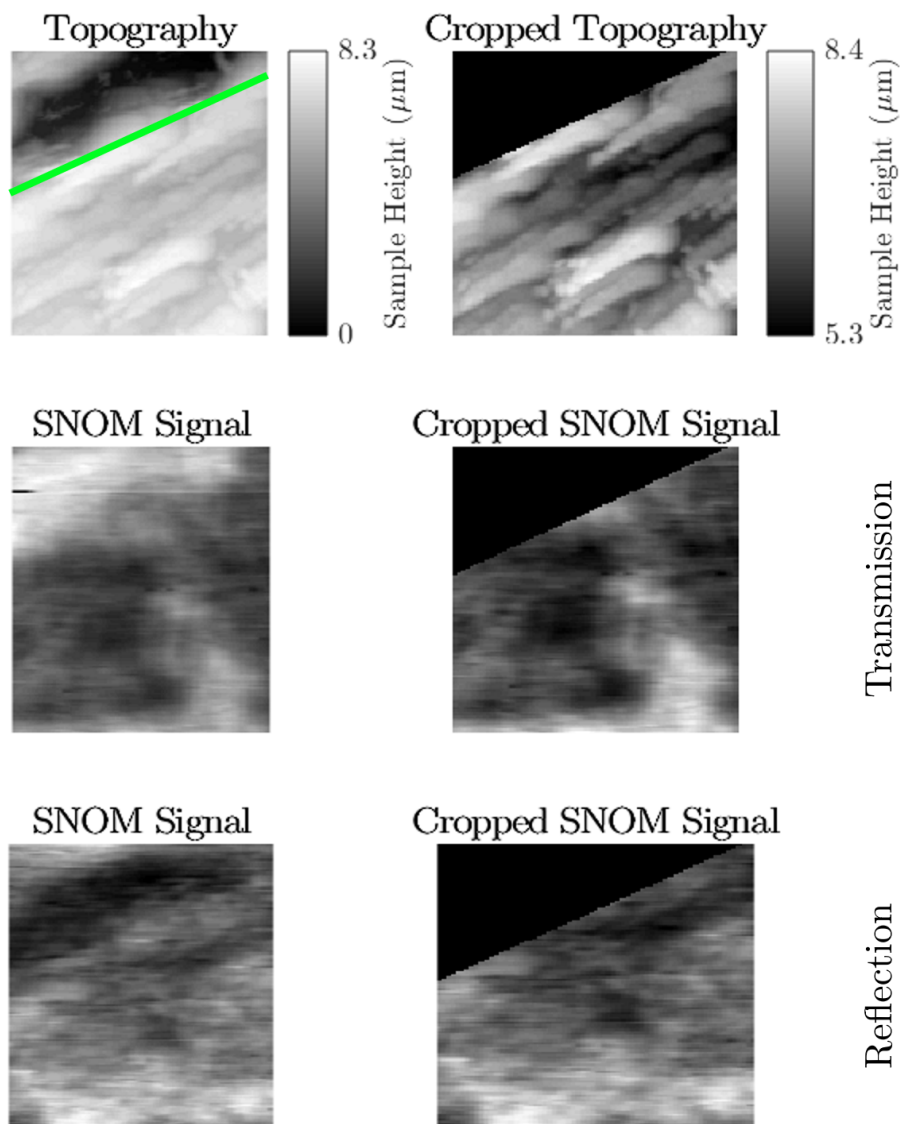


Figure 6.5: The mask applied to the forward-directed set C images in reflection and transmission in order to remove the topographic artefact that was a result of the significant offset between the SNOM signal and topography images. The green line indicates the line above which the data was discarded. Note that the mask applied to the reflection and transmission images was slightly different due to the drift in the sample between the two sets of data, and that the backward-directed images also had a slightly different mask due to the spatial offset between the two directions.

6.2.1 Image Sets

Images forming set C were taken on a sample of OAC tissue in a nominally $250 \times 250 \mu\text{m}$ area. The topographic and optical signals in these images were significantly offset, an effect that can arise easily when using cleaved fibres as described in section 5.2.5. The resulting difference between the two areas led to a significant topographic artefact, similar to that seen in set B above, which had to be removed from the image by removing the upper left corner of the image with a mask, shown in figure 6.5.

The set C images, after preprocessing and matching to a microscope image area are shown in figure 6.6. The final size of the images was found to be approximately $230 \times 210 \mu\text{m}$ based upon the size of the matched microscope image area, giving a pixel size of $1.7 \mu\text{m}$, though the sizes of the images for reflection and transmission, as well as the forward- and backward-directed scans were all slightly different from each other. As with set B the matching of this area was difficult as the topography could not be used due to significant tip and topographic artefacts, but the SNOM images show many details that can be used to match up the images, though this is less accurate than using a clear topography image. In these images a band of cancerous epithelial tissue can be seen on the right side of the area, showing as bright in the $6.50 \mu\text{m}$ reflection image, and dark in the $8.05 \mu\text{m}$ reflection image. The transmission images, as expected, do not seem to give as high a resolution, showing much more diffuse and general regions of signal, and seeming to have less contrast that can be directly related to the sample morphology. The same trend in resolution as observed in sets A and B can be seen in both imaging modes: the longer wavelengths generally give sharper detail in the SNOM signal images.

Image set D was taken on a benign Barrett's oesophagus sample over a nominal $250 \times 250 \mu\text{m}$ scan area, as for set C. This image set was also found to have a large offset between the topography and SNOM signal image acquisition locations, though the absence of extreme variations in topography like those seen for sets C and B meant that there was no strong topographic artefact in the images. The backward-directed set of images of set D, was found to be the better of the two directions, and are shown in figure 6.7. The final matched sample area size was found to be smaller than that for set C, due to a different location on the piezo-drive response curves, and was $152 \times 149 \mu\text{m}$ with a pixel spacing of $1.4 \mu\text{m}$. The resolution of the transmission images appears to be better than seen for set C, while the reflection images show a much more uniform signal level over the majority of the image area.

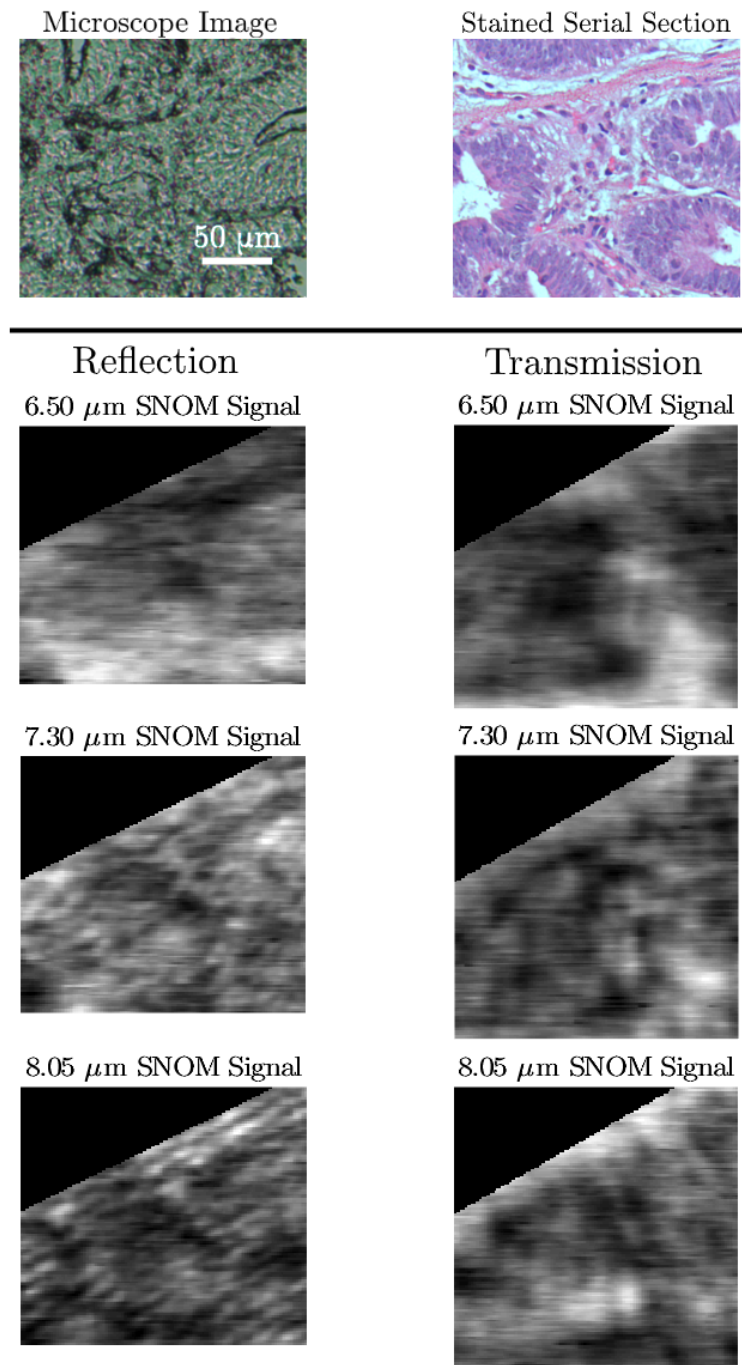


Figure 6.6: The forward-directed images comprising set C. These were taken in both reflection and transmission modes giving six images in total in each scan direction. The final image size was determined to be $230 \times 207 \mu\text{m}$ with a pixel spacing of $1.7 \mu\text{m}$. The reflection images show crisp, clear contrast much of which can be linked to features visible in the microscope image, whereas the transmission images have poorer resolution, as expected, and have fewer details that are directly comparable to the microscope images. The stained serial section is a representative image of the same rough area of tissue, but the difference between the section imaged and the stained section of the same tissue biopsy sample was too great to give an area showing the same structure.

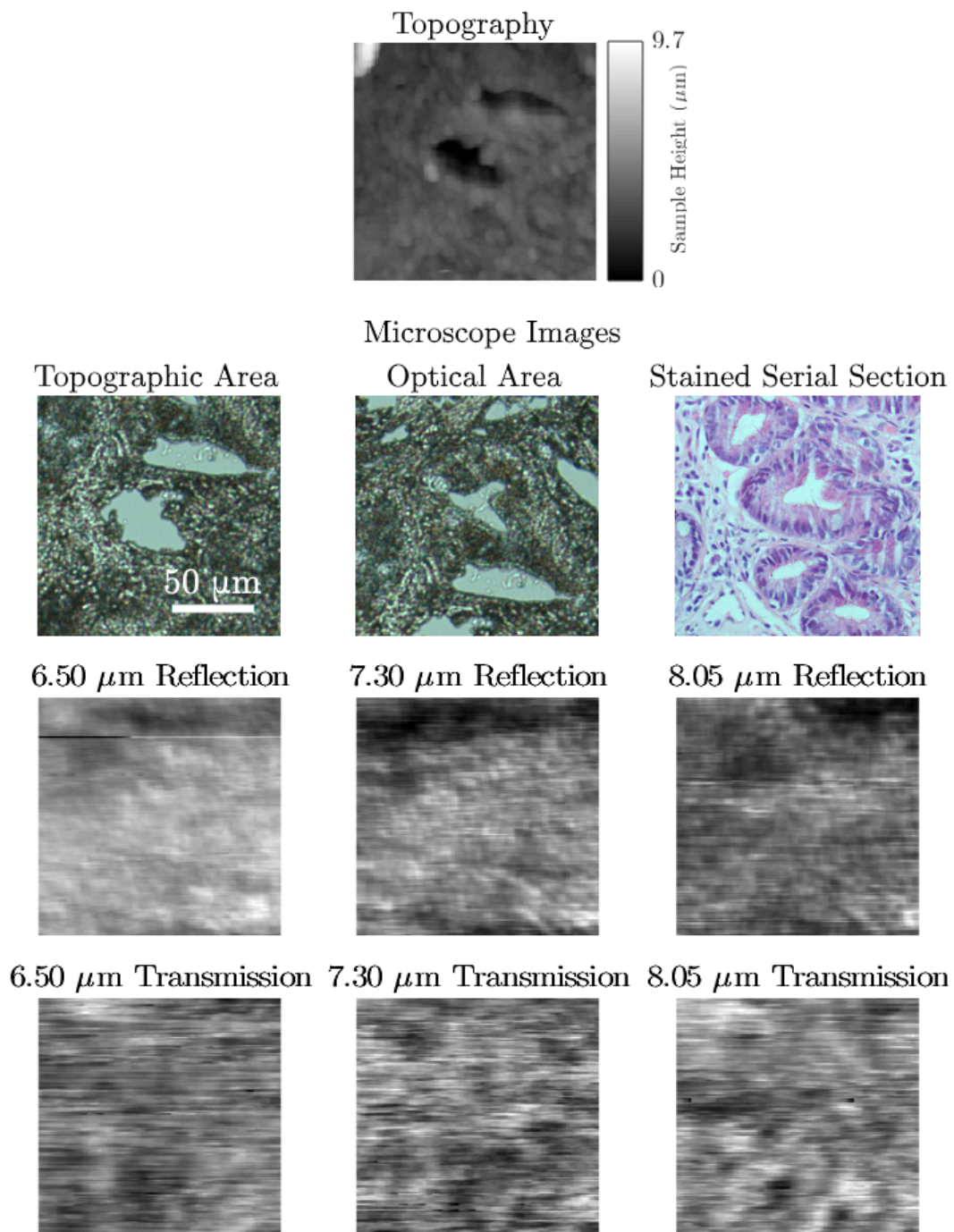


Figure 6.7: The backward-directed images comprising set D. As with set C six images were acquired in each scan direction, three in reflection and three in transmission imaging modes. The final image size was determined to be $152 \times 149 \mu\text{m}$ with a pixel spacing of $1.4 \mu\text{m}$. The topographic offset is demonstrated by the two microscope images of the imaged sample areas corresponding to the topography and SNOM signal. The stained serial section image is again a representative area of the stained section, rather than an exact match. The tissue structure in this sample can be mostly deduced from the opacity and layout seen in the microscope images, rather than using the stained image.

Given the more differentiated nature of a general Barrett's oesophagus sample presentation this is surprising. The stained section microscope image in figure 6.7 shows a representative

example of how the DNA in particular is structured into concentrated rings in the cross-section of the crypts characteristic of Barrett's oesophagus, yet the 8.05 μm images do not show such rings.

6.2.2 Tissue labelling of SNOM Image Sets

As described in section 4.6 it would be useful to relate the images obtained by the SNOM to the considerable body of work that exists pertaining to FTIR-HSI. In order to pursue this, the same MA that was developed using the FTIR-HSI was applied to each of these SNOM image sets. By aligning the images in each set to a common area, giving pixel registry between the different wavelengths, a similar data structure is produced to the FTIR-HSI data, essentially giving a three-point spectrum at each pixel. By doing this, the MA can be applied to the SNOM image sets in exactly the same way as was previously done for the FTIR-HSI results in section 4.6. The advantage of using MA on the SNOM images is that it is able to determine the best way to differentiate between the two tissue classifications based upon any sort of correlated behaviour within the training set. Following the same procedure for the analysis of the FTIR-HSI data, a training set was selected using a small portion of the image area of known tissue type, and the whole image was then labelled as the two tissue classifications that were modelled in each case using the MA. In both sets, only two tissue classifications were used, one corresponding to the epithelial tissue and one to the stroma tissue, giving the same rudimentary description of the samples found to be adequate in the previous MA applications.

Set C

The areas of set C used to train the MA is shown in figure 6.8, with the red coloured region used to train for cancerous epithelium and the yellow area for cancerous stroma. The two areas were chosen as reliable regions of tissue based on the microscope image and sufficiently separated from each other and gaps in the sample to be as reliable as possible. The metrics used were ratios of the pixel values at the different wavelengths, so using reflection or transmission images as individual sets themselves will only provide three possible metrics (and their reciprocals): 8.05/7.30, 8.05/6.50 and 7.30/8.05. However, if both reflection and transmission images are considered together as a single group of data then many more possibilities arise, with ratios taken between reflection and transmission giving access to

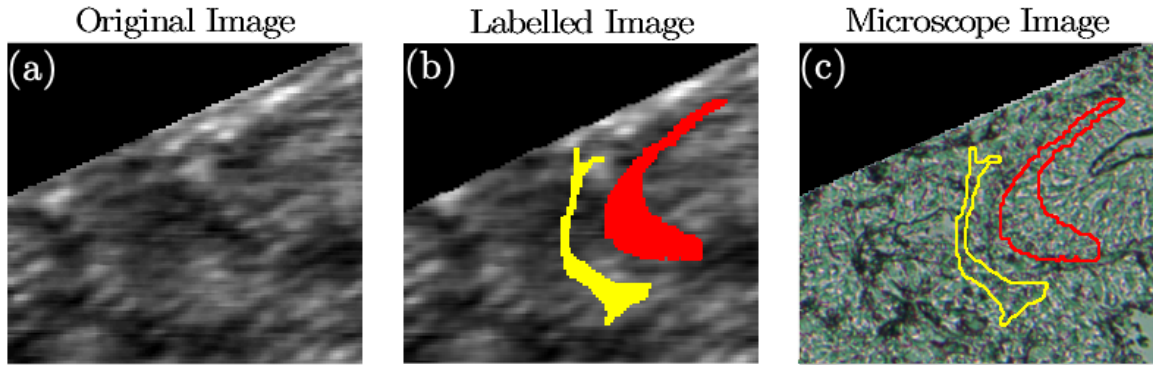


Figure 6.8: (a) An image from set C used to label the training set for set C, indicated by the red (cancerous epithelium) and yellow (cancerous stroma) coloured regions in the labelled image (b). Based on the microscope image (c), in which these two areas are highlighted, these two regions are reliable and separated.

potentially useful information.

The MA was run for all three of these situations, reflection only, transmission only, and the full data set. Given that there are only two tissue classifications used in these analyses, and the total confidence value, χ , for each pixel is set to 1, the information for labelling the sample is contained within the image of the confidence value for one classification. Where this value is above 0.5 the pixel is labelled as the tissue classification in question, whereas if it is less than 0.5 then it will be labelled as the other tissue. To this end the confidence value, χ of each pixel in the image was used to create a grayscale confidence image representing the likelihood that each pixel is adenocarcinoma tissue. The confidence images for cancerous epithelium were used and are shown in figure 6.9 for each of the different types of MA.

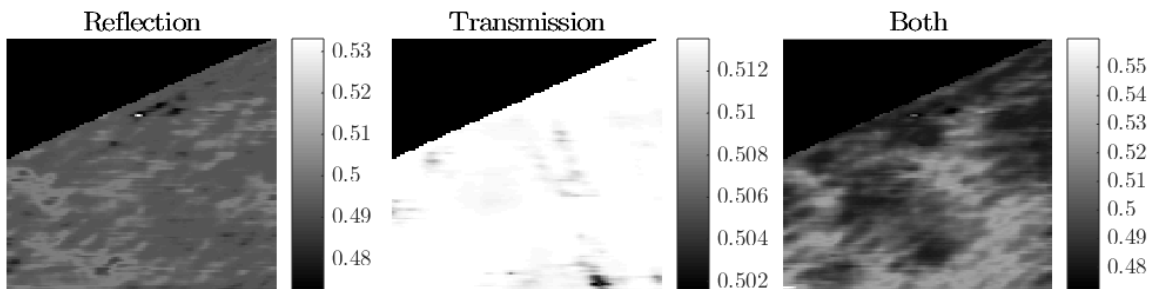


Figure 6.9: Confidence values for the cancerous epithelium tissue classification found for the three variants of the MA: reflection images only, transmission images only, and the full data set. The full data set gives a much more reliable labelling than the transmission or reflection data on their own, both of which are unable to reliably reproduce any labelling of the sample morphology. The full data set confidence image for cancerous epithelium shows a bright band of epithelial tissue labelled down the right side of the image, across the lower edge and up the left side, corresponding to epithelium tissue in the microscope image.

The reflection and transmission images alone do not produce a good labelling. The

transmission data especially gave a very small range of confidence values, ranging from 0.502 to 0.513, all of which are larger than the labelling threshold value of 0.5, meaning that the whole image area was labelled as cancerous epithelium. For the reflection data the confidence value range was larger, but still very close to 0.5, and does not seem to follow the sample morphology shown in the matched microscope image. The full data set, despite having similarly sized confidence values to the reflection MA, gives a mapping that is much more accurate. The confidence image for cancerous epithelium shows a bright band of epithelial tissue labelled down the right side of the image, across the lower edge and up the left side, corresponding to the epithelium tissue in the microscope image. The gap in the center of the upper region of cancerous epithelium on the right, seen in the microscope image, gives a much lower confidence for cancerous epithelium, meaning that it is labelled as cancerous stroma. For the SNOM images, a fully labelled image was not possible to obtain, so sensitivity and specificity values could not be calculated, but the labelling produced by the full data set of 6 images gives a good representation of the locations of cancerous epithelium tissue within the image area.

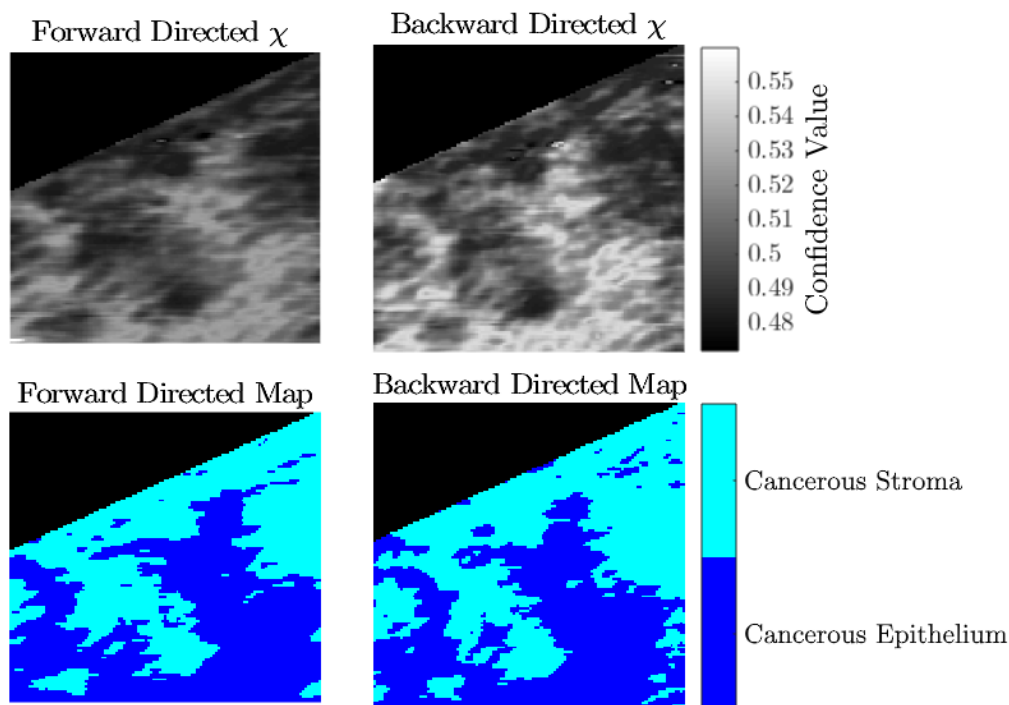


Figure 6.10: A comparison of the mappings produced by the MA of forward- and backward-directed images in set C. Both sets of images give mappings that show the same structures in the sample. There are slight deviations between the two images arising from the direction of scanning, the piezo-drive curves and noise in the image, but the two maps given by the MA are very similar.

Performing the tissue mapping again, with the same training set, on the backward-directed images of set C gives a very similar mapping. This mapping is shown in figure 6.10, with the two corresponding cancerous epithelium confidence value images. By highlighting the same areas of the two image sets, the MA must be sensitive to the information related to the position of the SNOM aperture, whether that is due to sample chemical variations or some other spatially dependent contrast mechanism.

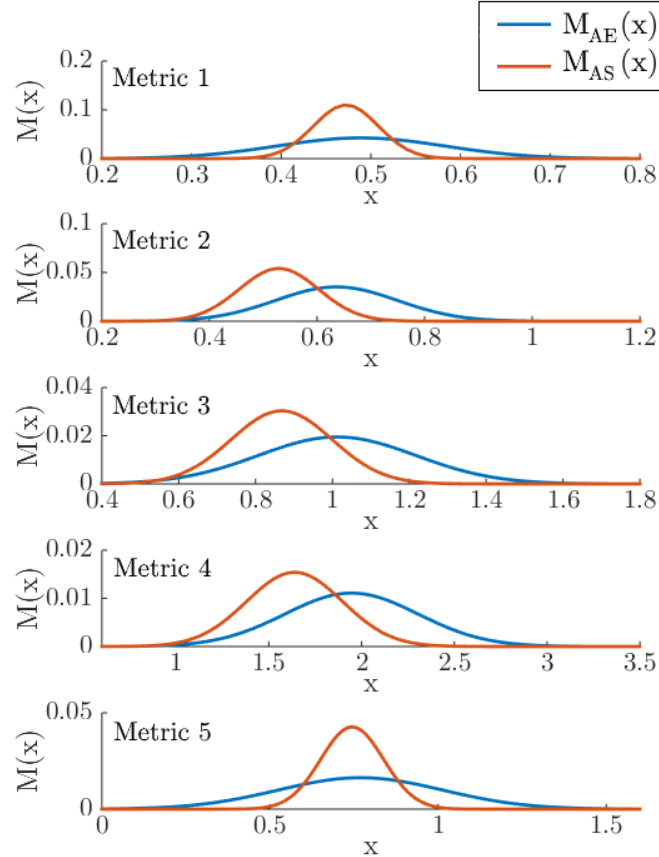


Figure 6.11: The five pairs of metric distributions identified as the most separated of the fifteen possible pairs of wavelengths for distinguishing the tissue classifications for set C. The curves all have a significant amount of overlap, causing confidence values that are very close to 0.5 and giving less reliable labelling of the tissues than was possible for FTIR-HSI data.

The metrics used for the full data set labelling show that the combination of the two imaging modes is necessary to give this tissue differentiation. The five metrics were:

$$\frac{8.05 \text{ Reflection}}{6.50 \text{ Reflection}}, \quad \frac{6.50 \text{ Transmission}}{7.30 \text{ Reflection}}, \quad \frac{6.50 \text{ Transmission}}{6.50 \text{ Reflection}}, \quad \frac{6.50 \text{ Transmission}}{8.05 \text{ Reflection}}, \quad \frac{6.50 \text{ Transmission}}{8.05 \text{ Transmission}}.$$

The second, third and fourth metrics are all cross-mode ratios, taking the 6.50 μm transmission image and finding the ratios with the three reflection images, while the first and fifth are from separate imaging modes. It is also of note that the most ‘useful’ wavelengths here

are 8.05 and 6.50 μm which are associated with DNA and protein biomarkers.

The distributions produced by these five metrics for each of the two tissue classifications are given in figure 6.11. All of the pairs of distributions have a significant area of overlap, meaning that the level of distinction between the two tissue types is low. The small confidence value range around 0.5 is as a direct result of the low level of separation of the metric distributions.

Set D

Following the success of labelling set C, the same process was applied to set D with a new training set defined, shown in figure 6.12. Two tissue classifications were used, as before, giving Barrett's epithelium (blue) and benign stroma (green) which were used to train the MA. The reflection data confidence images and associated mapping in both the forward and backward scan directions, given in figure 6.13, give a clear mapping with most pixels being one classification or the other, and very few with confidences ~ 0.5 , although the range of confidences is still very small. This is seen in the confidence images where the value tends to be either (relatively speaking) high or low but not in between.

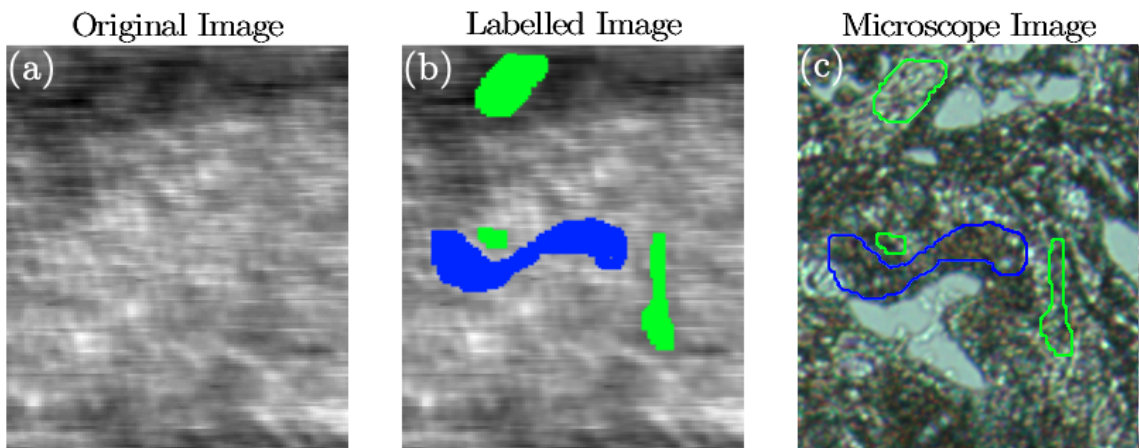


Figure 6.12: (a) One of the images from set D used to label the training set shown in (b) indicated by the blue (Barrett's epithelium) and green (benign stroma) coloured regions in the labelled image. (c) The same regions have been highlighted in the microscope image

The forward- and backward-directed labellings given by the MA for set D follow consistent structures in the images, the same regions have been labelled by the same classification in both, with variations that can be accounted for by the noise in the images and the slight non-linearity that remains from the piezo-drive after correcting as much as is possible. The

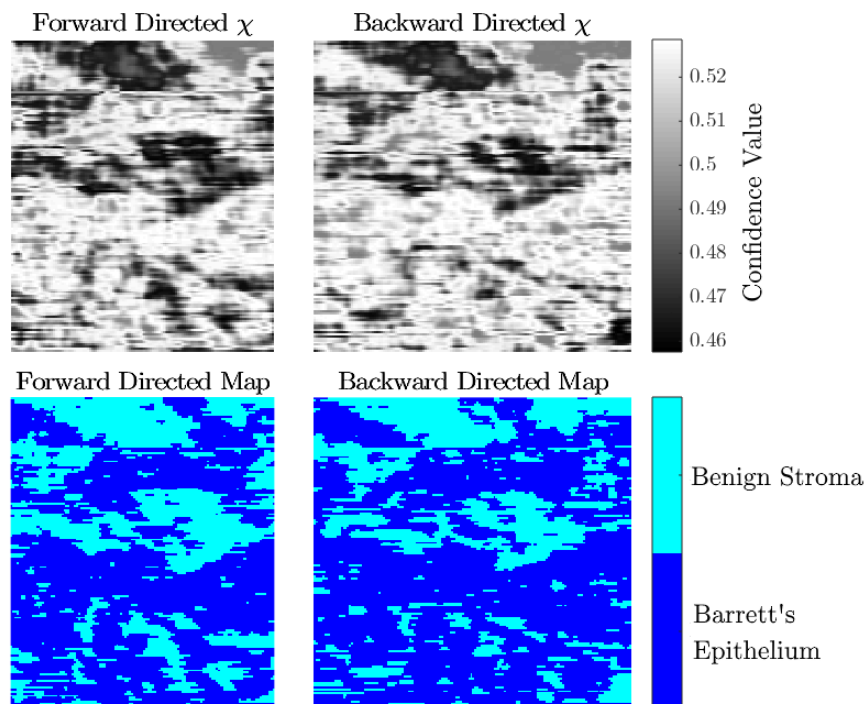


Figure 6.13: The Barrett's epithelium confidence images and corresponding tissue labelling produced by the application of MA to the reflection data for set D. Both the transmission data and taking the full data set give failed labellings in the same manner as the transmission data for set C did above.

mapping of tissue classifications does not, however, match up well with the sample morphology seen in the microscope image in figure 6.7. The same behaviour was noted for set C: three reflection images alone cannot accurately label the tissue classifications modelled in the image. Unfortunately both the transmission and full data set labelling did not produce a useful labelling of the sample. In the same way as for the transmission data for set C above, the confidence for one type of tissue consistently outweighed the other tissue type and the majority of the image area was labelled by one classification.

Conclusions from SNOM-MA

The application of MA to the SNOM sets above gave mixed results, with set C giving a good representation of the distributions of the two tissues within the image area but set D giving problems when the analysis was applied to this data set. The labelling problems for set D may have originated in several potential difficulties arising from applying MA to SNOM images. The first difficulty is that the SNOM images have a much higher noise level compared to the FTIR-HSI data, meaning that the metric values produced by a given classification will naturally produce broader distributions, and give fits that are less representative of a

consistent behavioural pattern and more likely to be affected by outliers, like those seen in figure 6.11. Furthermore, the SNOM has the potential to probe the tissue samples on a length scale much smaller than that possible with conventional microscopy techniques. While the four classifications cancerous epithelium, cancerous stroma, Barrett's epithelium and benign stroma worked well for the FTIR-HSI images, it is likely that the same simplified model of the sample does not hold for images sampled on this scale. It is not clear at which point the model would become invalid, nor what sort of more detailed model could be used: whether the classifications are simply made more specific, or whether each different region of the same tissue needs its own classification; the Barrett's epithelium tissue especially, as noted in section 4.5.5, can show very different presentations depending on the relative orientations of the section cut and the tissue. In addition, the lack of a classification corresponding to gaps in the sample will lead to mis-labelling of gaps as tissue and possibly effect the nearby pixels, seen in the labelling produced for set C where the gap in the sample in the center of the cancerous epithelium region on the right caused the gap and a region of cancerous epithelium around it to be labelled as cancerous stroma.

Another confounding factor that must be considered is the influence of the large offsets between the SNOM signal and topography. The lack of co-location between these signals means that the SNOM aperture is not maintained at a constant height from the surface, which can lead to topographic artefacts like the ones removed from Sets B and C, but will also give a more subtle influence to the image contrast that cannot be removed or normalised. This offset also adds the complication of matching the SNOM signal images to a different microscope image area. This is not as reliable as matching good topographic images as the contrast seen in the SNOM signal is much less dependent on how the sample appears under a visible light microscope. The difficulty in matching accurately also removes the ability to identify gaps in the image area that could have been used to train for an additional class.

Despite the problems in labelling the SNOM image areas using the MA above, the results obtained for set C show the potential for MA to label SNOM images. The complicated nature of the measured signal can be abstracted and circumvented by using MA and a map of tissues within the image can be reproduced. The two imaging modes were both required to give a good labelling of set C, but in set D the issues arising from the broad, overlapping distributions did not allow a reliable labelling to be acquired. Development of the MA to remedy this difficulty, using different fitting methods or another way of defining

the confidence coefficients, is necessary to provide a more reliable analysis technique for SNOM images.

In order to provide a useful analysis of a tissue sample it is necessary to expand the analysis beyond labelling a SNOM image using a sub-set of the pixels within it. As with the FTIR-HSI data a training set that would work to label any SNOM image set is needed. The problem with defining such a set is that the values in the SNOM images from one set to another are sufficiently variable, in a non-controllable manner, to make a training set defined from one image unlikely to successfully label another. It is only by using a training set defined from within the image that the relative behaviour of the individual SNOM signal images can be taken into account. Normalisation of the SNOM images to the FEL intensity gives a first approximation to remedying the variable nature of the values in each image, but more robust methods of standardising the values in SNOM signal images need to be determined in order to give more generally applicable analyses.

6.2.3 Other Approaches to Analysis

In order to progress the development of the SNOM image analysis, some method must be found of using the values in a SNOM signal image to produce another image with values that are independent of the confounding factors that can influence the value of the SNOM signal. Rather than using the values of each pixel, one possible method is looking at its relationship to the other pixels around it, giving a 'local' measure of some property that can be linked to the signal arising from the sample chemistry.

An example of this could be a local measure of the variability of the sample. In each of the three types of tissue, different structures and ordering should give a different value for this local variation, and a variation with wavelength depending on how these structural changes are mirrored in the biomarker distributions. Considering the DNA distributions given by $\lambda = 8.05 \mu\text{m}$ in each tissue should give different signatures. In cancerous epithelial tissue the cells are relatively uniform with enlarged nuclei occupying the majority of the cell, thus a low variability should be calculated. In Barrett's epithelium tissue the cells should have a relatively uniform presentation as well, but with two distinct regions formed by the basally located nuclei and the luminal cell body, giving concentric regions of low variability with a band of high variability at the transition zone in-between. The cancerous stroma and benign stroma tissues will be much less ordered and should give higher values of this

variability measure.

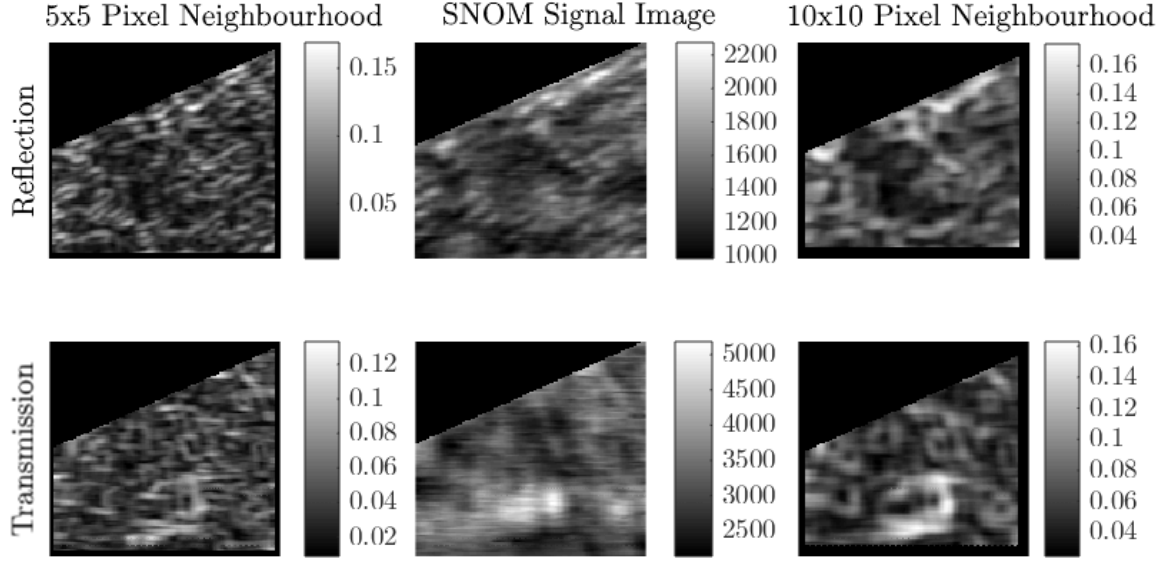


Figure 6.14: Sigma Over Mean (SOM) images made using the $8.05 \mu\text{m}$ SNOM signal images in reflection and transmission. The left hand SOM images were based on the SOM value for a 5×5 pixel area around each pixel in the original image, while the right hand SOM images were using a 10×10 pixel area.

To give a measure of the local variability, the standard deviation of a small area around each pixel was calculated, divided by the area mean, and the resulting values were used to form another image: $SOM(x, y) = \frac{\sigma_{local}}{\mu_{local}}$ referred to as the sigma over mean (SOM) images. By varying the size of this area, different length scales could be probed and very different images were produced. The SOM images at $8.05 \mu\text{m}$ wavelength are shown in figure 6.14. The two length scales used, 5×5 and 10×10 pixels, give very different types of images. For the shorter length scale, much detail is given in the SOM images, but they are also much more susceptible to the noise in the SNOM signal images. Conversely the longer length scale is less susceptible to noise, but gives a less detailed image. The detail in the image, however, is no longer a measure that is as important as it is in the SNOM images: if the SNOM signal was at high resolution then the SOM measure will have used this information to give the values within the calculated images and the length scales that the SOM values vary over will not necessarily be directly related to this resolution.

The transmission and reflection images originally had dramatically different value ranges, but after applying the SOM calculation, the ranges are almost the same. The values are now more dependent on the relative behaviour of each pixel to its neighbours, rather than on its numerical value. Using the longer length scale SOM image in reflection, it can be

seen that the cancerous epithelium tissue seems to give a more uniform lower value than the cancerous stroma, which gives speckled high values. It is clear that the shorter length scale images seem to be too susceptible to the noise in the images to draw out any of the sample behaviour. What is also clear, however, is that, while some of the behaviour described above can be seen in the longer length scale images, the tissues do not form sufficiently separated regions of correlated behaviour, and so a MA cannot be applied to this data.

These results do show that such a method gives a way of standardising the values within the SNOM images. Developing more reliable methods of analysis is necessary to further the understanding of the SNOM and the tissue imaged. In order to progress the analyses further, however, more reliable imaging and sampling of the SNOM signal images is essential. The development of the SNOM instrument during this work has significantly improved the quality and reliability of the images obtained, but further development and refinement is necessary.

6.3 Conclusions to Phases I-IV

The development of the SNOM instrument over phases I to IV dramatically improved the quality and reliability of the images that could be acquired. While for phases II and III these images were less reliable in terms of wavelength stability and the scan areas were less directed, the contrast seen in the SNOM images can be linked to general tissue structures and also helped identify potential issues with topographic changes.

The SNOM images acquired during phase IV of SNOM imaging were much more reliable and gave encouraging results from a simple MA based on four simplified tissue classifications across the two sets of images. The first set of these images, set C, was able to produce an approximate map of the cancerous epithelium tissue within the image area, using a small subset of pixels of cancerous epithelium and cancerous stroma to train the MA, identified using the matched microscope image. Although the second set of phase IV images, set D, did not produce as reliable a map, the structures identified in both the forward- and backward-directed images were consistent. The MA, therefore, was able to identify correlated behaviour within sub-regions of the SNOM images, though in the case of set D this was not indicative of the tissue areas in the matched microscope images. The results on set C demonstrate that the SNOM images obtained were internally self-consistent, in that the pixel values within

an image could be related to the tissue being imaged. There is no evidence, however that the pixel values in one set are compatible with those in another set.

For the MA to be applied more effectively, as a general technique that can be applied to any image set, a more standardised analysis must be done that is able to give images with values independent of any pedestal offset or scaling factor that might arise from undesired external sources. The simplification to two tissue classifications in each image is also not necessarily valid on the length scales probed by SNOM, and with complex tissue samples defining more appropriate and accurate classifications becomes almost impossible. To be able to identify potential chemical signatures of the different tissue components, the current focus of ongoing work builds on the findings presented here, using cell cultures of single cell phenotypes. These samples provide the opportunity to understand the building blocks of the tissues and further develop the ALICE IR-SNOM instrument. This development, phase V of SNOM imaging, is aimed towards using etched fibres instead of cleaved fibres. By etching sharp tips onto the end of the fibre, the aperture is potentially much smaller, and higher spatial resolution can be reached. A further, significant improvement that arises from etched fibres is that the potential topography-SNOM signal offset is greatly reduced, ideally to zero. Phase V and a brief outline of some preliminary results are described below.

6.4 Phase V: Further SNOM Development

Phase V of SNOM imaging builds upon the findings of phases I to IV and moves towards smaller, higher spatial resolution images on single cell culture samples. These samples are dramatically different from the tissue sections imaged in previous phases, the cells are grown onto the CaF_2 sample slide and then fixed in the same way as the tissue biopsy samples with formalin¹. Rather than sectioning a block of tissue, the cells produce a partial monolayer on the slide and have the tendency to spread out. Because of this the topography of these cells is less extreme than the tissue sections and much more smoothly varying. This allows etched fibres to be used more easily without as great a risk of breaking and therefore much higher spatial resolutions to be obtained.

The cell cultures give samples consisting of a single cell type grown from a single donor patient. Imaging on a sample consisting of one type of cell makes the information in an

¹Cell culture growth and processing was performed by Dr J. Dinesh Kumar, Department of Cellular and Molecular Physiology, Institute of Translational Medicine, University of Liverpool

image set less sensitive to the image area, and more consistent over multiple image areas, avoiding complications that arose from the spatial variation of the tissue samples. The cell types being investigated are commercial oesophageal adenocarcinoma epithelial cell lines (OE33 and OE19), a commercial oesophageal squamous cell carcinoma cell line (OE21, a non-Barrett's associated non-metaplastic carcinoma), and cancer-associated myofibroblasts (CAM), a component of the stroma tissue taken from a cancerous area and adjacent tissue myofibroblasts (ATM), the same type of cell from an area adjacent to the cancer, both of which were acquired by collaborators in the Institute of Translational Medicine, University of Liverpool Further details for these samples are given in appendix A. It is hoped that by finding a signature of each of these tissue components, and more, the formation and progression of oesophageal cancer can be characterised and understood.

6.4.1 Phase V Image Set

A preliminary image set acquired on a sample of OE19 oesophageal adenocarcinoma epithelial cells over a single epithelial cell using an etched and Au-coated fibre is shown in figure 6.15. The procedure used for preparing the slides is given in appendix B.3. The set of images were acquired in the transmission imaging mode, with a nominal size of $50 \times 50 \mu\text{m}$ with a pixel size of $0.67 \times 0.67 \mu\text{m}$. These images have excellent signal-to-noise and very clear optical contrast that differs at each wavelength. The topography image shows a single cell measuring approximately $40 \mu\text{m}$ across surrounded by bare CaF_2 slide, with a large nucleus characteristic of cancerous cells. The cell is larger than was typically seen in the tissue samples, a result of growing the cells onto the slide without the influence and pressure of other cells around it.

The wavelengths imaged in phase V correspond to specific absorption bands of biomarkers (see table 2.1), as was the case in earlier phases, with the addition of a lipid (fatty compounds) signal wavelength at $5.71 \mu\text{m}$. The cell samples do not require dewaxing and so the lipid signal, associated with the membranes of the cell particularly around the nucleus and the cell membrane itself, is preserved and can be imaged using the SNOM. The lipid image at $5.71 \mu\text{m}$ shows a relatively uniform signal, higher than over the slide, over the main area of the cell, with a slight reduction, corresponding to stronger absorption, where the nucleus is located. The images at 6.06 and $6.50 \mu\text{m}$, corresponding to the amide I and II bands of proteins, both give similar images, although the $6.50 \mu\text{m}$ image is noisier, with a

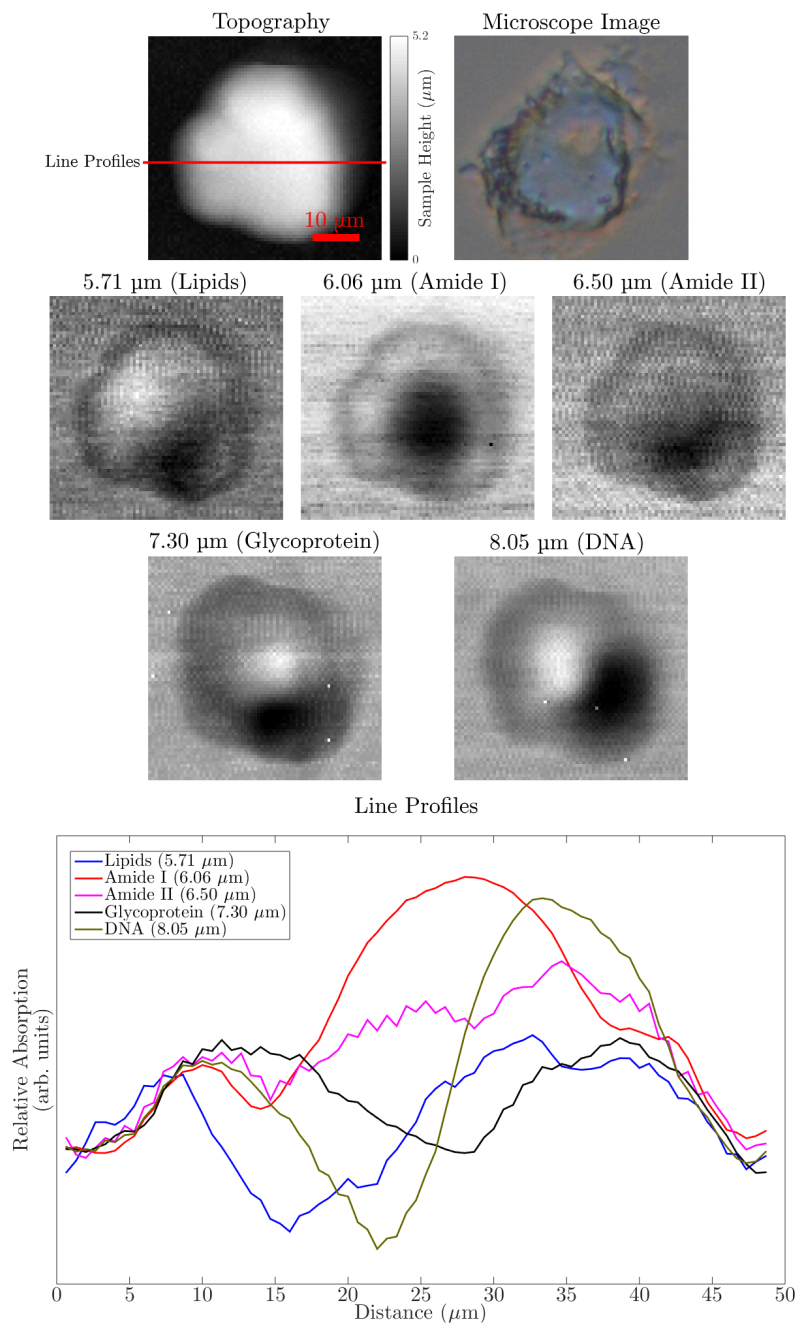


Figure 6.15: Transmission SNOM signal images acquired during phase V of SNOM imaging on a single OE19 oesophageal Epithelial cell, using an etched tip, showing very clear optical contrast linked to the cell structure. The images are nominally $50 \times 50 \mu\text{m}$ with 75×75 pixels. The cell nucleus can be easily seen in the images in the center-right of the lower half of the cell. In addition to the images line profiles have been extracted from the SNOM signal images, plotted against distance. The profiles were all taken from the line indicated in the topography and inverted to give a measure of the absorption at each position along the line. While the amide I signal shows a smooth, broad peak in the profile, the DNA signal displays a trough-peak combination. The amide I and amide II signals are well correlated, with the exception of the region where the DNA signal changes rapidly, taken to be the edge of the nucleus. The lipid profile follows the same general shape as the DNA signal, possibly a result of the lipid bilayer around the nucleus.

darker region in the center of the cell around the nucleus where the light is absorbed by the contents of the cell. In contrast to the amide images, the image at $7.30\ \mu\text{m}$ shows a darker cell compared to the slide background level, and a bright center region. The absorption at $7.30\ \mu\text{m}$ is less able to be assigned to a single type of biomarker, but this image should resemble glycoprotein and protein distributions in the sample. The fact that the image at $7.30\ \mu\text{m}$ image is so different from the amide images is interesting, and suggests that it is not necessarily appropriate to assign this to only these two biomarkers, and that other biological effects need to be considered. The image assigned to DNA at $8.05\ \mu\text{m}$ is also interesting, in that the center of the cell is much brighter than the background signal level over the bare slide, but adjacent to this bright region is a much more absorbing region that is much darker than the background level.

To highlight the relationship between the signals, line profiles have been plotted in the graph in figure 6.15, taken along the indicated line shown in the topography image. These profiles have been inverted to represent a measure of the absorption, and therefore the concentration of the corresponding biomarker, at each point along the line and have been normalised to the mean value of the first four points of the line profile in order to show the change relative to the value over the CaF_2 slide. The amide I profile in red ($6.06\ \mu\text{m}$) shows the absorption in the center of the cell as a smooth trough over the cell, while the green DNA profile ($8.05\ \mu\text{m}$) has a peak/trough combination over the same range. The DNA profile shows that the nucleus of the cell is located to the right of the center at the maximum of the $8.05\ \mu\text{m}$ profile, corresponding to the dark spot observed in the corresponding image in figure 6.15.

The amide II line profile in pink ($6.50\ \mu\text{m}$) shows a similar peak over the line as seen in the amide I profile, but with a small peak at the point where the DNA signal increases dramatically, associated with the boundary of the nucleus, further suggesting a chemical cause for the contrast seen in these images. The difference between the amide I and II images can be accounted for by the differing sensitivities of these absorption bands to the secondary structure of the proteins in the cell. It is well established that FTIR is capable of distinguishing structural changes in proteins, for example Litvinov et al. [93] used FTIR spectroscopy to investigate the α -helix to β -sheet transition in fibrin, a protein crucial for blood clotting processes. The different secondary structures, α -helices and β -sheets, are the result of different hydrogen bonding arrangements between the peptide bonds of the

proteins, resulting in differing chemical environments for the functional groups responsible for the absorption of IR light. The energy levels of the vibrational modes of the C=O stretch and N–H bend in the proteins are affected by these different environments and so the apparent positions and shapes of the corresponding peaks in IR spectra can vary significantly. The correlation between the variation in the amide II signal and the apparent location of the nucleus, compared to the smooth curve seen for the amide I signal, suggests that the different signals recorded could be a result of the presence of histone proteins, the proteins that bind to DNA and fold and compact it to fit in the cell nucleus. These histone proteins have a distinct chemical environment, hydrogen bonded to the DNA strands themselves, giving a different response to the signal measured by the SNOM.

The blue lipid signal profile ($5.71\ \mu\text{m}$) shows a similar shape to the DNA profile, but with a wider peak over the nucleus. This is likely to be a response to the lipid bilayers that form the membranes. For the majority of the cell area, the transmission image should be sensitive to two of these bilayers forming the upper and lower surfaces of the cell, while over the nucleus an additional two bilayers surrounding the nucleus. This explains the peak seen over the nucleus as well as the larger size of this dip in the signal than that seen for the DNA signal. One unexplained effect is the decreased lipid absorption over the rest of the cell compared to the background value, it is not clear why this is the case, and further investigations will allow more detailed conclusions to be drawn.

The spatial resolution of the images is hard to determine accurately as there are no sharp edges, but based on the optical response to the edges of the cell, it appears to be approximately $1\ \mu\text{m}$. The edges of the cell show clearly as increased absorption in all five wavelengths relative to the background value over the slide, but with differing widths, and the measure of resolution was determined from the sharpest, found for the lipid profile. These images were taken in the transmission imaging mode and as such have no enhancement of the resolution arising from the geometry of tip and sample as the reflection mode does. The $1\ \mu\text{m}$ resolution therefore gives an approximate measure for the size of the aperture at the tip of the fibre.

It can be seen from these images that while the SNOM signal images are very clear, the topography is somewhat ‘fuzzy’ as a result of a topographic artefact arising from a larger than ideal tip. The good resolution of the SNOM signal means that the size of the tip has not adversely affected the aperture size. It is also apparent that these was a small change to the

cell shape between imaging the 7.30 μm image and the 6.50 μm image acquired sequentially afterwards. A small piece of the cell seems to have been broken off or removed from the top left corner, but this does not seem to have influenced the tip in any way. By avoiding the area that changed, the image set can still be used to investigate the cell.

6.5 Future Work

The image set presented here and others are the subject of current analysis and further future experimental plans. A total of 234 SNOM image pairs (forward- and backward-directed) at different wavelengths on the five cell lines described above have been acquired and are currently being analysed. The development of the ALICE IR-FEL and SNOM instrument during this work has allowed clear, sub-cellular resolution IR images of oesophageal cells to be acquired. The images of cells provide many advantages over the tissue specimens images previously. The simpler presentation both aids analysis and minimises some of the confounding factors that influenced the SNOM signal on tissue, and the smaller size allows for higher spatial resolution images to be taken, giving a better investigation of the cells themselves. In terms of analysis, the images from cells have the potential to be standardised much more easily. One possibility is to standardise the images to the value corresponding to the slide with no cell on it, which was not possible with tissue, as the gaps in the tissue were often too small or poorly resolved topographically. Removing the topography-SNOM signal offset using etched fibres also minimises the topographic influence on the SNOM signal, and makes matching to image areas much more reliable. As seen in the images in figure 6.15 the optical contrast given by the cells is much easier to link directly to the features observable in both the topography and visible light microscope images.

To develop this work further studies are in progress that includes images taken on different types of cells, with additional experimental time to acquire high numbers of images on many different types of cell. This will give a stronger basis from which to approach the problem of understanding the behaviour of cancer, by allowing the characterisation of spectral and spatial signatures of different types and stages of the cells involved. Using SNOM to investigate these cell cultures gives the potential to understand the building blocks of the tissues that have been imaged previously, and to probe the sub-cellular development and progression of cancer at a length scale unreachable by conventional IR-microscopy.

This thesis demonstrates for the first time that the combination of an IR-FEL and fibre-based SNOM can yield images of biological materials such as cancerous cells, shown in section 6.4, and tissue [94] with an unrivalled high spatial and spectral resolution. A preliminary report on the application of this methodology, in collaboration with Lancaster University and Lancashire Teaching Hospitals NHS Trust Foundation, to cervical cancer cells [95] was recently published. In addition, more than 200 further high quality images have been acquired on oesophageal cell cultures and are currently under analysis. The instrumentation developed in this work has considerable potential for fundamental studies of the origin and nature of cancer and in the development of more accurate cancer diagnosis.

The application of any new technique, in this case SNOM using an IR-FEL, to an important problem such as the analysis of cancerous tissue can be fraught with technical difficulties which cannot be foreseen at the outset. The optimism associated with the development of such techniques to new fields is an important driver of scientific progress. However, if such projects are to be successful, it is essential that the technical difficulties are identified and addressed in a logical and coherent manner. This thesis gives a clear account of the technical hurdles associated with the application of an IR-SNOM to the cancer field. As this work shows these difficulties can all be overcome and the field is now ripe for exploitation.

APPENDIX A

SAMPLE INFORMATION

A.1 Tissue Samples

Oesophageal biopsy samples were obtained from patients recruited from a population that had been referred for diagnostic OGD either by their primary-care general practitioner or by another clinical service at the same hospital (Royal Liverpool and Broadgreen University Hospitals NHS Trust). The participants were aged 18 years and over and all gave informed written consent. The study was approved by Royal Liverpool and Broadgreen University Hospitals NHS Trust.

The samples were taken from patients with histories of either Barrett's oesophagus with no histological evidence of dysplasia, or Barrett's associated oesophageal adenocarcinoma. The samples were dewaxed in 10% formalin and embedded in paraffin wax before being cut to 5 μm thick sections using a microtome. The sections were then mounted on 2 mm thick CaF_2 disks for imaging by floating the wax sections on water onto the disks before gently heating the disk to bond the section to the surface.

A.2 Cell Cultures

OE33 and OE19 human Caucasian oesophageal adenocarcinoma and OE21 human Caucasian oesophageal squamous cell carcinoma commercial cell lines were obtained from HPA Culture Collections (Sigma, Dorset, UK). Human primary myofibroblasts had previously been generated from patients undergoing surgery for oesophageal cancer. The patients, and

the myofibroblasts obtained from them have previously been reported. This work had been approved by the Ethics Committee of the University of Szeged, Hungary and all patients gave written, informed consent.

Cells were cultured at 37°C in a 5% CO₂ atmosphere in Roswell Park Memorial Institute (RPMI 1640) growth media (Sigma) supplemented with 2 mM glutamine (Sigma), 10% v/v foetal bovine serum (FBS) (Invitrogen, Paisley, UK) and 1% v/v penicillin/streptomycin (Sigma) until they reached 70-80% confluence. The culture medium was replenished at two-day intervals.

A.3 Cell Culture Growth Procedure

Calcium fluoride discs (20 mm diameter x 2 mm thick, Crystran Ltd, Poole, UK) were sterilised using ethanol and rinsed with ultra-pure water and left to air-dry overnight. The discs were irradiated with UV for 30 minutes to ensure sterility. The sterile discs were then placed in each well of a tissue culture twelve-well plate (Corning, New York, USA). The cells ($2 \times 10^4 \text{ ml}^{-1}$) were seeded on each disc and incubated in a 5% CO₂ incubator at 37°C for two days. After two days the media was removed and the cells were fixed with a 4% v/v paraformaldehyde (PFA) (ThermoFisher Scientific, Loughborough, UK) solution and stored in 1x phosphate buffered saline (PBS) solution at 4°C until required.

APPENDIX B

PROCEDURES

B.1 Sample Dewaxing Procedure

The tissue samples were dewaxed prior to imaging by immersing the disks with the samples mounted on in three successive baths of Xylene (Sigma) for 15 minutes each before rinsing in isopropyl alcohol (Sigma) and leaving to air dry for at least 2 hours. This protocol produced wax- and contaminant-free samples very reliably.

B.2 Fibre Etching and Gold Coating Procedure

The chalcogenide (As_2Se_3) glass fibres are very fragile and have various layers to protect the core. The outer layers of the fibre were removed to leave about 2 cm of the 170 μm diameter core and cladding material. The end was then etched in a 7:3 mixture of sulphuric acid (GPR Grade, Fisher Scientific, Loughborough, UK) and 30 wt% hydrogen peroxide solution (Sigma), known as Piranha solution, covered with a 1 – 2 mm deep 2,6,10,14-tetramethylpentadecane (TMPD or pristane) solution (Sigma). The fibre was then lowered into the solution such that the last $\sim 4 - 5$ mm of the fibre was in the piranha solution which etched the fibre into a tip using convection currents, which are responsible for shaping the tip profile [96]. Once the end of the fibre had fallen off it was left for an additional 30 s before removal, then rinsed with methanol and dried with argon.

The Au coating was achieved by thermal evaporation in a dedicated high vacuum chamber, which incorporated a rotating fibre mounting facility in order to provide an even coated

film together with a film thickness monitor. The approximate size of the aperture was controlled by mounting the fibre rotation mount on a linear position sensitive mounting to adjust the position of the tip in the chamber. The etched fibres were then Au coated to give a thickness of ~ 30 nm on the thickness monitor. The resulting Au coated fibre tips were characterised using an optical microscope to check for general film uniformity, but could not, within the scope of this work, be assessed further in terms of appraising the aperture size due to constraints in budget and time.

B.3 Cell Slide Preparation for Imaging

Prior to imaging the CaF₂ slide containing the fixed cells were rinsed at least three times with ultra-pure (18.2 M Ω /cm) water (Millipore, Watford, UK). The rinsed slide was then removed from the well plate, the back surface wiped with water to ensure complete removal of any phosphate residue and then left to dry in the slide holder for a minimum of 90 minutes.

APPENDIX C

MATLAB CODE

This appendix details the use of MATLAB for the data handling and analysis during this work. The majority of the code used to process this data was purpose-built for specific applications, but much use was made of built-in MATLAB functions where possible.

C.1 RMie-EMSC

The RMie-EMSC algorithm was developed for MATLAB and so is ideal for application to the images obtained in this work. The parameters for the algorithm allow for a high degree of tunability for different imaging circumstances, but the suggested parameters were generally appropriate for the images obtained. The Matrigel spectrum included with the algorithm was used to perform the correction as no other reference spectrum could be obtained within the scope of this work. A spectral range of $1000 - 3800 \text{ cm}^{-1}$ was used (the maximal overlap between the supplied reference spectrum and the spectral range of the data collected) for scatterers of diameter $2 - 8 \mu\text{m}$ and average refractive index $1.1 - 1.5$ with all other parameters using the recommended settings. The algorithm used 10 values for scattering parameters and ran for 8 iterations.

C.2 Principle Component Analysis

In this work MATLAB's `pca` function was used with the singular value decomposition algorithm, without centering the data so as to preserve the values in the spectrum. Programmatically, `pca` takes an input matrix of the data set to be processed, with columns

representing the positions in the n dimensions (here the spectral values) and rows representing the observations (here the pixels of the image). The function produces several outputs: the *Loadings*, a matrix with columns containing the projection of the PCs onto the original dimensions of the data set in descending order of variance, the *Scores*, the input data rows projected onto the new PCs, and the *Variances*, a vector of variances of each of the PCs.

C.3 Hierarchical Cluster Analysis

The MATLAB functions used for HCA form a chain of processes. The `pdist` function takes an $m \times p$ matrix of m observations in p -dimensions and calculates the distance between the observations returning a vector of length $\frac{m(m-1)}{2}$ encoding the distances between every pair of points using the distance measure in equation 3.2. This output is then given to the `linkage` function which calculates an $(m - 1) \times 3$ matrix encoding the binary tree from which the dendrogram, and ultimately the clustering, is produced. To view the tree, the function `dendrogram` is used, displaying the links and distances between each of the joined clusters graphically. After determining the appropriate number of clusters, the matrix of cluster identifications is produced by the `cluster` function, taking the linkage matrix produced earlier and producing a vector of length m assigning a cluster number to each observation.

C.4 k-Means Cluster Analysis

The MATLAB function `kmeans` was used in this work to calculate the KCA results. This function takes the data input in the same way as HCA, a matrix of m observations \times p dimensions, but also requires the number of clusters to calculate, producing the vector of cluster identifications in the same format as HCA.

C.5 Fourier Transform Filtering

The MATLAB `fft2` and `ifft2` functions were used in this work to compute the FT using a fast Fourier transform algorithm and transform the masked FT back into an image. The transform was then shifted using `fftshift` to give the $f_x, f_y = 0$ pixel as the centre of the transform to aid visualisation and then the mask shown in figure 3.7 was applied simply by setting the undesired pixels to zero in the FT. The mask was defined in terms of the

centre and so is insensitive to changes in image size (if those changes are less than of orders of magnitude) which may have occurred due to the piezo non-linearity correction and series alignment performed in earlier stages of the SNOM preprocessing.

C.6 Other Functions

The other functions, as well as the MATLAB workspaces used during this work are available upon request from Prof. Peter Weightman, Oliver Lodge Laboratory, University of Liverpool.

REFERENCES

- [1] D. Forman, Review article: oesophago-gastric adenocarcinoma – an epidemiological perspective, *Aliment. Pharmacol. Ther.* **20** 55 (2004).
- [2] GLOBOCAN 2012 v1.0 - *Cancer Incidence and Mortality Worldwide: IARC Cancer-Base No. 11*, Available Via <http://globocan.iarc.fr/Default.aspx>, accessed 2016-10-22.
- [3] R. D. Odze, Diagnosis and grading of dysplasia in Barrett’s oesophagus, *J. Clin. Pathol.* **59** 1029 (2006).
- [4] R. K. Sahu, S. Mordechai, Fourier transform infrared spectroscopy in cancer detection, *Future. Oncol.* **1** 635 (2005).
- [5] S. Drake, *Galileo at Work: His Scientific Biography* (Courier Dover Publications) (1978).
- [6] E. Hecht, A. Zajac, *Optics*, 2nd edn. (DA Information Services, Reading, Mass) (1974).
- [7] P. R. Griffiths, J. A. De Haseth, *Fourier Transform Infrared Spectrometry*, 2nd edn. (Wiley, New York) (2007).
- [8] S. W. Smith, *Digital Signal Processing: A Practical Guide for Engineers and Scientists* (Newnes) (2003).
- [9] M. A. Lauterbach, Finding, defining and breaking the diffraction barrier in microscopy – a historical perspective, *Opt. Nano.* **1** (2012).
- [10] E. Abbe, *Archiv für mikroskopische Anatomie*, vol. 9 (F. Cohen) (1873).

REFERENCES

- [11] B. Alberts, A. Johnson, J. Lewis, M. Raff, K. Roberts, P. Walter, *Molecular Biology of the Cell*, 4th edn. (Garland Science, Ch. 4, pp. 191–234) (2007).
- [12] I. E. Clark, M. W. Dodson, C. Jiang, J. H. Cao, J. R. Huh, J. H. Seol, S. J. Yoo, B. A. Hay, M. Guo, *Drosophila pink1* is required for mitochondrial function and interacts genetically with parkin, *Nature* **441** 1162 (2006).
- [13] K. L. A. Chan, S. V. Hammond, S. G. Kazarian, Applications of Attenuated Total Reflection Infrared Spectroscopic Imaging to Pharmaceutical Formulations, *Anal. Chem.* **75** 2140 (2003).
- [14] P. Champness, *Electron diffraction in the transmission electron microscope*, Royal Microscopical Society (Great Britain) (Bios scientific publishers) (2001).
- [15] J. B. Pendry, Negative Refraction Makes a Perfect Lens, *Phys. Rev. Lett.* **85** 3966 (2000).
- [16] A. Grbic, G. V. Eleftheriades, Overcoming the Diffraction Limit with a Planar Left-Handed Transmission-Line Lens, *Phys. Rev. Lett.* **92** 117403 (2004).
- [17] E. H. Synge, A suggested method for extending microscopic resolution into the ultra-microscopic region, *Philos. Mag.* **6** 356 (1928).
- [18] E. A. Ash, G. Nicholls, Super-resolution Aperture Scanning Microscope, *Nature* **237** 510 (1972).
- [19] H. Heinzelmann, D. W. Pohl, Scanning near-field optical microscopy, *Appl. Phys. A* **59** 89 (1994).
- [20] U. Dürig, D. W. Pohl, F. Rohner, Near-field optical-scanning microscopy, *J. Appl. Phys.* **59** 3318 (1986).
- [21] T. Hartmann, R. Gatz, W. Wiegräbe, A. Kramer, A. Hillebrand, K. Lieberman, W. Baumeister, R. Guckenberger, A Scanning Near-Field Optical Microscope (SNOM) for Biological Applications, in D. W. Pohl, D. Courjon, eds., *Near Field Optics*, no. 242 in NATO ASI Series (Springer Netherlands) (1993).
- [22] D. W. Pohl, W. Denk, M. Lanz, Optical stethoscopy: Image recording with resolution $\lambda/20$, *Appl. Phys. Lett.* **44** 651 (1984).

- [23] G. Binnig, H. Rohrer, C. Gerber, E. Weibel, Surface Studies by Scanning Tunneling Microscopy, *Phys. Rev. Lett.* **49** 57 (1982).
- [24] D. J. Müller, J. Helenius, D. Alsteens, Y. F. Dufrêne, Force probing surfaces of living cells to molecular resolution, *Nat. Chem. Biol.* **5** 383 (2009).
- [25] E. Betzig, J. K. Trautman, J. S. Weiner, T. D. Harris, R. Wolfe, Polarization contrast in near-field scanning optical microscopy, *Appl. Opt.* **31** 4563 (1992).
- [26] E. Betzig, J. K. Trautman, T. D. Harris, J. S. Weiner, R. L. Kostelak, Breaking the Diffraction Barrier: Optical Microscopy on a Nanometric Scale, *Science* **251** 1468 (1991).
- [27] L. A. Nagahara, H. Yanagi, H. Tokumoto, Spectroscopic measurements of thin organic films using near-field scanning optical microscopy, *Nanotechnol.* **8** A50 (1997).
- [28] A. Cricenti, R. Generosi, P. Perfetti, J. M. Gilligan, N. H. Tolk, C. Coluzza, G. Margaritondo, Free-electron-laser near-field nanospectroscopy, *Appl. Phys. Lett.* **73** 151 (1998).
- [29] B. B. Goldberg, H. F. Ghaemi, M. S. Ünlü, W. D. Herzog, Characterization of Materials and Devices by Near-Field Scanning Optical Microscopy, *MRS Proceedings* **406** (1995).
- [30] A. Cricenti, R. Generosi, M. Luce, P. Perfetti, G. Margaritondo, D. Talley, J. S. Sanghera, I. D. Aggarwal, N. H. Tolk, A. Congiu-Castellano, M. A. Rizzo, D. W. Piston, Chemically Resolved Imaging of Biological Cells and Thin Films by Infrared Scanning Near-Field Optical Microscopy, *Biophysical Journal* **85** 2705 (2003).
- [31] A. Cricenti, S. Colonna, M. Girasole, P. Gori, F. Ronci, G. Longo, S. Dinarelli, M. Luce, M. Rinaldi, M. Ortenzi, Scanning probe microscopy in material science and biology, *J. Phys. D: Appl. Phys.* **44** 464008 (2011).
- [32] J. Generosi, G. Margaritondo, M. Kropf, H. Hirling, S. Catsicas, K. Johnsson, N. H. Tolk, D. W. Piston, A. Cricenti, Photobleaching-free infrared near-field microscopy localizes molecules in neurons, *J. Appl. Phys.* **104** 106102 (2008).
- [33] A. D. Smith, M. R. F. Siggel-King, G. M. Holder, A. Cricenti, M. Luce, P. Harrison, D. S. Martin, M. Surman, T. Craig, S. D. Barrett, A. Wolski, D. J. Dunning, N. R. Thompson, Y. Saveliev, D. M. Pritchard, A. Varro, S. Chattopadhyay, P. Weightman,

- Near-field optical microscopy with an infra-red free electron laser applied to cancer diagnosis, *Appl. Phys. Lett.* **102** 053701 (2013).
- [34] E. Betzig, R. J. Chichester, Single Molecules Observed by Near-Field Scanning Optical Microscopy, *Science* **262** 1422 (1993).
- [35] A. Cricenti, R. Generosi, M. Luce, P. Perfetti, J. S. Sanghera, I. D. Aggarwal, N. H. Tolk, D. Vobornik, G. Margaritondo, D. W. Piston, V. Manni, S. Grimaldi, A. Lisi, S. Rieti, Low-frequency electromagnetic field effects on functional groups in human skin keratinocytes cells revealed by IR-SNOM, *J. Microsc.* **229** 551 (2008).
- [36] B. Knoll, F. Keilmann, Near-field probing of vibrational absorption for chemical microscopy, *Nature* **399** 134 (1999).
- [37] D. V. Kazantsev, H. Ryssel, Apertureless SNOM imaging of the surface phonon polariton waves: what do we measure?, *Appl. Phys. A* **113** 27 (2013).
- [38] E. Yoxall, M. Navarro-Cía, M. Rahmani, S. A. Maier, C. C. Phillips, Widely tuneable scattering-type scanning near-field optical microscopy using pulsed quantum cascade lasers, *Applied Physics Letters* **103** 213110 (2013).
- [39] A. Dazzi, R. Prazeres, F. Glotin, J. M. Ortega, Local infrared microspectroscopy with subwavelength spatial resolution with an atomic force microscope tip used as a photothermal sensor, *Optics Letters* **30** 2388 (2005).
- [40] N. Hayazawa, Y. Inouye, Z. Sekkat, S. Kawata, Metallized tip amplification of near-field Raman scattering, *Opt. Comm.* **183** 333 (2000).
- [41] H. Amrania, L. Drummond, R. C. Coombes, S. Shousha, L. Woodley-Barker, K. Weir, W. Hart, I. Carter, C. C. Phillips, New IR imaging modalities for cancer detection and for intra-cell chemical mapping with a sub-diffraction mid-IR s-SNOM, *Faraday Discuss.* (2016).
- [42] D. B. Talley, L. B. Shaw, J. S. Sanghera, I. D. Aggarwal, A. Cricenti, R. Generosi, M. Luce, G. Margaritondo, J. M. Gilligan, N. H. Tolk, Scanning near field infrared microscopy using chalcogenide fiber tips, *Mater. Lett.* **42** 339 (2000).

- [43] D. T. Schaafsma, R. Mossadegh, J. S. Sanghera, I. D. Aggarwal, J. M. Gilligan, N. H. Tolk, M. Luce, R. Generosi, P. Perfetti, A. Cricienti, G. Margaritondo, Singlemode chalcogenide fiber infrared SNOM probes, *Ultramicrosc.* **77** 77 (1999).
- [44] D. Vobornik, G. Margaritondo, J. S. Sanghera, P. Thielen, I. D. Aggarwal, B. Ivanov, N. H. Tolk, V. Manni, S. Grimaldi, A. Lisi, S. Rieti, D. W. Piston, R. Generosi, M. Luce, P. Perfetti, A. Cricienti, Spectroscopic infrared scanning near-field optical microscopy (IR-SNOM), *J. Alloys and Compd.* **401** 80 (2005).
- [45] D. A. G. Deacon, L. R. Elias, J. M. J. Madey, G. J. Ramian, H. A. Schwettman, T. I. Smith, First Operation of a Free-Electron Laser, *Phys. Rev. Lett.* **38** 892 (1977).
- [46] M. K. Hong, S. Erramilli, P. Huie, G. E. James, A. G. Jeung, Scanning near-field infrared microscope with a free electron laser illumination source, *Proc. SPIE* **2863** 54 (1996).
- [47] E. Montgomery, J. R. Goldblum, J. K. Greenson, M. M. Haber, L. W. Lamps, G. Y. Lauwers, A. J. Lazenby, D. N. Lewin, M. E. Robert, K. Washington, M. L. Zahurak, J. Hart, Dysplasia as a predictive marker for invasive carcinoma in Barrett esophagus: A follow-up study based on 138 cases from a diagnostic variability study, *Hum. Pathol.* **32** 379 (2001).
- [48] P. Sharma, E. I. Sidorenko, Are screening and surveillance for Barrett's oesophagus really worthwhile?, *Gut* **54** i27 (2005).
- [49] V. Conteduca, D. Sansonno, G. Ingravallo, S. Marangi, S. Russi, G. Lauletta, F. Dammacco, Barrett's esophagus and esophageal cancer: an overview, *Int. J. Oncol.* **41** 414 (2012).
- [50] S. A. C. McDonald, T. A. Graham, D. L. Lavery, N. A. Wright, M. Jansen, The Barrett's Gland in Phenotype Space, *Cell. Mol. Gastroenterol. Hepatol.* **1** 41 (2015).
- [51] I. Ben-Porath, M. W. Thomson, V. J. Carey, R. Ge, G. W. Bell, A. Regev, R. A. Weinberg, An embryonic stem cell-like gene expression signature in poorly differentiated aggressive human tumors, *Nat Genet* **40** 499 (2008).
- [52] M. Meurens, J. Wallon, J. Tong, H. Noël, J. Haot, Breast cancer detection by Fourier transform infrared spectrometry, *Vib. Spectrosc.* **10** 341 (1996).

- [53] R. K. Sahu, S. Argov, S. Walfisch, E. Bogomolny, R. Moreh, S. Mordechai, Prediction potential of IR-micro spectroscopy for colon cancer relapse, *Analyst* **135** 538 (2010).
- [54] M. J. Baker, E. Gazi, M. D. Brown, J. H. Shanks, P. Gardner, N. W. Clarke, FTIR-based spectroscopic analysis in the identification of clinically aggressive prostate cancer, *B. J. of Cancer* **99** 1859 (2008).
- [55] Z. Hammody, S. Argov, R. K. Sahu, E. Cagnano, R. Moreh, S. Mordechai, Distinction of malignant melanoma and epidermis using IR micro-spectroscopy and statistical methods, *Analyst* **133** 372 (2008).
- [56] K. Gajjar, L. D. Heppenstall, W. Pang, K. M. Ashton, J. Trevisan, I. I. Patel, V. Llabjani, H. F. Stringfellow, P. L. Martin-Hirsch, T. Dawson, F. L. Martin, Diagnostic segregation of human brain tumours using Fourier-transform infrared and/or Raman spectroscopy coupled with discriminant analysis, *Anal. Methods* **5** 89 (2012).
- [57] M. J. Baker, J. Trevisan, P. Bassan, R. Bhargava, H. J. Butler, K. M. Dorling, P. R. Fielden, S. W. Fogarty, N. J. Fullwood, K. A. Heys, C. Hughes, P. Lasch, P. L. Martin-Hirsch, B. Obinaju, G. D. Sockalingum, J. Sulé-Suso, R. J. Strong, M. J. Walsh, B. R. Wood, P. Gardner, F. L. Martin, Using Fourier transform IR spectroscopy to analyze biological materials, *Nat. Protocols* **9** 1771 (2014).
- [58] T. D. Wang, G. Triadafilopoulos, J. M. Crawford, L. R. Dixon, T. Bhandari, P. Sahbaie, S. Friedland, R. Soetikno, C. H. Contag, Detection of endogenous biomolecules in Barrett's esophagus by Fourier transform infrared spectroscopy, *Proc. Nat. Acad. Sci.* **104** 15864 (2007).
- [59] D. Senthamil, A. Chezian, Ammonia Induced Biochemical Changes on the Muscle Tissues of the Fish *Cyprinus carpio* FT-IR Study, *Research Journal of Environmental Toxicology* **8** 117 (2014).
- [60] MathWorks United Kingdom - *MathWorks – Makers of MATLAB and Simulink*, <http://uk.mathworks.com/>, accessed 2016-06-04.
- [61] P. Bassan, A. Kohler, H. Martens, J. Lee, H. J. Byrne, P. Dumas, E. Gazi, M. Brown, N. Clarke, P. Gardner, Resonant Mie scattering (RMieS) correction of infrared spectra from highly scattering biological samples, *Analyst* **135** 268 (2010).

- [62] P. Bassan, H. J. Byrne, F. Bonnier, J. Lee, P. Dumas, P. Gardner, Resonant Mie scattering in infrared spectroscopy of biological materials—understanding the 'dispersion artefact', *Analyst* **134** 1586 (2009).
- [63] P. Bassan, A. Kohler, H. Martens, J. Lee, E. Jackson, N. Lockyer, P. Dumas, M. Brown, N. Clarke, P. Gardner, RMieS-EMSC correction for infrared spectra of biological cells: extension using full Mie theory and GPU computing, *J. Biophotonics* **3** 609 (2010).
- [64] A. Kohler, J. Sulé-Suso, G. D. Sockalingum, M. Tobin, F. Bahrami, Y. Yang, J. Pijanka, P. Dumas, M. Cotte, D. G. van Pittius, G. Parkes, H. Martens, Estimating and correcting mie scattering in synchrotron-based microscopic fourier transform infrared spectra by extended multiplicative signal correction, *Appl Spectrosc* **62** 259 (2008).
- [65] H. Martens, E. Stark, Extended multiplicative signal correction and spectral interference subtraction: New preprocessing methods for near infrared spectroscopy, *J. Pharmaceut. Biomed.* **9** 625 (1991).
- [66] M. J. German, A. Hammiche, N. Ragavan, M. J. Tobin, L. J. Cooper, S. S. Matanhelia, A. C. Hindley, C. M. Nicholson, N. J. Fullwood, H. M. Pollock, F. L. Martin, Infrared Spectroscopy with Multivariate Analysis Potentially Facilitates the Segregation of Different Types of Prostate Cell, *Biophys. J.* **90** 3783 (2006).
- [67] P. Lasch, W. Haensch, D. Naumann, M. Diem, Imaging of colorectal adenocarcinoma using FT-IR microspectroscopy and cluster analysis, *Biochim. Biophys. Acta* **1688** 176 (2004).
- [68] Q. Zhong, C. Yang, F. Großerüschkamp, A. Kallenbach-Thieltges, P. Serocka, K. Gerwert, A. Mosig, Similarity maps and hierarchical clustering for annotating FT-IR spectral images, *BMC Bioinformatics* **14** 333 (2013).
- [69] M. Blanco, J. Coello, H. Iturriaga, S. Maspoch, C. d. l. Pezuela, Effect of Data Preprocessing Methods in Near-Infrared Diffuse Reflectance Spectroscopy for the Determination of the Active Compound in a Pharmaceutical Preparation, *Appl. Spectrosc.* **51** 240 (1997).
- [70] G. Bertotti, I. D. Mayergoyz, *The Science of Hysteresis*, vol. 3 (Academic Press, Chapter 4), google-Books-ID: 88W3fMqNkRwC (2005).

REFERENCES

- [71] R. Zhao, L. Quaroni, A. G. Casson, Fourier transform infrared (FTIR) spectromicroscopic characterization of stem-like cell populations in human esophageal normal and adenocarcinoma cell lines, *Analyst* **135** 53 (2009).
- [72] H. Fabian, N. A. N. Thi, M. Eiden, P. Lasch, J. Schmitt, D. Naumann, Diagnosing benign and malignant lesions in breast tissue sections by using IR-microspectroscopy, *Biochim. Biophys. Acta* **1758** 874 (2006).
- [73] E. Gazi, M. Baker, J. Dwyer, N. P. Lockyer, P. Gardner, J. H. Shanks, R. S. Reeve, C. A. Hart, N. W. Clarke, M. D. Brown, A Correlation of FTIR Spectra Derived from Prostate Cancer Biopsies with Gleason Grade and Tumour Stage, *Eur. Urol.* **50** 750 (2006).
- [74] B. Bird, M. Miljkovic, M. J. Romeo, J. Smith, N. Stone, M. W. George, M. Diem, Infrared micro-spectral imaging: distinction of tissue types in axillary lymph node histology, *BMC Clin. Pathol.* **8** 8 (2008).
- [75] STFC ASTec - *ALICE Accelerator Diagrams*, <http://www.astec.stfc.ac.uk/ASTeC/Alice/accelerator/36006.aspx>, accessed 2014-03-12.
- [76] Thorlabs - *Plano Metallic Mirrors*, http://www.thorlabs.de/navigation.cfm?guide_id=2317, accessed 2016-06-08.
- [77] CorActive - *IR Fibers*, <http://coractive.com/products/mid-ir-fibers-lasers/ir-fibers/index.html>, accessed 2016-05-30.
- [78] C. Barchesi, A. Cricenti, R. Generosi, C. Giammichele, M. Luce, M. Rinaldi, A flexible implementation of scanning probe microscopy utilizing a multifunction system linked to a PC-Pentium controller, *Rev. Sci. Instrum.* **68** 3799 (1997).
- [79] M. Roper, Internal Report ACPO-RPT-0006: Wavefront Propagation Modelling of the ALICE IR FEL Beamline, Tech. Rep. ACPO-RPT-0006, STFC Daresbury Laboratory (2011).
- [80] Ophir Photonics - *Pyrocam IIIHR Beam Profiling Camera*, <http://www.ophiropt.com/laser--measurement/beam-profilers/products/Beam-Profiling/Camera-Profiling-with-BeamGage/Pyrocam-IIIHR>, accessed 2016-06-06.

REFERENCES

- [81] Crystran - *Silica Glass (SiO₂) Optical Material*, <http://www.crystran.co.uk/optical-materials/silica-glass-sio2>, accessed 2016-05-30.
- [82] Evanescent Optics Inc. - *The Wave Guide, Modes and Evanescent Tails*, <http://www.evanescentoptics.com/technical-info/?id=4>, accessed 2016-06-08.
- [83] J. Anderson, Leica Biosystems - *An Introduction to Routine and Special Staining*, <http://www.leicabiosystems.com/pathologyleaders/an-introduction-to-routine-and-special-staining/>, accessed 2016-06-06.
- [84] E. Betzig, G. H. Patterson, R. Sougrat, O. W. Lindwasser, S. Olenych, J. S. Bonifacino, M. W. Davidson, J. Lippincott-Schwartz, H. F. Hess, Imaging Intracellular Fluorescent Proteins at Nanometer Resolution, *Science* **313** 1642 (2006).
- [85] J. K. Trautman, E. Betzig, J. S. Weiner, D. J. DiGiovanni, T. D. Harris, F. Hellman, E. M. Gyorgy, Image contrast in near-field optics, *J. Appl. Phys.* **71** 4659 (1992).
- [86] E. Meyer, H. J. Hug, R. Bennewitz, *Scanning Probe Microscopy: The Lab on a Tip* (Springer Science & Business Media) (2013).
- [87] HITRAN - *HITRAN on the Web*, <http://hitran.iaao.ru/molecule/bands>, accessed 2014-11-20.
- [88] NIST - *Carbon dioxide*, <http://webbook.nist.gov/cgi/cbook.cgi?ID=C124389&Type=IR-SPEC&Index=1#IR-SPEC>, accessed 2014-11-20.
- [89] L. Quaroni, A. G. Casson, Characterization of Barrett esophagus and esophageal adenocarcinoma by Fourier-transform infrared microscopy, *Analyst* **134** 1240 (2009).
- [90] J. C. Y. Wang, J. E. Dick, Cancer stem cells: lessons from leukemia, *Trends Cell Biol.* **15** 494 (2005).
- [91] A. Cricenti, M. Luce, N. H. Tolk, G. Margaritondo, Near Field Optical Microscopy Imaging with a Free Electron Laser in the 110 Micron Spectral Range: Overview and Perspectives, *Nanosci. Nanotechnol. Lett.* **3** 913 (2011).
- [92] National Instruments - *NI myDAQ*, <http://www.ni.com/mydaq/>, accessed 2016-06-06.
- [93] R. Litvinov, D. Faizullin, Y. Zuev, J. Weisel, The alpha-Helix to beta-Sheet Transition in Stretched and Compressed Hydrated Fibrin Clots, *Biophys J* **103** 1020 (2012).

REFERENCES

- [94] M. Pilling, private correspondence, Dr Pilling, Prof. Peter Gardner's Lab, Manchester Institute of Biotechnology, is in the process of analysing SNOM results on prostate cancer tissue obtained in our collaborative work.
- [95] D. E. Halliwell, C. L. M. Morais, K. M. G. Lima, J. Trevisian, M. R. F. Siggel-King, T. Craig, J. Ingham, D. S. Martin, K. Heys, M. Kyrgiou, A. Mitra, E. Paraskevoidis, G. Theophilou, P. L. Martin-Hirsch, A. Cricenti, M. Luce, P. Weightman, F. L. Martin, Imaging cervical cytology with scanning near-field optical microscopy (SNOM) coupled with an IR-FEL, *Sci. Rep.* **6** 29494 (2016).
- [96] M. A. Unger, D. A. Kossakovski, R. Kongovi, J. L. Beauchamp, J. D. Baldeschwieler, D. V. Palanker, Etched chalcogenide fibers for near-field infrared scanning microscopy, *Rev. Sci. Instrum.* **69** 2988 (1998).